2023

EFFECTS OF CONFINEMENT ON IONIC LIQUIDS AND DEEP EUTECTIC SOLVENTS FOR THE DESIGN OF CATALYTIC SYSTEMS, ELECTROCHEMICAL DEVICES, AND SEPARATIONS

Andrew Drake
University of Kentucky, andrew.d.drake@outlook.com
Author ORCID Identifier:
https://orcid.org/0000-0002-6793-5658
Digital Object Identifier: https://doi.org/13023/etd.2023.388

STUDENT AGREEMENT:

I represent that my thesis or dissertation and abstract are my original work. Proper attribution has been given to all outside sources. I understand that I am solely responsible for obtaining any needed copyright permissions. I have obtained needed written permission statement(s) from the owner(s) of each third-party copyrighted matter to be included in my work, allowing electronic distribution (if such use is not permitted by the fair use doctrine) which will be submitted to UKnowledge as Additional File.

I hereby grant to The University of Kentucky and its agents the irrevocable, non-exclusive, and royalty-free license to archive and make accessible my work in whole or in part in all forms of media, now or hereafter known. I agree that the document mentioned above may be made available immediately for worldwide access unless an embargo applies.

I retain all other ownership rights to the copyright of my work. I also retain the right to use in future works (such as articles or books) all or part of my work. I understand that I am free to register the copyright to my work.

REVIEW, APPROVAL AND ACCEPTANCE

The document mentioned above has been reviewed and accepted by the student's advisor, on behalf of the advisory committee, and by the Director of Graduate Studies (DGS), on behalf of the program; we verify that this is the final, approved version of the student's thesis including all changes required by the advisory committee. The undersigned agree to abide by the statements above.

Andrew Drake, Student

Dr. Barbara L. Knutson, Major Professor

Dr. Zach Hilt, Director of Graduate Studies

EFFECTS OF CONFINEMENT ON IONIC LIQUIDS AND DEEP EUTECTIC SOLVENTS FOR THE DESIGN OF CATALYTIC SYSTEMS, ELECTROCHEMICAL DEVICES, AND SEPARATIONS

DISSERTATION

A dissertation submitted in partial fulfillment of the
requirements for the degree of Doctor of Philosophy in the
College of Engineering
at the University of Kentucky

By
Andrew Drake
Lexington, Kentucky
Co- Directors: Dr. Barbara L. Knutson, Professor of Chemical Engineering
and Dr. Stephen E. Rankin, Professor of Chemical Engineering
Lexington, Kentucky
2023

https://orcid.org/0000-0002-6793-5658

ABSTRACT OF DISSERTATION

EFFECTS OF CONFINEMENT ON PROPERTIES OF IONIC LIQUIDS AND DEEP EUTECTIC SOLVENTS FOR THE DESIGN OF CATALYTIC SYSTEMS, ELECTROCHEMICAL DEVICES, AND SEPARATIONS

Confinement of ionic liquids (ILs) and deep eutectic solvents (DESs) within mesoporous materials such as silica helps to control the local environment within the pores for applications such as catalysis, electrochemistry, and absorption. Silica thin films with 2.5 and 8 nm pores and micron-sized silica particles with pore diameters of 5.4 and 9 nm were synthesized to study the effect of nanoconfinement on ILs 1-butyl-3-methylimidazolium hexafluorophosphate ([BMIM][PF_6]), 1-butyl-3-methylimidazolium chloride ([BMIM][Cl]), and DESs reline and ethaline (choline chloride and urea or ethylene glycol). Silica thin films with vertically aligned, well ordered, and accessible pores were synthesized via the evaporation-induced self-assembly (EISA) method with cetyltrimethylammonium bromide (CTAB) templated EISA and titania doping giving 2.5 nm pores and Pluronic P123 (P123) templated films with a neutrally charged substrate giving 8 nm pores. Grazing incidence small angle x-ray scattering (GISAXS) and transmission electron microscopy (TEM) characterization gave evidence that the pores were aligned perpendicular to the substrate. Micron-sized mesoporous silica nanoparticles were synthesized through a sol-gel hydrothermal aging method where CTAB and P123 are used for templating and the pore diameter may be controlled through temperature, with higher temperatures giving larger pore sizes (2-12 nm).

Diffusion properties of confined ILs is relevant to understanding how solute molecules will behave when entering and moving through the confined IL. The diffusivity of a probe molecule to serve as an example solute are two fluorescent dyes rhodamine 6G (R6G), a cationic dye, and 4-(dicyanomethylene)-2-methyl-6-(4-dimethylaminostyryl)-4H-pyran (DCM), a neutral dye. The dyes were mixed with [BMIM][PF_6] and confined within mesoporous silica microparticles with 5.4 and 9 nm pores. The 9 nm diameter

particles were functionalized (tethered) with an IL-like molecule, 3-methyl-1-[3-(trimethoxysilyl)propyl]-1-imidazolium chloride [TMS-MIM][Cl]. The fluorescence recovery after photobleaching (FRAP) technique in confocal microscopy was used to estimate the diffusivity of the probes within the confined IL. Water saturated particles and pore diameter differences did not significantly impact the diffusion. The cationic dye had a lower diffusivity than the neutral dye from interactions between the dye and pore wall and anion of IL, while tethering increased the diffusivity of the dye by making the interior of the pore more hydrophobic. These results are important for diffusion considerations of species to catalytic sites in nanoconfined IL.

To further understand the interactions between ILs and the silica substrate, mesoporous silica thin films were synthesized with 3.5 and 8.5 nm pores and loaded with [BMIM][Cl]. The 8.5 nm pores were also functionalized with [TMS-MIM][Cl]. The films were characterized with x-ray photoelectron spectroscopy to measure the electronic environment of the elements within the sample. Bulk IL only has one peak in the nitrogen spectra due to the shared positive charge on the imidazolium ring. After confinement, a second peak at lower binding energy (BE) appeared from interfacial interactions between the imidazolium group in the IL with the pore wall of the silica. The reduction in positive charge on the imidazolium from this interaction causes a reduction in BE. This work gives insight into the ordering and location of the IL within the pores and is an important consideration since catalysis occurs on the surface of a material.

DESs are an emerging area of alternative solvents; often considered analogous to ILs, they are made of natural components that are customizable (choline chloride and urea being the classical example) but are still usually highly viscous so confinement is still advantageous. They can be used as a solvent for catalysis with metal additives, so the diffusion of $FeCl_3$ was studied using cyclic voltammetry. Mesoporous silica thin films with 3 and 8 nm pores were synthesized as above on Fluorine-doped Tin Oxide glass slides and used as a working electrode. The diffusion was calculated using the Randles-Sevcik equation where the diffusion can be calculated by varying the voltage scan rate and measuring the peak current output for either the oxidation or reduction event of the probe molecule. The diffusion of $FeCl_4^-$ in reline was hindered significantly in both pore diameters compared to the bulk value, while ethaline had pore size dependent accessibility. This result is beneficial to catalysis and electrochemical research with redox active species.

KEYWORDS: Mesoporous silica, nanoconfined ionic liquid, x-ray photoelectron spectroscopy, diffusion, tethered ionic liquid, deep eutectic solvent

Andrew Drake

7/25/2023

Date

EFFECTS OF CONFINEMENT ON IONIC LIQUIDS AND DEEP EUTECTIC SOLVENTS FOR THE DESIGN OF CATALYTIC SYSTEMS, ELECTROCHEMICAL DEVICES, AND SEPARATIONS

By
Andrew Drake

Dr. Barbara L. Knutson
Co-Director of Dissertation

Dr. Stephen E. Rankin
Co-Director of Dissertation

Dr. Zach Hilt
Director of Graduate Studies

7/25/2023
Date

DEDICATION

To my incredible wife Ashlin Niedzwiecki Drake. Thank you for your unwavering support through this journey.

ACKNOWLEDGMENTS

I would first like to express my most sincere appreciation and thanks to my advisors Dr. Barbara Knutson and Dr. Stephen Rankin for their guidance, support, and expertise throughout the course of completing this degree. Their guidance helped me overcome numerous challenges and has helped me gain confidence in my abilities as a researcher. Moreover, they consistently supported me in all my endeavors, gave me the freedom to pursue areas of personal interest, and remained devoted to my success. My committee members Dr. Qing Shao and Dr. Jian Shi provided excellent advice and opinions to help complete the work in this dissertation. I would also like to thank Dr. Folami Ladipo for synthesizing chemicals for us and exploring new areas together. Dr. Doo Young Kim also provided extremely helpful advice to help finish this dissertation.

In addition, I also appreciate my lab members Dr. Yuxin He, Dr. Arif Khan, Dr. Mahsa Moradipour, Joshua Garay, Aniruddha Shirodkar, Sayma Afrin, Kayla Daugherty, and Isfandiyar Eminli for their support and help. I also would like to thank Lauren Mehanna, who was a wonderful friend throughout my time at UK; our coffee breaks helped me make it through stressful days. The group in the electron microscopy department (Dr. Nico Briot, Dr. Dali Qian, and Dr. Mike Detisch) were always helpful and had good advice.

I cannot overstate the importance of the support of my wife, Ashlin Neidzwiecki Drake. Without her, completing this degree would have been impossible. In moments of uncertainty and exhaustion, she offered guidance and a comforting presence. She also celebrated every milestone and triumph with me along my journey and pushed me further to succeed. Her belief in me and willingness to go above and beyond to support me created a solid foundation for my success. It is with deep gratitude that I acknowledge the immense

role my wife played, and I am forever indebted to her. Finally, I want to thank the rest of my family, especially my parents, Dennis Drake and Dena Spiesz for their support.

TABLE OF CONTENTS

LIST OF TABLES

LIST OF FIGURES

CHAPTER 1. INTRODUCTION

Alternative solvent systems are necessary to reduce the hazards of working with toxic and volatile organic carbon solvents to improve safety and reduce emissions to the environment. Ionic liquids (ILs) are an alternative solvent that are salts made up of a poorly coordinated cation and anion and generally exist as a liquid below 100 °C.[1-3] The applications for ionic liquids have grown over the last couple of decades due to their attractive qualities such as low vapor pressure,[4] high thermal stability,[5] high ion conductivity,[6] and tunable properties.[7] ILs are well-suited for are the dissolution of lignin[8], removal of contaminants in waste streams[9], and carbon capture.[10] ILs have also been mixed with halometallate salts to enhance their catalytic behavior,[11] which enables them to be used for Friedel-Crafts acylation or alkylation, esterification, and other uses in catalysis.[12] ILs suffer from high viscosity, high cost, and questionable toxicity, so their use in industrial processes is currently limited.

Deep eutectic solvents (DESs) are a class of alternative solvents that are analogous to ILs.[13, 14] DESs are made of two components, a hydrogen bond donor and hydrogen bond acceptor, that are usually solid but form a liquid when mixed and are held together by strong hydrogen bonds.[15] In DESs, the real eutectic point temperature is lower than the ideal eutectic point temperature due to enthalpy driven deviations from ideality.[13, 16] DESs are similar to ILs because they have low melting temperatures, low vapor pressure, and are tunable.[17] They also typically have high viscosity but are more attractive than ILs because they have lower cost, are usually made from greener components that are safe[17, 18] (choline chloride, urea, glycerol, etc.), and are more sustainably sourced than ILs.

Supported systems have been developed to mitigate the problems associated with the use of ILs and DESs.[19, 20] Confinement significantly reduces the volume of solvent needed and makes them easier to work with. Thermophysical properties of ILs and DESs such as transport phenomena,[21, 22] crystallization and melting,[23, 24] and local assembly[4, 22] can change significantly upon confinement when compared to the bulk solvents. The goal of this dissertation is to relate the observed changes in thermophysical properties to local transport and solvent environments in confined ILs and DESs using mesoporous silica as a model substrate. Success of this work will advance the scientific techniques and understanding of confined alternative solvents to engineer nanoconfined solvent platforms for applications in catalysis, separations, and electrochemical devices.

Mesoporous silica materials are good candidates as supporting matrices because they have tunable porosity, scalable synthesis, stable chemical and thermal properties, and are easily functionalized.[25] The research presented in this dissertation is primarily focused on understanding imidazolium ILs and choline chloride-based DESs confined within mesoporous silica thin films and microparticles. The evaporation induced self-assembly (EISA) surfactant templated sol-gel process was used to synthesize mesoporous silica thin films and sol-gel synthesis was used to synthesize micron-sized mesoporous silica particles. Silica thin films with orthogonally oriented accessible pores of approximately 3.5 nm and 8.5 nm in diameter were synthesized[26,27] to allow the comparison of pore size effects on IL and DES confinement. Mesoporous silica micro particles were synthesized via a hydrothermal treatment.[28-30] The synthesis temperature affects the pore size of the resulting particles, ranging from about 2-10 nm.

In **Chapter 3**, confocal microscopy is used to investigate the transport properties and diffusion of dye-loaded IL confined within mesoporous silica microparticles using the fluorescence recovery after photobleaching (FRAP) technique.[31] Micron sized mesoporous silica particles are well-suited for this technique since they are large enough to visualize with the confocal microscope and the high intensity laser is able to completely pass through the particles. The ionic liquid 1-buty-3-methylimidazolium hexafluorophosphate ([BMIM][PF_6]) was used as the model IL since it is relatively low viscosity (ease of loading) and hydrophobic, minimizing the uptake of water during imaging process. The diffusion coefficients were compared for the neutral dye molecule 4-(dicyanomethylene)-2-methyl-6-(4-dimethylaminostyryl)-4H-pyran (DCM) for different pore diameters. The effect of water and grafting of an IL-like molecule, 3-methyl-1-[3-(trimethoxysilyl)propyl]-1H-imidazol-3-ium chloride ([TMS-MIM][Cl]) was investigated. A positively charged dye, Rhodamine 6G, was also used to examine the effect of charge on the probe on the transport properties. The results of this chapter demonstrate that pore diameter (5-9 nm) and IL hydration in nanoconfined ILs do not play a significant role in transport of solutes. Solute charge causes interactions between the charged IL components and the solute which slows down transport, while surface functionalization leads to improved transport. This shows that nanoconfined IL system diffusion is tunable based on surface and solute properties.

The ordering of ILs within mesoporous materials has an impact on their thermophysical properties as demonstrated by shifts in thermal transition temperatures[32] and evidence of interactions between the IL and support.[1] The work in **Chapter 4** presents research towards using x-ray photoelectron spectroscopy (XPS) as a technique for

elucidating interfacial interactions between [BMIM][Cl] and mesoporous silica thin films. [BMIM][Cl] is another commonly studied and representative IL and has a simple anion that can easily be characterized by XPS. The high-resolution spectra are used to elucidate interactions between the IL and silica with a direct measurement in support of molecular dynamics and quantum mechanical modeling of the system in which ordering of the IL along the pore walls is predicted.[33, 34] Changes in the electronic environment of the elements comprising the cation and anion are interpreted as a function of pore diameter and pore surface chemistry (tethering with an IL-like molecule, [TMS-MIM][Cl]). This chapter answers the question of how nanoconfined ILs behave at interfaces in mesoporous silica using a directly measurable technique. It also improves understanding of nanoconfined IL orientation towards the design of supported IL systems for catalysis and separations.

The use of XPS to examine the effects of confinement was extended to ionic liquids with halometallate ions, which are of intense interest due to their use in catalysis.[35] In confined systems, these catalytic sites may be present along the surface of the supporting material. The effect of confinement on the properties of confined [BMIM][$FeCl_4$] is investigated using XPS in **Chapter 5**. The results highlight fundamental differences between the interaction of ILs with halometallate and a traditional ILs in confinement.[36]

DESs are an emerging area of research and are promising solvents for electrochemical devices in energy storage.[37] The transport properties of iron (III) chloride and iron acetylaceontate within confined DESs is explored in **Chapter 6**. Choline chloride (ChCl) is mixed with urea (U) or ethylene glycol (EG) in a 1:2 molar ratio (ChCl:U or EG = 1:2) with heat to synthesize reline or ethaline, respectively. These DESs are commonly

studied and have wide electrochemical windows that make them good for electrochemical storage.[38] Using iron-based probes as the redox active molecules is attractive because iron is not as toxic or expensive as other metals used in electrochemistry. This investigation examined the effects of solvent components, probe charge, and pore diameter on the accessibility of iron to the surface of the electrode using cyclic voltammetry (CV).

The dissertation is concluded in **Chapter 7** by summarizing the highlights of each chapter and includes a discussion of future directions. Future directions include the tethering of DESs to mesoporous silica materials for supported DES catalysis applications. Tethering the DES to a support prevents leaching while facilitating its catalytic ability. Additionally, the future directions include using mesoporous titania thin films to oxidize lignin and melanoidin compounds. The oxidation of these compounds upgrades them to yield valuable platform chemicals using byproducts from the distillery and agricultural industries.

CHAPTER 2. BACKGROUND

2.1 Applications of Ionic Liquids and Deep Eutectic Solvents

ILs have been candidates for solvent applications and reaction media for several decades. They were discovered over a century ago in 1914, where Walden was one of the earliest scientists searching for salts that were liquid at low enough temperatures for his equipment to measure electrical conductivity without special adaptations.[39, 40] He synthesized ethylammonium nitrate, which had a melting point of 12 °C.[39, 40] The usefulness of ILs was not discovered for several decades. One of the first applications of ILs that led to their popularity was the demonstration of Friedel-Crafts reactions in [EMIM][$AlCl_4$] in 1986.[41] Since then, the amount of research using ILs for various applications has increased dramatically. Some of the more recent exciting applications of ILs are the extraction of lignin from biomass[42] and the electrochemical valorization of CO_2.[43]

ILs have been shown to be a useful solvent for the production of 5-(hydroxymethyl)furfural (HMF).[44] HMF is an important precursor to biofuels and may be a key product of commercial biorefineries.[45] The isomerization of D-glucose to D-fructose and subsequent dehydration to HMF catalyzed by Lewis/Brønsted acids has been identified as a potential route to HMF production, but suffers from low yields and unwanted byproducts using conventional methods.[44, 46] The use of halometallate components within ILs facilitate their use as catalysts for HMF production while being safer to handle at high reaction temperatures due to their high thermal stability and low volatility. Fourier

transform infrared (FTIR) spectroscopy has demonstrated that ILs possess Lewis and Brønsted acidity properties when halometallate ions are added[47] so that ILs may be used instead of traditional liquid acids like H_2SO_4 and HF. X-ray photoelectron spectroscopy (XPS) of halometallate ILs also show that their Lewis acidity correlates with shifts in binding energy of the metal and nitrogen of the imidazolium cation.[11] Therefore, ILs are not only a good solvent for biomass, but can also be used to upgrade it into more useful chemicals in a safer way than conventional solvents.

One of the most useful properties of ILs is their ability to be tailored to a specific task by changing the cation or anion. Common cations are dialkyl imidazolium, n-alkyl pyridinium, and tetraalkylammonium based cations, and some common anions are halides (Br, Cl, I), nitrate, tetrafluoroborate, hexafluorophosphate, bis-(trifluoromethanesulfonyl)imide, and metal halides, but this list is by no means exhaustive.[19] These ILs can be further tailored by adjusting the chain lengths on the cation. The following work will focus on using imidazolium based ILs 1-butyl-3-methylimidazolium chloride or hexafluorophosphate ([BMIM][Cl] or [BMIM][PF_6]).

In addition to catalysis, ILs are also useful in separations because they can associate through hydrogen bonding, hydrophobic interactions, or electrostatic interactions with solute molecules.[48, 49] Some combinations are favorable for use as a stationary phase in gas chromatography, owing to their high thermal stability and low volatility.[49, 50] The solubility of CO_2 is favored in many ILs, which makes them good candidates for carbon capture.[51, 52] Other solvents for separations have concerns and challenges of solvent evaporation, limited temperature range, and low solubility depending on the solute. ILs

address these challenges by having high thermal stability, low vapor pressure, and many opportunities for favorable interactions due to their complex structure.

Deep eutectic solvents are similar to ILs in that they are tunable, low melting, low vapor pressure solvents. The seminal work of DES was published by Abbott in 2003, where choline chloride and urea were mixed together in a 1:2 mole ratio with heating to yield a eutectic mixture with a melting point of 12 °C.[14] Eutectic mixtures that feature melting temperature depression are not new. Mixtures have been used for various applications such as tin and lead for soldering material, joining two metals together through brazing, or a mixture of $NaNO_3$ and KNO_3 to make a molten salt for solar energy storage. The unique characteristic of a DES is that the actual eutectic temperature has negative deviations from the ideal eutectic temperature.[13, 16] In Figure 1, an example phase diagram is presented for a eutectic mixture (adapted from Abranches).[16] A hypothetical ideal eutectic mixture between two components would have a eutectic temperature ($T_{E,\ ideal}$) that is lower than the average melting temperature at any point in the composition, but a DES has a eutectic temperature that deviated significantly from ideality (T_E) due to strong interactions between the components.[16, 53]

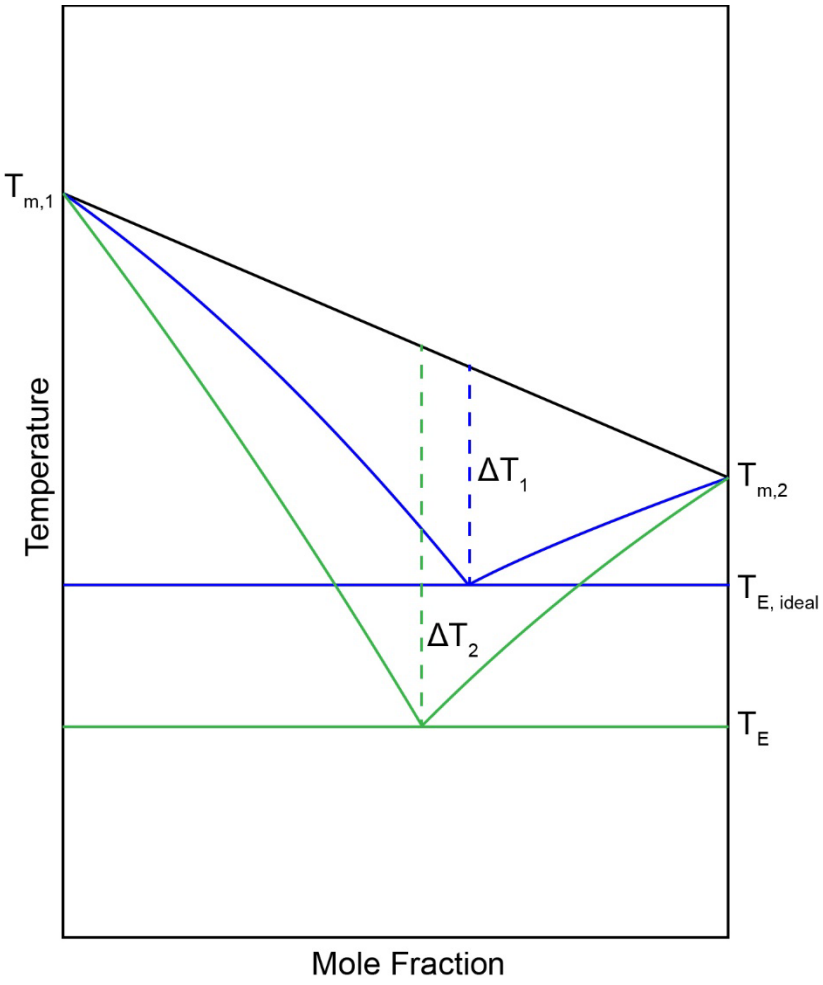

Figure 1. General representation of the phase diagram for an ideal eutectic mixture (blue) and deep eutectic mixture (green). Adapted from Abranches.[16]

DESs are made of a hydrogen bond donor (HBD) and hydrogen bond acceptor (HBA). The components used for the HBD and HBA are numerous in the literature. HBAs can range from organic salts like choline chloride, trimethylammonium chloride, or tetrabutylammonium bromide to metals such as $ZnCl_2$.[17] HBDs have an equally large number of choices, such as urea, glycerol, or glycolic acid. These have been branched out to natural components like betaine, vanillin, or menthol for either HBD or HBA to make so-called natural DES (NADES).[54, 55]

The applications of DESs are also vast and span many disciplines. One prominent application of DESs is the adsorption of CO_2.[56] Some DESs are able to dissolve lignin for valorization into aromatic compounds.[57] Recently, DESs were considered for applications in energy storage such as in redox flow batteries.[58] They have also been used for the electrodeposition of metals[37] and the Lewis acid catalyzed dehydration of carbohydrates to HMF.[59] DESs are advantageous in each of these applications because they, like ILs, have high thermal stability and low volatility. In contrast to ILs, DESs are made of greener and cheaper components and are easy to prepare, making them more economical and safer to use.

Confinement in mesoporous materials has potential processing advantages for both ILs and DESs. Both types of solvents usually have high viscosity, while ILs are more problematic due to their high cost. Another problem with these solvents is the potential to leak into product streams and the high affinity for the solvents to the products they make during catalysis. Recovery of solutes from these solvents is difficult because of their low vapor pressure.[60] A few common strategies to remove solutes from DES and ILs are liquid-liquid extraction using another solvent or precipitation of the solute using an anti-solvent,[60] but these could require use of VOCs, which reduces the benefits of ILs and DESs as alternative solvents. The challenges of product and catalyst recovery along with high viscosity make both solvent systems difficult to scale up in manufacturing, and the high cost and potential toxicity of ILs exacerbate the issues. Supported IL and DES systems may provide an approach to ensure that their advantageous properties can be maintained while reducing the drawbacks of viscosity, cost, and solvent loss.[56, 61]

2.2 Confinement of Ionic Liquids and Deep Eutectic Solvents on Mesoporous Silica Thin Films and Nanoparticles

The confinement of ILs and DESs within mesoporous materials exploits their favorable solvent properties while mitigating unfavorable bulk transport properties and costs. Mesoporous silica is an ideal support for alternative solvents because it offers a high surface area for interactions between the solvent/support, large volume within the pores, and is easily functionalized to obtain versatile and customizable surface chemistry. This dissertation focuses on mesoporous silica in two distinctly different forms – micron sized particles and thin films. Micron sized particles are useful because they have tunable mesopores on the order of 5-15 nm and are large enough in diameter to be observed using confocal microscopy.[30] More general applications of mesoporous silica particles are found in chromatography and drug delivery.[25, 62] With confined solvents such as ILs, they are also convenient to use in other characterization techniques like DSC or FTIR.[32, 63] Silica particles are made by the sol-gel technique where an acidic solution is aged at a certain temperature for several days while the silica condenses around micelles formed by added surfactants.[28] Above a certain critical micelle concentration, the nonpolar chains segregate from the aqueous phase into the oil phase and overcome the repulsion effect of the polar headgroups, forming micelles.[64] The type of micelle formed (spherical, cubic, etc) is determined by the ratio of the volume of a hydrophobic chain divided by the length of the hydrophobic chain and the area of the hydrophilic headgroup.[65] When the ratio is between 1/3 and 1/2, cylindrical micelles are formed.[65] The micelles begin to aggregate forming the template for the hexagonally ordered pores. A silica precursor (tetraethylorthosilicate, or TEOS, used in this study) condenses around these micelles to form the solid phase of

the mesoporous silica particle in several steps. TEOS first undergoes hydrolysis with water in the solution to exchange the ethanol groups with hydroxyl groups with silicon.[66] The hydrolyzed silicon can either participate in alcohol or water condensation to form alkoxy bonds with other silicon groups to complete the reaction.[66] Finally, after the silica pore walls are formed, the surfactant is removed using heating or washing with a solvent.

Mesoporous silica thin films have unique advantages and can create a uniform thin layer along a substrate. If the pores are vertically aligned, the pores are accessible to solutes. When coated on a microporous support, these thin films create a composite membrane. When coated on an electrode, the mesoporous thin films can be used in electrochemistry. Mesoporous silica thin films are synthesized using generally the same chemistry, but use a dip-coating evaporation induced self-assembly technique to form pores from the sol solution.[27] The thickness of the film is determined by the concentration of the surfactant and silica precursor solution. More dilute solutions lead to thinner films. Generally, the dip-coated films are on the order of 100-200 nm thick.[26] Mesoporous silica films can be deposited on several substrates such as glass slides, silicon wafers, anodic alumina membranes, and more depending on the anticipated application.[67]

The interaction of the hydrophilic headgroups with the substrate dictates the orientation of the pores. Hydrophilic headgroups prefer to interact with a glass slide substrate, leading to hexagonal pores that are oriented parallel with respect to the substrate and not accessible to solutes.[67] The hydrophilic and hydrophobic portions of the surfactant are equally attracted to a neutrally charged surface, yielding vertically aligned pores.[67] Therefore, the substrate and a top layer (another glass slide) are modified and sandwiched together after dip-coating to give vertically aligned porous silica films.[67] Another method

to vertically aligned pores (≈ 2.5 nm) was found by adding titanium isopropoxide to the surfactant (CTAB)/precursor mixture which causes anisotropic stress during calcination to form smaller pores without the need of substrate modification.[27]

The procedure for the physical confinement of ILs in silica primarily fall into one of two categories: *in-situ* or post-synthesis impregnation.[32, 68-70] *In-situ* confinement is achieved by adding the IL during the synthesis for the support material, such as the addition of [BMIM][PF_6] to the solution during sol-gel synthesis of mesoporous silica matrices.[71] ILs have also been used as structure directing agents in mesoporous silica like in the electrochemically assisted self-assembly of mesoporous silica thin films using [C_{16}MIM][Cl].[72] This dissertation focuses on the post-synthesis impregnation technique for ILs, where the solvent is added after synthesis of the support, typically via solvent deposition. An advantage of this technique is that the surfaces of the support may be functionalized prior to IL impregnation to further customize the material for specific tasks. Another benefit of the post-impregnation technique is that the amount of solvent confined within the pore is more easily controlled and the procedure easier to perform.[19]

In addition to physical confinement, surface modification of the support material with IL is possible. A large concern with using alternative solvents is their potential to leach into product streams. Tethering, or covalent attachment of the solvent to the substrate is a method of not only changing surface properties but also a way to avoid leaching. Silica is readily functionalized using a trimethoxysilylpropyl (or ethoxy) group to bond to the silica surface with the other side containing the desired functional group. This procedure is commonly used for surface functionalization such as for amines and thiols.[28, 73] Following this method, Gruttadauria[74] used 1,3-dimethyl-3-(3-trimethoxysilylpropyl)-

imidazolium chloride for the L-proline-catalyzed aldol reaction to tether an IL-like molecule to silica. Other groups have investigated using tethered ILs with iron present in the anion for catalysis.[75, 76]

Nanoconfined solvents behave differently than bulk-phase solvents. In confined ILs, the thermal transition properties can change in unexpected ways. For example, the melting temperature of [EMIM][Br] increased from 83 °C to 88 or 105 °C when confined within mesoporous silica with 7.1 and 3.7 nm diameter pores, respectively.[68] The direction of melting or crystallization temperature shifts depend on the IL being used and the supporting material.[19] Shifts in melting and crystallization temperatures are attributed to interactions between the IL and the pore wall, but may also be general confinement effects described by the Gibbs-Thomson equation.[77]

Changes in physical properties of confined ILs are typically explained by the interactions between the IL and pore wall.[19, 78] Computational tools such as molecular dynamics simulations (MDs) and quantum mechanics simulations are frequently used to probe these interactions since it compliments experimental work. For instance, Sha et al. used MDs to demonstrate the double layer stacking formation that occurs when [BMIM][PF_6] is near a negatively charged surface, with the $[BMIM]^+$ cation being closest to the surface.[79] The ability to form double layers is extremely important to consider when designing supported IL systems. Sha observes that the diffusivity within the double layer is significantly reduced, which would negatively impact transport for catalysis or adsorption.[79] In another study, Sieffert et al. use MD simulations of $[BMIM]^+$ with several anions (Cl^-, PF_6^-, BF_4^-, and Tf_2N^-) on quartz surfaces and found that the negatively charged anion participates in hydrogen bonding with the silanol (Si-O-H) surface groups, so the

double layering is reversed.[80] Sieffert also finds that the surface polarization impacts whether or not the anions will be attracted to this surface.[80] Molecular dynamics and other simulation techniques are highly valuable and support traditional experimental methods, for which it is more difficult to determine the exact orientation at the interface between the confined IL and the support.

Advanced characterization techniques are required for studying heterogeneous systems with a solid matrix and confined liquid. Additional techniques to further characterize the impact of nanoconfinement on solvent/support interactions and transport properties would expand the tools available to studying these systems and look at these properties from a different perspective. Electrochemical impedance spectroscopy (EIS) was used by our group to show the impact of confinement on the transport of hydrophobic and hydrophilic redox molecules through mesoporous silica thin films.[21] Diffusion of solutes within confined ILs can be directly measured by confocal microscopy.[30,81] Transport properties within confined ILs determine the rates of solute uptake and release and mobility, thereby affecting separations, catalysis and electrochemistry.

The surface interactions impact the catalytic properties of confined ILs. An example is the catalytic CO_2 cycloaddition of epoxides in [BMIM][$ZnCl_3$] confined on SilicaGel 60 (6 nm pore diameter, 50-200 micron diameter particle size).[69] Using different reactants, conversion and carbonate yield significantly improved when comparing neat IL to confined IL on the silica support.[69] The authors attribute this improvement to an increased CO_2 adsorption capacity due to higher surface area between the gas and IL and the reduced mass transfer limitations relative to the bulk IL. Additionally, the authors hypothesize that IL-cages are formed on the silica support, which enhances the local charge density and

modulates IL orientation at the solvent/support interface, subsequently leading to surface polarization and specific ion adsorption.[69]

Fourier transform infrared spectroscopy (FTIR) is a common technique used to identify interfacial interactions between ILs and support materials by examining shifts in the imidazolium ring carbon.[1, 82] He et al. used silicon wafers as the substrate to study the effects of confinement on ILs within mesoporous silica films using FTIR and demonstrated that the primary interaction site between the IL and silica was hydrogen bonding between the C-H carbon bridging the two nitrogen atoms in the imidazolium ring.[1] XPS expands on this by directly probing the interactions in a quantifiable manner. In this dissertation, deposition of mesoporous silica thin films onto silicon wafers facilitates the use of XPS to probe interfacial interactions between ILs and the substrate. Mesoporous silica thin films are particularly suitable for XPS since they are uniformly thick, well ordered, and have vertically aligned pores. The interactions between ILs and the support material are important to consider for catalysis applications, where a reactant may need to diffuse through the layer of IL and reach a surface reaction site. XPS can also measure metallic species toward designing confined ILs for catalysis where the oxidation state and strength of a halometallate IL are directly related to the ability of those ILs to perform catalysis.

While analogous to ILs, DESs are fundamentally different since they contain at least two different components, a hydrogen bond donor (HBD) and hydrogen bond acceptor (HBA), rather than a single species. Confined DES applications are still being explored but likely have similar applications as confined ILs. For example, the capacitance of choline chloride:ethylene glycol (ChCl:EG, or ethaline) was enhanced by over 10% when confined within 2D graphene oxide nanochannels, making the solvent good for

supercapacitor applications.[83] The use of DESs as solvents for adsorption may be enhanced through confinement by providing a larger surface area contact between the DES and solute solution. One prominent application of confined DESs is the selective adsorption of CO_2.[56, 84, 85] Confining increasing amounts of reline onto mesoporous silica gel (up to 10% (w/w)) increases CO_2 capture relative to the bare support.[56] This was hypothesized to be caused by strong hydrogen bonding interactions between CO_2, the DES, and silica support.[56]

The substrates for confined DESs are similar to that of ILs. Porous silica is a frequently investigated support owing to its tunability and low cost.[23, 56, 84-86] Graphene oxide nanoslits has also been characterized as a support in CO_2 capture.[87] The pore filling techniques is similar to ILs. Solvent deposition is the most common technique, were the DES is dissolved into another solvent and added to porous particles, mixed, then the other solvent is removed by evaporation.[84] For graphene oxide, a droplet of DES was placed on top of a porous graphene nanosheet that self-adsorbed into the pores, while excess DES was removed by spinning the sheet.[87] A route to DESs tethered to the substrate similarly to ILs is investigated in Appendix 4 using the work by Cao as a basis.[88]

DESs are often considered an analogue to ILs in their potential applications, but few studies report the properties of confined DESs. DES interactions with a substrate may be more subtle than ILs as DESs are primarily held together by hydrogen bonds,[15] and could lead to different interaction mechanisms with a host material in confinement. Characterization of confined DESs is a growing field with most studies using molecular dynamics.[89-92] MDs have determined that the cationic species and HBD will preferentially interact with the support interface, leading to atomic ordering at the nanoscale.[93] On charged surfaces, the cationic portion of the HBA in DESs typically resides closest to a

negatively charged surface, while the anionic portion resides closest to a positively charged surface.[92] It is hypothesized that this will lead to similar property changes in confined DESs as ILs since there is local ordering, but DESs also have a third component that imparts additional complexity to the system.

Theoretical MDs are supported by an increasing number of publications that investigate the interfacial properties of DESs with a substrate using techniques such as atomic force microscopy (AFM) or neutron scattering.[90, 94] FTIR results indicate that each component of reline (choline chloride:urea) preferentially interacts with the silica pore walls through hydrogen bonds when confined within mesoporous silica particles.[85] Both AFM and neutron scattering experiments agree with MDs that typically, the HBD (glycerol or ethylene glycol) forms the first layer or is a mixed layer along charged substrates.[90, 94]

To our knowledge, the effect of confinement on transport properties in DESs has not been reported. Bulk phase electrochemical techniques provide some basis for comparison for the transport properties of redox-active species in DES.[95, 96] Cyclic voltammetry has been used to show differences in probe transport for bulk phase DESs where less viscous DESs have faster transport and water can also speed up transport, and could be used to characterize confined DES properties in a simpler method than AFM or neutron scattering.[38, 96-99] In applications for separations, the ability to screen solutes based on charge, pore diameter, or solvent properties is desirable and could be probed using electrochemical methods such as cyclic voltammetry. Chapter 5 investigates the transport properties of iron chloride within reline (choline chloride:urea) and ethaline (choline chloride:ethylene glycol). This project lays the groundwork for future studies of confined DES transport. A better understanding of how and why these changes in properties due to

confinement affect transport and solvation will improve the design of confined solvents for future applications.

2.3 General Characterization Techniques

2.3.1 Confocal Microscopy

Confocal microscopy is a technique that is generally used to image biological samples using a laser to excite cells tagged with dyes. Different parts of a cell can be tagged with dyes that have different emission wavelengths and overlaid on top of each other to yield a single image where parts of the cell of interest are distinguishable from each other. The dyes are fluorescent, and therefore usually contain many aromatic rings within their structure, such as commonly used dyes like fluorescein or Texas red. In confocal microscopy, the dye in a sample is first excited by a laser with a certain wavelength corresponding to the excitation energy of the dye. The energy promotes an electron from the ground state (S_0 in Figure 2) to the excited state (S_1) within the dye, which quickly returns to the ground state, releasing light. After excitation but before returning to the ground state, the electron undergoes vibrational relaxation and is the reason that the emitted light has a longer wavelength than the excitation light.

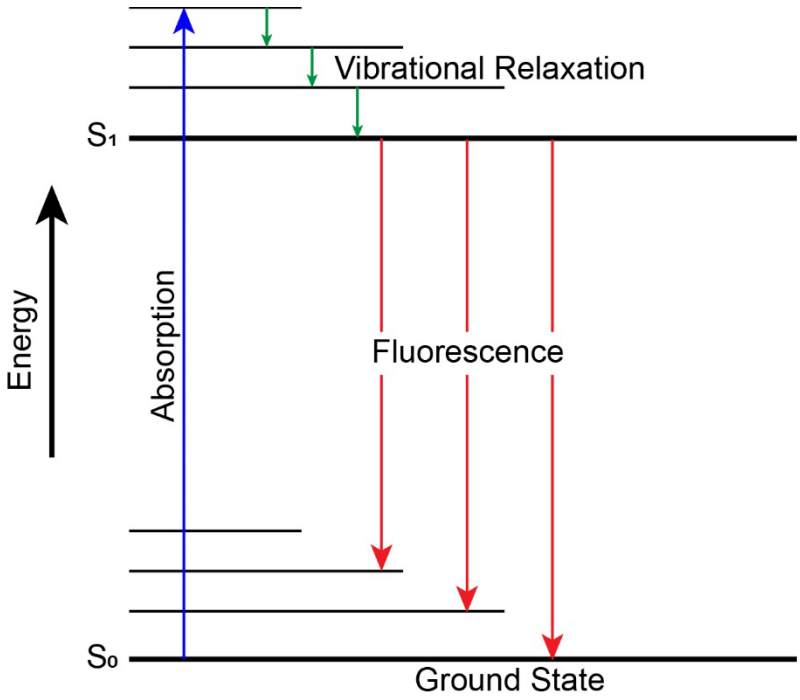

Figure 2. Jablonski Energy Diagram for the fluorescence process. A ground state electron (S0) is promoted to an excited state (S1) and undergoes vibrational relaxations before falling back down to the ground state.

A disadvantage to using confocal microscopy for imaging is that the dye can be irreversibly changed while imaging in a process called photobleaching. Photobleaching reduces the intensity of the fluorescence over time and can be a problem during long imaging times. However, this disadvantage can be harnessed to provide information about diffusivity of the probe molecule (the dye) in the sample by intentionally photobleaching a small area and allowing the surrounding dye to diffuse in to maintain equilibrium in a technique called Fluorescence Recovery After Photobleaching (FRAP). This technique was described first by Axelrod in 1976 to measure the transport of proteins and lipids in cell membranes.[100] Since then, it has been used extensively in the biological sciences to describe the transport of small molecules, especially with proteins.[101-103]

FRAP has been used to measure diffusion in bulk phase ILs. Santhosh et al. used FRAP to measure the diffusivity of 4-(*N*,*N*'-dimethylamino) benzonitrile (DMABN) within [BMIM][PF_6].[81] The group found that the diffusion coefficient of DMABN in the IL was 0.25 $\mu m^2/s$, while the Stokes-Einstein equation predicted a diffusivity of 1.75 $\mu m^2/s$.[81] They attribute this order of magnitude difference to the to a higher local microviscosity around the probe molecule than the bulk viscosity of the medium. In a more recent study, Stephens et al. used a zwitterionic, hydrophilic dye ATTO 647 dissolved in hexyl- and octylmethylimidazolium chloride of different micron-scale film thicknesses (1, 10 and 100 μm) when coating a glass surface.[104] An increase in the IL tail length from 6 to 8 generally led to a decrease in diffusivity, which was attributed to increased nanoheterogeneity of the longer hydrocarbon tail. Increases in temperature led to increased diffusion in both IL samples due to a weaker hydrogen bond network and subsequent increase in Brownian diffusion.[104] Interestingly, the thinnest film (1 μm) had the highest diffusion, with the other two film thicknesses (10 and 100 μm) having about the same diffusivity. They attribute this to a decreased local viscosity near the substrate due to intermolecular interactions.[104]

The confocal microscopy FRAP method employed in **Chapter 3** built upon previous work in our lab using FRAP to study the diffusion of lipids confined within mesoporous silica particles.[30] As in Chapter 3, micron sized mesoporous silica particles with different pore diameters (5.4 and 9 nm) were used as supports to investigate transport in confined lipids. The extension of this technique to ionic liquids was inspired by studies from Sasmal et al. and Werner et al.[105, 106]. In these works, fluorescence correlation spectroscopy (FCS) was used to determine bulk phase translational diffusion coefficients

of fluorescent probe molecules. Werner et al. used [BMIM][PF_6] as the solvent for cationic (rhodamine 6G), neutral (DCM), and anionic dyes (fluorescein) and found that the highest diffusivity was with the anionic dye, followed by the neutral, and finally the cationic dye.[106] The addition of 3% (v/v) water to [BMIM][PF_6] led to a roughly 65 to 100% increase in diffusion of the dyes due to a reduction in viscosity. Sasmal et al. revisited this topic using dyes that were closer to the same size but still either cationic (coumarin 480), neutral (DCM), or anionic (coumarin 343) and a different IL ([C_5MIM][Br] or [BF_4].[105] They found that in both ILs, the diffusion coefficient was fastest with the cationic probe and slowest with the neutral probe. This result demonstrates that ILs are complex and small changes to the components can have large impacts on their properties.

2.3.2 X-ray Photoelectron Spectroscopy

X-ray photoelectron spectroscopy (XPS) is a highly sensitive technique that is most commonly used in materials science for the characterization of metals. In XPS, x-rays are impinged upon a sample at a specific wavelength. With enough energy, the x-ray can cause core-level electrons to be ejected from the sample. These photoelectrons are very low energy and can be lost if they interact with anything in their path, so the entire process is kept under ultra-high vacuum (typically below 10^{-8} mbar). The photoelectrons are directed toward an analyzer where they are counted and sorted according to their kinetic energy (KE). KE is directly related to the amount of energy required to remove the electron from its orbital around the nucleus of the atom it came from, also known as binding energy (BE). The BE can be calculated using Equation 1:

$$BE = h\nu - KE - \varphi \quad (1)$$

where *hv* refers to the energy of the incident x-ray photon and ϕ is the work function of the spectrometer. This equation quantifies the photoelectric effect first described qualitatively by Hertz in 1887 and explained by Einstein in 1905 based off the early theory of quantum physics by Planck, earning Einstein a Nobel Prize in 1921.

The BE measured is highly sensitive to the element that a photoelectron came from, its core level, and the electronic environment around that atom. A relevant example is the XPS spectrum of carbon in fluorinated poly(vinyl alcohol) (PVA).[107] Beamson et al. changed the functionality of the alcohol portion of PVA to a ketone with one side toward the polymer backbone and the other containing CF_3 (see Figure 3). In interpreting XPS, carbon is frequently considered a contaminant and is used as a reference point for charge correction and the straight chain C-C bond is cited as having a BE of 284.5 eV.[108] In Beamson's work, they found four peaks in the fluorinated PVA corresponding to the four carbons labeled in Figure 3. From C(1)→C(4), the BE increases from 284.5 to 294 eV. Even the modest increase of 1.5 eV between C(1) and C(2) demonstrates that XPS is capable of differentiating slight differences in chemical environment.

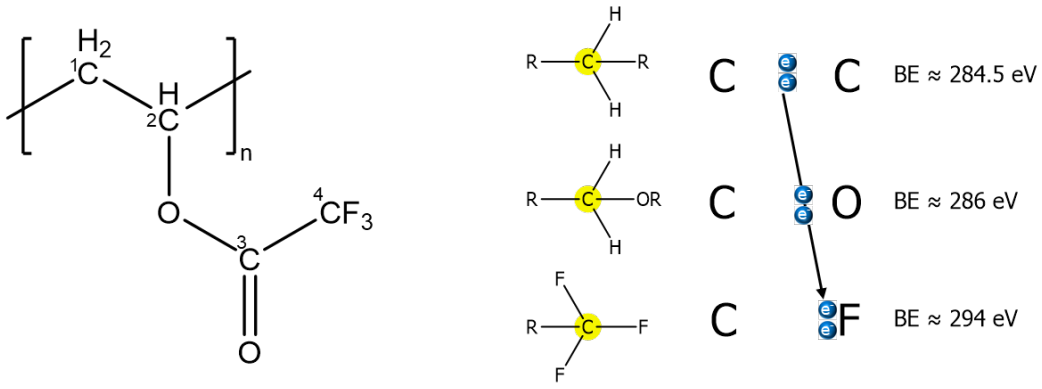

Figure 3. The structure of fluorinated poly(vinyl alcohol) adapted from Beamson et al.[107] On the right is three of the four carbon environments and a cartoon of the electron distribution between carbon and the right side R, O, or F group due to electronegativity.

XPS has been used extensively in IL characterization. An early example of ILs studied using XPS was by Smith to measure the spectra of 1-ethyl-3-methylimidazolium ethylsulfate.[109] This work was significant because it demonstrated that ILs had low enough volatility to be studied using UHV techniques. They also dissolved a catalyst ($Pd(OAc)_2(PPh_3)_2$) within the IL and showed that it was not very soluble in the IL since the oxidation state of Pd shifted from +2 to 0 after 90 minutes and showed that XPS could be used to screen the stability of catalytic ILs. This work was exciting because it opened the possibility of using XPS to study ILs for catalysis.

Since then, the amount of ILs studied with XPS has grown significantly.[110-115] The work that significantly motivated our work was a publication by Taylor that estimated the acidity and basicity of halometallate-based ILs using XPS.[11] Taylor found that increasing the amount of halometallate salts dissolved into ILs (namely $ZnCl_2$ into [OMIM][Cl]) led to a positive shift in the BE for the peaks related to nitrogen, the metal, and chloride. These

increases correlated well with Gutmann Acceptor numbers reported by Estager on the same system.[116]

Few XPS studies of confined ILs exist and their analysis and the interpretation of peaks is limited. For example, Su et al. used XPS to verify the integrity of [EMIM][Br] on mesoporous silica particles after confinement, but their main focus was to use the confined IL for the cycloaddition of CO_2 to propylene oxide.[69] Gupta synthesized silica ionogels with [EMIM][Br] and observed that there was extra peaks likely related to ILs interacting with the surface.[117] In this case, the IL was added during the synthesis of the ionogel. Silica particles are not an ideal substrate for XPS because they are round and need to be stuck to the surface to prevent them from flying away during analysis. Therefore, we investigate the interactions between confined ILs and silica using mesoporous silica thin films cast onto silicon wafers.

2.3.3 Grazing-incidence small angle x-ray scattering

Grazing-incidence small-angle x-ray scattering (GISAXS) is an important tool in characterizing mesoporous materials because of its ability to measure ordered structures at long length scales (up to 100 nm) and determine pore spacing and alignment of the pores.[26] While transmission electron microscopy (TEM) gives a direct image of the pore diameter, it is a destructive method. GISAXS leaves the sample intact for further use. GISAXS can be applied to a vast array of materials with significant ordering and is useful in protein characterization, polymer films, and inorganic materials such as nanoparticles.[118-120] The difference in electron density between two distinct materials gives rise to the peaks seen in the technique.

GISAXS is performed by placing the sample parallel with the x-ray beamline and tilting the sample at a slight angle of incidence. After scattering, the x-ray is captured by a 2D detector on the opposite side of the sample; see Figure 4 for an example of GISAXS scattering geometry. There are three components to the scattering, but the two measured vector components of scattered x-rays (k_f) on a 2D detector is in-plane (q_y, Figure 4) and out-of-plane scattering (q_z).

The angle of incidence (α_i) upon a sample is important as it determines the depth of x-ray penetration. Below the so-called critical angle, x-rays undergo total external reflection and only penetrate a few nanometers into the film surface.[121] This gives good sensitivity of features that are only present on the surface of a sample. Above the critical angle, the x-rays pass through the surface of the film, giving information for the whole film. While GISAXS can give information on nanoparticle arrangement and morphology on the surface of a substrate,[122] our group is primarily interested in oriented, porous, thin films. GISAXS provides information on pore spacing and orientation of the pores in these thin films. Vertically aligned pores correspond to having vertical bars on either side of the directly reflected x-ray, while horizontally aligned pores will have bars extending in the in-plane direction from the direct beam. Figure 4 has hypothetical example GISAXS patterns for both of these cases.

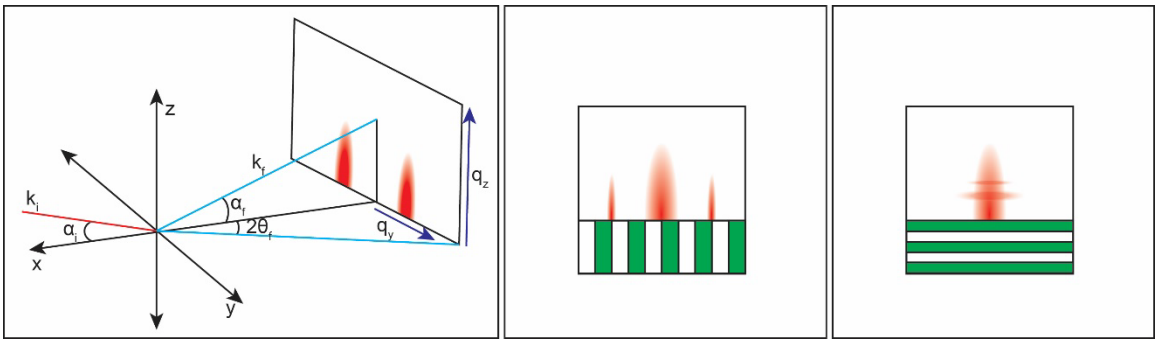

Figure 4. Left: GISAXS geometry where k_i and k_f are the incoming and exiting waves, α_i and α_f are the incident and exit angles, $2\theta_f$ is the in-plane scattering angle, and q_y and q_z correspond to the out-of-plane and in-plane scattering, respectively. The middle and right figures are hypothetical GISAXS patterns for vertically aligned structures within a thin film (green and white bars) and structures with a lamellar-type structure (green and white horizontal bars). Adapted from gisaxs.de and Anton Paar.

Our group developed a method for synthesizing oriented silica and titania mesoporous thin films and used a synchrotron x-ray source to show the orientation of the films with respect to the substrate.[26] Since then, our lab has used GISAXS to characterize mesoporous silica materials with both synchrotron and lab based sources.[1, 27, 123] In this dissertation (**Chapters 4 - 6**), GISAXS is used to characterize the structure of mesoporous silica thin films to determine pore spacing and verify vertically aligned pore structures. This is advantageous because it gives this information without significantly damaging the films. An alternative method to characterize the film structure and pore size is to use transmission electron microscopy (TEM) since silica not is conductive and SEM would be challenging.[27] However, TEM would require the films to be scraped off of the substrate and destroyed while also being challenging to image.

GISAXS can also be used to determine pore spacing within mesoporous particles, as demonstrated in **Chapter 3**. The basis of the theory is the same – different electron

scattering density between open pores and the silica walls leads to peaks seen in transmission SAXS. Since the pores are randomly oriented in a powdered state, the pattern observed is a ring corresponding to the pore spacing.[124]

2.3.4 Cyclic Voltammetry

Cyclic voltammetry (CV) is an electrochemical technique that is useful for investigating the oxidation and reduction processes of molecular species. It is performed using a 3-electrode cell containing a reference electrode to measure the applied potential, the working electrode to study the material of interest where either oxidation or reduction is takes place, and a counter electrode for the opposite redox reaction to take place. In an experiment, the potential is swept back and forth at a constant rate to measure the current produced by the electrochemical reaction. An example plot of a typical CV curve is found in Figure 5. The shape of the plot typically looks like a duck and is related to the diffusion of the redox-active species and its subsequent reaction at the surface.

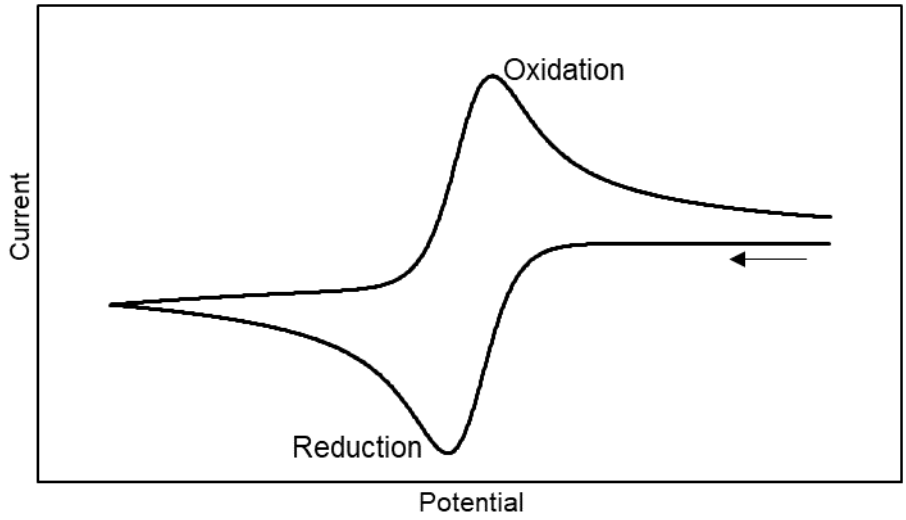

Figure 5. Typical cyclic voltammetry plot following the IUPAC convention. The potential is swept from the positive potential region to negative potentials, then back to positive. The right-hand/upper peak corresponds to oxidation while the left-hand/lower peak corresponds to reduction.

As the potential is scanned toward the reduction peak, the concentration of the species to be reduced is depleted, finally reaching a peak where the current is determined by the diffusion of that species to the surface from the bulk solution.[125] As reduction proceeds, the layer thickness of reduced species near the surface increases and slows down the diffusion of species to be reduced to the electrode, so the peak decreases. At the tail end, the potential scan direction is reversed, and oxidation begins to occur, producing the same effect. The peak separation depends on the kinetics of the reaction and the energy of activation for electrons to move between an electrode and a reactant. As the potential energy of the electrode is increased, electrons will move from the electrode to an unoccupied molecular orbital, or vice versa. If the rate constant is fast and the activation energy for the oxidation/reduction processes are low, electrons are easily moved back and

forth. If the potential energy needed to move an electron is large, a higher amount of current will be required to oxidize/reduce the analyte, and lead to peaks being farther apart. Assuming fast kinetics and a small potential energy barrier, Nicholson found that the reversible peak separation potential is 57 mV at 25 °C.[125, 126]

The diffusion of redox active probes can be determined by using the Randles-Sevcik Equation:

$$i_p = 0.446nFAC\left(\frac{nFvD}{RT}\right)^{1/2} \quad (2)$$

Where i_p is the peak current, n is the number of electrons involved in the electrochemical reaction, F is Faraday's constant, A is the area of the electrode, C is the concentration of the probe in bulk solution, v is the scan rate in the experiment, R is the ideal gas constant, T is the temperature, and D is the diffusion coefficient.[125] The Randles-Sevcik equation assumes that the reaction is completely reversible and has fast kinetics so that the reaction is limited by the diffusion of the redox species.

Cyclic voltammetry has been used with both DESs and mesoporous materials. One of the first groups to probe DESs with electrochemistry was Yue et al., who studied the electrochemical behavior of reline without a probe.[127] Using CV, Yue found that choline chloride underwent irreversible reduction at the cathode and formed ammonia gas and trimethylamine but determined that the amount of decomposition was small and did not affect the CV behavior of the solvent.[127] In another study, the redox behavior of iron chloride in reline was measured by Xu et al. as a potential new electrolyte for redox flow batteries.[38] They used CV to measure the diffusion of $FeCl_4^-$ (since $FeCl_3$ will create the complex with the free chloride from choline). The diffusivity of the probe is quasi-

reversible since the cathodic and anodic peak separation of 313 to 483 mV at scan rates of 10 to 50 mV/s is greater than 57 mV and the ratio of the oxidative and reductive peak current was close to unity. Quasi-reversible systems are slower than reversible and faster than irreversible systems and can be defined as having a rate constant greater than ($\sqrt{v}$) * 3.5 x10^{-4} and smaller than ($\sqrt{v}$) * 3.5, outside of which would constitute the irreversible and reversible regimes, respectively.[128] A range of the diffusivity is reported using the reversible and irreversible equations as the lower and upper bound, respectively. The resulting diffusivity was between 2.9 and 4.1 x10^{-8} cm^2/s, which is one order of magnitude lower than the probe in an aqueous system, but three times higher than an IL analogue.[38] Finally, Renjith et al. investigated the diffusion coefficients of relatively neutral or strongly positively/negatively charged probes in two DESs, reline and ethaline, as determined using the Randles-Sevcik equation.[129] Generally, ethaline had faster diffusion across all probe types due to its lower viscosity.

CV is also a tool used to characterize microporous materials. In an early study, Etienne measured the permeability of differently charged redox probes through mesoporous silica thin films.[130] The surface charge of silica is slightly negative due to the hydroxyl outer layer that can be deprotonated and is able to effectively screen charged molecules from the pores. This is demonstrated by Etienne et al. using mesoporous silica supported by an indium-doped tin oxide film on a glass slide. The current of the slightly negatively charged KI probe current is reduced in the silica coated electrode compared to the a non-coated ITO electrode, while the current from a more negatively charged probe $Fe(CN_6)^{3-}$ is almost entirely suppressed with these electrolytes in an aqueous system.[130] Conversely, attractive forces between positively charged probes and the pore walls are

found to enhance the current generated due to locally increased concentrations within the pores.[130] While it may be challenging to accurately measure diffusivity within porous electrodes,[131] a qualitative assessment of probe molecule transport through DES confined mesoporous silica is investigated in **Chapter 6**.

CHAPTER 3. EFFECT OF PORE-CONFINEMENT OF IONIC LIQUIDS ON SOLUTE DIFFUSION WITHIN MESOPOROUS SILICA MICROPARTICLES

3.1 Summary

The transport properties of the ionic liquid (IL) 1-butyl-3-methylimidazolium hexafluorophosphate ([BMIM][PF_6]) confined within silica microparticles with well ordered, accessible mesopores (5.4 or 9 nm diameter) was investigated. [BMIM][PF_6] confinement was confirmed using differential scanning calorimetry (DSC) and Fourier transform infrared (FTIR). The transport properties of the confined IL were studied using the neutral and cationic fluorescent probes 4-(dicyanomethylene)-2-methyl-6-(4-dimethylaminostyryl)-4H-pyran (DCM) and rhodamine 6G, respectively, through fluorescence recovery after photobleaching (FRAP) in confocal microscopy. The diffusivity of DCM in 9 nm pores is 0.026 ± 0.0091 $\mu m^2/s$, which is two orders of magnitude less than in the bulk ionic liquid. The pore size did not affect the diffusivity of DCM in unmodified silica nanopores. The diffusivity of the cationic probe is reduced by 63% relative to the neutral probe. Diffusivity is increased with water activity, where equilibrium hydration of the system leads to a 37% increase in DCM diffusivity. The most dramatic impact on diffusivity was tethering an IL-like methylimidazolium chloride groups to the pores, which increased the pore hydrophobicity and resulted in 3-fold higher diffusivity of DCM compared to bare silica pores. Subsequent exchange of the chloride anion from the tethering group with PF_6^- decreased the diffusivity to half that of bare silica. The diffusion of probe molecules is affected most strongly by the pore wall effects on probe interactions rather than by the pore size itself, which suggests that understanding pore wall diffusion is critical to the design of nanoconfined ILs for separations, catalysis, and energy storage.

3.2 Introduction

Ionic liquids (ILs) are salts with a typical melting point below 100°C,[1] where the combination of cation or anions can be changed to modify their solvent properties[2] and allow them to function as low vapor pressure "designer solvents".[3] ILs exist as a liquid at low temperatures because the component ions are large in size and have conformational flexibility, resulting in the liquid state being thermodynamically favorable.[132] Applications of ILs include the removal of toxic organics[48] or metals[9] from water, the extraction of organic materials from waste streams,[48] as solvents in catalysis,[133] for CO_2 capture,[10] as electrolytes in capacitors for energy storage,[134] and many other applications.[7] Several factors limit the use of ILs as bulk phase solvents: their cost, their viscosity and corresponding low mass transfer rate,[135, 136] and their potential toxicity,[137] emphasizing the importance of recovering ILs even in dilute solutions. Immobilization of ILs on surfaces or their confinement in a porous matrix with submicron path length takes advantage of their favorable solvent properties while mitigating the limitations of transport and solvent recovery in bulk phases.[10, 34, 61, 138]

Confinement of ILs in nanoscale pores alters their physical properties compared to the bulk phase. For example, shifts in the melting temperature (or other characteristic temperatures) of a confined IL have been observed as a function of pore wall chemistry, ionic liquid components, and the method of confinement (e.g. forming an ionogel or confining the IL after synthesis of the substrate).[19] Zuo et al. found by differential scanning calorimetry (DSC) that the glass transition temperature of 1-butyl-3-methylimidazolium tetrafluoroborate and 1-butyl-3-octylimidazolium tetrafluoroborate confined between alumina surfaces increased as the confinement length decreased due to interactions

between the BF_4^- anion and the positively charged alumina surface.[139] Other techniques to probe the interactions between ILs and pore walls in confined systems include solid-state NMR[24] and FTIR.[19] Molecular dynamics has been extensively used to study the layering of the ionic liquid cation with the pore walls through charge interactions,[79, 138, 140] from which changes in the physical properties are inferred.

In addition to physically loading the ILs on solid support or in pores, mesoporous silica has been modified by covalent attachment of IL-like moieties (such as 1-propyl-3-methylimidazolium chloride)[141] to the accessible silanol groups on the pore walls. Subsequently, additional (free) IL can be incorporated in the tethered pores. This method of confinement prevents leaching of the tethered IL and offers more stability of the supported IL.[142] Tethering an IL-like molecule to the surface changes the orientation and interactions of free IL with the surface, which is expected to affect the corresponding solvent properties in the pores. For instance, [BMIM][PF_6] and its analogues interact through H-bonding and electrostatic attraction of the cationic imidazolium ring to the surface of silica.[1] In the system of 1-octylimidazolium bis(trifluoromethylsulfonyl)imide confined within trioctylsilyl-grafted silica particles, the alkyl tail of the IL is oriented toward the functionalized surface of the silica if the pores are < 5 nm.[143] The surface can also be modified after tethering through ion exchange, with a goal of changing the counter ion of the tethered moiety and thus the IL itself. For example, the water contact angle of silica with tethered IL 1-alkyl-3-(3-triethoxysilylpropyl)imidazolium chloride on the surface increased from 24° to 42° after anion exchange from $[Cl]^-$ to $[PF_6]^-$, indicating that the surface became more hydrophobic.[144] The choice of anion is important depending upon the intended application of the material. For carbon capture applications, the CO_2 solubility

for [BMIM][PF_6] is greater than that of [BMIM][Cl],[145] so having [PF_6]$^-$ as the anion would be a better choice for the tethered species.

Mesoporous silica is frequently used as the solid substrate for the confinement of ILs because robust synthesis procedures lead to uniform, accessible, and tunable nanopores (5-15 nm) that are readily functionalized with various groups including amines or thiols.[73, 146, 147] Specifically, mesoporous silica provides high pore surface area and pore volume for IL loading,[32, 61, 117, 148] and ILs confined in mesoporous silica have been investigated as catalysts for asymmetric catalysis, Friedel-Crafts isopropylation, and trimerization reactions.[74, 149, 150] Confined ILs are also promising candidates for gas adsorption. Their high surface area, tunable properties, and high adsorption capabilities due to high affinity toward CO_2 make them ideal for carbon capture in gas separations.[151] Additionally, confinement reduces the amount of IL necessary to be used in practical applications, making them less cost prohibitive and improving safety by not allowing them to freely flow into waste streams or other solvents. Thus, in many applications, confinement of ILs into mesoporous materials makes them more attractive than bulk solvents.

Mesoporous silica can be synthesized as thin films, nano- or microparticles, or directly on membrane supports,[26, 30, 67] which can be broadly translated to applications of mesoporous silica in drug delivery, biosensing, separations, and catalysis. The sol-gel synthesis of ordered mesoporous silica used in this study uses self-assembled surfactants or block copolymers to form templates for the pores, followed by silica condensation with co-assembled micelles, and removal of the surfactant or block copolymer template to result in ordered, well defined pores.[152] This study uses micron-sized SBA-15 type mesoporous silica, which have well-ordered hexagonally arranged pores with a tunable pore size (5-15

nm). In addition, the micron-sized particles are sufficiently large to be imaged with confocal microscopy. An important benefit of supported or confined ILs as separation or reaction solvents relative to bulk ILs is the reduced transport path length through these viscous fluids. Traceable fluorescent probe molecules have been used to measure the translational diffusion in bulk ILs. Specifically, confocal microscopy has been used to study diffusion rates in bulk ionic liquids[81] through visualization of dye transport measured as fluorescence recovery after photobleaching (FRAP). FRAP takes advantage of the photobleaching of dyes excited by a laser in a defined area of the sample and the recovery of fluorescence over time as unbleached probe molecules diffuse back into the bleached spot. Other groups have used fluorescence correlation spectroscopy (FCS),[105, 106] a technique based on autocorrelation analysis of fluctuations of fluorescence intensity within a constant volume, to study the diffusivity of dyes in bulk ionic liquid systems. While the two methods provide similar information in principle, they differ in that FCS probes smaller volume and time scales (<1 s and diffusivity down to 0.05 mm^2/s) while FRAP probes larger volume and time scales (>>10 s and lower diffusivities than FCS).[153] Diffusion in bulk ILs is fast enough for FCS to be applied. Werner et al. used FCS to study the diffusivity within neat [BMIM][PF_6] using three differently charged dyes: rhodamine 6G (cationic), DCM (neutral), and fluorescein (anionic) and found that the anionic dye had the fastest diffusivity, followed by the neutral dye. Additionally, when water was added to the system, the diffusivity increased by approximately 65-70% for all dyes.[106] Sasmal et al. measured the diffusivity of three separate dyes within neat 3-pentyl-1-methylimidazolium bromide, [PMIM][Br], and [PMIM][BF_4] using FCS and found that the dye charge and hydrophobicity played a significant role in the diffusivity of the probe

from either attractive forces between the probes and IL or the reorientation of the probe within the IL.[105] FCS shows that changes to the probe or the environment in bulk solvents leads to significant changes in transport.

The transport properties in ILs are further affected by nanoconfinement. Many molecular dynamics studies have been performed of ILs near surfaces and confined in pores.[154] Specifically for [BMIM][PF_6] confined in 7.2 nm nanoslits with amorphous silica walls, Pal et al. reported a significant reduction in diffusivity at 300 K, where a strongly ordered first layer of ions at the pore wall had roughly 2 orders of magnitude less mobility than at the center of the pore.[155] In their case, the silica was modeled as a fully protonated, neutral surface with PF_6^- bound in the first layer by hydrogen bonding[156]; in real systems, deprotonation of silica is likely to lead to stronger charge interactions with $[BMIM]^+$ and possibly a stronger impact on diffusion. Similar findings of slowed diffusion near solid surfaces were found by MD for silica[157, 158] and other materials such as carbon.[159, 160] One study of graphene oxide nanopores suggested the possibly of enhanced diffusion due to the creation of free volume by movement of IL ions to the pore wall.[161] Nuclear magnetic resonance experiments have shown diffusion and relaxation dynamics consistent with slower dynamics due to nanoconfinement,[162, 163] for example with 2 orders of magnitude slower diffusion of both $[EMIM]^+$ cations and bis(fluorosulfonyl)imide anions.[164] Electrochemical measurements also show reductions in conductivity for nanoconfined ILs.[165-167] Small ions used by these techniques such Li^+ and H^+ are able to freely diffuse within nanoconfined ILs and self-diffusion is not significantly limited within mesopores,[143, 162] but larger molecules such as dyes can interact with the IL and change its diffusive properties.[106, 168-170] While there has been several studies using fluorescence to

measure diffusion of organic probes in bulk phase ILs and self-diffusion using NMR[162, 164], there are still opportunities to study the diffusion of solutes within confined ILs. Additionally, there are no studies of the effect of pore surface functionalization on the diffusion of probe molecules though confined IL except for in mesoporous thin films using electrochemistry[21].

In this work, we explore the diffusion of dye molecules within confined IL to probe effects of confinement using confocal microscopy. Confocal microscopy is employed to directly probe the effect of confinement on transport of fluorescent probe molecules in physically confined and tethered [BMIM][PF_6] within synthesized mesoporous silica microparticles with 5.4 and 9 nm diameter pores. [BMIM][PF_6] is a commonly studied hydrophobic ionic liquid that has been researched extensively as a model IL due to its relatively low viscosity and low melting point. A hydrophobic IL was required since the particles were suspended in water during the confocal experiments. The bare particles were characterized with nitrogen porosimetry to determine the pore diameter and FTIR and DSC were used to confirm confinement of the IL. The effect of pore size was studied by changing the average pore diameter of the silica through the hydrothermal aging temperature. Neutral (DCM) and cationic (R6G) probes were used to understand the effect of dye charge on transport. The effect of water uptake was studied by immersion of the particles with confined IL in water for 24 hours since most ILs have at least a small amount of water in them and readily pick up water from the atmosphere or contact of hydrophobic ILs with aqueous media. The walls of the silica particles were functionalized with an IL-like molecule, 3-methyl-1-[3-(trimethoxysilyl)propyl]-1H-imidazol-3-ium chloride ([TMS-MIM][Cl]), to examine how tethering (which is a strategy to control IL leaching)

might affect the diffusion of the probe molecules. The results below will show that the transport through confined IL on mesoporous silica is primarily dominated by surface and electrostatic interactions. The insensitivity of transport to pore diameter and water effects in supported ILs shown below also means they are flexible and can be used in situations where water may be present. Confined ILs may best find their application in CO_2 capture in flue gases since they have a high affinity to the gas and may be regenerated after use. This work shows that gas adsorption would likely not be dependent on water in the gas stream or particle design, leading toward more cost-effective solutions to limit greenhouse gases.

3.3 Methods and Materials

3.3.1 Materials

The ionic liquid 1-butyl-3-methylimidazolium hexafluorophosphate (>97%) ([BMIM][PF_6]) was purchased from Sigma Aldrich. 200 proof anhydrous ethanol was purchased from Koptec (Deacon Labs). For the synthesis of microparticles, Pluronic 123® was purchased from BASF, tetraethylorthosilicate (99%) from Alfa Aesar, hydrochloric acid (6 N) from VWR Chemicals BDH, and cetyltrimethylammonium bromide (CTAB) (99.8%) from MP Biomedicals. The dyes used were 4-(dicyanomethylene)-2-methyl-6-(4-dimethylaminostyryl)-4H-pyran (DCM) (>95%) from TCI America and rhodamine 6G (R6G) (>99%) from Acros Organics. Chloroform was purchased from Macron Fine Chemicals. All materials were used as received without further purification.

3.3.2 Silica Microparticle Synthesis

The synthesis of micron-sized mesoporous silica particles with controlled pore size via hydrothermal treatment was adapted from Gartmann's modified procedure[28] from the work of Katiyar,[29] and previously used in our lab.[171] Initially, a few grams of P123 in a beaker was melted in an oven at 80°C, of which 3.10 grams was poured into a round bottom flask. 0.465 grams of CTAB was dissolved in 20 mL of DI water, stirred for 10 minutes, and added to the P123. This solution was stirred continuously at room temperature throughout the rest of the procedure. 7.8 mL of 200 proof ethanol and 49.5 mL of 1.5 M HCl were added to the solution and stirred until a clear, homogeneous solution formed, which took about 45 minutes. Particle formation was initiated by adding 10 mL of TEOS dropwise to the solution and stirring the mixture for 2 hours. The solution was then poured into a Parr 4748A Teflon lined bomb (200 mL capacity) at room temperature and then placed into a preheated oven and aged for 72 hours. The pore size of the particles was modified by adjusting the thermal aging temperature[28] where large pore size particles (9 nm) were aged at 125 °C and smaller pore size particles (5.4 nm) were aged at 65 °C. After three full days, the particles were removed from the bomb and mixed with a high-speed mixer to homogenize the solution, then filtered and rinsed with DI water. The particles were then placed in a single walled Whatman cellulose extraction thimble and underwent Soxhlet extraction with 200 mL of ethanol for 24 h. Afterwards, the particles were dried under vacuum at 80°C overnight and characterized.

3.3.3 [TMS-MIM][Cl] Synthesis and Tethering; Ion Exchange

The tethering IL 3-methyl-1-[3-(trimethoxysilyl)propyl]-1H-imidazol-3-ium chloride ([TMS-MIM][Cl]) was synthesized by first making a mixture of N-methylimidazole (2.00 mL, 25 mmol) and (3-chloropropyl)trimethoxysilane (4.59 mL, 25 mmol) in toluene (40 mL) and refluxing the mixture for 36 hours. After cooling to room temperature, the supernatant solution was removed with a pipette. The remaining oil was washed with 10 mL diethyl ether three times to remove any remaining reactants, and then dried under reduced pressure at room temperature. The product was collected as a colorless oil (6.80 g, 97%). ^{1}H and ^{13}C NMR spectra of the prepared IL-like organosilane confirmed the identity of the material, as reported by literature.[172, 173] Toluene and diethyl ether were dried and distilled by standard procedures prior to use.[174]

The procedure for tethering the ionic liquid presented by Gruttadauria et al.[74] was adapted to functionalize the silica pore walls. Initially, 100 mg of silica microparticles (BJH adsorption surface area of 445.7 m^2/g) with a pore diameter of 9 nm were vacuum dried at 140°C overnight. 0.20 g of the tethering ionic liquid, [TMS-MIM][Cl] (0.73 mmol), was dissolved into 15 mL of chloroform, and the silica microparticles were added to the solution. The mixture was refluxed for 26 hours at 65 °C and then cooled to room temperature. The microparticles were filtered from the solution and washed with 50 mL of acetonitrile and 50 mL diethyl ether, then dried overnight to produce a white solid, the tethered 9-nm silica particles. Nitrogen adsorption was used to verify that the pore diameter and volume had decreased due to the functionalization of the pore walls.

A portion of the tethered silica particles underwent further modification to exchange the chloride anion to the desired $[PF_6]^-$ based on the procedure by Vangeli et

al.[142, 144] Briefly, ion exchange began by stirring 25 mg of tethered particles in 1 mL of a 67.5 mM solution of $NaPF_6$ in water. After 24 hours, the particle solution was centrifuged and the spent $NaPF_6$ solution was decanted and mixed with three drops of 1% $AgNO_3$ in DI water. If a cloudy appearance was present (indicative of chloride ions), the particles were dispersed into fresh $NaPF_6$ solution and left to stir for 24 more hours. The ion exchange procedure was repeated until no chloride ions were detected by $AgNO_3$. Afterward, the particles were rinsed with methanol and refluxed with 5 mL of methanol at 70°C for 30 minutes, filtered, and dried.

3.3.4 Silica Microparticle Characterization

Nitrogen adsorption was used to characterize the pore diameter distributions and total specific surface area of the microparticles before and after functionalization and IL loading using a TriStar 3000 automatic sorption analyzer (Micromeritics Instrument Corp., Norcross, GA). The instrument uses volumetric adsorption of nitrogen at 77 K to allow calculation of the specific surface area and pore diameter based on the Brunauer, Emmett, and Teller (BET) isotherm and adsorption branch of the Barrett, Joyner, and Halenda (BJH) method, respectively.[171] Prior to the characterization, samples were degassed at 140°C for a minimum of 4 hours under flowing nitrogen.

Small-angle x-ray scattering (SAXS) data were collected on the unloaded particles to further characterize the pore-to-pore distance. The silica particles were mounted in the powder sample holder of a Xeuss 2.0 SAXS laboratory beamline (Xenocs Inc., Holyoke, MA) equipped with a 30W microfocus Cu K-α source (λ = 1.54 Å) and Pilatus3 200K detector. Scattering data was collected for 10 minutes in transmission SAXS mode. The

sample to detector distance was set at 2.3 m calibrated using silver behenate. The location of the (100) peaks were determined by azimuthal integration of the 2D patterns.

A Nicolet Nexus 470 FTIR instrument (Thermo Fisher Scientific, Waltam, MA) was used to collect IR spectra of the samples from 400 to 4000 cm^{-1} at room temperature to confirm confinement of the IL and tethering of [TMS-MIM][Cl] to the mesoporous silica. Spectra were taken with a resolution of 1.928 cm^{-1} using at least 300 scans. The sample chamber is continuously purged with dry, low CO_2 air to prevent interference from water vapor and CO_2 gas. Samples were pressed into KBr pellets at about 1 wt% and data was collected approximately two minutes after the samples were placed into the sample chamber to purge ambient air from the chamber. The FTIR spectrum of neat [BMIM][PF_6] liquid was collected using a multi-reflection attenuated total reflectance (ATR) accessory (PIKE Technologies, Fitchburg, WI) equipped with a ZnSe trough.

3.3.5 Loading of Silica Microparticles with ILs

Ionic liquids were loaded into the mesoporous silica using solvent deposition. The volume of IL that we used to load into the nanoparticles was determined from the pore volume measured from nitrogen adsorption. In a representative experiment, particles with 9 nm diameter pores (e.g., 9 nm particles) with a total pore volume of 1.51 cm^3/g were vacuum dried in an oven at 140°C overnight. Approximately 10 mg of the 9 nm particles, 15.1 μL of IL, and 151 μL of ethanol were sonicated in a 2 mL centrifuge tube for 90 minutes. Afterward, the particles were vacuum dried in an oven at 80°C to remove the ethanol. The amount of IL was scaled accordingly with the change in pore volume of the 5.4 nm pore particles and tethered particles. IL without dye was used in FTIR and DSC measurements for all materials.

For confocal microscopy, fluorescent dye was added to the IL prior to loading in the particles. The target molarity of the dye in the IL was 20 μM so that the dye was easily seen in the microscope, but not high enough to cause self-quenching. Using DCM as an example, 6.06 mg of the DCM (0.02 mmol) was dissolved in 10 mL of 200 proof ethanol by sonicating for 10 minutes to make a solution of 2 mM dye. From this solution, 10.1 μL was mixed with 1 mL of [BMIM][PF_6] to make a final solution of 20 μM. The final concentration was the same for both DCM and R6G. After the dye was added, the rest of the confinement procedure was the same as neat IL loading. The effect of water on the system was studied by first confining 10 mg of particles with IL as above; after the particles were dried, 1 mL of water was added to the centrifuge tube. The particles were left immersed in water for 24 hours with no agitation before measurement.

3.3.6 Differential Scanning Calorimetry of IL-Loaded Silica Microparticles

Differential scanning calorimetry (DSC) measurements were taken to confirm the confinement of the ionic liquid in 9-nm pore diameter bare and tethered mesoporous silica particles and tethered particles. A shift in the direction or disappearance of the cold-crystallization temperature or melting temperature indicates confinement of an IL.[71] Samples were prepared by placing 5-15 mg of the silica into a hermetically sealed aluminum pan in a nitrogen environment to prevent water uptake during the experiment. A Q200 DSC (TA Instruments, New Castle, DE) was used to measure the DSC curves from the sample with a blank reference pan and with the sample chamber purged with continuous flowing nitrogen. Samples were first cooled to -90°C at 10 °C/min and held isothermally for 10 minutes, then heated to 25 °C at a rate of 10 °C/min and held isothermally for 10 minutes. A second cooling step to -90 °C at 10 °C min was performed,

followed by another isothermal step for 10 minutes. Finally, the sample was heated at a slow rate of 0.5 °C/min to 25 °C to complete the experiment.

The shift in melting temperature caused by interfacial free energy in nanoscale liquids is generally described by the Gibbs-Thomson equation. The relationship for a difference in melting point can be described for liquids confined within cylindrical pores using the following equation:

$$T_{fp}^{0} - T_{fp} = \frac{\vartheta^{S}\sigma^{SL}}{s^{L} - s^{S}}\left(\frac{1}{R_1} + \frac{1}{R_2}\right) = \frac{\vartheta^{S}T_{fp}^{0}\sigma^{SL}}{\Delta H_f}\left(\frac{1}{R_1} + \frac{1}{R_2}\right) \quad (3)$$

where T_{fp}^{0} is the equilibrium freezing/melting temperature of a flat interface, T_{fp} is the equilibrium freezing/melting temperature of a curved interface, ϑ^{S} is the solid molar volume, s^{L} and s^{S} are the described molar entropies of the liquid and solid, respectively, R_1 and R_2 are the principle radii of curvature of the curvature of the interface, and ΔH_f is the latent heat of fusion at the flat interface melting temperature.[77]

3.3.7 Confocal Microscopy

Confocal microscopy was performed with a TCS SP5 confocal microscope (Leica Microsystems, Deerfield, IL) equipped with an Argon laser using 488 nm as the excitation wavelength for the DCM dye, and 538 nm for the Rhodamine 6G dye. The microscope is outfitted with an environmental chamber to maintain constant temperature, humidity, and CO_2 levels. The objective used in this study was a 63x oil objective with Type F immersion fluid. Glass slides and cover slips were cleaned using 80% ethanol/water and lens paper to remove smudges and dust. Microparticles were dispersed in DI water just before placing them into the microscope to maintain a refractive index close to that of the immersion fluid

for FRAP measurements. Using a precision pipette, 7 μL of the particle dispersion was placed onto the glass slide and the cover slip was carefully pressed down. The sample was then placed upside-down in the inverted microscope. A schematic of the photobleach process is shown in Figure 6, along with a sample of the data processing. Each FRAP measurement was performed within a focal plane passing through the center (depth) of a microparticle. A circular region of interest (ROI) with a diameter of 500 nm (orange outline, Figure 6(a)) was chosen at the midpoint between the center and edge of the particle in the focal plane. A 500 nm cylindrical laser pattern with the same excitation wavelength as for imaging was used to photobleach the ROI over the course of 6.5 s. Images were collected over a time span of 250 s while the unbleached dye diffused into the bleached area, and the pixel intensity within the ROI was averaged with the Leica FRAP Wizard software. An example of the raw images before and just after photobleaching (t = 0 s), during recovery, and at the end of the experiment are shown in Figure 6(b). The total fluorescence intensity in the ROI vs. time from the same FRAP experiment is shown as a representative example in Figure 6(d).

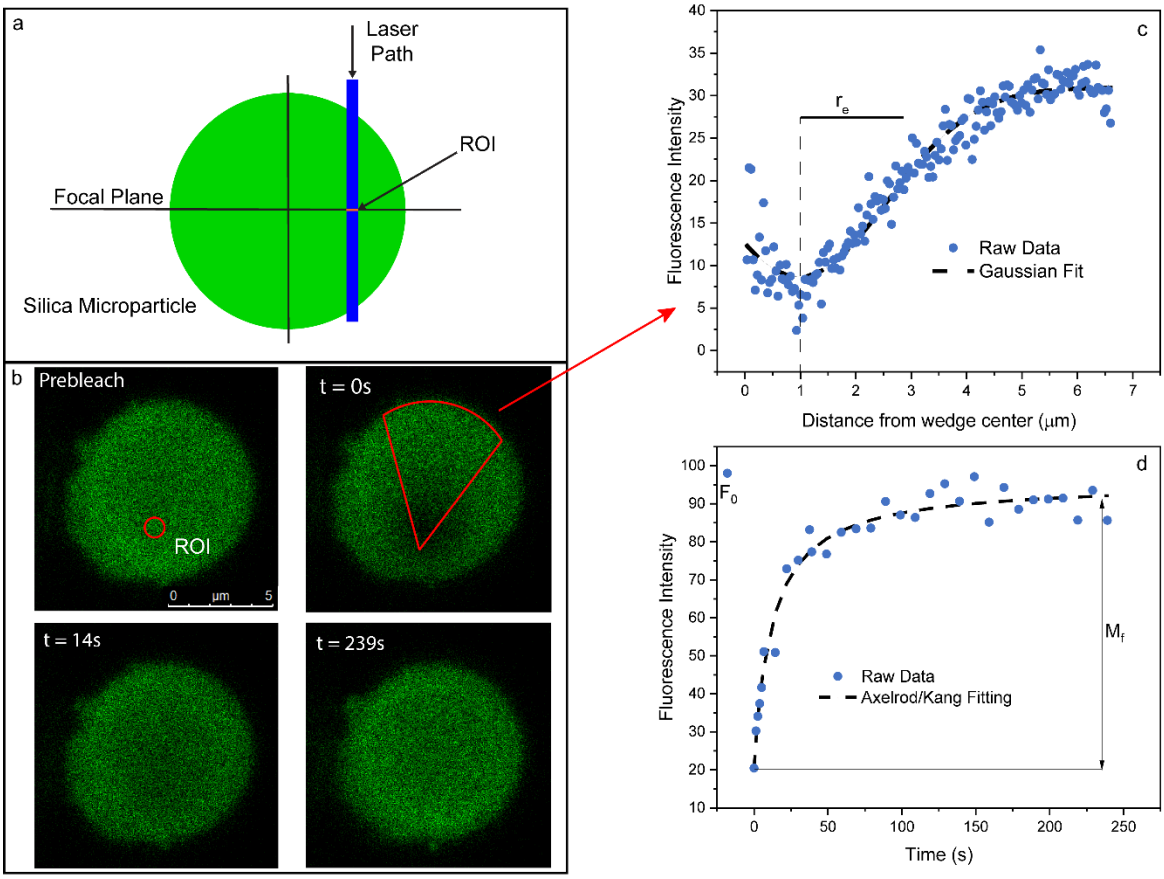

Figure 6. Schematic diagram of the FRAP Technique. The location of the measurement (ROI) was taken halfway between the center and the edge of the particle, denoted by the red circle during prebleach measurements. The wedge shape at t=0s, or 1st postbleach image, was used to fit a Gaussian curve on the top right plot to find effective radius. The pixels within the ROI were averaged over the course of the experiment and were fit with the Axelrod/Kang method, with example data in the bottom right plot.

After data collection, the raw intensity measurements within the ROI were fitted to find the diffusivity. First, the effective radius (r_e) of the bleached spot was determined to account for the diffusion of dye during the photobleaching process by fitting a Gaussian equation to the bleach profile of the first postbleach frame:[175]

$$F(x) = F_0 + Ae^{-(x-x_c)^2/\left(\frac{r_e^2}{\ln(2)}\right)} \quad (4)$$

In this equation, F(x) is the azimuthally averaged pixel fluorescence intensity within a wedge centered near the bleach spot extending radially from 0 to x microns outward toward the unbleached side of the particle (illustrated in Figure 6(b) at t = 0 s), x_c is the center of the bleach spot, and A is the amplitude of the intensity and was obtained with ImageJ[176] version 1.53a and the Radial Profile Angle plugin. The effective radius (r_e) is the half width at half maximum of the bleach spot. The fluorescence data was fit to the above equation by nonlinear regression using MATLAB version 2020b with F_0, A, x_c, and r_e as adjustable parameters. A typical fit is illustrated in Figure 6(c).

Next, the average intensity within the ROI for each individual FRAP measurement was plotted as a function of time and fitted using the model presented by Kang[31], which is a modification of the Axelrod model[100] for diffusion into a bleached area that initially has a Gaussian intensity profile. The raw intensity values, F(t), were fitted with equation 5:

$$F(t) = F_i\left[1 - \frac{K}{1+\gamma^2+\frac{2t}{\tau_D}}\right]M_f + \left(1-M_f\right)F_0 \quad (5)$$

where F_i is the prebleach fluorescence intensity, γ is the ratio of the nominal and effective radius (r_n/r_e), τ_D is the characteristic diffusion time, t is the experiment time in seconds, M_f is the mobile fraction, and F_0 is the initial postbleach fluorescence intensity (t = 0 s). In this case, r_n = 500 nm. K is defined as

$$K = \frac{F_i - F_0}{F_i}(1+\gamma^2) \quad (6)$$

This model was fit to the F(t) data by nonlinear regression using M_f and τ_D as adjustable parameters with Microsoft Excel's Solver plugin.[177] After regression, the characteristic diffusion time t_D was used to calculate the diffusion coefficient using the following equation:

$$D = \frac{r_e^2 + r_n^2}{4\tau_D} \tag{7}$$

The diffusivity values were individually calculated for each measurement and averaged together to yield an average diffusivity value and standard deviation for each sample. The coefficients of determination (R^2) for the fitting of the FRAP datasets are reported in Appendix Table A.1.1.

3.4 Results and Discussion

3.4.1 Particle Synthesis and Characterization

Spherical silica particles with micron-scale particle diameter were chosen for this study because their spherical morphology and scale are appropriate for imaging using confocal microscopy.[30] Table 1 lists the pore diameters measured using nitrogen adsorption for the base particles used for each experiment and the pore size distributions of the particles determined by the BJH method are shown in Figure 7. The particles have a uniform mesoporous structure consistent with previous studies.[171] Increasing the hydrothermal aging temperature from 65 to 125 °C increases the hydrophobic volume of the micelle templates resulting in a larger micelle and pore diameter after synthesis,[171] leading to mesoporous silica microparticles with 5.4 and 9 nm mesopores, respectively. After tethering the 9 nm porous silica with [TMS-MIM][Cl] (an IL-like molecule), the pore volume of the particles decreased by 33% from 1.51 to 1.03 cm^3/g. The average pore

diameter also decreases from ≈ 9 nm to 8.0 nm. This result is expected because the tethered molecule takes up space on the pore wall surface and leads to a smaller pore volume and pore diameter. After confinement of the [BMIM][PF_6] to the tethered-9 nm silica, nitrogen is unable to adsorb to the pore interiors since the pores are completely filled with IL, resulting in a surface area too small to be accurately measured by nitrogen adsorption (data not shown). Confocal imaging of confined ILs as in Figure 6 demonstrate that the pores are not simply blocked with IL but are completely full. SAXS was performed on the particles without confined IL and the results agree with the nitrogen adsorption data. In the supporting information, the azimuthally averaged SAXS patterns (Appendix Figure A.1.1) have peaks corresponding to a pore-to-pore distance of 11.1, 7.96, and 11.2 nm for 9 nm, 5.4 nm, and tethered 9-nm porous silica respectively. The pore diameter in the tethered particles is reduced after functionalization while pore-to-pore distances remain the same, consistent with the expected effect of tethering.

Table 1. Silica diameter, pore volume, and surface area results from nitrogen adsorption and BET calculations. The tethering on the 9 nm silica reduces the pore diameter, volume, and surface area significantly due to pore wall functionalization. The q-value of the first peak, related to the pore-to-pore distance, is also listed.

Particles	Pore Diameter (nm)	Pore Volume (m^3/g)	Pore Surface Area (m^2/g)	q peak ($Å^{-1}$)	Pore-to-Pore distance (nm)
9 nm silica	9	1.51	445.7	0.0652	11.1
5.4 nm silica	5.4	1.03	653.9	0.091	7.96
Tethered 9-nm silica	7.8	0.992	319.4	0.0649	11.2

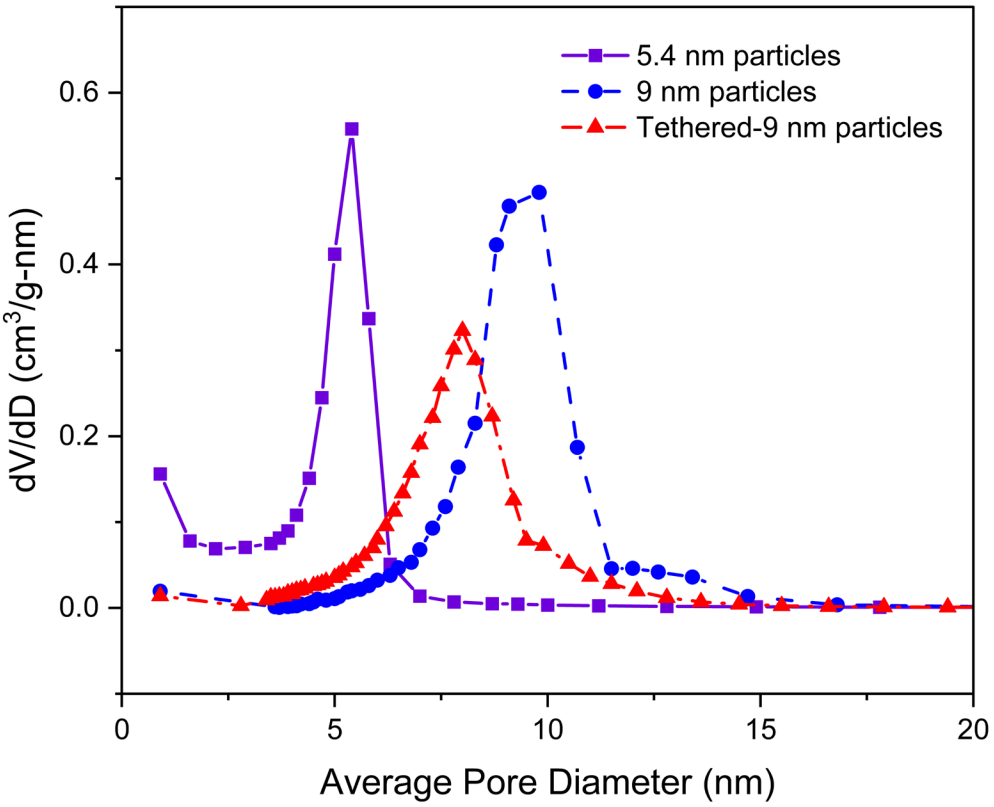

Figure 7. Effect of hydrothermal aging temperature, surface functionalization, and confinement on pore diameter distributions. Squares (purple, solid line) represent the bare 5.4 nm mesoporous silica particles, circles (blue, dashed line) represent the bare 9 nm mesoporous silica particles, triangles (red, dash-dot) represent the bare tethered 9 nm silica particles.

3.4.2 Fourier Transform Infrared Spectroscopy

Fourier transform infrared (FTIR) spectroscopy was used to confirm ionic liquid loading and tethering in the microparticles. The FTIR spectra of the neat and confined

[BMIM][PF_6] are presented in Figure 8. In the bare 9 nm silica particles, the peaks at ≈1070 (shoulder near 1200), 950, and 800 cm^{-1} are attributed to antisymmetric Si-O-Si stretching, Si-O-H stretching, and symmetric Si-O-Si stretching vibrations, respectively.[178] In the neat [BMIM][PF_6], the peaks between 2800-3000 cm^{-1} arise from the υ_s, υ_{as}, and Fermi resonance C-H vibrational modes from the alkyl tail of the IL, while the features above 3000 cm^{-1} are due to the same vibration modes from aliphatic carbons in the imidazolium ring.[179] The peaks at 1575 and 1167 cm^{-1} are assigned to stretching modes in the imidazolium ring. The bands between 1500 and 1300 cm^{-1} are attributed to bending modes for CH_2, CH_3, and C-CH.[179] Lastly, the peaks between 750 and 900 cm^{-1} correspond to stretching vibrations of the PF_6^- anion, with smaller peaks at 750 and 650 cm^{-1} being attributed to complex bending and out of plane bending respectively.[179] The full spectra can be found Appendix Figure 1.1.2

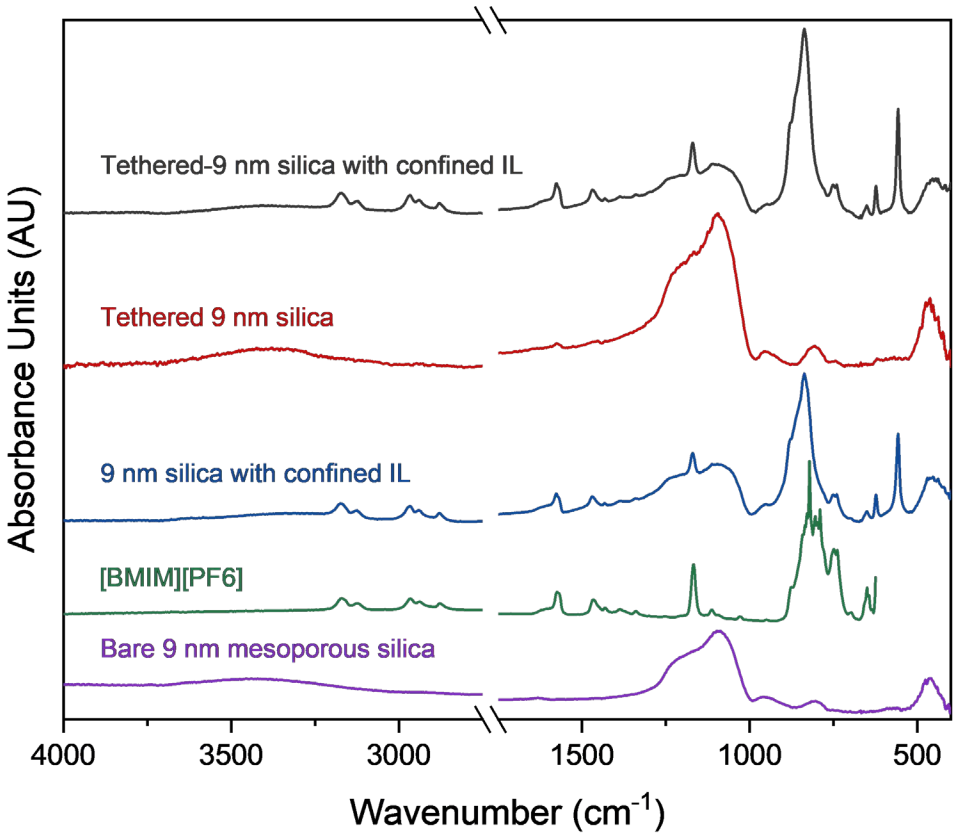

Figure 8. FTIR spectra in the range of 4000-400 cm-1 for bare 9 nm mesoporous silica particles, pure IL ([BMIM][PF6]), confined IL on 9 nm mesoporous silica, bare tethered-9 nm silica, and tethered-9 nm silica with confined IL.

The spectrum of the confined IL within the mesopores of the silica is almost an additive combination of the spectra of bare silica and [BMIM][PF_6], but there are slight shifts for peaks associated with the IL. The N=C– stretching, C=C–, and ring stretching peaks shift from 1575 to 1577 cm^{-1}, 1467 to 1469, and 1167 to 1170 cm^{-1} respectively. The higher wavenumber peaks at 3171 and 3124 shift to 3174 and 3125 cm^{-1}. In the alkyl chain,

the peaks shift from 2878, 2938, and 2966 to 2879, 2941, and 2967 cm^{-1} respectively. The imidazolium ring peaks have larger shifts to higher energy (higher wavenumber) than the alkyl chain peaks and can be attributed to interactions of the imidazolium ring with the pore walls.[1, 70] Previous FTIR and molecular dynamics studies have demonstrated that the cation from the imidazolium ring can preferentially interact with the silica pore wall.[1, 80] That interaction is found here from the changes to the peaks related to the imidazolium headgroup of the IL. At the same time, the bands associated with PF_6^- shift to higher wavenumbers and may broaden to some extent, reflecting a more heterogeneous solvation environment when confined in silica nanopores. The peaks from organic groups in tethered but not confined IL are much less pronounced, but new peaks at 1576 and 1461 cm^{-1} are present and correspond to N=C– and C=C– ring stretching from the IL,[1] providing further evidence that [TMS-MIM][Cl] was successfully grafted to the interior pore wall surface. [BMIM][PF_6] was confined within the tethered-9 nm silica and the spectrum is shown in Figure 8. A fully functionalized pore wall would prevent interactions between the IL and pore wall by eliminating the sites where the interaction could occur. There are no significant differences between the peak locations of the imidazolium groups in the FTIR spectra of confined compared to tethered and confined IL. This indicates that some unreacted -OH groups on the pore wall surfaces exist in the tethered-9 nm silica with confined IL for the imidazolium/pore wall interaction to occur.

3.4.3 Differential Scanning Calorimetry

The DSC curves used to study the melting point transition temperature of the IL's with and without confinement are presented in Figure 9. The DSC curves for the bare silica substrate and tethered silica substrate without confined IL demonstrate that the support

materials do not contribute to the observed phase behavior of the confined IL samples. The magnitude of the heat flow values has been multiplied by a constant in each curve to fit them on the same plot. The neat [BMIM][PF_6] exhibits a cold crystallization peak at -40 °C, two crystal-crystal transition peaks at -21.6 and 2.9 °C, and a melting peak at 10.5 °C as the temperature is increased and are near values reported in the literature.[180, 181] After confinement, the melting peak of the IL shifts down slightly to 8.6°C and confirms that the IL is confined within the mesoporous silica, as expected according to the Gibbs-Thomson equation. Another interesting observation is that the crystal-crystal phase transition processes either no longer occur or their peaks are too small to be seen, perhaps because it is not energetically favorable for the transition to occur under confinement. The magnitude of the melting point shift is consistent with DSC curves of confined [BMIM][PF_6] within ionogels and capillary-confinement within mesoporous silica.[32, 71] It has been widely reported that the shift of melting or cold crystallization peaks is an indicator that the IL has successfully been confined within a porous structure.[19, 24, 32, 68] This shift can increase or decrease the melting or crystallization based on many factors, some of which are the pore diameter, pore wall chemistry, synthesis method, and cation/anion components.[19] Another important factor that may lead to melting point elevation is pore wall-induced layering in the IL, which may help to stabilize crystallites in the pores.

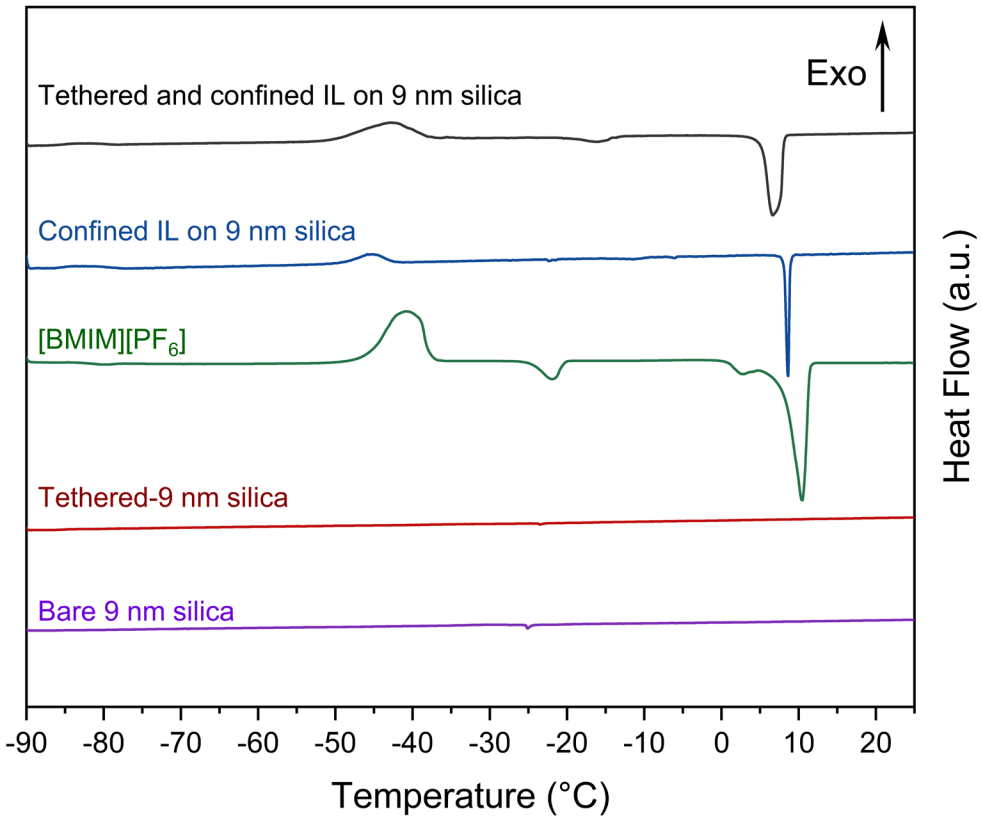

Figure 9. DSC curve of pure [BMIM][PF6], confined IL within 9 nm mesoporous silica particles, and tethered-9 nm particles with confined IL. The heating rate is 0.5°C/min from -90°C to 25°C and display cold crystallization, crystal-crystal phase transition, and melting temperatures. The magnitude of the curves have been adjusted to fit on the same graph. Bare 9 nm silica particles and tethered silica without confined IL are also included.

Confinement of [BMIM][PF_6] within tethered 9-nm particles led to a further melting point decrease to 6.6°C. Molecular dynamics simulations of [BMIM][PF_6] on a quartz surface suggest that the imidazolium cation from the IL preferentially interacts with the negatively charged silica surface, forming a layer of cations.[79] Tethering the IL replaces the partially deprotonated Si-O-H bonds on the pore walls with a positively charged imidazolium ring. The smaller pore diameter and increased solid-liquid surface free energy

after tethering would cause the melting point to decrease further according to the Gibbs-Thomson equation. Water contact angle is a good indicator of interfacial tension where the increase in water contact angle corresponds with an increase in surface energy. A glass plate has a water contact angle of 12° when cleaned with chromic acid,[182] whereas the contact angle is 24° for a glass surface functionalized with a monolayer of [TMS-MIM][Cl],[144] signaling that the surface has become more hydrophobic. Density functional theory and AFM measurements of adhesion force by Zhang et al. also show that for [BMIM][PF_6], a cationic surface has a weaker interaction with the IL than neutral or anionic surfaces, which corresponds to a higher IL contact angle (and increased surface energy).[183] The combined effect of increasing surface energy and smaller pore diameter reduces the melting point of [BMIM][PF_6] further than only confinement.

3.4.4 Confocal Microscopy

The diffusion of the fluorescent dyes within nanoconfined ionic liquids was investigated using the FRAP technique. The equator or vertical axis mid-point of the particle was used to accurately measure the diffusivity, as illustrated in Figure 6. The values of diffusivity were found by first determining the effective radius of the Gaussian bleach profile in the first collected image (Figure 6(c)) and fitting the fluorescence intensity vs. time data, as illustrated in Figure 6(d) and discussed in the Methods section. The resulting diffusivity values are summarized in Figure 10. The large standard deviation in diffusivity implies heterogeneity of the confined IL/dye system. Ionic liquids have been reported to have a microheterogeneous nature which may contribute to the uncertainty.[81, 184] Additionally, mesoporous silica particles can have heterogeneity between different individual particle FRAP measurements.[185] The diffusion coefficients reported here are an

ensemble average over the area probed, which after bleaching is complete gives an effective radius of several mm (e.g. Figure 6(c)).[186]

The effect of confinement and pore size on the diffusivity of the neutral DCM probe using mesoporous silica particles with pore diameters of 5.4 and 9 nm was measured. The resulting DCM diffusivities are 0.024 ± 0.019 $\mu m^2/s$ and 0.026 ± 0.0091 $\mu m^2/s$ for 5.4 and 9 nm pore diameters, respectively. It was hypothesized that a reduction in pore diameter would result in more IL/pore wall interactions due to the increased surface area, and that therefore the dye would not be able to diffuse as easily through the system. The lack of a statistically significant difference between small and large size pores could mean that the relative amount of IL interacting with the pore wall does not play a large role in the diffusivity of the neutral probe moving through the nanopore. As the size of the pore is decreased from 9 to 5.4 nm, the surface area increases from 446 to 654 m^2/g, and the SAXS pore-to-pore distances are 11.1 and 8 nm for the particles, respectively. This implies that the pore wall is relatively similar between the two samples ($\approx$ 2.1 and 2.6 nm pore walls for 9 and 5.4 nm diameters respectively) and the smaller pores are more constricted, but it has little effect on diffusivity. Because both particles have pores large enough to permit dye molecules to pass each other in the pores, a more extreme change in conditions may be required to significantly alter diffusivity in the confined system.

Compared to its diffusivity in bulk [BMIM][PF_6], the DCM dye diffuses nearly two orders of magnitude slower in nanoconfined ILs. Werner et al. studied the bulk diffusion of DCM in [BMIM][PF_6] using FCS and reported a value of 1.74 $\mu m^2/s$.[106] It is worth mentioning that the absolute diffusion coefficients can vary between FCS and FRAP measurements of the same system since the techniques measure diffusion in different time

windows, scales, and contexts.[153] The diffusivity of 4-(N,N′-dimethylamino) benzonitrile (DMABN) in bulk [BMIM][PF_6] measured by FRAP was reported as 0.25 $\mu m^2/s$ by Santhosh et al.[81] The DMABN probe is less bulky than DCM but the 5-fold difference in diffusivity highlights the potential discrepancies between the two techniques. Regardless, confinement causes a significant reduction in the diffusion of the dye. There are two possible reasons for this. The first is the increase in the pathlength that a molecule needs to travel in a porous material due to the pore volume and tortuosity. Using reconstructed electron tomography models, Hochstrasser et al.[187] developed an empirical model of these effects for SBA-15. Using the Stokes radius of DCM (0.44 nm)[106] and assuming the pore fraction (0.69) and tortuosity (1.41) of SBA-15 reported by Hochstrasser et al., (D_{eff}/D_{bulk}) for DCM diffusion of 0.24 and 0.33 are calculated for 5.4 and 9 nm porous silica used here. This does not explain the ratio observed of ~0.013, so the second factor affecting the diffusion of silica-nanoconfined IL is molecular interactions with the pore wall. Pal et al. performed molecular dynamics simulations of [BMIM][PF_6] confined in uncharged silica nanopores and found a significant reduction in overall diffusivity (by about a factor of 3) relative to bulk IL, and a spatially-dependent reduction by two orders of magnitude in the layer of ions closest to the pore wall.[155] The layering observed by Pal et al. was driven by hydrogen bonding of PF_6^- with silanols, and Sha et al. showed that ion layering and its effects on reducing diffusivity of [BMIM][PF_6] is increased by adding a negative charge to the confining surface.[33] Thus, ion layering contributes to a reduction of diffusivity both by increasing local viscosity and by reducing the accessible pore volume with layers of rigid ions near the pore wall. Consistent with this idea, it has been reported that confinement in even relatively large conical pores (without tortuosity) reduced the

diffusivity of fluorescein isothiocyanate in a 20% glyercol/water mixture by over 10-fold.[188]

With a lack of effect of pore size on diffusivity observed for the 5.4 and 9 nm pores, the remaining confined IL systems are compared to that of the neutrally charged DCM in [BMIM][PF_6] which has been loaded in silica particles with 9 nm pores. The effect of charge of the dye was examined for the cationic dye (R6G) in the same pore size material. The effect of hydration of the neutral probe molecule was studied by immersing the particles in water approximately 24 hours prior to imaging; this sample was prepared to study the robustness of the system to an aqueous environment. An IL-like molecule ([TMS-MIM][Cl]) was covalently attached to the pore wall in the tethered-9 nm silica sample, changing the pore wall chemistry and interactions between IL and pore wall. Lastly, to see the effect of the counterion, the [TMS-MIM][Cl] group was first tethered, and then the $[Cl]^-$ anion was exchanged for $[PF_6]^-$ to match the anion with the confined IL.

The diffusivities for the neutral (DCM) and cationic (R6G) dyes were found to be 0.026 ± 0.0091 and 0.011 ± 0.0049 $\mu m^2/s$, respectively. Werner et al found that cationic dye diffusion was ≈20% slower than neutral in bulk [BMIM][PF_6] using FCS[106] and our results show a larger reduction in diffusivity (almost 60%) in the confined system. The difference between the dyes in the bulk phase may be from interactions between the cationic dye and anion of the IL but could also be from a size difference as the cationic dye is bulkier than the neutral dye.[105] In the confined system, the effect of tortuosity due to the larger size of the cationic dye would be expected to decrease the diffusivity by only about 10%,[187] so that is still not enough to explain the observed decrease. The cationic dye could interact with either the negatively charged $[PF_6]^-$ from the IL or the silica pore walls. The

compounded effect of these interactions, along with possible effects of ion layering induced by the pores (increasing local viscosity at the pore walls), likely leads to a slower diffusivity in the confined system, as there are more potential sites that the dye can associate with.

The particles were immersed in water for confocal microscopy to provide an appropriate refractive index medium for imaging. While [BMIM][PF_6] is hydrophobic, there could potentially be an effect of a small amount of water taken up by the IL. Not only is the presence of water a potential factor in our diffusivity measurements, but understanding the effect of humidity and or aqueous environments on the diffusivity in IL's is important to its commercial application as a confined solvent. To address this, the confined ILs were immersed in water with no agitation for 24 hours to study the response of the system to water. After this treatment, the diffusivity was 0.035 ± 0.013 $\mu m^2/s$, which is not statistically different from the value measured for the sample that was not saturated with water (0.026 $\mu m^2/s$). Over the time of exposure ($\approx$ 24 hours), it is likely that water entered the pores and reached saturation levels with [BMIM][PF_6]. Like prior studies, the average increase in diffusivity is most likely from the decrease in viscosity of the mixture.[106] The apparent increase in diffusivity after water exposure in our system is consistent with the diffusivity increase by FCS reported by Werner et al. upon adding 3 vol% water to bulk phase [BMIM][PF_6] (1.74 to 3.0 $\mu m^2/s$).[106] Schröder used voltammetry to show that the diffusivity of a neutral redox probe molecule *N,N,N',N'*-tetramethyl-*p*-phenylenediamene in bulk phase [BMIM][PF_6] doubled from 2.6 to 5.2 $\mu m^2/s$ when the concentration of water was raised from 0 to 5% (w/w).[189] They also report an increase of an order of magnitude from 1.1 to 10 $\mu m^2/s$ when using the cationic probe methyl viologen and 6% (w/w) of water in the IL,[189] although the drastic increase in diffusivity may be

unreliable since the concentration of water is much higher than its solubility limit in [BMIM][PF_6].[106] In our experiments, the IL was not mixed with water before confinement and may be a reason for the modest increase in diffusivity, although it could just be that the reduction in diffusivity caused by confinement reduces the ability of hydration to enhance probe mobility.

When the 9 nm pore walls were tethered with an IL-like molecule, [TMS-MIM][Cl], the diffusivity of the DCM dye in confined IL was found to increase to 0.078 ± 0.019 $\mu m^2/s$. The significant diffusivity increase is likely a result of a change in molecular interactions caused by charge and hydrophobicity changes within the pores since smaller pores did not present a significant change. When [TMS-MIM][Cl] is covalently attached to the pore wall, the negative charge of the silica surface is screened or reversed by the imidazolium groups, and the environment within the pore becomes more hydrophobic (similar to the bulk IL). The surface interaction of [BMIM][PF6] has been shown to become weaker as the silica surface becomes less negative due to functionalization with cationic groups.[190] Since DCM is a hydrophobic dye (log $P_{o/w}$ is close to that of *n*-hexane), it should be more mobile in this environment. The result is consistent with prior observations of the transport of 1,1′-dioctadecyl-4,4′-bipyridinium dibromide (DBD), a hydrophobic redox probe with a high log $P_{o/w}$.[21] DBD did not encounter significant hindrance to diffusion after the pore walls of an 8 nm silica thin film were tethered with [TMS-MIM][Cl] while a more hydrophilic redox probe experienced diffusion resistance through the same pores.[21] The DBD probe is larger and matches the charge of the pore wall, while DCM is smaller and is a neutral dye. This result is also supported by recent AFM measurements of surface interactions between ILs and functionalized silica.[190]

Interaction forces between the bare silica surface are much stronger than with a positively charged surface with a quaternary ammonium group.[190] It would follow that the lower interaction force between IL/silica would lead to a larger diffusivity. Tethering is often used to ensure IL does not leach from the system during use, so this counterintuitive result is significant because it shows that a reduction in pore diameter due to tethering does not necessarily lead to a decrease in diffusivity in a condensed pore-confined phase.

As a last system variable studied, the counterion of the tethering group was exchanged so that a mixture of chloride and hexafluorophosphate groups would not be present in the pores. The tethered particles underwent ion exchange to change the $[Cl]^-$ ion to $[PF_6]^-$ by exposing the functionalized particles to a $NaPF_6$ solution. While this was hypothesized to further accentuate the hydrophobic environment of the nanopores compared to the tethered-9 nm system with confined IL, it resulted in a significant decrease in diffusivity to 0.012 ± 0.0046 $\mu m^2/s$. As discussed above, the water contact angle for a Si/SiO_2 surface functionalized with [TMS-MIM][Cl] changed from 24° to 42° after the Cl^- anion was exchanged with PF_6^- on silica thin films, indicating increasing hydrophobicity that is correlated with a decrease in surface energy.[144, 183] The tethered-9 nm with confined IL system establishes that higher hydrophobicity within the pores relative to bare silica or a positively charged surface leads to higher diffusivity, so the lowered diffusivity is unexpected. The decrease is likely related to an increase in difficulty in loading IL after ion exchange. In Appendix A.1.3, an image of an example particle demonstrates much higher heterogeneity in dye loading compared to the other particle treatments. Such heterogeneity could be caused by incomplete ion exchange, partial blocking of the pores, or damage to the pore structure during the ion exchange procedure. Whatever is the cause

of the heterogeneous loading, it causes an increase in the effective tortuosity for a network of pores incompletely filled with IL.

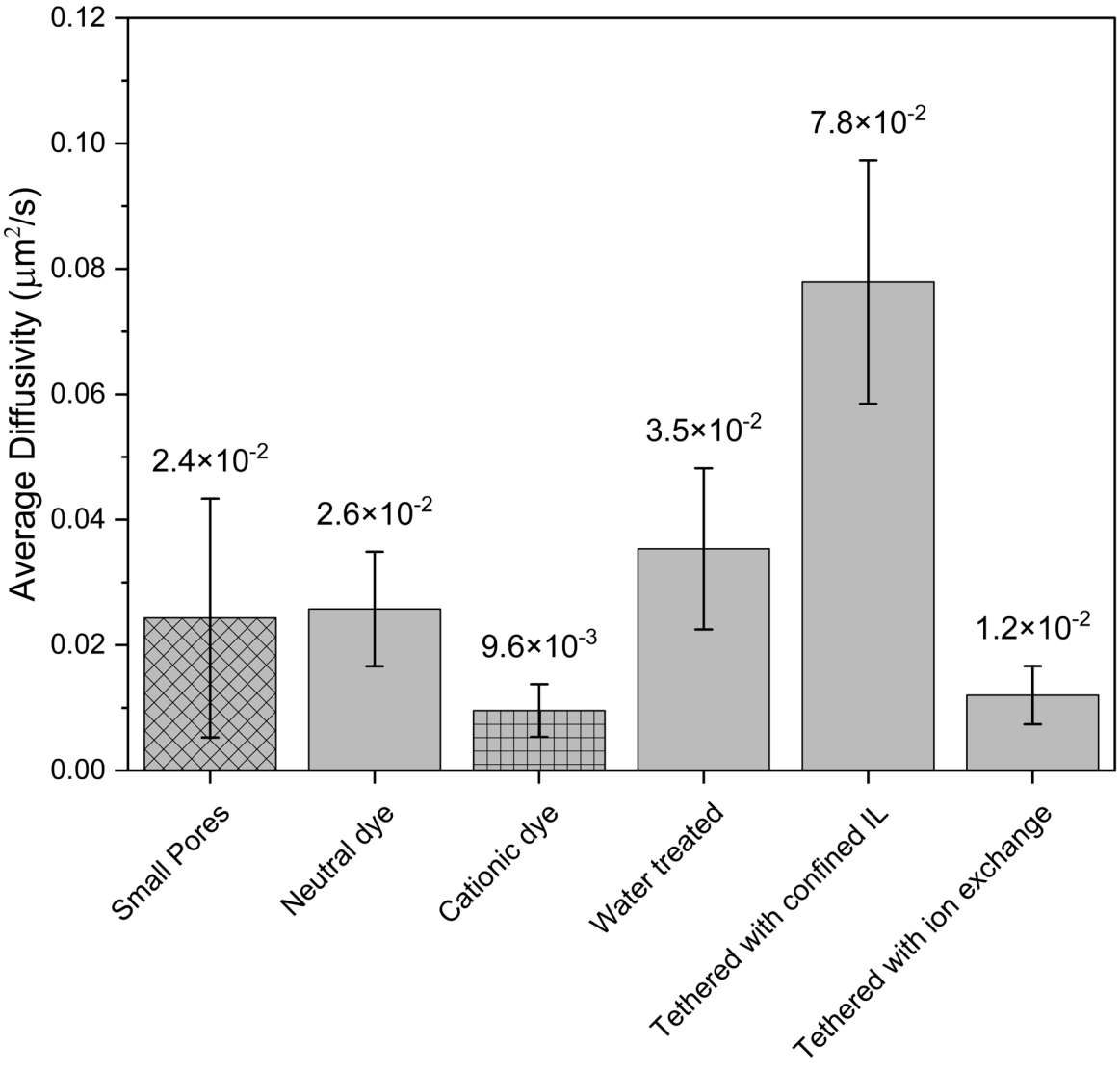

Figure 10. Diffusivity of ionic liquid within microparticles measured by the FRAP method in confocal microscopy as a function of pore diameter, dye charge, water effects, pore wall tethering, and tethering with ion exchange. Error bars represent the standard deviation of each data set. The default dye used was DCM and the default pore diameter was 9 nm. In the small pore case (left-most bar with a diamond fill pattern), the dye used is DCM and pore diameter is 5.4 nm. In the cationic dye case (third from left, grid pattern), the pore diameter is 9 nm and dye used is R6G.

3.5 Conclusion

Confocal fluorescence microscopy, differential scanning calorimetry, FTIR, and nitrogen porosimetry were used to study the diffusivity and properties of probe dye molecules in [BMIM][PF_6] confined within mesoporous silica microparticles. Nitrogen porosimetry was used to determine the pore diameter and texture of the silica microparticles and show a difference in pore diameters due to hydrothermal treatment, and a decrease in pore diameter after tethering the pores with methylimidazolium chloride groups. DSC showed that the IL was successfully confined within the pores of the silica and shifts in the melting and cold crystallization temperatures demonstrate shifts toward lower temperature upon confinement consistent with what is expected from the Gibbs Thomson equation. FTIR also demonstrated that ILs were successfully confined from shifts in the bands associated with IL due to attraction to the pore wall.

The diffusivity of neutral fluorescent probe DCM was first measured in 9 nm pore diameter particles to show the ability of the FRAP technique to effectively measure the diffusivity. The diffusivity of the DCM in the confined system is about two orders of magnitude lower than in the bulk phase, which is typical of what is observed for diffusion of probe molecules in confined fluids. The similarity of DCM diffusivity between small and large pores demonstrate that the system is robust to pore diameter changes within relatively large mesopores relative to the probe diameter. The cationic dye (R6G) had a lower diffusivity than the neutral DCM because of the interactions between the dye with the IL and pore wall. A simulated water immersion experiment did not lead to significant changes in diffusivity, but the average diffusivity was higher after increasing the water content of the system by immersion for 24 h. Water may mix with the IL within the pores

to reduce the effective viscosity of the confined IL system, leading to a small reduction of viscosity and increase in diffusivity.

The most significant effects on diffusivity of the DCM probe are found when an IL-like methylimidazolium group is tethered to the pore surface. When the surface is functionalized, the increase in diffusivity is likely caused by the increase of hydrophobicity within the pores. Since DCM is a hydrophobic probe, it moves more easily in this environment. Exchanging the anion of the tethered species to match the IL anion led to a drastic decrease in diffusion and highly heterogeneous dye distribution in the particles. The ion exchange may have not been successful for all tethered sites and led to the observed heterogeneity in the images, or the pore structure may have been altered during the ion exchange procedure.

Understanding the transport of dye molecules in confined ILs is crucial to the development of supported IL systems in separations, heterogenous catalysis, and batteries. Bulk ILs have faster transport properties, but the challenges of using them due to their high viscosity and cost makes confinement a desirable solution. This study complements the findings published using fluorescence methods to study diffusion in bulk systems. The large decrease in diffusivity of confined IL compared to bulk phase highlights the importance of pore wall interactions, charge, and electrostatics when designing confined systems. To understand the implications of the measured diffusivities, we can consider use of [BMIM][PF_6] supported in 9 nm pores of a mesoporous silica membrane for pertraction of pollutants such as bis-phenol A. Based on a distribution coefficient from water into [BMIM][PF_6] of K_D=400[191] and assuming a 1 mm thick active layer (=t) with the diffusivity measured for the tethered, confined IL, the permeance would be $P = K_D D/t =$

400×(0.0779 mm^2/s)/(1 mm) = 31.2 mm/s. This compares favorably to polymer-based supported ionic liquid membranes, where permeance values are on the order of 10^{-2} to 10^{-3} mm/s.[192]

Water and pore size did not significantly alter the diffusion in confinement meaning these design parameters are less important in confined IL systems than in bulk ILs, expanding their possible applications. For example, CO_2 capture in flue gases would be an appropriate application due to the high affinity of many ILs to CO_2. Since the pore size does not significantly limit diffusion, the particle synthesis for this application is not as stringent, and water in flue gas would not significantly change the diffusive properties of CO_2 adsorption leading to longer material lifespan. Tethering also shows that the transport properties can be modified by adjusting the support/IL interfacial chemistry to achieve slower or faster transport. From this work, it is clear that confined ILs offer high flexibility in their design parameters that makes them more viable to use in various applications, such as pertraction of organic solutes or CO_2 capture.

CHAPTER 4. PROBING INTERACTIONS BETWEEN CONFINED IONIC LIQUIDS AND MESOPOROUS SILICA USING X-RAY PHOTOELECTRON SPECTROSCOPY

4.1 Summary

The interfacial structure of the ionic liquid (IL) 1-butyl-3-methylimidazolium chloride ([BMIM][Cl]) confined within mesoporous silica thin films is examined as a function of pore size (3.5 and 8.5 nm diameter pores) and surface functionalization. Mesoporous silica thin films with vertically aligned, accessible pores were synthesized by dip-coating and the structure was characterized by grazing incidence small angle x-ray scattering. The IL was loaded into bare films or films covalently tethered with an IL-like functional group (3-methyl-1-[3-(trimethoxysilyl)propyl]-1H-imidazol-3-ium chloride [TMS-MIM][Cl]), which changed the surface charge from negative to positive. X-ray photoelectron spectroscopy (XPS) was used to study the interface between the physically confined ionic liquid (IL) and the silica substrate. The imidazolium group of the IL interacts strongly with the positively charged, deprotonated surface of the silica and presents as a shift in the carbon and nitrogen spectra in XPS. Tethering was successful and had the same shifts due to incomplete surface coverage. The chlorine speciation was dependent on the pore diameter of the films, where free chloride exists in 8.5 nm pore films, and chlorine shares a proton from the pore wall in 3.5 nm pore film. The use of XPS to probe interfacial interactions between low vapor pressure solvents and nanoporous supports advances the design of confined ILs for catalysis and separations from knowledge of the local solvent structure and environment.

4.2 Introduction

Ionic liquids (ILs) are a class of solvents that are salts possessing low melting points, typically under 100°C. They have been studied as an alternative to traditional organic solvents since they have good thermal stability, high ionic conductivity, and their properties can be tuned to dissolve organic materials by changing the cation or anion.[1] ILs have been used for several diverse applications such as electrolytes, in catalytic systems as the reaction media, and as a solvent for separations.[9, 46, 133, 134] Despite the promising properties of ILs, their cost and unfavorable transport properties limit their widespread use in industrial applications.[193] Confining or supporting ILs have the advantage of requiring less IL and reducing leaching from the system.[78] Confinement affects the local structure of ILs and their corresponding local properties.[1] For example, the melting point of 1-butyl-3-methylimidazolium bromide increases and tributylhexadecylphosphonium bromide are depressed upon confinement into mesoporous silica.[194] In another example, the glass transition temperature 1-butyl- and 1-octyl-methylimidzolium tetrafluoroborate increases as a function of the pore size when confined within anodic alumina supports.[139] The interfacial properties between the IL and supporting material, particularly potentially charged materials such as silica, are important when translating the properties of ionic liquids to applications. These properties can be important for predicting diffusion, ion transfer, and local solubilization.

X-ray photoelectron spectroscopy (XPS) is used in materials science to determine the elemental and chemical states of surface layers to understand the surface properties.[195] XPS samples are almost exclusively solid in nature due to the limitation of XPS requiring ultra-high vacuum ($<10^{-8}$ mbar), resulting in the evaporation of any volatile components.

The low vapor pressure of ILs provides a unique opportunity for their local structure to be studied using this technique. Smith et al. demonstrated the stability of bulk ILs (1-ethyl-3-methylimidazolium ethylsulfate) in XPS and distinguish the electronic environment of carbon.[109] XPS has since been used to study a multitude of ILs and expanded to catalysis in bulk ILs with the addition of metal salts into the system.[11, 113, 115, 196, 197]

Fewer XPS studies have addressed the effect on the confinement of ILs on a porous support. Fortunato et al. investigated [BMIM][PF_6], [OMIM][PF_6], and [C_{10}MIM][BF_4] supported on polyvinylidene fluoride (PVDF) membranes.[198] XPS was used to evaluate the stability of supported ILs after exposure to closed-loop circulation deionized water on both sides of the membrane. While only 60% of the IL remained in the membrane after water exposure, the authors concluded that this is likely due to the removal of a surface layer of IL and the confined IL was not displaced from the pores.[198] With respect to ILs confined in mesoporous silica, Su et al. studied the confinement of [EMIM][Br] in mesoporous silica particles where the IL was added during the synthesis of the silica network as opposed to post-synthesis impregnation.[69] XPS data were used to verify the integrity of the confined IL since their main objective was the cycloaddition of CO_2 to propylene oxide.[69] Gupta et al. further advanced the characterization of interactions between mesoporous silica ionogels and [EMIM][Br] using deconvoluted XPS spectra by identifying shifts for the elements within the IL related to interactions with the surface.[117]

Molecular dynamics simulations on imidazolium-based IL's on silica surfaces indicate that the primary interaction is between the positively charged imidazolium ring and the negatively charged silica wall.[80] It is often reported that ILs form a nanostructure when near a silica surface,[4] and it would be useful to have additional methods that evaluate

the effect of nanostructures on local solvent environments. To this end, transmission FTIR, which can pass through thin solid samples like nanoparticles or mesoporous thin films, provides averaged information about the IL state through the entire pore. Several groups have used FTIR to characterize confined ILs and there results are consistent with the interactions observed by molecular dynamics.[1, 34, 199] XPS probes similar information but can also probe more subtle changes in the electronic environment of a material, can more easily characterize the oxidation state of metal-based anions (such as $FeCl_4^-$),[196] and can estimate solvent Lewis acidity since supported halometallate ILs have applications in catalysis.[11]

Most literature utilizing XPS to study ILs focuses on ILs with a longer length chain for the cationic group, [C_nMIM][X], where $n \geq 8$ and X = Cl^-, NTf_2, BF_4, or one of the other many common anions.[114] Other common cations include pyridinium, pyrridolinium, phosphonium, sulfonium, and ammonium based ILs. Other groups have studied the effects of alternating the bulk IL anion/cation and cation chain length in detail and gives credibility to the highly tunable nature of this class of solvents.[112, 197] 1-butyl-3-methylimidazolium chloride ([BMIM][Cl]) was chosen for this investigation of confinement effects because of the simplicity of the XPS analysis (with relatively few constituents) and potential for measurable changes in the electronic environments for these constituents. [BMIM][Cl] is also a commonly studied IL for catalysis and biomass dissolution[8, 200]

Here, the effects of nanoconfinement on the electronic environment of ILs confined within mesoporous silica was evaluated as a function of pore size and surface functionalization with an IL-like moiety. [BMIM][Cl] was confined in mesoporous silica thin films with pore channels vertically aligned with respect to the substrate.[26, 27] The tri-

block copolymer Pluronic P123 (P123) was used for templating vertically aligned mesoporous silica films with a diameter of ≈ 8.5 nm, while titania doping and cetyltrimethylammonium bromide (CTAB) was used to achieve films with approximately 3.5 nm diameter pores. Physical confinement of the IL was studied to elucidate interactions between the surface of the pore wall and the IL in both 3.5 and 8.5 nm diameter, vertically aligned silica pores. The surface charge of the support material was also changed by covalent attachment (tethering) of the IL-like molecule 3-methyl-1-[3-(trimethoxysilyl)propyl]-1H-imidazol-3-ium chloride ([TMS-MIM][Cl]) to the 8.5 nm pore surface. This work highlights the ability of XPS to elucidate subtle interactions between low vapor pressure solvents and the surface of their support material, and the potential for quantitative analysis of the extent to which the solvent interacts with the surface.

4.3 Methods and Materials

4.3.1 Materials

Deionized water, toluene (ACS grade), acetonitrile (99.5%), and acetone (99.5%) were purchased from VWR. Titanium (IV) isopropoxide (TIP, 97%) was purchased from Beantown Chemical (Hudson, NH). Cetyltrimethylammonium bromide (CTAB, 99+%) and 1,6-diisocyanatohexane (98%) were purchased from Acros Organics. Glycerol (ACS Grade) was purchased from Macron Fine Chemicals. Tetraethylorthosilicate (TEOS) (99%) and potassium bromide (FTIR Grade) were purchased from Alfa Aesar. Pluronic P123 (poly(ethylene oxide)-block-poly(propylene oxide)-block-poly(ethylene oxide) copolymer (M_n ≈ 5800) was purchased from BASF. Sulfuric acid (95-98%) and hydrochloric acid (6 N) were purchased from BDH Chemicals. NoChromix and 1-butyl-

3-methylimidazolium chloride ([BMIM][Cl], 98+%) were purchased from Aldrich; anhydrous ethanol (200 proof) was purchased from Koptec. Toluene and diethyl ether (both ACS grade) for the synthesis of [TMS-MIM][Cl] were purchased from Pharmco-Aaper. The substrates used were silicon wafers from University Wafer Inc. Most materials were used as received. [BMIM][Cl] was purified by recrystallization from acetonitrile prior to use.

The tethering IL, 1-[3-(trimethoxysilyl) propyl]-1-imidazolium chloride ([TMS-MIM][Cl]), was synthesized by first making a mixture of N-methylimidazole (2.00 mL, 25 mmol), 3-chloropropyl-trimethyoxysilane (4.59 mL, 25 mmol), and toluene (40 mL) and refluxing for 36 hours. The mixture was left to cool to room temperature and the supernatant was removed with a pipette. The resulting oil was washed with diethyl ether (10 mL 3 times) to remove unreacted materials, and then dried under reduced pressure at room temperature. The product was a colorless oil (6.80 g, 97%) with the identity of the tethering IL verified by ^{1}H and ^{13}C NMR spectra comparison to the reported literature data.[172, 173] Toluene and diethyl ether were dried and distilled by standard methods before use.[174]

4.3.2 Film Synthesis

Mesoporous silica thin films were synthesized according to our previous work using CTAB (3.5 nm pores) or P123 (8.5 nm pores) as a template.[21, 26, 27] Both were made by an evaporation-induced self-assembly (EISA) process on silicon wafers. For 8.5 nm porous silica, a chemically neutral surface for P123 was first created so that the micelle template aligned in a normal orientation relative to the substrate surface, creating accessible pores.[26] Silicon wafers and glass slides were first cleaned by submerging them in a solution

of NoChromix for 24 hours. The wafers/slides were removed from the NoChromix and rinsed several times with DI water and one time with ethanol to aid drying and dried in a 100°C oven. The coating to make them chemically neutral was prepared by dissolving 359.3 mg P123 into 89 mL acetone to create a 0.696 mM solution. An equimolar amount of 1,6-diisocyanatohexane (10 μL) was added while stirring in a nitrogen glove bag. The solution was removed from the glove bag and 3 drops of glycerol were added to the solution while stirring for at least 10 minutes. This solution was kept stirring until dip-coating. The wafers/slides were dipped in the neutral solution and removed at a rate of 7.6 cm/min to create modified substrates that were left dry at 100°C for at least 24 hours.

The silica dip coating solution was prepared from TEOS, 200 proof ethanol, DI water, and HCl together in a final molar ratio of $1:3.8:1:5x10^{-5}$ and refluxed for 1.5 hours at 70°C. Afterward, additional HCl and DI water was added to bring the concentration of HCl to 7.34 mM, followed by stirring for 15 minutes and aging at 50°C in a water bath for 15 minutes. A second solution of P123 dissolved into ethanol to achieve a molar ratio of 0.01:18.7 was prepared. The two solutions were combined and allowed to stir for an additional 10 minutes before dip-coating. The final silica precursor solution had a molar ratio of TEOS:ethanol:H_2O:HCl:P123 of 1:22:5:0.004:0.01. A modified wafer from the previous step was dip-coated in this solution at the same speed (7.6 cm/min), sandwiched in-between two modified glass slides, and placed into a glass petri dish in a 50°C oven. The silica films were aged at 50°C for 24 hours, followed by drying at 100°C for 24 hours. To remove the cross-linked polymer template and surfactant, the films were calcined in air at a rate of 0.5°C/min to 500°C for 4 hours.

CTAB templated, Ti-doped silica films were synthesized according to previous work in our lab.[27] Silicon wafers were first cleaned by submerging them in NoChromix solution overnight, followed by rinsing with water and ethanol as with in P123 templated films. The dip coating solution was prepared by first adding 60 μL of titanium (IV) isopropoxide to 2.4 mL anhydrous ethanol while in a nitrogen filled glove bag (solution 1). Solution 1 was sealed within the glove bag with parafilm and stirred for 3 hours. Solution 2 was prepared by combining 0.98 mL anhydrous ethanol, 1.42 mL TEOS, 0.21 mL DI water, and 0.27 mL 0.1 M HCl and stirred for one hour. After solution 1 had stirred for 3 hours, solution 2 was added to solution 1 dropwise with vigorous mixing for 5 minutes. Next, 0.12 mL DI water, 1.03 mL anhydrous ethanol, and 323.12 mg CTAB were added to the solution, followed by stirring for an additional 5 minutes. Lastly, 3.42 mL of anhydrous ethanol was added, and the solution was left to stir for 1 hour. Afterward, the previously cleaned wafers were dip coated in this solution at 6 cm/min and cured at 50°C for 48 hours. The template was then removed by calcining the films at 450°C for 1 hour.

The IL-like molecule was tethered to the P123 templated by first dissolving 15 mg of [TMS-MIM][Cl] into 10 mL chloroform in a nitrogen glove bag. Bare P123-templated silica films were submerged into the solution and heated in an oil bath held at 60°C with reflux.[201] After 26 hours, the films were removed from the solution, immediately rinsed with DI water followed by ethanol, and dried with nitrogen.

4.3.3 Film Characterization

The structures of the P123 and CTAB-templated films were characterized using GISAXS (Xenocs Xeuss 2.0) with a microfocus Cu-Kα beam (λ = 1.54 Å) and a Pilatus3 200K detector. The samples were mounted on a flat GISAXS sample holder at an incidence

angle of 0.14°. The sample-to-detector distance was kept at 350 and 1700 mm for P123 and CTAB templated films, respectively, and was calibrated using silver behenate drop-cast onto a glass slide prior to measurement.[202] The total time in the beam was 2 minutes for each sample. The location of the 100 peaks related to the spacing between two planes of pores were determined by averaging the out-of-plane intensity as a function of the x-axis.

4.3.4 X-ray Photoelectron Spectroscopy

XPS was performed using a Thermo Scientific K-Alpha XPS system with a monochromated Al-Kα source (1486.6 eV) with a collection angle of 0°. The spot size of each point was 200 μm, each having 10 scans for the survey and each high-resolution (HR) scan with a dwell time of 10 and 50 ms, respectively. Survey spectra were recorded using a pass energy of 200 eV and high-resolution scans used a pass energy of 35 eV. Charge neutralization of the sample was achieved using a flood gun integrated into the system. The energy resolution of the instrument for high-resolution and survey scans was 0.1 and 1.0 eV, respectively. IL samples were dried in a vacuum oven at 100 °C overnight prior to use in XPS. Pure IL samples were prepared by placing a small droplet of the IL onto a clean silicon wafer surface, while confined samples were placed on the surface of the mesoporous film and pressed with a freshly cleaned silicon wafer to physically confine the IL into the pores. When choosing a spot, the camera equipped on the XPS was used to find a spot on the film where there was no visible excess IL present on the film surface.

Thermo Avantage software was used for data analysis. HR spectra were fitted using Shirley peak background. The pure IL spectra was charge-corrected by setting the aliphatic C 1s peak location at 285.0 eV. This shift is commonly used in IL literature,[11,

[114, 197] with recognition that the fit is valid for $[C_nMIM]^+$ cations where $n \geq 8$. The pore walls of the confined samples are made of silica, which has a well-documented peak BE for Si = 103.5 eV,[203] making it simple to cross-correlate the shift and show that setting the aliphatic C 1s peak at 285.0 eV is appropriate for this system. Generally, the HR spectra were fitted with a Gaussian/Lorentzian mix of 70/30 and a FWHM fit parameter of 0.8:1.9 eV after charge correction.

The fitting procedure for the HR spectra of the pure IL followed the method for imidazolium based ionic liquids with a structure of C_nC_1MIM where C_n and C_1 are covalently bound to the nitrogen in the imidazolium ring.[11, 204-206] In the procedure, the C_{alkyl} peak was centered at 285 eV, the rest of the peaks were added about 1, 1.5, and 2 eV higher BE relative to C_{alkyl}, and Avantage fitted the peaks using the convolve method. The pure IL spectra served as the starting point for fitting the spectra of the confined IL. In the confined IL, the Si 2p peak was first centered at 103.5 eV. The C 1s peaks in the confined IL samples were highly constrained to have the same full-width half-max and charge separation as the pure IL and additional peaks necessary to fit the spectra were added as described below.

4.4 Results and Discussion

4.4.1 Film Synthesis and Characterization

Grazing incidence small angle x-ray scattering (GISAXS) was used to verify that the mesoporous silica thin films have vertically aligned pores with respect to the substrate

and to determine the pore spacing of the films. Figure 11 shows representative 2D GISAXS patterns for films templated with P123 (a) and CTAB (b).

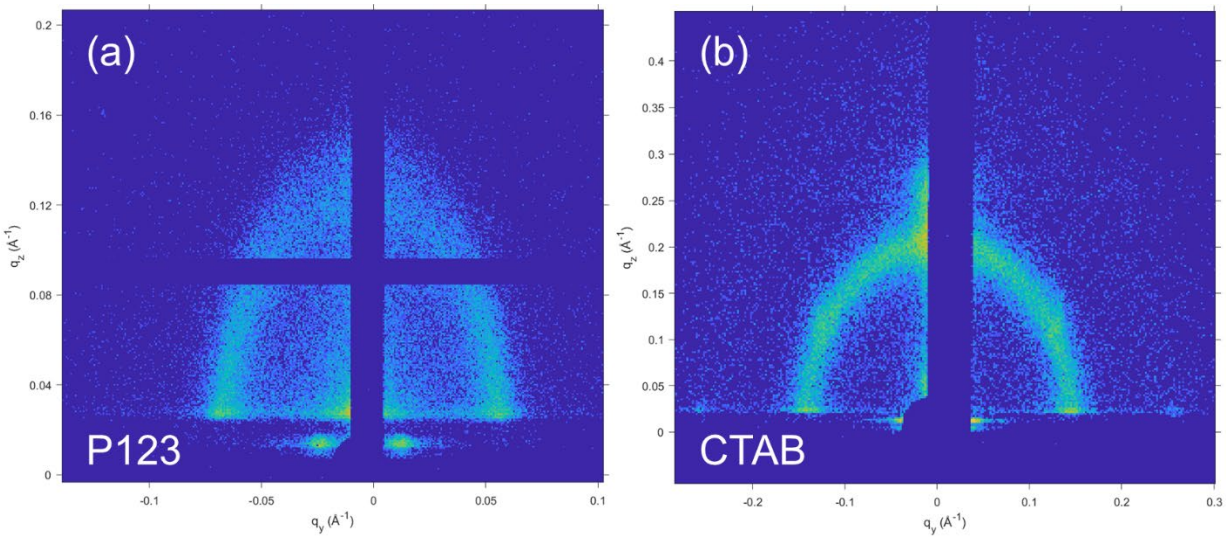

Figure 11. 2D GISAXS pattern of P123 templated silica thin film (a), CTAB templated titania doped silica (b).

The ring in the GISAXS pattern is elongated due to the unidirectional contraction of the thin film perpendicular to the substrate from the removal of the surfactant through calcination.[207] The d-spacing, or center-to-center distance between planes of pores, is calculated from the location of the vertical rods in the (100) and ($\bar{1}$00) planes. The d-spacing is calculated from q using equation 8:

$$d = 2 * \pi/q \tag{8}$$

where q is the scattering vector (units of Å^{-1}) for the in-plane (q_y) or out-of-plane (q_z) components corresponding with scattering parallel and perpendicular with respect to the substrate. In 1D scattering techniques, q is analogous to 2θ, and in SAXS q can be found by taking the azimuthal average of intensity around the direct beam center. For P123 films,

q_y = 0.059 Å^{-1} and the d-spacing ≈ 10.6 nm. The corresponding center-to-center pore distance of a hexagonal close packed is 2/√3 x d-spacing, or ≈12.3 nm. The pore wall thickness is not given by GISAXS[21, 67, 208] so it is inferred from other work on the same material. Coquil et al. estimated the pore wall thickness of P123 templated thin films to be between 3-5 nm,[208] making the pore diameter 8.3 ± 1 nm for P123 films. Other studies within our group have reported pore diameters of 9 ± 1.3 nm for the same materials using TEM, so the pore diameter is assumed to be 8.5 nm.[1, 67]

A route to a mesoporous silica thin film with a smaller pore size uses CTAB, a smaller surfactant template, combined with titania doping.[21] The GISAXS patterns of the CTAB templated film after calcination are presented in Figure 11 (b). Calcination removes the surfactant template and transforms the disordered pore structure into orthogonal hexagonal close packed structure through thermal contraction during calcination.[27] The d-spacing of the CTAB templated films is 4.8 nm (from q = 0.145 Å^{-1}), corresponding to a pore center-to-center distance of 5 nm. The pore wall thickness of CTAB templated silica thin films are about 1-2 nm,[21] meaning the pore diameter of these materials is about 3.5 ± 0.5 nm.

4.4.2 XPS Survey Spectra and Bulk IL

The survey and high-resolution C 1s, N 1s, and Cl 2p spectra are shown for pure IL [BMIM][Cl] in Figure 12, which also includes the corresponding atomic percentages (inset). There are no contributions from silicon or oxygen, indicated that there is no measurable contamination from silicone greases or water in the sample. In addition, the atomic percentages of the C, Cl, and N are near their expected values (inset).

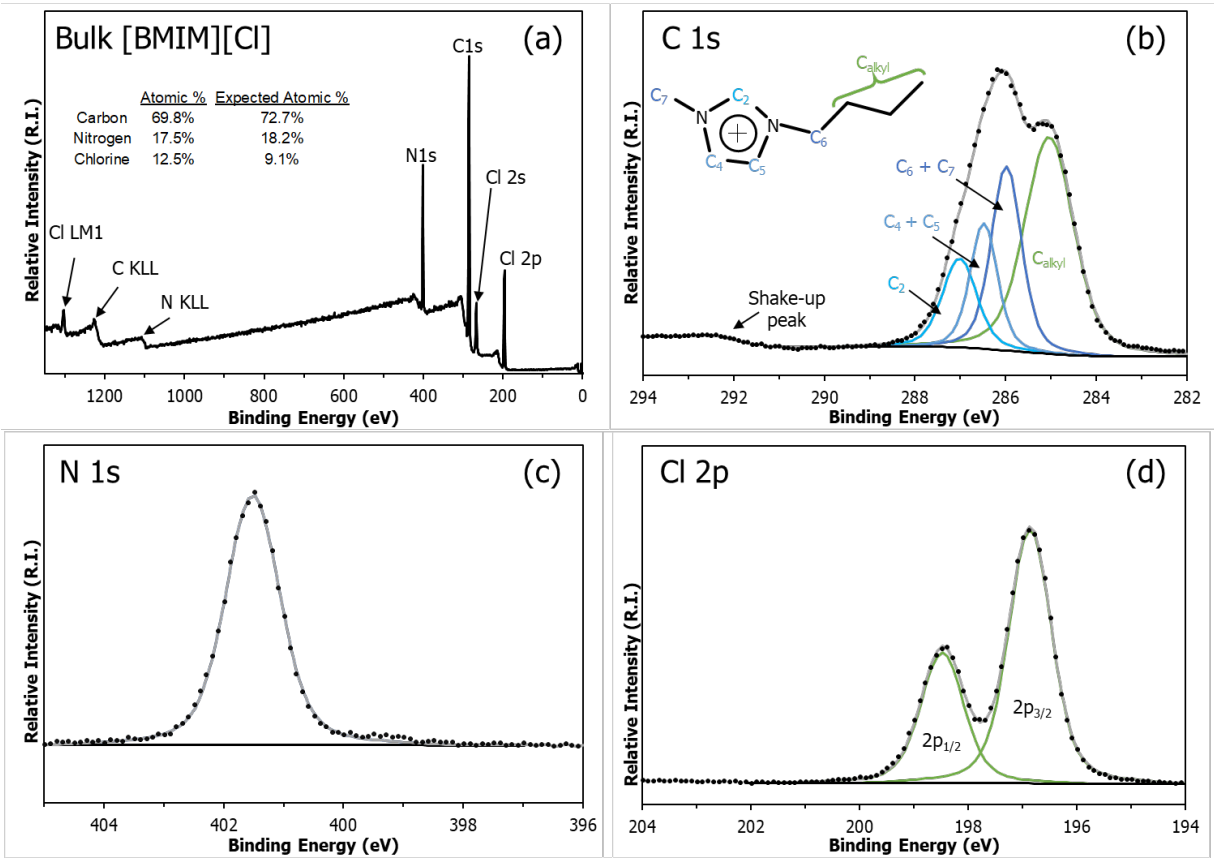

Figure 12. XPS spectra of (a) bulk [BMIM][Cl] with an inset table of expected and actual atomic %, (b) high resolution carbon C 1s spectrum with color-coded peak assignments, (c) high resolution N 1s spectrum, and (d) high resolution Cl 2p spectrum.

The deconvoluted carbon HR spectrum of the bulk IL is displayed in Figure 12 (b). The HR peaks are well-defined and show no signs of x-ray damage. Four energy environments of the imidazolium cation contribute to the C 1s spectra, as labeled in Figure 12 (b). The carbons on the long tail of the imidazolium exhibit the same energy environment, referred to as the aliphatic C 1s (C_{alkyl}) signal. The remaining three peaks are related to the imidazolium ring carbons ($C_{2,4\text{-}5}$) and *N*-bound methyl and methylene carbons ($C_{6\text{-}7}$) within the cation.[11, 111, 112] The nitrogen N 1s HR spectra (Figure 12 (c)) only has one peak. This is expected since the nitrogen in the imidazolium ring shares a positive

charge. Due to spin orbit splitting, the chlorine Cl 2p spectra (Figure 12 (d)) has two peaks with an intensity ratio of 0.5:1 for the $2p_{1/2}$ and $2p_{3/2}$ peaks and a separation of 1.63 eV;[11] the $2p_{3/2}$ peak is centered at 196.9 eV. Since the peak is near the value reported by literature in the correct ratios, is well fit, the Cl 2p spectra does not display any extra features, there is only one chlorine environment in the system.

XPS was performed on mesoporous silica thin film of with varying pore diameter (3.5 nm and 8.5 nm) with physically confined IL as shown in Figure 13. In the case of the 8.5 nm pores, the effect of surface chemistry on confinement was also examined. The pore wall surface was modified by covalently tethering a positively charged, IL-like molecule ([TMS-MIM][Cl]) to the porous silica. XPS of the tethered film without confined IL was used to confirm that tethering was successful. The survey and HR spectra for the tethered film without additional physically confined IL are presented in Appendix Figure A.2.1. The C 1s peak is large and broad rather than an uneven peak like in pure [BMIM][Cl]. The N 1s peak is also broad but is centered at 401.9 eV after charge correction which is close to the pure IL. The Cl 2p peak is present, but very noisy due to low concentration of chlorine. Since tethering only covers the surface of the IL, the small signal-to-noise ratio is expected.

The survey scans the pure IL, films with confined IL, and tethered films with confined IL are presented in Figure 14. The survey scan of the pure IL is the same as in Figure 12, and only shows contributions from C 1s, N 1s, and Cl 2p. In the survey scans of the confined ILs in the 3.5 nm, 8.5 nm, and tethered 8.5 nm films, there are no additional peaks from contamination and the ratio of oxygen to silicon is near the expected value for

all cases. The peaks from C 1s, N 1s, and Cl 2p are also still present in the confined ILs and are close to their expected ratios.

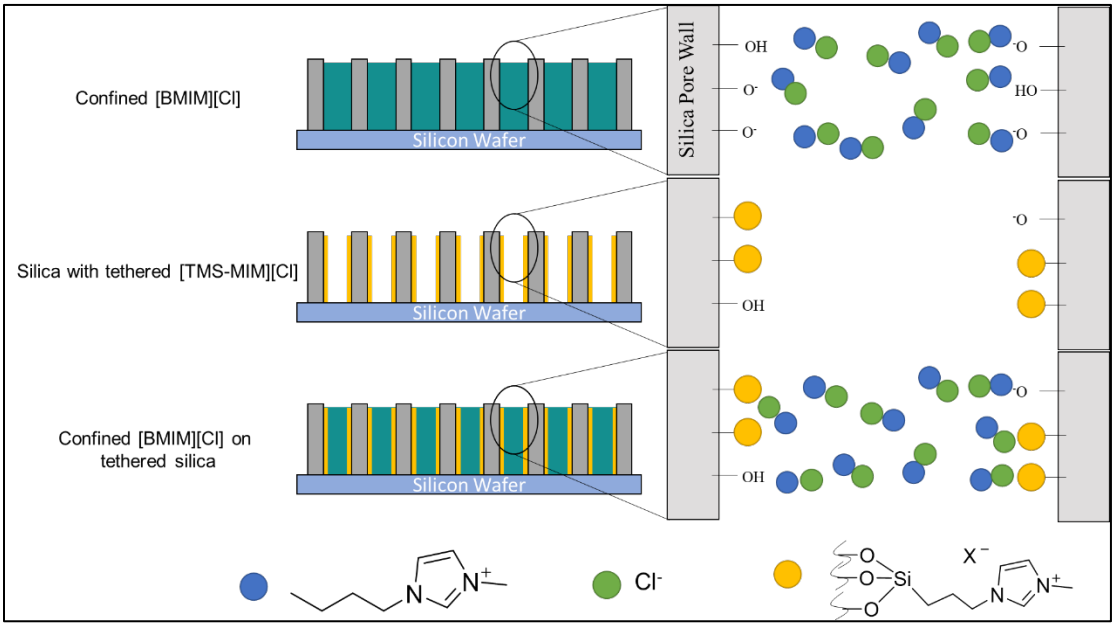

Figure 13. Schematic of film treatments examined by XPS. The 3.5 nm and 8.5 nm confined data is represented by the top-most figure (Confined [BMIM][Cl]). The middle and bottom figures represent the silica with a tethered IL-like molecule and tethered film with confined IL. The structures of [BMIM][Cl] and [TMS-MIM][Cl] are provided.

The relative stoichiometries for the IL-loaded silica thin are obtained from the survey scans. The significant signal from oxygen and silicon along with the peaks of the IL indicate that IL in the pores contributes to the observed spectra. These measured stoichiometries are compared to theoretical stoichiometric values of IL-filled pores based on the pore geometry in Table 2. The full details of the theoretical value calculation can be found in Appendix Figure A.2.2. The measured stoichiometric excess of IL species relative to theoretical values suggests that XPS is also probing a nanoscale layer of IL along the top surface of the porous films.

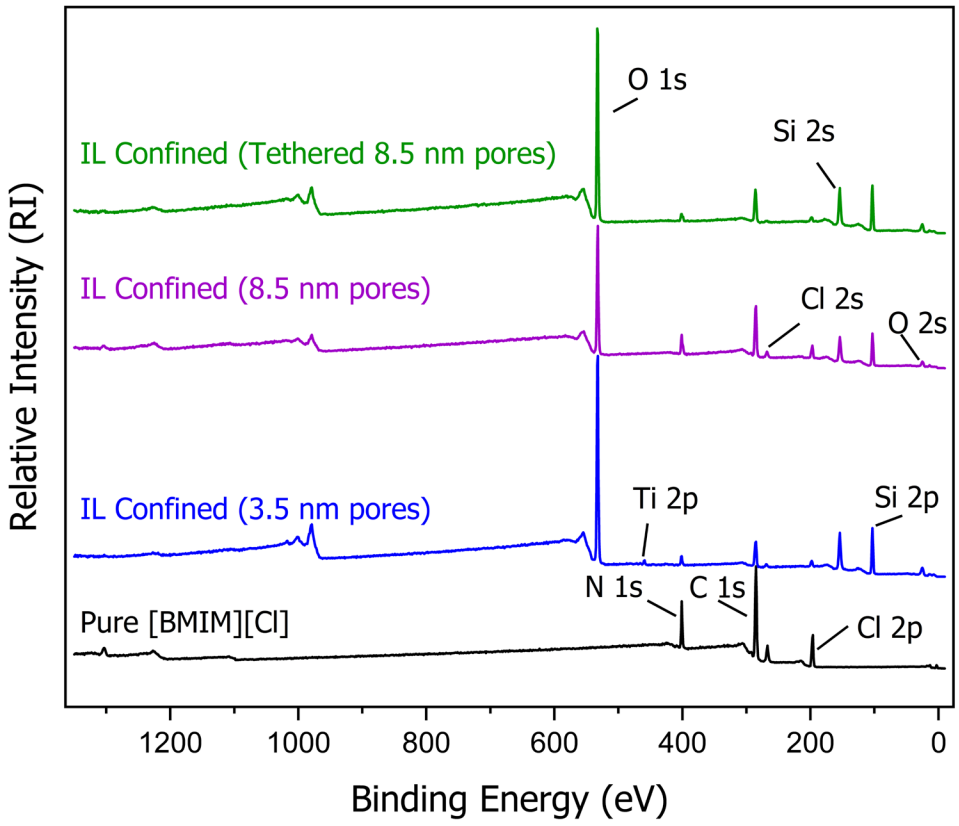

Figure 14. Survey spectra of bulk and confined ILs. From the bottom to the top is the bulk [BMIM][Cl] (black), the IL confined within 3.5 nm pore silica (blue), 8.5 nm pore silica (purple), and tethered and confined 8.5 nm pore silica (green).

Table 2. Measured and theoretical elemental values of IL confined in 3.5 nm pores and 8.5 nm pores of silica thin films.

	3.5 nm Pores Atomic %		8.5 nm Pores Atomic %		Tethered 8.5 nm Pores Atomic %	
Species	Measured	Theoretical	Measured	Theoretical	Measured	Theoretical
Si	20	28	19	29	26	29
O	38	58	32	59	50	59
C	30	9.5	37	8.4	23	8.4
N	8.2	2.4	8.8	2.1	3.8	2.1
Cl	3.6	1.2	3.4	1.1	1.2	1.1

4.4.3 Carbon, Nitrogen, and Chloride High Resolution Spectra

The high resolution (HR) spectra provide more detail on the environment of the confined ILs. Carbon C 1s is abundant in the IL and can give insight into the imidazolium ring interactions. Nitrogen N1s and chlorine Cl 2p are readily interpreted HR spectra. The only contribution for N1s is the shared energy state within the nitrogen of the imidazolium ring. The energy state of the chloride is easily interpreted since it is a lone anion. The HR spectra for Si 2p and O 1s were measured but did not exhibit any anomalies since they make up the bulk of the pore walls and are not present in the IL. These spectra can be found in Appendix A.2.3.

In interpreting the carbon environment, the C 1s spectra (Figure 15) is broadened and shifted to slightly higher BE for the confined ILs relative to bulk IL. The carbon spectra were deconvoluted by highly constraining the confined IL spectra to contain the three peaks in the bulk phase IL since it is expected that bulk IL is present within the center of the pore and on the surface of the thin film. Two additional peaks (orange and yellow) were required to fit the spectra of the confined ILs, indicating two new environments for carbon within these systems. The alkyl tail is unlikely to participate in new interactions, so these environments most likely reflect interactions of the imidazolium ring carbons or possible contamination on the film surface. Survey and HR scans of representative bare films are shown in Appendix Figure A.2.4. The pristine silica surface had adventitious carbon contamination near 285 eV before confinement, but no nitrogen signal was detected. Adventitious carbon contamination, typically non-polar, short chain hydrocarbons, is not uncommon and does not hinder in the interpretation of carbon electronic environments of ILs.[110, 111, 209]

Peaks related to the carbons of the imidazolium group are shifted in both the positive (to 287.4 eV) and negative (286.5 eV) directions for the confined ILs relative to the bulk IL imidazolium ring peaks. Imidazolium ring peak shifts are associated with a change in the partial positive charge of the ring. A more neutral charge would make it easier to remove an electron from the shell of carbon, thus increasing the kinetic energy and reducing the binding energy of that electron. The opposite is true for a more positive partial charge on the imidazolium ring. Neutralization of the ring charge (lower BE) may result from the IL interacting with the negatively charged silica pore wall. In the case of increasing ring charge (higher BE), it is possible that the chloride forms $[Cl\text{-}H\text{-}Cl]^-$ with the proton from the silanol groups along the pore wall and leaves the cation without an associated anion.[210] The contribution of the lower BE (more neutral) is more prevalent in the IL confined in 3.5 nm pores, which has higher pore surface area for interactions than the 8.5 nm pore thin films. The C 1s peaks in the tethered-confined system in 8.5 nm pores are similar to the confined system of the same pore size. The tethering of [TMS-MIM][Cl] introduces a positive surface charge which should prevent the surface interactions with the imidazolium ring. However, the lower BE (more neutral) peaks are present in the tethered 8.5 nm pore films, although broader than in bare 8.5 nm films, suggest incomplete surface coverage by the IL-like functional group. There is also another peak at the higher BE, which may indicate that portions of the IL underwent cross-linking after the hydrolysis of the silanol bond from the tethering IL. Overall, the peaks in the tethered IL are similar to the non-functionalized 8.5 nm pore films with confined IL, which may indicate that the pore walls are not completely functionalized and some unreacted silanol groups remain, leading to the decrease in binding energy.

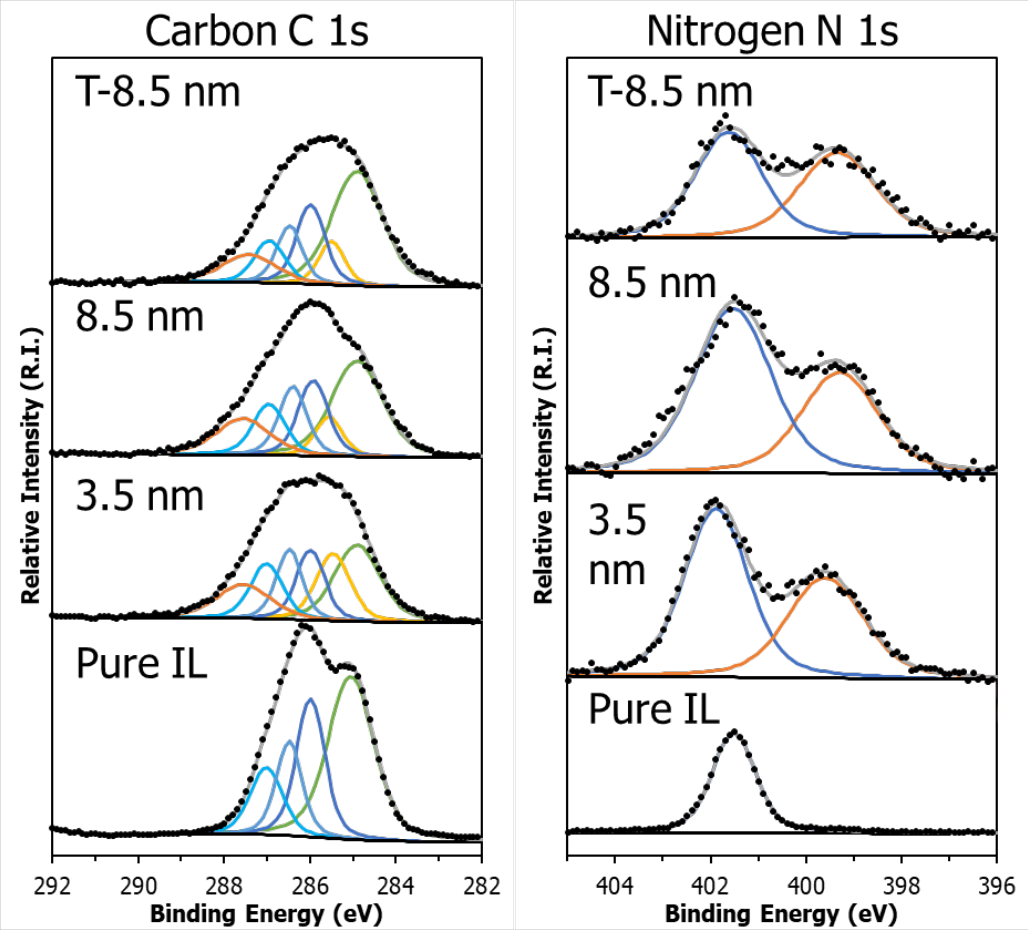

Figure 15. High resolution C 1s and N 1s spectra of bulk and confined ILs. From bottom to top: bulk IL, IL confined within 3.5 nm porous films, IL confined within 8.5 nm films, and IL confined within tethered-8.5 nm films.

In contrast to carbon, nitrogen offers a much simpler fitting approach because it is exclusively present in the cation of the IL. Historically, groups studying ILs with XPS have employed a variety of anions, with nitrogen-containing anions being prevalent in many cases.[112, 113, 115, 196, 197, 205] However, the choice of chloride as the anion simplifies the interpretation of the nitrogen spectra; observed shifts in the nitrogen spectra on confinement are attributed to interactions of the imidazolium cation. Since both nitrogen

atoms share a positive charge in the imidazolium ring, there is only one peak present at 401.5 eV in the HR scan for pure IL, as shown in the pure IL N 1s spectrum in Figure 15. Upon confinement, a large second peak is present at lower BE (≈ 399.5 eV) in for all three treatments of confined IL. We attribute this to strong interactions between the imidazolium ring and the silica pore wall. We hypothesize that this second signal is a result of neutralization of the imidazolium ring positive charge. The high surface area of the mesoporous substrate leads to an enhancement of this signal. This result is consistent with molecular dynamics simulations of IL systems on charged surfaces, which predict layering of the IL along the surface due to electrostatic interactions[80, 211] XPS is able to directly probe these electronic environments, indicating a unique IL environment at the pore wall and in the bulk (the center of the pore and at the film surface). The lower BE peak associated with nitrogen is also present in the tethered-confined IL, suggesting that tethering does not block the interaction of the free IL with the silica surface. Other researchers have also noted a second peak with lower BE in the nitrogen spectra of mesoporous silica or titania particles with confined IL, but the peak is small and not further interpreted.[69, 212]

The existence of nitrogen peaks at lower BE than the bulk IL is consistent with the hypothesis that the imidazolium ring directly interacts with the silica surface and charge neutralization occurs between the IL and silica. The small size of the chloride anion allows for maximum interaction of the imidazolium ring with the surface. The size of the anion has an impact on the orientation of the cation.[213] Larger anions cause a larger tilt of the imidazolium ring and move it slightly farther from the surface of the silica. Furthermore, the high degree of cohesion force between IL and the surface will lead to charge neutrality

at the local level.[213] Angle resolved XPS also supports the hypothesis that ILs form layers along a solid substrate. The 2-dimensional growth of a molecular layer of [C_1MIM][Tf_2N] and [BMIM][Tf_2N] on freshly cleaved mica was monitored by ARXPS.[214] Near the surface, the contribution of the imidazolium cation of the IL (BE ≈ 402 eV) to the nitrogen peak increased relative to the anion ([Tf_2N], BE ≈ 400.5 eV). This was attributed it the imidazolium ring being directly adsorbed to the surface.[214]

FTIR has also been used to characterize confined ILs and probe the interaction between the IL and the substrate. He et al. found that hydrogen bonding between the C_2 carbon of [BMIM][Cl] (Figure 12) and the silica pore wall caused the C-H stretching peak to be redshifted when confined within mesoporous silica thin films.[1] The peaks between C=N– and C=C– in the imidazolium ring did not shift significantly in the FTIR spectrum.[1] Verma et al. also showed that the peak related to the C_2 carbon shifts upon confinement within mesoporous silica particles.[82] The FTIR results imply that the interaction between the IL and silica pore wall is through a single carbon, while the XPS results show that the interaction has an impact on the energy level of the whole imidazolium ring. Both FTIR and XPS point to strong interactions between the imidazolium ring and the silica, and each have different advantages as a technique. One advantage of XPS is that it is more sensitive to subtle changes in the electronic structure of the IL. Additionally, XPS can probe the Lewis acidity of the IL confined in the pores and more easily study metallic anion speciation and oxidation state,[11, 196] making XPS a better tool to characterize confined halometallate ILs for catalysis applications. XPS may also be better at characterizing the electronic environment of the anion, depending on its composition, as seen with the chlorine speciation.

The chloride Cl 2p spectrum for the pure IL in Figure 16 shows the characteristic doublet of chlorine due to spin orbit splitting. Spin orbit splitting occurs because of the different angular spin momentum of the electrons in the p, d, or f orbital levels, resulting in two peaks appearing for every single energy environment in the system. The gap between the two peaks for chlorine is 1.6 eV and the ratio of the $2p_{3/2}$ to $2p_{1/2}$ is 2:1.[196] Chloride is in one electronic environment in the pure IL and exists as the anion to $[BMIM]^+$. The position of the $2p_{3/2}$ peak depends on the cation alkyl tail length. The peak location in [OMIM][Cl] is centered at 197.1 eV,[11] while this work agrees the literature values for [BMIM][Cl] of 196.9 eV.[196]

Nanoconfinement of [BMIM][Cl] introduces new peaks in the chlorine spectra, which are shifted to more positive BE relative to the $2p_{3/2}$ peak of 196.9 eV and indicate a change in the chloride environment. In the case of confinement in 3.5 nm pores, the peak for Cl shifts upward to 197.8 eV, and there is a second peak centered at 200.5 eV. The positive direction of this shift implies that the environment of the chloride is more neutral, making it more difficult to remove electrons (increased BE). In silica with 8.5 nm pores, the original Cl peak is located similar to the pure IL (196.7 eV), suggesting that the larger pores of the P123 templated films allow for free chloride to exist within the center of the pore. There is also a second peak in ILs confined in 8.5 nm pores centered at 197.8 eV, which falls close to the same peak location as the first peak in 3.5 nm pores. Finally, the location of peaks in the chloride spectra of ILs loaded in tethered, 8.5 nm pores is similar to that of 3.5 nm pores, with peaks centered at 197.8 and 200.5 eV.

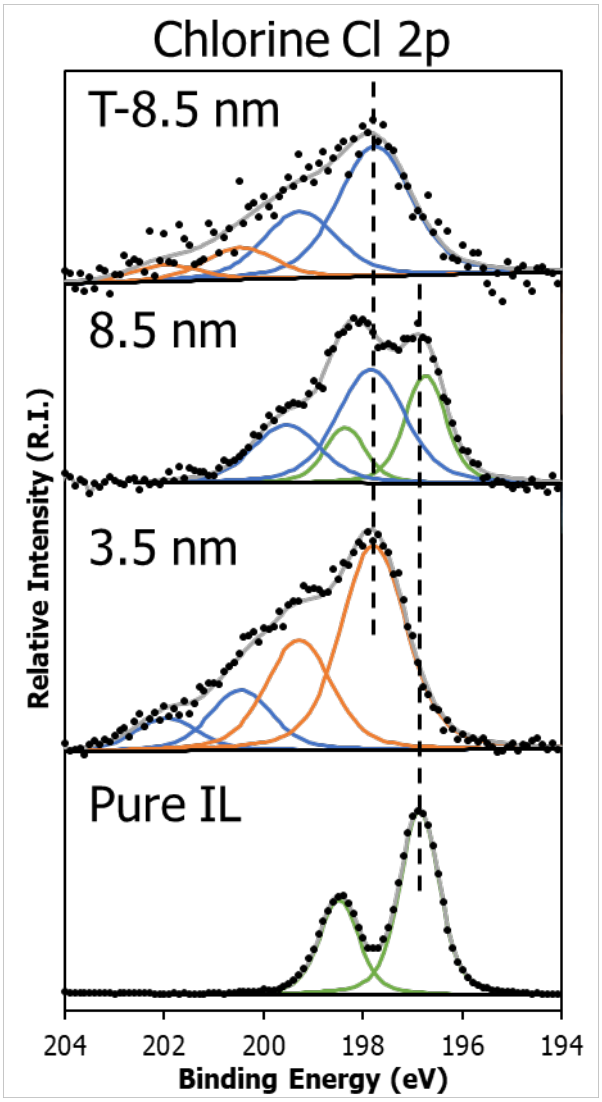

Figure 16. High resolution Cl 2p spectra for [BMIM][Cl] in bulk and confined within mesoporous silica thin films. From the bottom to the top is the bulk IL, IL confined within 3.5 nm silica, IL confined within 8.5 nm silica, and IL confined within tethered-8.5 nm silica. The dashed vertical lines represent the center of the Cl $2p_{3/2}$ in the pure IL and the first peak of the Cl $2p_{3/2}$ in the case with IL confined in 3.5 nm pores and are to guide the eye.

Observed shifts of chloride to higher binding energies upon confinement of [BMIM][Cl] suggest several types of potential surface interactions. Hydroxyl groups on the silica surface that are not deprotonated may participate in hydrogen bonding with

chloride to cause the modest shift to 197.8 eV in all 3 cases. This hypothesis is supported by MD simulations that show the chloride anion can participate in hydrogen bonding with a hydroxylated quartz surface.[80] Similarly, the BE of chloride is a function of the coordination strength or basicity of the anion, further supporting the hypothesis that the BE of chloride could be increased with hydrogen bonding interactions with the surface.[11] In the case of the peak at 200.5 eV in the 3.5 and tethered-8.5 nm pores, the shift is more typically consistent with organochloride compounds.[215] One possible cause is the deprotonation of surface hydroxyl groups, which can then form a $[Cl\text{-}H\text{-}Cl]^-$ anion arrangement that has been detected previously using NMR.[210, 216] The shifts to higher binding energy in all spectra clearly show that the pore size can significantly impact the speciation or interactions of the chloride anion.

4.4.4 Depth Profiling

We performed argon etching on the 8.5 nm pore films with physically confined [BMIM][Cl] by investigating the confined IL in the absence of a surface layer of IL on the film and establishing the uniformity of the confinement through the depth of the film. A profile of the relative intensities of the element in the confined film as a function of depth (etching time) is presented in Figure 17. Monatomic argon etching was carried out using 1 keV Ar^+ ions in five intervals of 20 seconds followed by 13 intervals of 80 seconds etching. There is a small change in the oxygen:silicon ratio from 1.67 to 1.63 after the first interval. Previous studies have shown that argon etching on amorphous metallic oxides can preferentially sputter oxygen from silica materials up to 1.2 atomic %.[217]

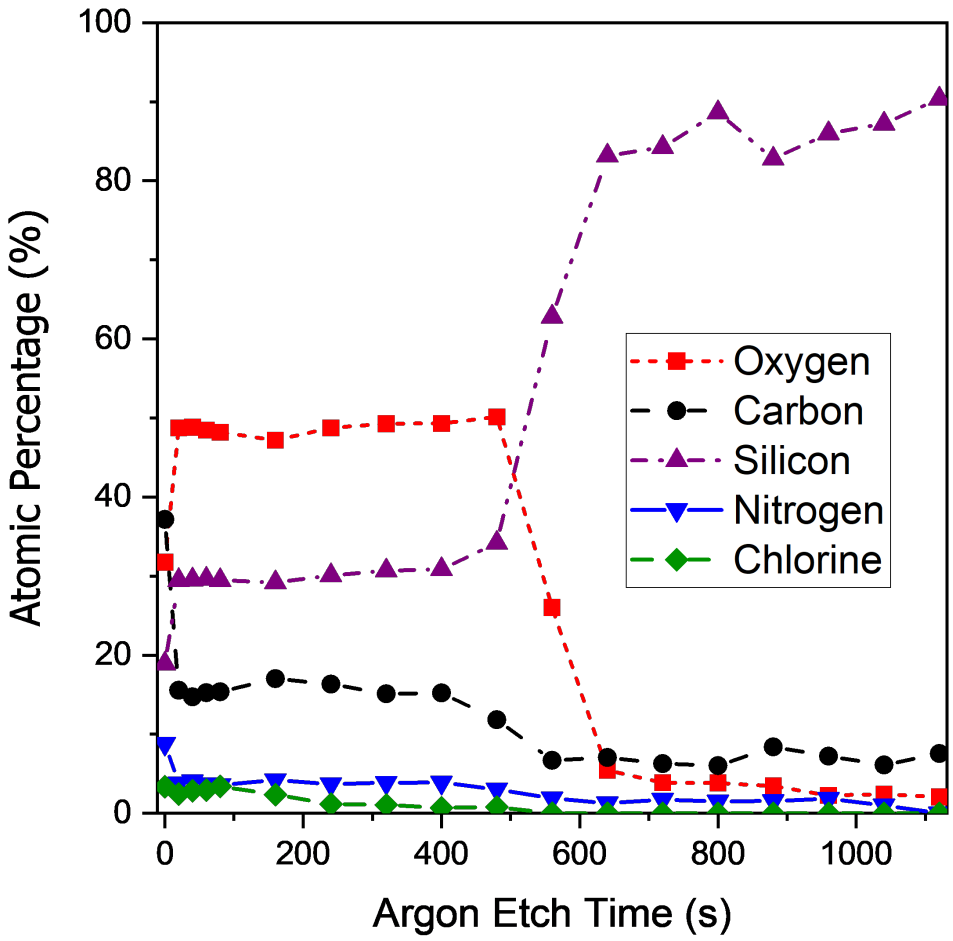

Figure 17. Relative atomic percentages of each element as a function of the duration of argon etching. Oxygen is denoted by a red square with a dotted line, carbon by a black circle with a dashed line, silicon with a purple upward-facing triangle with dash-dot, nitrogen by a blue line with downward-facing triangle, and chlorine by a green diamond with a dashed line.

The relative atomic percentages of the species present and shapes of the spectra are compared for any indications of damage. After etching for 20 seconds, the ratio of IL to silica approaches the theoretical value for IL-loaded, 8.5 nm pores (see Table 2); the atomic percentages of Si, O, C, N, Cl are 29.5, 48.8, 15.5, 3.8, and 2.4% respectively. The ratio

of C:N is 4.07, which is very close to the stoichiometric ratio of 4.0 for $[BMIM]^+$ and suggests that the cation is not significantly impacted by the argon beam. The chloride concentration is higher than expected during the first several etching intervals, then essentially disappears after 200s of etching. The initial increase of chloride could be due to local high concentrations within the pore due to interactions with the silica pore wall, and the decrease may be from the selective etching of chloride since it is the lightest component in the system. The formation of ArCl is possible and is well-known to cause interference for arsenic detection in ICP-MS.[218] After 500s of etching, the silicon wafer is reached and all signal aside from silicon is reduced dramatically. There is an overlap of the Si 2s with the Cl 2p line at high concentrations. For the purpose of this analysis, the chloride atomic % was set equal to 0 after it was apparent that the substrate was reached. Additionally, the nitrogen and chlorine peaks change shape immediately upon the first instance of etching (Appendix Figure A.2.5). The shift of the nitrogen to lower BE and chloride to higher BE are consistent with a larger number of interacting species present, which would correlate with the elimination of the surface IL layer on top of the pores. Chloride has a much more dramatic shift that may be due to the interaction with argon. Previous reports of ILs in literature suggest that argon etching causes irreversible damage to shorter chain ($n < 8$) ILs with guanidinium-based cations[219] and based on the peak shape change of chloride, this may hold true for the confined ILs as well. These results show that argon etching can be employed to remove surface layer IL contaminants to better probe the interior of the pores, but the ILs are subject to argon beam damage.

4.5 Conclusion

The interfacial interactions between ILs and mesoporous silica were elucidated using XPS. The mesoporous silica film substrates were synthesized by sol-gel techniques and characterized using grazing-incidence small angle x-ray scattering and the surface was functionalized with an ionic liquid like molecule to change the surface chemistry. XPS was shown to be a powerful technique for elucidating interactions between low vapor pressure solvents and mesoporous materials.

The deconvoluted carbon spectra had multiple electronic environments present in the IL and the broadening of the peaks was due to electrostatic interactions with the pore surface. The chloride spectra shifted to higher binding energy through either the formation of diatomic chlorine or bridging chloride with a pore wall proton within the pores. The prevalent chloride species depended upon the pore wall chemistry and diameter, where more dramatic shifts were observed with smaller or functionalized pores. The larger 8.5 nm pores without tethering allowed free space in the center of the pore for free chloride to exist, while tethered pores and smaller pores with high surface area had more hydrogen bonding with the pore wall or formed $[Cl\text{-}H\text{-}Cl]^-$ with a proton from the pore wall. The deconvoluted N 1s peaks were used to directly show the interaction between the positively charged imidazolium headgroup of the IL with the negatively charged walls of the mesoporous silica films. In confinement, a second nitrogen peak appeared having lower binding energy than bulk IL and is due to the more neutral charge character of the imidazolium ring interacting with the silica surface. These results are consistent with MD simulations of ILs at charged interfaces where cations and anions form alternating layers on the surface. The choice of IL, in which nitrogen is only present in the imidazolium

headgroup, allows this interaction to be directly probed by XPS and may be relevant to the quantification of the relative amount of free (bulk) and associated ILs in confinement. Oxygen and silicon are both present in the spectra in much greater amounts than bulk IL and provide sufficient evidence that the region being probed is within the pore and not just surface adsorbed IL. Argon etching showed that the top layer of IL was able to be removed, but possible interactions between monatomic argon and chloride hinders the interpretation after etching.

This work demonstrates the ability to study subtle interactions of low vapor pressure solvents in a confined matrix using XPS. This is advantageous because it is another technique that gives quantitative and qualitative information about the IL electronic environment within porous substrates and is complimentary to other techniques such as FTIR. XPS on confined ILs could be expanded to IL systems where the acidity and electronic environment of the catalyst site can be investigated.

CHAPTER 5. NANOCONFINEMENT OF HALOMETALLATE IONIC LIQUIDS WITHIN MESOPOROUS SILICA

5.1 Summary

The interface between the confined ionic liquid (IL) 1-butyl-3-methylimidazolium tetrachloroferrate [BMIM][$FeCl_4$] within 3.5 nm mesoporous silica thin films is investigated using x-ray photoelectron spectroscopy (XPS). Mesoporous silica thin films with accessible pores oriented orthogonally with respect to the substrate were synthesized by evaporation induced self-assembly and characterized by grazing-incidence small-angle x-ray scattering. The IL was physically confined within the pores and XPS was used to probe the interface between the IL and the silica support. The IL was also mixed with pyridine and supported onto 8 nm mesoporous silica microparticles to evaluate the acidity using FTIR. FTIR showed that the addition of iron gave the IL Lewis and Brønsted acidity properties that were maintained when confined within the pores. Comparing [BMIM][Cl] to [BMIM][$FeCl_4$] using XPS showed that the charge of anion was more delocalized with the addition of iron and was less able to accept hydrogen bonds. The confined [BMIM][$FeCl_4$] interacted with the pore wall in a different way than [BMIM][Cl], where the anion was situated more closely to the pore wall than the cation. The peak location of iron in XPS shifted downward when the IL was confined and suggests enhanced charge transfer with the pore wall. The results demonstrate the use of XPS to the solvent and catalytic environment of halometallate ILs of nanoconfined ILs.

5.2 Introduction

Ionic liquids (ILs) are a class of solvents that are salts that have low melting points (under 100°C). They have been proposed as an alternative to traditional organic solvents

since they have good thermal stability, high ionic conductivity, and their properties are tunable by modifying the cation or anion.[1] ILs have been used many different applications such as electrolytes, the reaction media in catalytic systems, and as a solvent for separations. [9, 46, 133, 134] The industrial adoption of ILs is limited by their cost and unfavorable transport properties.[193] Confined IL systems that support the IL on a solid, porous material require less IL and reduce leaching from the system.[78] Confinement changes local ordering and impacts their physical properties.[1] For example, the melting point of 1-butyl-3-methylimidazolium bromide increases and tributylhexadecylphosphonium bromide is depressed upon confinement into mesoporous silica.[194] In another example, the glass transition temperature 1-butyl- and 1-octyl-methylimidzolium tetrafluoroborate increases as a function of the pore size when confined within anodic alumina supports.[139] Interfacial properties between ILs and their host materials are important when considering property changes like diffusion, ion transfer, or local solubilization in confined IL applications.

Halometallate salts are commonly dissolved within ILs to improve their catalytic ability. In an early example, iron (III) chloride was added to 1-butyl-3-methylimidazolium chloride ([BMIM][Cl]) to synthesize [BMIM][$FeCl_4$] as a recyclable catalyst for the cross-coupling of alkyl halides.[35] The use of an abundant, inexpensive, and less toxic metal like iron generated interest in using the IL as a catalyst. The use of magnetic anions, which can be recovered for reuse using an electric field, addresses the concern of high cost of ILs and the potential for IL leaching into product streams.[220] Confinement of the IL is an additional way to significantly reduce the amount of IL used. Confinement also reduces the mass transport limitations that are frequently encountered by the high viscosity of ILs. Confined

metallic ILs have been investigated for applications such as the oxidative desulfurization of H_2S.[136]

X-ray photoelectron spectroscopy (XPS) is a commonly used technique for determining elemental and chemical states with a goal of understanding the surface properties of metallic interfaces.[195] While XPS samples are typically solid due to the requirement of measurements in ultra-high vacuum, the low vapor pressure of ILs allows them to be characterized by XPS. [11, 109, 113, 115, 196, 197] One particularly useful feature of XPS is the ability to measure the oxidation state of metallic species within the material of interest. In the bulk phase, XPS is also useful to evaluate the hydrogen bond (H-bond) accepting ability and acidity of the anion and the basicity of the anion.[11, 196] Generally, it is found that addition of metals to the IL increases acidity of the IL and lowers its ability to accept hydrogen bonds.[11, 196]. From angle-resolved XPS (ARXPS), the aliphatic carbon tail of the common magnetic IL [BMIM][$FeCl_4$] orients itself toward the vacuum/IL interface with the imidazolium ring pointing toward the bulk IL.[221] When comparing the anion position between bulk [BMIM][Cl] and [BMIM][$FeCl_4$] using ARXPS, the [$FeCl_4$]$^-$ anion is situated closer to the vacuum interface than [Cl]$^-$. The difference between the orientation of [BMIM][Cl] and [BMIM][$FeCl_4$] at the IL/vacuum interface suggests differences in interfacial properties at a solid support or in confinement.

The limited investigations of metallic ILs/support interfaces suggest potential differences between interactions of metallic and traditional non-metallic ILs with surfaces. In one study, [EMIM][$FeCl_4$] was found to solidify when cooled below 285 K to a product with a crystal diffraction pattern, but did not solidify when confined within mesoporous silica nanoparticles.[222] The pores were filled with 37% volume fraction of IL. The lack of

phase transition is attributed to the interactions between the IL and the pore wall.[222] Additionally, the magnetic susceptibility of the confined IL is reduced due to restricted molecular arrangements of the IL within the pores.[222] From Raman spectroscopy, 1-ethyl-3-methylimidazolium tetrachloroferrate [EMIM][$FeCl_4$] interacts with mesoporous silica nanoparticles through H-bonding between the tetrachloroferrate anion and protonated hydroxyl groups.[36] Upon confinement, the Raman peaks for carbon related to imidazolium in [EMIM][$FeCl_4$] did not change, but the peak related to asymmetric Fe-Cl stretching broadens and slightly shifts, which could indicate that the interaction between the IL is between the anion and the pore wall.[36] In contrast, the interaction between [BMIM][Cl] and mesoporous silica is through hydrogen bonding with the C_2 carbon in the imidazolium ring, as determined by FTIR.[1] Similarly, in molecular dynamics simulations of nonmetallic IL interfaces, the interaction between the support material and the IL is typically through the IL cation.[80, 211]

In this work, XPS is extended to probe the interactions of a nanoconfined halometallate IL. The electronic environment of confined [BMIM][$FeCl_4$] is examined in mesoporous silica thin films (3.5 nm pores) with pore channels vertically aligned with respect to the substrate. The pores are templated by cetyltrimethyammonium bromide (CTAB) doped with titania.[26, 27] [BMIM][$FeCl_4$] is chosen because it has been used in catalysis applications and precedent exists for characterization of its confinement using FTIR and Raman spectroscopy.[35, 36, 136] The spectra of the IL was first measured in bulk phase to compare to literature data, then confined within 3.5 nm mesoporous silica thin films to elucidate interactions between the IL and the pore wall. This work demonstrates the ability

of XPS to probe interactions between support materials and catalytic low vapor pressure solvents, which is important for the design of heterogeneous catalytic systems.

5.3 Methods and Materials

5.3.1 Materials

Deionized water, toluene (ACS grade), and acetonitrile (99.5%) were purchased from VWR. Titanium (IV) isopropoxide (TIP, 97%) was purchased from Beantown Chemical (Hudson, NH). Pluronic P123 was purchased from BASF. Cetyltrimethylammonium bromide (CTAB, 99+%) was purchased from Acros Organics. Tetraethylorthosilicate (TEOS) (99%) and potassium bromide (FTIR Grade) were purchased from Alfa Aesar. Sulfuric acid (95-98%) and hydrochloric acid (6 N) were purchased from BDH Chemicals. NoChromix and 1-butyl-3-methylimidazolium chloride ([BMIM][Cl], 98+%) were purchased from Aldrich; anhydrous ethanol (200 proof) was purchased from Koptec. Dried pyridine (0.0075% water maximum) was purchased from SeccoSolv. Anhydrous iron (III) chloride (99.7%) was purchased from MP Biomedicals. The substrates used were silicon wafers from University Wafer Inc. All materials were used as received except for [BMIM][Cl] which was purified before use.

5.3.2 Silica Synthesis

Silica thin films templated using CTAB and Ti-doping and cast on polished silicon wafers were synthesized as described in our previous work.[27] Silicon wafers were cleaned using NoChromix solution, rinsed using DI water, and oven dried prior to casting. The dip coating solution was prepared by first adding 60 μL of titanium (IV) isopropoxide to 2.4 mL anhydrous ethanol while stirring in a nitrogen filled glove bag (solution 1). Solution 1

was sealed within the glove bag with parafilm, then removed from the bag and stirred for 3 hours in air. Solution 2 was prepared outside of the glove bag while solution 1 was stirring by combining 0.98 mL anhydrous ethanol, 1.42 mL TEOS, 0.21 mL DI water, and 0.27 mL 0.1 M HCl and left to stir for 1 hour. After solution 1 had stirred for 3 hours, solution 2 was added to solution 1 dropwise with vigorous mixing for 5 minutes. Next, 0.12 mL DI water, 1.03 mL anhydrous ethanol, and 323.12 mg CTAB were added to the solution, followed by stirring for an additional 5 minutes. Lastly, 3.42 mL of anhydrous ethanol was added, and the solution was left to stir for 1 hour. Afterward, the previously cleaned wafers were dip coated in this solution at 6 cm/min and left to hang in a 50°C oven in air to cure for 48 hours. The template was then removed by calcining the slides in air at 450°C for 1 hour. The structure of the CTAB templated film was verified by GISAXS after calcination.

Micron-sized mesoporous silica particles were synthesized via an adapted version of Gartmann's modified procedure[28] from the work of Katiyar,[29] and has been previously used in our lab.[171] P123 was placed in a beaker and melted in an oven at 80°C, of which 3.10 grams was poured into a round bottom flask. CTAB (0.465 g) was dissolved in DI water (20 mL), stirred for 10 minutes, and added to the melted P123. This solution was stirred continuously at room temperature throughout the rest of the procedure. Dry, pure ethanol (200 proof, 7.8 mL) and 1.5 M HCl (49.5 mL) were added to the solution and stirred until a clear, homogeneous solution formed, which took about 45 minutes. Particle formation was initiated by the dropwise addition of TEOS (10 mL) to the solution and stirring the mixture for 2 additional hours. The solution was poured into a Parr 4748A Teflon lined bomb (200 mL capacity) at room temperature and then placed into a preheated

oven and aged at 125 °C for 72 hours. After three days, the particles were removed from the bomb and mixed with a high-speed mixer to homogenize the solution, then filtered and rinsed with DI water. The particles were then placed in a single walled Whatman cellulose extraction thimble and underwent Soxhlet extraction with 200 mL of ethanol for 24 h. Afterwards, the particles were dried under vacuum at 80 °C overnight and characterized with nitrogen adsorption using a Tristar 3000 instrument to characterize pore diameter and volume.

5.3.3 IL Synthesis

[BMIM][Cl] was recrystallized from acetonitrile in a water-free environment prior to use.[223] In a nitrogen glove bag, a small amount of [BMIM][Cl] (≈ 0.5-1 g) was placed into a 250 mL round bottom flask with a purge valve and glass stopper. The IL was received as a solid and was slowly dissolved by adding acetonitrile until a very small amount of [BMIM][Cl] remained as a seed crystal. Approximately 200 microliters of toluene (≈ -18 °C) was added to the saturated acetonitrile mixture. The solution was placed into a freezer to crystallize, which took about 30 minutes. If the IL did not crystallize, more toluene was added until crystallization was achieved. The rest of the cold toluene was added after crystallization (100 mL), and the recrystallized IL was filtered using a sintered disk in a water-free environment. The IL was dried at 100 °C under vacuum to remove any water. The purified IL was combined with an equimolar amount of anhydrous iron (III) chloride in a glove bag to synthesize [BMIM][$FeCl_4$].

For bulk phase experiments with pyridine as a probe of acidity, the IL was mixed with pyridine in a glove bag using a volume ratio of 1:5 pyridine:IL. The IL and pyridine were mixed in a vortex mixer until the solution was homogenous. Confinement of the IL

with pyridine was performed by first loading the IL into the micron sized mesoporous silica particles. IL loading was achieved by suspending the particles in ethanol, then adding pure IL equal to the pore volume of the particles obtained from BET. Typical amounts for the procedure were 0.01 g of particles, 151 μL of ethanol, and 15.1 μL of IL, assuming a measured pore volume of the particles was 1.51 cm^3/g. The particles were sonicated for 90 minutes, then dried in a vacuum oven at 80 °C. The dried particles were placed into a desiccator with a reservoir of pyridine (≈ 25 mL). The desiccator was pumped so that a vacuum was created, and then the pump was turned off to allow pyridine to fill the atmosphere within the desiccator. The particles were left exposed to pyridine vapor overnight by leaving their container open to the pyridine atmosphere, then used in FTIR experiments.

5.3.4 Film Characterization

The mesoporous films were characterized using GISAXS (Xenocs Xeuss 2.0) with a microfocus Cu-Kα beam (λ = 1.54 Å) and a Pilatus3 200K detector. The samples were mounted on a flat GISAXS sample holder at an incidence angle of 0.14°. The sample-to-detector distance was calibrated using silver behenate drop-cast onto a glass slide prior to measurement. The total time in the beam was 2 minutes for each sample. The location of the 100 peaks were determined by averaging the out-of-plane intensity as a function of the x-axis.

5.3.5 X-ray Photoelectron Spectroscopy

XPS was performed using a Thermo Scientific K-Alpha XPS system with a monochromated Al-Kα source (1486.6 eV) with a collection angle of 0°. The spot size of

each point was 200 μm, each having 10 scans for the survey and each high-resolution (HR) scan with a dwell time of 10 and 50 ms, respectively. Survey spectra were recorded using a pass energy of 200 eV and high-resolution scans used a pass energy of 35 eV. Charge neutralization was given to the sample using a flood gun integrated into the system. The energy resolution of the instrument for high-resolution and survey scans was 0.1 and 1.0 eV, respectively. IL samples were dried in a vacuum oven at 100 °C overnight prior to use in XPS. Pure IL samples were prepared by placing a small droplet of the IL onto a clean silicon wafer surface, while confined samples were placed on the surface of the mesoporous film and pressed with a freshly cleaned silicon wafer to physically confine the IL into the pores. When choosing a spot, the camera equipped on the XPS was used to find a spot on the film where there was no visible excess IL present on the film surface.

Thermo Avantage software was used for data analysis. HR spectra were fitted using Shirley peak background. The pure IL spectra was charge-corrected by setting the aliphatic C 1s peak location at 285.0 eV. This shift is commonly used in the ionic liquid literature,[11, 114, 197, 204-206] with recognition that the fit is valid for $[C_nMIM]^+$ cations where $n \geq 8$. The additional carbon peaks for the pure IL were added about 1, 1.5, and 2 eV higher BE relative to C_{alkyl}, and fitting was run by the software using the convolve method. In the confined samples, the silicon peak from the pore walls was set at 103.5 eV,[203] and the aliphatic carbon peak was allowed to vary between 284.8 and 285.1 eV. The other C 1s peaks in the confined IL were highly constrained to have the same FWHM and charge separation as the pure IL and new peaks were added to complete the fitting. Generally, the HR spectra were fitted with a Gaussian/Lorentzian mix of 70/30 and a FWHM fit parameter of 0.8:1.9 eV after charge correction.

5.4 Results and Discussion

5.4.1 Film Synthesis and Characterization

Grazing incidence small angle x-ray scattering (GISAXS) was used to verify that the silica films have pores vertically aligned with respect to the substrate and to determine the pore spacing of the films. A representative 2D GISAXS pattern for the CTAB-templated film is shown in Figure 18. The ring in the pattern is elongated due to the unidirectional contraction of the thin film perpendicular to the substrate from the removal of the surfactant through calcination.[207] The d-spacing, or center-to-center distance between planes of pores, is calculated from the location of the vertical rods in the (100) and ($\bar{1}$00) planes. The d-spacing is calculated from q_y using the Equation 9:

$$d = 2 * \pi / q_y \tag{9}$$

The scattering vector q (Å^{-1}) has components for the in-plane (q_y) and out-of-plane (q_z) scattering vectors corresponding with scattering parallel and perpendicular with respect to the substrate. The d-spacing of the CTAB templated films is 4.8 nm (from q_y = 0.145 Å^{-1}), corresponding to a pore center-to-center distance of 5 nm. The pore wall thickness of CTAB templated silica thin films are about 1-2 nm,[21] meaning the pore diameter of these materials is about 3.5 ± 0.5 nm.

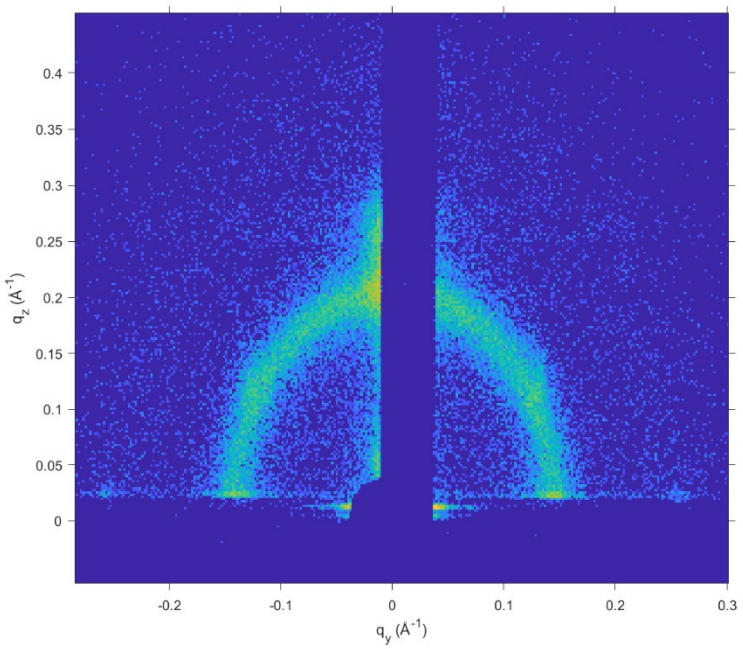

Figure 18. 2D GISAXS pattern of CTAB templated titania doped silica film with 3.5 nm pores.

5.4.2 XPS Spectra of Bulk IL

Figure 19 presents the survey and high resolution (HR) spectra for pure, bulk phase [BMIM][$FeCl_4$]. The only signals are from the components of the IL (C, N, Cl, Fe) (Figure 19(a)) and these atoms are present in close to their theoretical atomic % (see Figure 19(a) inset). The carbon C 1s spectrum in Figure 19(b) shows the characteristic shape of a $[BMIM]^+$ cation, where the alkyl tail and imidazolium ring carbons are separate. Interestingly, the imidazolium ring peaks shifts to a slightly higher BE by about 0.3 eV with the addition of $FeCl_3$. The shift of the imidazolium ring is consistent with the addition of iron to longer chain bulk phase ILs.[11] The nitrogen N 1s spectrum (Figure 19(c)) contains a single peak centered at 402.3 eV. This peak is 0.8 eV higher than in pure [BMIM][Cl] (401.5 eV). The increase in [BMIM][$FeCl_4$] nitrogen BE is consistent with

literature.[11, 196] The nitrogen binding energy has been correlated with the Kamlet-Taft hydrogen bond accepting ability, where a higher N 1s BE relates to a reduced hydrogen bond basicity of the anion.[196] A shift to more positive binding energy in both the nitrogen and carbon spectra could be due to the bulkier nature of $[FeCl_4]^-$ compared to chloride and a lower degree of charge transfer between them.[224] The chloride 2p spectrum has two sets of peaks (Figure 19(d)). One set is much larger than the other and is related to the $FeCl_4^-$ species within the IL. The amount of $FeCl_3$ added to the IL should be equimolar, and the smaller peak could indicate that the ratios are slightly off with an excess of [BMIM][Cl] but may indicate that the iron could have a mixed +3 and +2 oxidation state. The BE of the larger peak is 199.4 eV for the $2p_{3/2}$ peak, an increase from 196.8 eV observed for [BMIM][Cl]. The increase in BE is consistent with charge delocalization of the negative charge over the five atoms in the anion of $[FeCl_4]^-$.[196] The smaller peak may be free chloride within the IL. The lower binding energy is more consistent with free chloride being present since a lower BE is closer to the Cl spectra in [BMIM][Cl] but would also be consistent with a lower oxidation state of iron present in the system.

The Fe 2p spectrum contains many peaks that overlap (Figure 19(e)). The Fe 2p spectrum has spin orbit splitting effects resulting in the several peaks ($2p_{1/2}$) on the left-hand (high BE) side of the spectrum. This analysis will focus on the $2p_{3/2}$ peaks on the right side. In deconvoluted $2p_{3/2}$ peaks represent a primary Fe 2p peak for iron in the +3 oxidation state (centered at 711.9 eV), two additional peaks to account for multiplet splitting (714.5 and 712.8 eV) and a satellite peak (718.5 eV). A pre-peak was added at 709.9 eV and could indicate a mixed valence state of +2 and +3 iron within the sample. The main peak is consistent with iron in the +3 oxidation state and is expected for this IL.[11]

The BE of the main peak is 0.4 eV higher than a pure $FeCl_3$ powder (711.5 eV)[225] and may be a result of the increased acidity of the IL.[11]

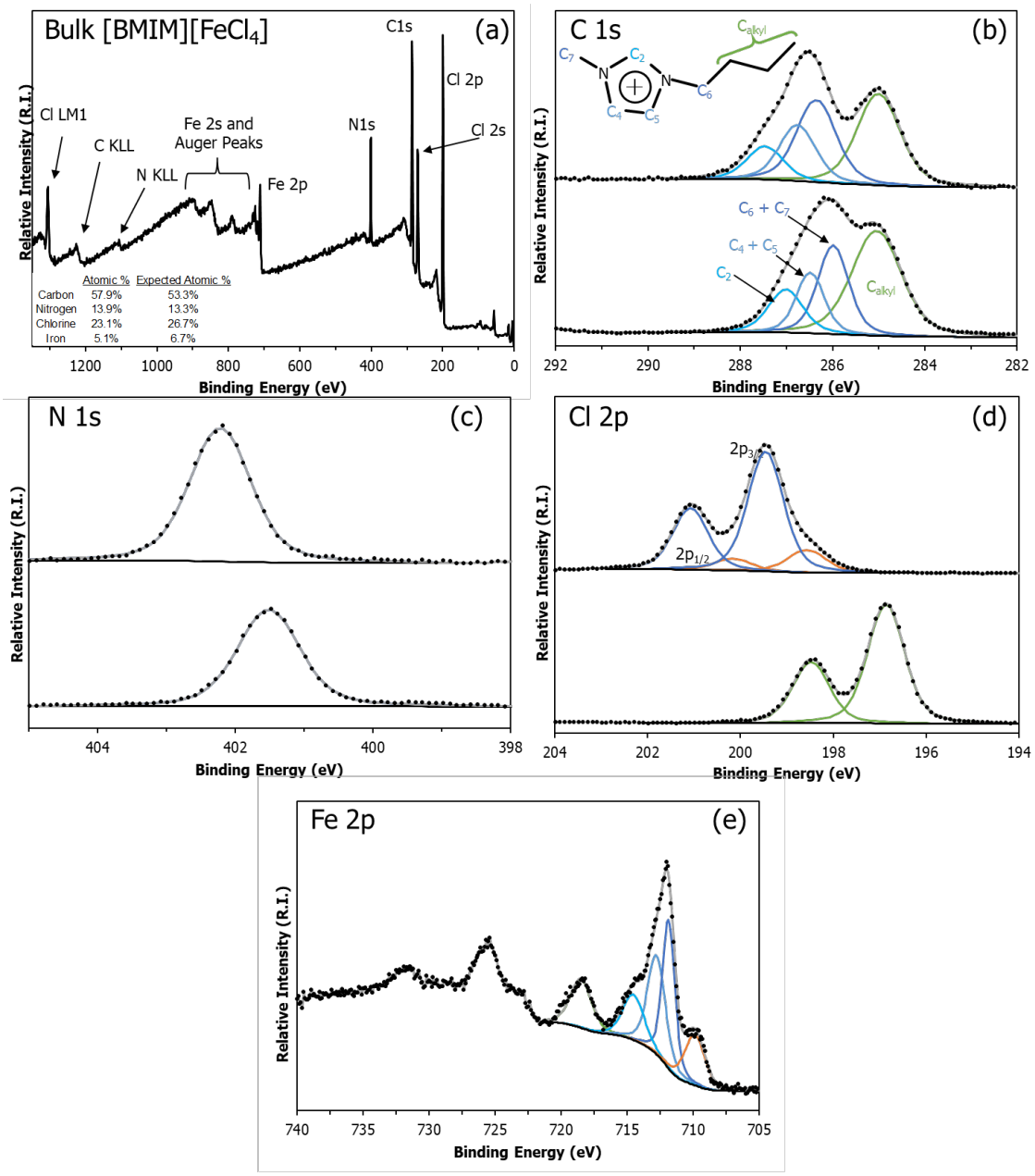

Figure 19. XPS spectra of (a) bulk [BMIM][$FeCl_4$] with an inset table of theoretical and actual atomic %, (b) high resolution carbon C 1s spectrum with color-coded peak assignments, (c) high resolution N 1s spectrum, (d) high resolution Cl 2p spectrum, and (e) high resolution Fe 2p spectrum. For each element, the top spectrum corresponds to [BMIM][$FeCl_4$] and the bottom spectrum is [BMIM][Cl].

5.4.3 High Resolution XPS Spectra of Confined [BMIM][$FeCl_4$]

The high-resolution spectra of the IL before and after confinement into 3.5 nm mesoporous silica thin films are presented in Figure 20 (carbon and nitrogen) and Figure 21 (chlorine and iron). In the confined C 1s spectra, the deconvolution of peaks becomes difficult to resolve in [BMIM][$FeCl_4$], as in the case of confined [BMIM][Cl]. The contribution from two more peaks is required to fit the carbon spectra. The new peak with higher BE (orange) is indicative of a more positively charged imidazolium ring, while the lower BE peak is related to the positive charge neutralization. Since the alkyl tail is not predicted to interact with the pore wall surface, these changes are related to different energy environments within the imidazolium ring. The fitting of carbon is more difficult to fit than other IL components since a single broad peak can be fit with many environments.[226] It should also be noted that the silica surface before confinement contained adventitious carbon contamination, but there was no nitrogen signal. A perfectly clean surface is difficult to achieve, and surface contamination is common in XPS studies,[110, 111, 209] and is not anticipated to impact the interpretation of interactions of IL in confinement. Regardless, there are significant changes to the carbon spectra upon confinement of [BMIM][$FeCl_4$] that are different than with confined [BMIM][Cl]; specifically, the more positively charged imidazolium ring case (orange) is not as prevalent in [BMIM][$FeCl_4$]. With [BMIM][Cl], it was hypothesized that this higher BE case may arise due to the chloride anion forming $[Cl\text{-}H\text{-}Cl]^-$ with a proton from the pore wall.[210] With iron present, a chloride dimer with a proton is less likely to form, and thus the peak would be smaller. Comparing the peak area between the alkyl tail contribution (green peak) and the neutralized imidazolium ring peak (yellow) reveals that the contributions from these

environments are similar between [BMIM][Cl] (alkyl:neutral 1:0.88 by area) and [BMIM][$FeCl_4$] (1:0.89).

The nitrogen spectra provide more clarity on the interactions of the imidazolium ring than the carbon spectra. Since only one nitrogen environment is present in the imidazolium ring, the peak is a more sensitive indicator of subtle changes in its electronic environment. In bulk phase [BMIM][$FeCl_4$] the increase in nitrogen binding energy (and thus lower basicity) is related to the increased delocalization of the negative charge on the anion.[11] With confinement of both [BMIM][Cl] and [BMIM][$FeCl_4$], a new peak is present at lower binding energy for the N 1s spectra. The new peak is related to the charge neutralization of the imidazolium ring at the interface between the IL and the pore wall. The ratio of these peaks is 1:0.6 in [BMIM][Cl] and 1:0.13 in [BMIM][$FeCl_4$], which could indicate that interactions between the imidazolium ring and pore wall are lower when iron is added. It could also be that $FeCl_4^-$ interacts strongly with the pore wall surface so that there is competition between the imidazolium and tetrachloroferrate for surface sites. Interestingly, the main peak location of the N 1s spectra is similar in bulk [BMIM][$FeCl_4$], confined [BMIM][$FeCl_4$], and confined [BMIM][Cl] and is centered within 0.2 eV of 401.8 eV. The relationship between the basicity of the anion and the peak position of the nitrogen in ILs[196] may indicate that the hydrogen bond accepting ability of the confined [BMIM][$FeCl_4$] anion is similar to the bulk [BMIM][$FeCl_4$]. FTIR shows that IL will preferentially interact with the pore wall surface through the C_2 carbon of the IL.[1, 82] However, XPS implies a stronger electrostatic interaction between the imidazolium ring and the wall and has an impact on the electronic environment within the whole imidazolium ring rather than a single carbon. The strong interaction between the IL and surface due to

electrostatic interactions leads to IL ordering along the pore wall.[80, 211] The different interactions between halometallate ILs and the pore wall could lead to a different ordering than proposed for non-metallic ILs.

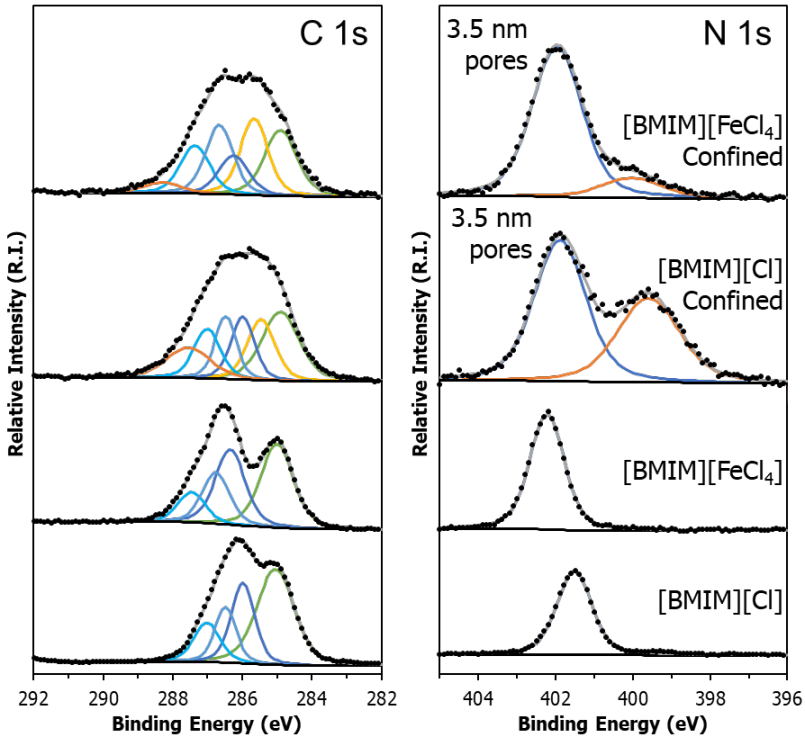

Figure 20. High resolution C 1s and N 1s spectra of the unconfined and confined ILs. From bottom to top: pure [BMIM][Cl], pure [BMIM][$FeCl_4$], [BMIM][Cl] confined within 3.5 nm porous films, [BMIM][$FeCl_4$] confined within 3.5 nm porous films.

The HR chloride Cl 2p spectra for the ILs are shown in Figure 21. In [BMIM][Cl], there is a set of peaks related to the $2p_{3/2}$ and $2p_{1/2}$ spin states for chlorine. The $2p_{3/2}$ and $2p_{1/2}$ peaks are separated by 1.6 eV with a ratio of 2:1 due to spin orbit splitting.[196] Since the two peaks always come in pairs, all BEs from this point will refer to the $2p_{3/2}$ as the primary peak unless specified. In bulk phase [BMIM][$FeCl_4$], the primary peak for chloride is centered at 199.4 eV, which is 2.6 eV higher than for bulk [BMIM][Cl]. The

increase in BE is related to the greater charge delocalization around chloride, where five atoms share the negative charge in $[FeCl_4]^-$ compared to just one in $[Cl]^-$.[196] In the confined system, the [BMIM][Cl] spectrum is fit with two peaks at higher BE than the bulk IL. These peaks could be due to hydrogen bonding with hydroxyl groups present on the pore wall surface. If $[Cl\text{-}H\text{-}Cl]^-$ is formed, it would lead to charge delocalization and an increase to the BE which may explain the second peak. In confined [BMIM][$FeCl_4$], the chloride peaks broaden and slightly decrease in BE. Since there is significant overlap, it is not trivial to deconvolute the different electronic environments of the confined $[FeCl_4]^-$ anion. The significant result of confinement is that the BE of chloride is reduced compared to bulk [BMIM][$FeCl_4$]. Lower BE for chloride is an indication of the reduction in strength of the interaction between the imidazolium ring and the $[FeCl_4]^-$ anion.[227] This could also indicate an increase in free chloride anions due to association between $[FeCl_4]^-$ and the pore wall and is consistent with the nitrogen spectra. Previous XPS studies have shown that iron (III) chloride has a high affinity toward deprotonated silica surfaces,[228, 229] which support this hypothesis.

The iron Fe 2p spectra of bulk and confined [BMIM][$FeCl_4$] are shown in Figure 21. Like chloride, it has spin-orbit splitting peaks so there are two sets of peaks separated by 13.5 eV, consistent with literature.[196] Since the $2p_{1/2}$ and $2p_{3/2}$ peaks do not overlap, only the $2p_{3/2}$ peaks are used to investigate the effects of confinement on iron. Iron has multiple artifacts in XPS due to shake-up processes and multiplet splitting processes that convolute the spectrum. In the bulk IL spectrum, there is a large peak centered at 711.9 eV, consistent with iron in the +3 oxidation state.[11, 196] The spectrum of the confined

[BMIM][$FeCl_4$] is shifted to lower BE compared to the bulk value, where the primary peak is located at 709.9 eV.

The decrease in binding energy of the metal anion is consistent with increased charge transfer with the pore wall.[227] A decrease of 0.3 eV was observed in tethered [BMIM][$ZnCl_3$] compared to $ZnCl_2$ metal and is consistent with the direction of the shift observed in our data.[227] For comparison, the shift we observe is ≈ 1.6 eV to lower binding energy because the Fe $2p_{3/2}$ peak for $FeCl_3$ is centered at 711.5 eV.[11] These shifts are also consistent with charge transfer in non-metallic, bulk phase ILs. In bulk ILs, charge transfer increases between the cation (1-octyl-3-methylimidazolium, OMIM) and anion as the size of the anion is reduced, with the largest anion being tris(pentafluoroethyl)trifluorophosphate and the smallest being chloride.[224] A higher degree of charge transfer lowers the binding energy of the imidazolium ring peak in carbon and nitrogen peak related to the cation in XPS.[224] In another study, angle resolved XPS showed that both cations and anions in both 1-methyl-3-methylimidazolium or 1-octyl-3-methylimidazolium bis(trifluoromethyl)imide close to the surface of gold substrates (one or less molecular layer of IL) had a reduction in binding energy by about 1 eV due to either charge transfer or enhanced screening of the excited IL core hole near the gold surface.[209] The binding energy of chloride also shifts to lower BE (Figure 21) and is with enhanced charge transfer between the anion and pore wall. Raman spectroscopy also shows significant interactions between 1-ethyl-3-methylimidazolium tetrachloroferrate confined within mesoporous silica.[36] The interaction between the anion and silica causes increased frequency of asymmetric stretching of the Fe-Cl bond, which may be due to hydrogen bond interactions between the pore wall.[36] The band related to the C_2 carbon in the imidazolium

ring also remains unchanged in the Raman spectra.[36] This may indicate that the primary mode of interaction between the IL and surface of the pore wall is actually through the metallic anion species rather than the cation.

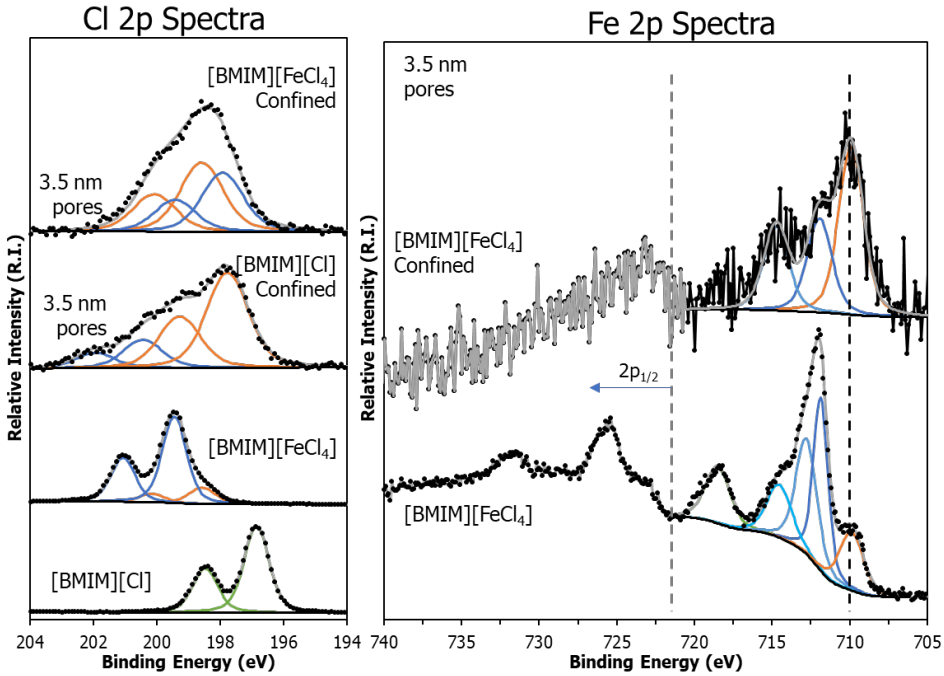

Figure 21. High resolution spectra of pure and confined ILs. The high-resolution Cl 2p spectra contains pure/confined [BMIM][Cl] and pure/confined [BMIM][FeCl4]. The Fe 2p spectra compares pure and confined [BMIM][FeCl4]. The pore diameter used was 3.5 nm for confined ILs. The left-hand side of the Fe spectra contains the $2p_{1/2}$ peaks.

5.4.4 Lewis Acidity Probed by FTIR

A key feature of halometallate ILs is their ability to behave as acids for catalysis. Taylor et al. showed that the BE of the metal peak for halometallate ILs in bulk increases with increasing acidity.[11] The increase in acidity was correlated with an increase in mole fraction of $ZnCl_2$ added to [OMIM][Cl]. When the mole fraction of $ZnCl_2$ was increased above 0.33, the system became strongly Lewis acidic because complex anions zinc-based

anions were the dominant species, while below 0.33 mole fraction, free chloride was the dominant anion.[11] While the BE is reduced in the XPS spectra of the Fe 2p peak, it is hypothesized to be related to the interactions between the anion and the pore wall, and not a reduction in the acidity of the IL.

To directly measure the acidity, the FTIR spectra of a confined IL/pyridine mixture was analyzed. Pyridine is commonly used as a probe of Lewis and Brønsted acidity (LA or BA) in various systems from bulk ILs to solid catalysts.[47, 230] Pyridine can donate the lone pair of electrons from nitrogen and form a complex with a LA site. Pyridine accepts a proton a Brønsted acid and forms pyridinium.[230] The addition of pyridine (1:5 pyridine:IL by volume) to [BMIM][$FeCl_4$] leads to two new peaks forming in the FTIR spectra of the ILs in Figure 22. In the bulk [BMIM][$FeCl_4$] spectra, the new peaks appear at 1534 and 1487 cm^{-1}, consistent with literature values[47] and correspond to Brønsted and mixed Brønsted/Lewis acid sites, respectfully. They arise from the adsorption of the pyridinium and pyridine ions to BA or LA sites.[230]

Micron sized mesoporous silica particles (8 nm diameter pores) were synthesized according to the procedure in Chapter 3.[28, 30] The pore diameter was characterized using nitrogen porosimetry to demonstrate that they had ≈ 8 nm pores. The IL was loaded via solvent deposition and exposed to a pyridine atmosphere where pyridine was absorbed into the confined IL. Silica with adsorbed pyridine also no peaks related to BA sites, but has a small peak related to LA sites near 1447 cm^{-1}.[230] The peaks related to LA and BA sites are present in confined [BMIM][$FeCl_4$], while they are not present in confined [BMIM][Cl]. The peak corresponding to LA sites at 1445 cm^{-1} in the bulk [BMIM][$FeCl_4$] is heavily reduced, disappears, or is overlapped with the broad peak at 1465 cm^{-1} related to C=C-

stretching in the imidazolium ring,[1] which could indicate that BA sites are dominant. Thus, tetrachloroferrate anion is necessary for LA/BA in the IL and the IL retains LA/BA activity in confinement. The presence of LA and BA sites also confirms that the confined [BMIM][$FeCl_4$] can still act as an acid, although the XPS results indicate that the metallic anion interacts strongly with the pore wall in confinement. Therefore, the shifts in the confined iron spectra are primarily related to pore wall interactions and not indicative of changes in acidity.

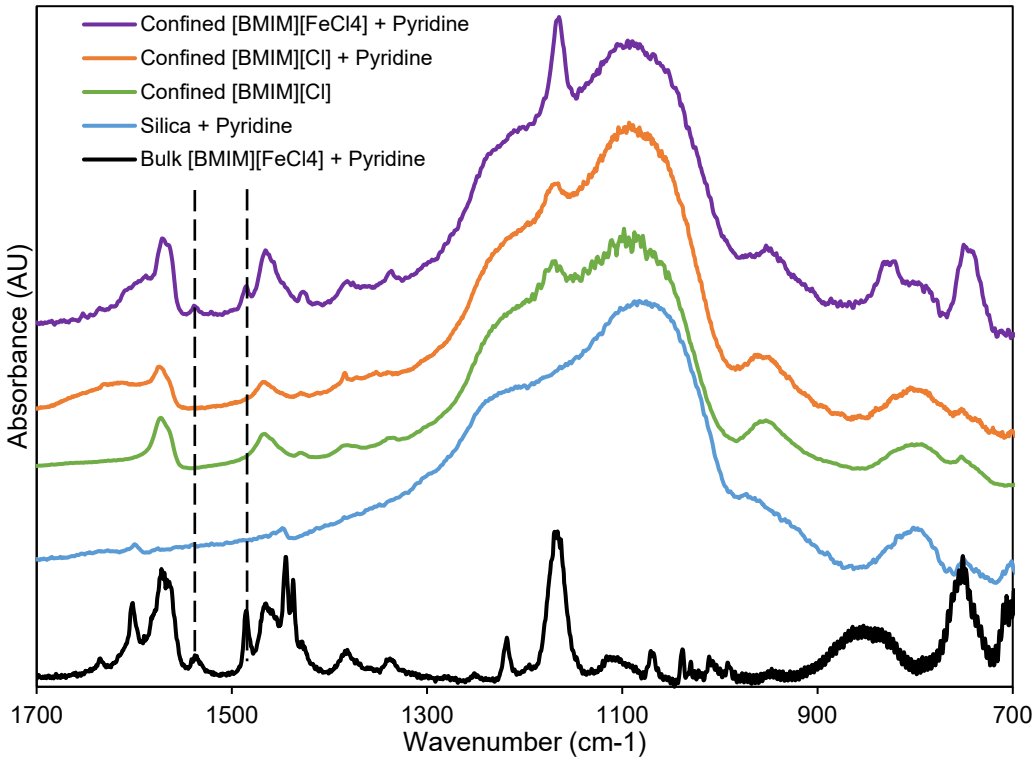

Figure 22. FTIR spectra of ILs in bulk and confined with pyridine. The dashed lines at 1534 and 1487 cm^{-1} are to guide the eye.

5.5 Conclusion

Interactions between the confined halometallate IL [BMIM][$FeCl_4$] and [BMIM][Cl] in mesoporous silica supports (3.5 nm diameter pores) were compared using XPS. Int the bulk IL, the tetrachloroferrate anion causes a shift in the nitrogen spectra to higher BE, indicating a reduced hydrogen bond accepting ability of the anion. The chloride peak in the bulk halometallate IL increased in BE from the delocalized negative charge across the anion. Iron was found to be in the +3 oxidation state and had a higher BE than pure $FeCl_3$ powder because of increased acidity.

The XPS spectra of the confined [BMIM][$FeCl_4$] clearly demonstrated that the IL interacts with the pore wall surface. The carbon spectrum broadened and due to multiple electronic environments present from the interactions with the pore wall surface. The nitrogen spectrum of [BMIM][$FeCl_4$] had a second peak at lower BE due to the same interactions with the pore wall, but these interactions were less prevalent than with [BMIM][Cl]. The lower peak area may be due to competition for pore wall interactions with the anion. In the chloride spectrum of [BMIM][$FeCl_4$], the BE broadens significantly and shifts toward more negative values. The negative shift could be due to reduction of the interaction strength with the imidazolium ring or free chloride anions within the pore. Iron in the bulk phase IL has a peak consistent with the +3 oxidation state that shifts significantly to lower BE upon confinement. This decrease is consistent with a lower acidity of the anion, but also indicates that there may be enhanced charge transfer with the pore wall. The peak shifts of iron, nitrogen, and chloride together could indicate that the primary mode of interaction between iron based ILs is through the anion rather than the

cation. In [BMIM][Cl], the strong interactions between the imidazolium ring and the pore wall surface are more suppressed than with [BMIM][$FeCl_4$].

Ordering along the pore wall surface is important to consider for catalysis applications. The high reduction in binding energy of iron could indicate a lower acidity, but the FTIR spectra of [BMIM][$FeCl_4$] confined within mesoporous silica particles shows that the IL is still able to act as a Lewis and Brønsted acid. This work demonstrates that XPS is a useful technique for understanding interfacial interactions of confined low vapor pressure solvents within porous materials and can improve the design of confined halometallate ILs for catalysis applications.

CHAPTER 6. TRANSPORT PROPERTIES OF IRON-BASED REDOX PROBES THROUGH CONFINED DEEP EUTECTIC SOLVENTS WITHIN MESOPOROUS SILICA THIN FILMS

6.1 Summary

The transport properties of iron based redox probes iron (III) chloride and iron acetylacetonate in deep eutectic solvent (DES) filled mesoporous silica thin films are compared as a function cylindrical pore diameter (3 vs. 8 nm). Cyclic voltammetry (CV) is used to characterize the transport of the probes from bulk DES through the mesoporous silica films coated to the interface of fluorine-doped tin oxide layers used as the working electrode. Reline (choline chloride:urea 1:2 mole ratio) and ethaline (choline chloride:ethylene glycol 1:2) were used as the solvents for the probes. Ethaline has a much lower viscosity than reline and $FeCl_4^-$ has faster diffusivity by an order of magnitude in a bulk solution. Iron chloride in ethaline retains bulk-like diffusion through 8 nm mesoporous silica but has a reduction in apparent diffusivity by 3 orders of magnitude in the 3 nm mesoporous silica. The $FeCl_4^-$ in reline has a large reduction in diffusivity compared to bulk values, by 3 and 4 orders of magnitude the FTO coated with silica with 8 and 3 nm diameter pores, respectively. The neutrally charged redox probe, iron acetylacetonate, was able to reach the electrode through the 8 nm pores when dissolved in ethaline but has reduced diffusivity within the 3 nm pores. These results show that transport through the films depends primarily on the viscosity of the solvent but is strongly influenced by the interaction of the redox probe with the pore wall, as dictated by charge. The ability to tune the transport of the solute through confined DESs using pore diameter and solvent composition is crucial in the design of confined DES systems for separations and energy storage applications.

6.2 Introduction

Deep eutectic solvents (DESs) are an increasingly important class of alternative solvents that have valuable properties such as low vapor pressure, high thermal stability, and tunability. They are synthesized by combining two compounds (typically solids at room temperature) to produce a liquid with a low melting point, generally below room temperature. DESs are unique because their melting temperature is lower than the ideal eutectic melting temperature due to strong interactions (usually hydrogen bonding) between the components. Ionic liquids (ILs) continue to be studied extensively and are often compared to DESs because ILs also have low volatility, high thermal stability, and tunability, among other similarities, but are inherently different since ILs are comprised of a single cation-anion pair while DESs are two distinct molecular species. DESs are more attractive than ILs because they are less toxic, cheaper, and may be sourced from sustainable materials (natural DESs).[54] Several applications have been found for DESs in catalysis,[231] separations,[56] and energy storage as a few examples.[232] Despite their promising properties, DESs are typically highly viscous, with some combinations reaching into the 10,000 cP range.[233]

In the bulk phase, DESs have been used in many of the same ways as ILs. For example, ILs and DESs were used in tandem for the selective solvent extraction of manganese, cobalt, nickel, and lithium from sulfuric acid media to improve recyclability of batteries by Zante et al.[234] By carefully choosing the IL and DES, each metal was able to be selectively separated from the acid mixture, allowing them to be used again in manufacturing.[234] A DES containing $ZnCl_2$ and ethylene glycol was demonstrated to have a good electrochemical window and high energy density, making it useful for

supercapacitor applications.[235] Xia et al. showed that adding $AlCl_3 \cdot 6H_2O$ to choline chloride:glycerol improved the DESs ability to break down lignin carbohydrate complexes from lignocellulose.[236] ILs have been explored for these types of applications and DESs improve upon them by being safer and more cost effective. The use of metal additives to DESs (or even making the DES with a metal itself) is a convenient way to impart catalytic and electrochemical activity. As with ILs, a problem in DES catalysis is that the reasons that they are useful solvents also make it difficult to extract the products of catalysis or the solvent itself may end up in the product stream. Because of this and their high viscosity, DESs may be confined within mesoporous materials to prevent them from leaching while using their good solvent and catalytic properties, while also making them easier to handle and improving their surface area for catalysis or adsorption applications.

Confinement of DESs into mesoporous materials is advantageous to several areas of applications. The field of confined DESs is still very new, so while there are few current studies on applications, there are a few promising areas. There are several studies that show confined DESs to be effective media for adsorption. Choline chloride and urea (1:2 mole ratio), also known as reline, confined onto nanoporous silica gel was able to efficiently adsorb CO_2 from a 99% pure gas environment of CO_2.[56, 84, 85] The high affinity of the DES for CO_2 makes it a good candidate for CO_2 capture from flue gas streams. Continuing green solvent concept, a confined betaine:lactic acid natural DES was used in mesoporous silica as a substrate for the synthesis of furfural from corn husk biomass.[237] The choline chloride:ethylene glycol DES confined within graphene oxide nanochannels has been reported as a membrane for energy storage electrodes.[83] The ionic conductivity and energy density of the DES was largely improved with confinement and helps pave the

way for cheaper and safer energy storage. Confinement also changes the properties of the solvent and while this has mostly been demonstrated for ILs,[32, 78] the same is expected to be true for DESs as well. In one example, the melting temperature of reline shifted to lower temperatures when confined within 50 to 300 nm pore diameter controlled pore glasses.[23] In a study using molecular dynamics, Zhang et al. found that confined reline had higher flow resistance when confined between charged nanoslits (2 nm) due to the preference for urea to interact with the pore wall.[238] With the applications of confined DESs in catalysis or separations, it is imperative to study the transport of probe molecules dissolved within the DES through mesoporous materials.

Cyclic voltammetry (CV) is a useful technique to study transport of a probe species since the redox probe being used must diffuse to the electrode in order to be oxidized or reduced. It has been used extensively to study the transport of different probes from aqueous solutions through mesoporous silica materials.[72, 130, 239] In particular, Etienne et al. showed using cyclic voltammetry that a mesoporous silica thin film deposited onto an electrode is able to effectively screen solutes from the pores due to the repulsion of negatively charged probes by the negatively charged pore walls of the silica, whereas a positively charged probe accumulates.[130] Together with other electrochemical techniques such as electrochemical impedance spectroscopy, rate-dependent cyclic voltammetry can also be used to characterize the transport properties of redox probes.[21] The diffusivity of a probe is related to the peak current observed in CV and the rate of change of voltage as demonstrated by Mohamed et al., where the diffusivity of several different redox species through mesoporous silica increased as the pore diameter was increased comparing 2 to 5 nm diameter pores.[240] Here, we chose to use cyclic voltammetry as the characterization

technique due to its simplicity and ability to differentiate significant changes in the transport of redox probes.

Mesoporous silica is an ideal nanoconfinement substrate because it is easy to synthesize, can be functionalized, and has tunable porosity making it a good candidate as a supporting matrix for DESs. The pore size available for mesoporous silica films is related to the type of surfactant used. For example, Mohamed was able to make pores with 2-5 nm diameter using surfactants with alkyl chain lengths ranging from 14 to 24.[240] Using Pluronic P123 as a surfactant, the pores are typically larger than 8 nm.[241] One challenging aspect of mesoporous silica films is ensuring that the pores are accessible because generally, the interaction between the surfactant and the surface leads to a preferred orientation of cylindrical pores aligned parallel to the substrate surface.[21] Several methods have been developed to overcome this challenge such as using magnetic fields, electrochemical methods, and chemically neutral surfaces during dip coating.[241-243] Walcarius et al. showed that vertically oriented 3 nm diameter pores could be synthesized using cetyltrimethylammonium bromide (CTAB) surfactant and the electrochemical self-assembly method.[243] Our group was able to synthesize Pluronic block copolymer templated 8-10 nm mesoporous silica films on several substrates like anodic alumina, glass slides, or silicon wafers by first modifying the substrate with a chemically neutral layer of crosslinked block copolymer before silica deposition.[21, 241] The functionalized surface is neutral to the monomers of the Pluronic pore template, so instead of a preferred orientation to planar pores, they are vertically aligned instead. We also demonstrated the synthesis of a mesoporous silica film with smaller pores by using CTAB as a surfactant with titania

doping, which destabilizes the silica porous structure to produce accessible 2-3 nm mesopores during thermal processing of the films.[27]

In this work, cyclic voltammetry is used to study the transport properties of two iron probes ($FeCl_4^-$) and iron acetylacetonate, ($Fe(Acac)_3$) through mesoporous silica thin films with 3 or 8 nm pores deposited on FTO-coated glass slides submerged in either reline (choline chloride:urea) or ethaline (choline chloride:ethylene glycol) DESs. In DESs containing choline chloride, the free chloride molecule is able to form an $FeCl_4^-$ counteranion. Miller et al. demonstrated using x-ray absorption near edge structure measurements that tetrahedral $FeCl_4^-$ complexes in DESs (ethaline in their work) form when the ratio of Cl:Fe is greater than 4:1.[37] Thus, the $FeCl_4^-$ probe used in this work is assumed to be a negative charge. The surface of mesoporous silica often has a slightly negative charge and can effectively screen anionic species from entering the pores.[130] For example, Etienne et al. showed that the peak current for negatively charged probes I^- and $Fe(CN)_6^{3-}$ was reduced when the ITO glass slide working electrode was coated with a mesoporous silica thin film.[130] At a fixed scan rate, the peak current from iodide was reduced by nearly half (85 to 44 μA), while the peak current from ferrocyanide was reduced by over 90% due to the higher magnitude of the negative charge.[130] The neutral redox probe, ferrocenemethanol, had a larger reduction peak since it is neutral before being oxidized, and the resulting positively charged species is attracted to the silica pore walls and increases the concentration within the pores and the current.[130] In our case, we chose use a neutral probe, $Fe(Acac)_3$, in addition to $FeCl_4^-$ since the probe will be negatively charged upon reduction and pushed out of the pores. The DESs were chosen because they are commonly studied DESs known to have different viscosity and melting properties, and

slightly different interactions with charged surfaces such as silica. Understanding the role of redox probe charge, pore diameter, and solvent type will lead to better supported DES systems since these characteristics have an impact on what is able to enter and diffuse through the pores for applications such as separations, catalysis, and energy storage.

6.3 Methods and Materials

6.3.1 Materials

For the DESs, choline chloride (high purity grade) and urea (high purity grade) were purchased from VWR. Ethylene glycol (99.8%, anhydrous) was purchased from Thermo Fisher Scientific, iron (III) chloride (99.7%) was purchased from MP Biomedicals, and iron (III) acetylacetonate (99%) was purchased from Strem Chemicals.

For film synthesis, fluorine-doped tin oxide coated glass slides (FTO slides) purchased from Sigma-Aldrich were used as the substrate. A 10 cm by 10 cm square FTO glass sheet was cut into smaller pieces of 4x2.2 cm to facilitate their use in electrochemical experiments. Deionized water and acetone (99.5%) were purchased from VWR. Pluronic P123 (poly(ethylene oxide)-block-poly(propylene oxide)-block-poly(ethylene oxide) copolymer ($M_n \approx 5800$) was purchased from BASF. Glycerol (ACS grade) was purchased from Macron Fine Chemicals, 1,6-diisocyanatohexane (98%) and cetyltrimethylammonium bromide (CTAB, 99%+) from Acros Organics, tetraethylorthosilicate (TEOS, 99%) from Alfa Aesar, ethanol (200 proof) from Koptec, 6N HCl from BDH Chemicals, and titanium isopropoxide (TTIP, 97%+) from Beantown Chemical (Hudson, NH).

6.3.2 Deep Eutectic Solvent Synthesis and Sample Preparation

The DESs were synthesized following methods reported in the literature.[38, 96, 244] Choline chloride (ChCl) was first dried in a vacuum oven at 90 °C overnight to remove traces of water. Choline chloride and urea (U) or choline chloride and ethylene glycol (EG) were mixed in molar ratios 1:2 ChCl:U (reline) or ChCl:EG (ethaline), respectively, in a round bottom flask under nitrogen, and then heated and stirred at 60 °C until a clear liquid was formed (usually 2-3 hours). The solvents were kept sealed under nitrogen and stored in a desiccator until use.

For chloride complexes, iron (III) chloride was added to 25 mL of each DES to make 0.1 M solutions. Consistent with prior studies in the literature,[245] iron chloride was hydrated before dissolving into the DES by exposing the salt to air for 24 hours, verified by the orange color and nonhygroscopic nature when handling. These solutions were stirred under vacuum for 24 hours to dissolve $FeCl_3$ and to degas the samples for cyclic voltammetry. For acetylacetonate complexes, iron acetylacetonate was added at a concentration of 0.001 M to 25 mL of ethaline and the same stirring procedure was performed. Both solvents tended to crystallize at room temperature during prolonged storage, so they were usually heated to 50 °C to melt before use and remained liquid during the experiment after cooling to room temperature. The temperature of the experiment was controlled with an oil bath set to 30 °C.

Confinement of the DES into silica particles was performed by suspending the particles in ethanol, then adding pure DES equal to the pore volume obtained from BET. Typical amounts for the procedure were 0.01 g of particles, 151 μL of ethanol, and 15.1

μL of DES, since the pore volume of the particles was 1.51 cm^3/g as in Chapter 3. The particles were sonicated for 90 minutes, then dried in a vacuum oven at 80 °C.

6.3.3 Silica Synthesis

Silica thin films were synthesized according to previous work done in our lab[67]. The first step in film synthesis for large pore films is to create a chemically neutral surface so that the micelle templates align normal to the substrate surface during aging. FTO coated glass slides were first cleaned by sonication for 20 minutes in DI water, then 20 minutes of sonication in acetone, and then at least 20 minutes of UV ozone treatment in a Bioforce Nanoscience UV.TC.110. The side with a conductive FTO coating was verified by using a multimeter and the coated side was placed facing upward during UV-ozone treatment. On the same day, the solution to make the slides chemically neutral was prepared by dissolving 359.3 mg P123 into 89 mL acetone to create a 0.696 mM solution. An equimolar amount of 1,6-diisocyanatohexane (10 μL) was added while stirring in a nitrogen glove bag. The solution was removed from the glove bag and 3 drops of glycerol was added to the solution while stirring. This solution was kept stirring until the dip-coating apparatus was ready, with a minimum stir time of 10 minutes. Glass slides were dipped in the neutral solution and removed at a rate of 7.6 cm/min to create a modified glass slide that was left to hang in a 100 °C oven overnight.

A second solution to deposit the silica film was prepared by adding TEOS, 200 proof ethanol, DI water, and HCl together in a final molar ratio of $1:3.8:1:5x10^{-5}$ and refluxing this solution for 1.5 hours at 70 °C. Afterward, additional HCl and DI water was added to bring the concentration of HCl to 7.34 mM, followed by stirring for 15 minutes. The solution was then aged at 50 °C in a water bath for 15 minutes. A solution of P123

dissolved into ethanol to have a molar ratio of 0.01:18.7 was prepared and left stirring during this time. The two solutions were combined and allowed to stir for an additional 10 minutes before dip-coating with the modified glass slides. The final silica solution had a molar ratio of TEOS:Ethanol:H_2O:HCl:P123 = 1:22:5:0.004:0.01. A modified glass slide from the previous step was dip-coated in this solution at the same speed (7.6 cm/min), sandwiched in-between two modified glass slides from the previous step, and placed into a glass petri dish. Extra glass slides were placed on top to ensure good contact between all the slides. The petri dishes containing silica films were aged in a 50 °C oven for 24 hours, followed by drying in a 100 °C oven for 24 hours. To remove the cross-linked polymer template and surfactant, the slides were calcined in air at a rate of 0.5 °C/min to 500 °C for 4 hours. The films were characterized using grazing incidence small angle x-ray scattering (GISAXS) to verify that their vertically oriented mesopore structure prior to confinement experiments.

CTAB templated, Ti-doped silica films were synthesized according to previous work in our lab.[27] FTO coated glass slides were cleaned the same way as for the 8 nm, P123 templated films. The dip coating solution was prepared by first adding 60 μL of titanium (IV) isopropoxide to 2.4 mL anhydrous ethanol in a nitrogen filled glove bag (solution 1). Solution 1 was sealed within the glove bag with parafilm and stirred for 3 hours. Solution 2 was prepared outside of the glove bag while solution 1 was stirring by combining 0.98 mL anhydrous ethanol, 1.42 mL TEOS, 0.21 mL DI water, and 0.27 mL 0.1 M HCl and left to stir for 1 hour. After 3 hours of stirring solution 1, solution 2 was added to solution 1 dropwise with vigorous mixing and stirred for 5 minutes. Next, 0.12 mL DI water, 1.03 mL anhydrous ethanol, and 323.12 mg CTAB were added to the

solution, followed by stirring for an additional 5 minutes. Lastly, 3.42 mL of anhydrous ethanol was added, and the solution was left to stir for 1 hour. Afterward, the previously cleaned wafers were dip coated in this solution at 6 cm/min and left to hang in a 50°C oven in air to cure for 48 hours. The template was then removed by calcining the slides in air at 450°C for 1 hour using a heating rate of 1 °C/min. Both P123 and CTAB templated film structure was verified by GISAXS after calcination.

Micron-sized mesoporous silica particles were synthesized via an adapted version of Gartmann's modified procedure[28] from the work of Katiyar,[29] and has been previously used in our lab.[171] P123 was placed in a beaker and melted in an oven at 80°C, of which 3.10 grams was poured into a round bottom flask. CTAB (0.465 g) was dissolved in DI water (20 mL), stirred for 10 minutes, and added to the melted P123. This solution was stirred continuously at room temperature throughout the rest of the procedure. Dry, pure ethanol (200 proof, 7.8 mL) and 1.5 M HCl (49.5 mL) were added to the solution and stirred until a clear, homogeneous solution formed, which took about 45 minutes. Particle formation was initiated dropwise addition of TEOS (10 mL) to the solution and stirring the mixture for 2 additional hours. The solution was poured into a Parr 4748A Teflon lined bomb (200 mL capacity) at room temperature and then placed into a preheated oven and aged at 125 °C for 72 hours. After three full days, the particles were removed from the bomb and mixed with a high-speed mixer to homogenize the solution, then filtered and rinsed with DI water. The particles were then placed in a single walled Whatman cellulose extraction thimble and underwent Soxhlet extraction with 200 mL of ethanol for 24 h. Afterwards, the particles were dried under vacuum at 80°C overnight and characterized

with nitrogen adsorption using a Tristar 3000 instrument to characterize pore diameter and volume.

6.3.4 X-ray Scattering Characterization

The films were characterized in a vacuum chamber (<1 mbar) using GISAXS (Xenocs Xeuss 2.0) with a microfocus Cu-Kα beam (wavelength =1.54 Å) and a Pilatus 3 200K detector. The samples were mounted on a flat GISAXS sample holder with an incidence angle of 0.14°. Silver behenate drop-cast onto a glass slide was used to determine the sample-to-detector distance which was kept between 350 and 1700 mm depending on the pore spacing of the film being measured. The measurement time for each sample was 2 minutes. The location of the (100) peaks were determined by averaging the out-of-plane scattering intensity as a function of the in-plane scattering vector, using a q_z range of 0.2 to 0.4 $Å^{-1}$. Wide angle x-ray scattering (WAXS) on the mesoporous silica particles was done by placing the particles in the powder holder with a sample-to-detector distance of 342 cm.

6.3.5 Fourier Transform Infrared and Differential Scanning Calorimetry

The DESs were characterized using a Thermo Nicolet iS50 FTIR instrument on solid samples (urea and choline chloride) or liquid films (ethylene glycol, reline, and ethaline) using a Smart iTX accessory with a diamond window in an ATR configuration. Solid or liquid samples were placed directly on the diamond window for measurement. The spectra were taken in a range from 400 to 4000 cm^{-1} with a resolution of 0.4821 cm^{-1}.

DSC was performed using a Q200 DSC (TA Instruments, New Castle, DE) and 5-15 mg of sample. The DSC heating procedure was to first increase the temperature to 80 °C at 10 °C/min, then cool to -55 °C at 10 °C, and then heat to 80 °C at 0.25 °C/min.

6.3.6 Electrochemical Characterization

Electrochemical experiments were performed using a CH Instruments CHI660D Electrochemical Workstation. The redox probes used in the experiments were iron chloride ($FeCl_4^-$) and iron acetylacetonate ($Fe(C_5H_7O_2)_3$ or $Fe(Acac)_3$). Cyclic voltammetry was conducted in a three-electrode cell with the platinum counter electrode, working electrode, and quasi-reference electrode (Ag wire within the solvent of interest) submerged in 25 mL of the DES. The working electrode was either a glassy carbon electrode, fluorine doped-tin oxide coated glass slide (FTO slide), or an FTO slide coated with either 3 or 8 nm mesoporous silica thin films. The glassy carbon electrode (GCE, 0.071 cm^2) from CH Instruments was polished before use. The DES was either ethaline or reline and contained iron chloride (0.1 M), $Fe(Acac)_3$ (0.001 M), or no probe during the experiments. For cyclic voltammetry, the solution was held at 30 °C using an oil bath to maintain temperature consistency between measurements. The typical electrochemical window used was [-0.2:1.2] or [-1.2:1.2] V during cyclic voltammetry, and the scan rate was kept at 50 mV/s. For multiple scan rate curves in the supporting information, the upper and lower potential bounds were modified between 1 to 1.4 V and -0.2 to -0.4 V to keep the peaks within the window.

6.4 Results and Discussion

6.4.1 Film Characterization

Grazing incidence small angle x-ray scattering (GISAXS) was used to verify the pore structure of the silica films on top of the FTO coated glass slides. GISAXS can be interpreted to determine both the orientation and pore-to-pore center distance for the films using the representative 2D GISAXS patterns shown in Figure 23 for (a) 3 nm films templated with CTAB and (b) 8 nm films templated with P123.

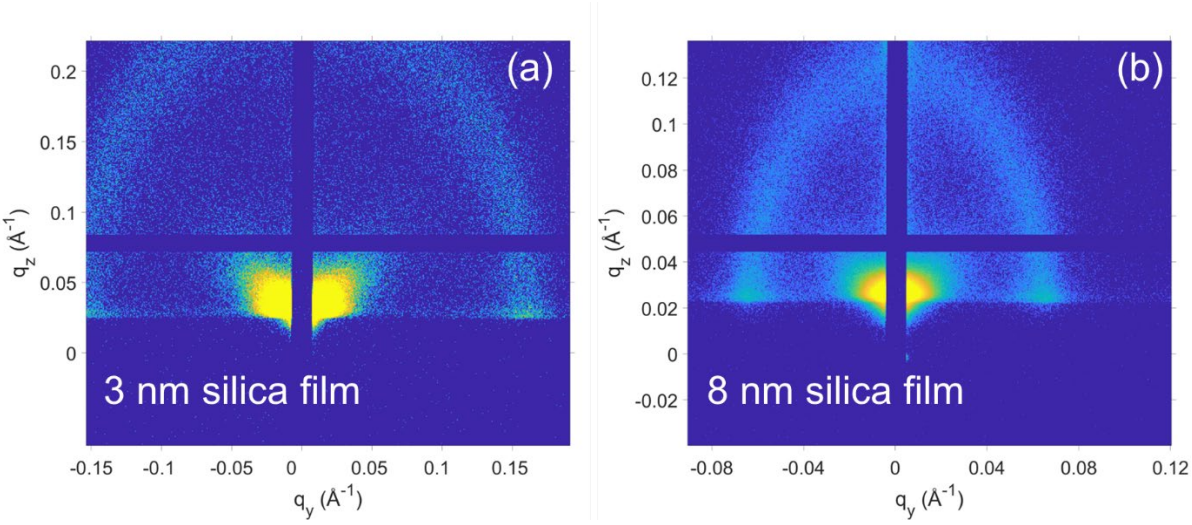

Figure 23. 2D GISAXS patterns of (a)3 nm silica films templated with CTAB and (b) 8 nm silica films templated with P123.

The rings present in the pattern are elongated in the q_z direction due to unidirectional contraction of the thin film perpendicular to the substrate from removal of the surfactant through calcination.[27] The spacing between the center of each plane of pores is called the d-spacing, and can be calculated form the location (q_y) of most intense spots on the left and right of the reflected beam (the yellow spots in Figure 23), which is also the

position of the Yoneda band. The following equation allows transitioning between d-spacing and q-space (reciprocal space):

$$d = \frac{2\pi}{q} \tag{10}$$

The scattering vector q_y corresponds to scattering parallel with respect to the substrate and gives information about spacing between the pores. Mesoporous silica thin films with small pores were synthesized in our lab using CTAB and titania doping as the template for the pores[27] and the 2D GISAXS pattern after calcination can be found in Figure 23(a). The q_y for the CTAB templated films is 0.159 $Å^{-1}$, yielding a d-spacing of ≈ 4 nm. Since these films have P6mm hexagonal symmetry, the d-spacing yields plane-to-plane distance, so the result must be multiplied by 2/√3, giving a pore-to-pore distance of 4.6 nm. GISAXS does not account for pore wall thickness, but other experimental evidence showed that the pore wall thickness of these films is between 1-2 nm.[21] This would indicate that our films are between 2.6 and 3.6 nm in diameter, so we estimate that the pore size is likely around 3 nm.

For P123 templated films, $q_y = 0.0696$ corresponding to a pore-to-pore distance of 10.4 nm. The pore wall thickness was estimated to be between 3-5 nm for hexagonal mesoporous silica thin films, corresponding to pores between 5.4 and 7.4 nm in diameter.[208] Our group has reported these films as having pore diameters as high as 9 ± 1.3 nm from TEM images, so the small pores are unexpected.[21, 67] A reasonable estimate is likely around 8 nm for the pores used in this study.

6.4.2 FTIR of Bulk Phase DES

The FTIR spectra of the DESs are presented in Figure 24. The spectra show the interactions that develop between the components upon mixing within their respective solvent. Choline chloride is the common component between both solvents and has many peaks in the 750-1500 cm^{-1} region. The peaks of interest for choline chloride are at 951 and 1479 cm^{-1} corresponding to asymmetric CCO vibrations and CH_3 rocking motions.[246] Choline chloride also has a broad peak in the 3000 to 3500 cm^{-1} range related to OH stretching and bending.[246] In urea, the three main peaks are centered at 1458, 1588, and 1675 cm^{-1} and correspond to asymmetric NH_2 stretching, symmetric CO stretching, and a combination of symmetric NH_2 bending and CO stretching, respectively.[246-248] There are also a set of peaks related to NH_2 symmetric and asymmetric stretching in the 3000 to 3500 cm^{-1} range.[246]

After forming reline, the asymmetric NH_2 stretching shifts down to 1430 cm^{-1}, the symmetric CO stretching shifts to 1604 cm^{-1}, and the symmetric NH_2 bending and CO stretching bands shift down to 1660 cm^{-1}. In the 3000 to 3500 cm^{-1} range, an intense peak appears at ≈ 3200 cm^{-1} which is lower than the most intense peaks in either component. The downward shift in DES FTIR spectra is consistent with the hypothesis that the solvent is held together by strong hydrogen bonds, because the NH, CO, and OH bonds are elongated causing a redshift.[246, 249] The FTIR spectrum of ethaline has two large sets of peaks in the fingerprint region of which the one centered at 1032 cm^{-1} is the largest, corresponding to the stretching vibration of the CO bond.[250] After the synthesis of ethaline, the CO bond shifts up to 1036 cm^{-1}. The shift towards positive wavenumber implies that there could be a lower strength of hydrogen bonding between the components of ethaline

than reline.[249] In diethylene glycol and triethylene glycol, the wavenumbers related to OH stretching are redshifted in the 3300 cm^{-1}.[251]

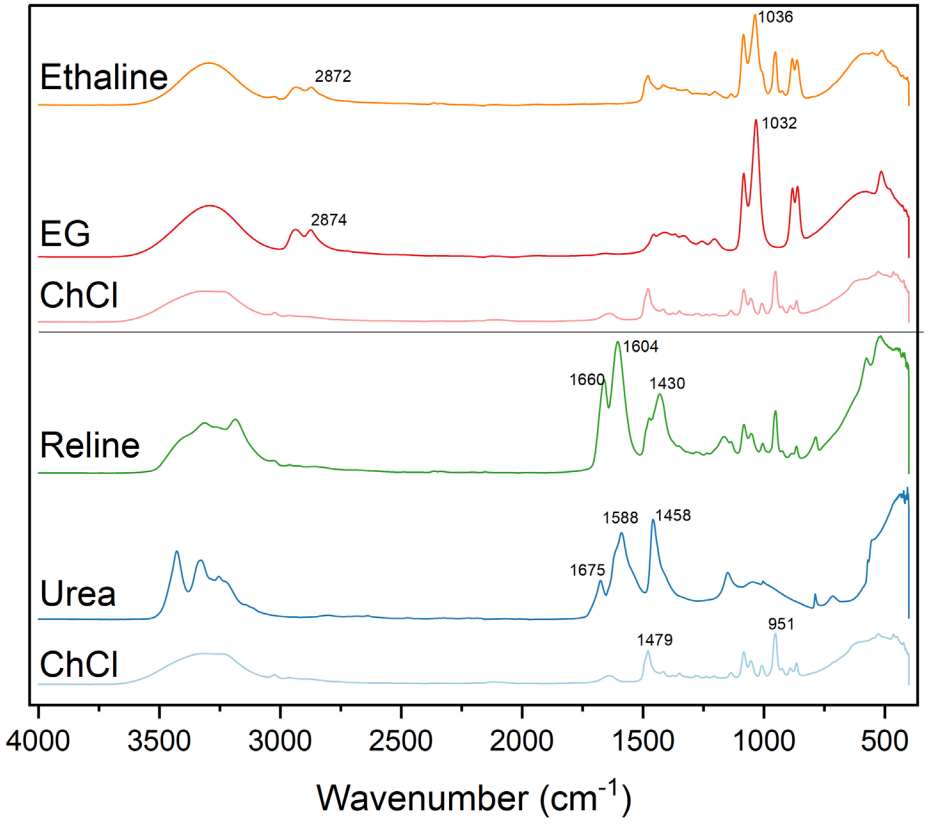

Figure 24. FTIR spectra of the DES components choline chloride, urea, and ethylene glycol and the mixed DESs reline and ethaline.

6.4.3 Unconfined DES Cyclic Voltammetry

Cyclic voltammetry (CV) was first used measure the response of the probe using a glassy carbon electrode (GCE) to compare to literature and shown in Figure 25(a). Without a probe, there were very small peaks for each solvent (<5 $\mu A/cm^2$) that could correspond to choline chloride degradation found in Appendix Figure A.3.1 and will be discussed more

in detail later. The magnitude of the oxidative current for ethaline (blue line, 2.34 mA/cm^2) is over 6 times higher than for reline (black line, 0.35 mA/cm^2), which correlates with observations in previous studies on the two solvents.[38, 96, 129, 244, 252] The peak separation in ethaline using GCE is 216 mV, and the ratio of the oxidation/reduction peak ($i_{p,o}/i_{p,r}$) current is 1.03. A fully electrochemically reversible system has a peak ratio of unity and a peak separation of 58 mV at 30 °C.[125] Since the peak ratio in this system is still near unity but the peak separation is greater than the ideal value, the system is quasi-reversible.[96] In reline using GCE, the peak separation is 318 mV, and the peak ratio is 0.96, so the reline system is also quasi-reversible.

Ethaline has a significantly lower viscosity than reline and is likely what contributes the most to the difference in current. Depending on the water concentration and temperature, ethaline has a reported viscosity between 36 and 66 cP,[83, 95, 253] while reline has a viscosity ranging from 552 to 1398 cP (maximum temperature of 30 °C).[254-256] The Stokes-Einstein relation is a good predictor of the mass transport of spherical species:

$$D = \frac{k_B T}{6\pi\eta r_h} \tag{11}$$

where D is the diffusion coefficient for the species, T is the absolute temperature, k_B is the Boltzmann constant, r_h is the hydrodynamic radius of the species, and η is the dynamic viscosity of the medium. Clearly, an order of magnitude decrease in the dynamic viscosity will result in an increase in the diffusion coefficient. The diffusion coefficient is relevant because the peak current depends on the diffusion coefficient. A fully reversible redox probe is described by the Randles-Sevcik equation:

$$i_p = 0.4463nFAC\left(\frac{nF\upsilon D}{RT}\right)^{\frac{1}{2}} \quad (12)$$

While an irreversible redox probe is described by the Nicholson-Shain equation:

$$i_p = 0.4958nFAC\left(\frac{nF\alpha\upsilon D}{RT}\right)^{\frac{1}{2}} \quad (13)$$

In these equations, i_p is the peak current measured in cyclic voltammetry, n is the number of electrons transferred in the redox event (1 in this case), F is Faraday's constant, A is the area of the electrode, C is the concentration of the redox probe, ν is the scan rate, α is the charge transfer coefficient, D is the diffusion coefficient, R is the ideal gas constant, and T is the absolute temperature. Alpha in equation 13 is calculated using equation 14 from the peak and half-peak potential (E_p and $E_{p/2}$):

$$\left|E_p - E_{\frac{p}{2}}\right| = \frac{48.5\ mV}{\alpha} \quad (14)$$

Using the peak current and potential from the CV curves in Figure 25(a) gives a diffusion coefficient range of 3.7 – 8.9 x10^{-9} and 1.9 – 3.4 x10^{-7} cm^2/s corresponding to the range between ideally reversible and irreversible behavior for reline and ethaline respectively using GCE. The current was varied and has a linear dependence on the square root of the scan rate shown in Appendix Figures A.3.2 and A.3.3. These values are within the range of reported literature values for reline (0.17 – 2.9 x10^{-8} cm^2/s)[96, 257] and ethaline (1.8 – 55 x10^{-8} cm^2/s).[232, 244] The order of magnitude difference in the diffusivity from these equations correlates with the order of magnitude difference in viscosity and demonstrates that the diffusion is likely a result of the difference in viscosity. The quasi-reversible nature in both solvents is due to sluggish kinetics and makes the peak separation large. The rate

constant of the redox reaction determines the peak separation.[128] A large peak separation is characteristic of diffusion processes that occur faster than mass transfer processes.

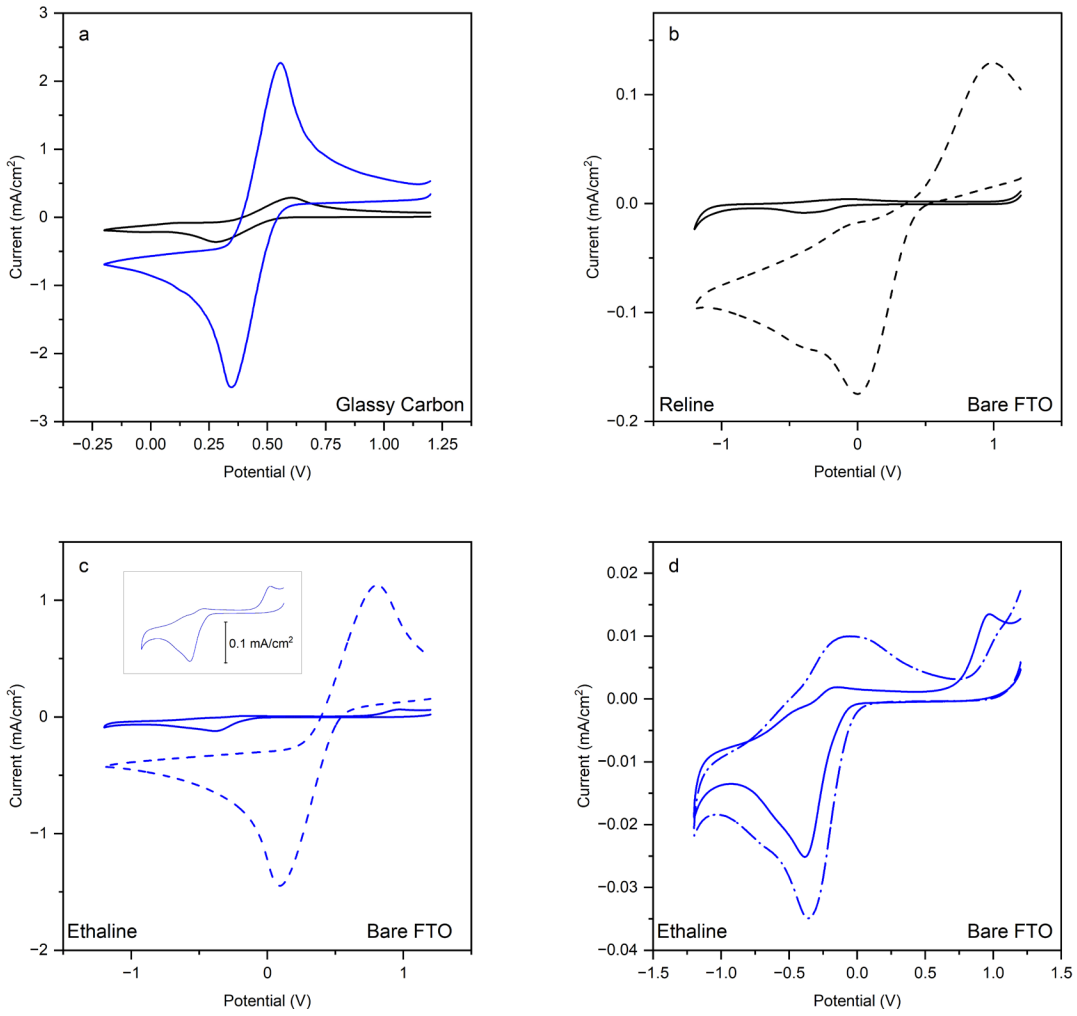

Figure 25. Cyclic voltammetry curves of (a) ethaline (blue) and reline (black) with 0.1 M $FeCl_4^-$ using GCE as the working electrode, (b) reline with no probe (solid) and 0.1 M $FeCl_4^-$ (dashed) using a bare FTO slide, (c) ethaline with no probe (solid) and 0.1 M $FeCl_4^-$ (dashed) using a bare FTO slide, and (d) ethaline with no probe (solid) and 0.001 M $Fe(Acac)_3$ (dash-dot) using a bare FTO slide. The inset in (c) is the magnified line of ethaline without a probe and has a scale bar of 0.1 mA/cm^2. All scan rates are at 50 mV/s.

The CV of reline with and without $FeCl_4^-$ using an FTO slide as the working electrode is presented in Figure 25(b). Without a probe, reline has a reduction peak at -0.4 V and a small oxidation peak at -0.16 V. These peaks are related to the irreversible decomposition of choline chloride, possibly to a combination of trimethylamine, water, vinyl alcohol, and dimethylethanolamine during reduction and diatomic chlorine during oxidation.[127] These products are small in concentration and do not impact the overall electrochemical behavior of the system.[127] With $FeCl_4^-$, the current increases due to the redox reaction of the $FeCl_4^-$ couple. The peak separation widens to 950 mV and the peak ratio becomes 0.60 in reline, which may be due to a decreased rate constant of electron transfer.[128] The broadening of the peak indicates that the kinetics of the reaction are more sluggish than with the GCE electrode. In ethaline with 0.1 M $FeCl_4^-$ (Figure 25(c)), the neat solvent has a small current and peaks related to choline chloride decomposition at high negative potential and has a dramatic increase in current when the iron is added. The peak separation in ethaline-$FeCl_4^-$ widens to 713 mV and the ratio is 0.93 compared to glassy carbon, so the system is still quasi-reversible. The inset in Figure 25(c) shows ethaline without a probe behaves like reline, where a reduction and oxidation peak can be observed related to reduction of choline and the oxidation of chloride. The faster kinetics of $FeCl_4^-$ redox reactions in ethaline makes it a better system for observing transport characteristics to the FTO electrode.

On FTO, the $Fe(Acac)_3$ redox probe (Figure 3(d)) peak appears to overlap with the degradation of choline in the reduction branch and has a small peak in the oxidation branch on FTO. The peak is not as pronounced as $FeCl_4^-$ because the concentration of $Fe(Acac)_3$ is lower (0.001 M) in ethaline due to low solubility.[258] The magnitude of the current is

higher in the system with the probe than without it, however, demonstrating that the probe is present. Generally, neutral or positively charged iron-based probes are not very soluble in DESs. This makes it challenging to probe the behavior of cationic or neutrally charged species through a porous layer on top of the electrode.

6.4.4 Confined DES Cyclic Voltammetry

The CV curves for both solvents were recorded with an FTO electrodes coated with mesoporous silica films of different pore diameters (3 and 8 nm). The curves for the porous electrodes without probes with FTO as the working electrode are found in Appendix Figure A.3.4. With a wide electrochemical window (-1.2 to 1.2 V), the reduction of choline is still present in both pore diameters, demonstrating that the electrode surface is still accessible to the solvent. The reduction current density of the neat solvent is lower using FTO as an electrode compared to the porous films. The porous films enhance the current density because of favorable interactions between the DES and the silica surface, thus increasing the local concentration within the pores.[130] Using FTIR, Ghazali et al. showed that reline interacts with the silica pore walls through hydrogen bonding, shifting the peak positions related to urea to higher wavenumbers.[85] Molecular dynamics simulations demonstrate that reline preferentially orders along charged graphene surfaces.[93] With a neutral or negatively charged surface (-0.32 C/m^2), there is a mixed layer of choline cations and urea molecules in a higher concentration compared to the bulk value.[93] Neutron scattering experiments in tandem with molecular dynamics show that ethaline also preferentially layers along a silicon oxide surface with the ethylene glycol and choline chloride both mixing at the interface.[94] In both of these solvents, the layer of chloride exists above the mixed choline/HBD layer at the interface.[93, 94] While the surface charge of silica can

change depending on the extent of protonation from neutral to negatively charged, the favorable interactions between the solvent and pore walls of the silica regardless of charge help ensure that the pores are completely filled with DES for electrochemical techniques.

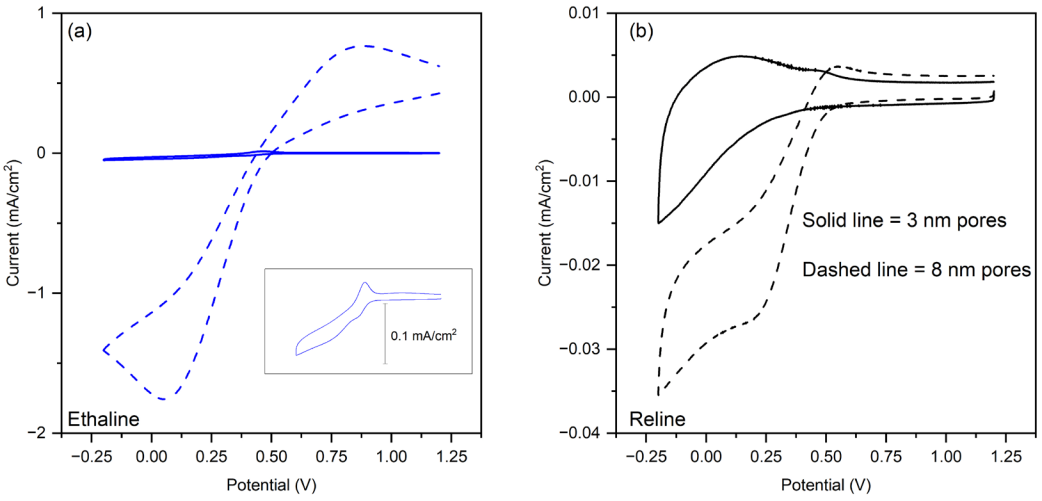

Figure 26. CV curves of DESs containing 0.1M $FeCl_4^-$ using FTO slides coated with silica with 3 nm (solid) or 8 nm (dashed) pores. The solvents are (a) Ethaline (blue curves) with an inset of the 3 nm pores and (b) reline (black curves).

The CV curves of ethaline with 0.1 M $FeCl_4^-$ have similar current density for FTO slides both with (Figure 26(a)) and without (Figure 25(c)) the 8-nm silica film present, but the peaks are broader when coated with the film, and the ratio of the current density favors reduction ($i_{p,o}/i_{p,r} \approx 0.6$). The first scans are shown here because no significant change was observed when running multiple scans using ethaline as a solvent, shown in Appendix Figure A.3.5. A peak ratio of $i_{p,o}/i_{p,r}$ less than unity implies that as the species is reduced, an irreversible reaction consumes the reduced species and it is no longer able to undergo oxidation. In mesoporous silica materials, charge also has an impact on the peak ratio. For example, ferrocenemethanol (Fc) becomes positively charged upon oxidation in an

aqueous solution, and due to favorable interactions between the positively charged Fc^+ and negatively charged silica, the reduction peak is enhanced and the peak ratio becomes less than unity.[130] In our system, the $FeCl_4^-$ becomes more negatively charged upon reduction, and the repulsion with the pore wall is likely to push the probe out of the pore. As oxidation starts to occur, the increased hindrance due to the higher negative charge reduces the current.

Regardless of the possible exclusion of the reduced iron complex, the large current density shows that the large pore diameter (8 nm) allows the $FeCl_4^-$ to easily reach the substrate. In contrast, the current density in 3 nm porous silica is dramatically reduced by about 1 order of magnitude, indicating that $FeCl_4^-$ is not reaching the FTO surface easily. The square root of the peak reductive current was plotted against the scan rate in another experiment to calculate the diffusion coefficient for the confined DESs with the full curves shown in Appendix Figure A.3.2. The diffusion coefficient for the FTO slide was 3.3×10^{-8} cm^2/s, which is an order of magnitude slower than the glassy carbon electrode and could be due to the slower kinetics with FTO as the working electrode. The diffusion coefficient for the 3 and 8 nm confined DES calculated using Equation 12 was 1.4×10^{-11} and 1.0×10^{-8} cm^2/s, so anionic solutes in 8 nm porous silica may still have diffusivity comparable to the bulk system while the diffusivity reduced by 3 orders of magnitude in 3 nm pores. The extreme reduction in diffusivity agrees with the observed reduction in current but we acknowledge that calculating the diffusion coefficient with porous systems using the Randles-Sevcik equation may not reflect the true diffusivity value because the concentration gradient formed during redox transport is larger than the thickness of the porous film on the electrode.[131]

The lower current density and transport characteristics in the 3 nm pores is likely a result of charge exclusion and viscosity; since the pores are smaller, the surface area they have is greater, and therefore the repulsion experienced by the $FeCl_4^-$ is greater. The local ordering of the DES along the pore wall also creates a higher viscosity within the pore. Molecular dynamics and neutron scattering show that there is ordering of ethaline along a silica interface up to 2 nm from the surface of the material before returning to a fully mixed, bulk system.[94] The small pore diameter of 3 nm means that the bulk-like environment is not present within the center of the pore, as there would be with the 8 nm pores. It is well known in confined IL systems that the local viscosity near surfaces increases by up to 2 orders of magnitude due to interactions between the IL and the surface,[259] which would contribute to a reduction in diffusion. Molecular dynamics also shows that lateral self-diffusion in ILs is reduced when near interfaces where molecular ordering takes place, regardless of the charge of the surface.[260] The effective diameter of the $FeCl_4^-$ probe in ILs is between 0.4 – 0.8 nm so the size of the probe may also be a contributing factor to the reduction in current density.[261, 262] DESs are similar to ILs in that they contain a component that has cationic and anionic parts, so the conclusion that local viscosity causes transport hindrance is likely still valid for DESs. The combination of high local viscosity, a large probe relative to the small pores, and charge repulsion contribute to the hindrance of the $FeCl_4^-$ anion transport within the pores.

The CV curves for the reline- $FeCl_4^-$ system (Figure 26(b)) have small current density in both pore diameters. This indicates that in reline, the $FeCl_4^-$ probe cannot effectively reach the FTO surface by passing through the pores. Like with the confined ethaline, the diffusion coefficients were calculated by using the reductive current and

multiple scan rates, and the full curves are found in Appendix Figure A.3.3. For the 3 and 8 nm porous silica, the apparent diffusion coefficients drop to 1.6 $x10^{-12}$ and 4.3 $x10^{-11}$ cm^2/s, respectively. In the case of the smaller, 3 nm diameter pores, the reduction in diffusivity was expected when compared to ethaline. Reline has a higher viscosity of at least one order of magnitude that will be further increased as the pore size is reduced due to the molecular ordering along the pore wall. Interestingly, the 8 nm diameter pores also have a very small reduction current density despite the pore center being much larger. This result is significant because the only difference between the two systems is exchanging ethylene glycol with urea. Molecular dynamics show that in reline, the center of the pore is bulk-phase DES since the molecular layering only extends out to about 1.2 nm or less on charged surfaces.[92] There are few studies on confined reline in mesoporous materials that help explain the observed reduction in transport properties. The works by Ghazali et al. show that reline confined in mesoporous silica nanoparticles is able to adsorb CO_2, but at high DES loadings, the adsorption capacity decreases.[56, 85] Our pores are completely filled with reline and the probe is slow to reach the substrate, consistent with the idea that high loadings of reline make the pores less accessible to solutes. The high viscosity of reline may make it difficult for iron transport through the solvent and the pores restrict the bulk phase transport of both DES and iron ions. Reline's high viscosity may "freeze" it within the pores and make transport very slow. Another barrier to transport of the iron to the surface may be urea itself. Urea is polar molecule and will orient itself on the surface of a charged electrode.[263] The competition with urea for room at the surface may make it more difficult for the iron to reach the surface.

Differential scanning calorimetry (DSC) can provide insight into the phase transitions of reline. To increase the amount of material for an accurate measurement, pure reline was confined in mesoporous silica microparticles (9 nm pore diameter) to give the DSC trace shown in Figure 27. We found that there were no peaks related to melting or crystallization between 218 and 353 K. DSC demonstrates that the DES does not change phase within the pores. The wide angle x-ray scattering pattern of the confined reline in 9 nm porous silica microparticles shown in Appendix Figure A.3.6 shows that there are only peaks related to the pore-to-pore spacing of the silica, and none related to a crystal phase of DES, meaning that the DES could exist as a liquid or amorphous solid within the pores. The difference between transport properties for the two DESs is actually advantageous. The CV results comparing the transport of $FeCl_4^-$ in both solvents show that the system is highly tunable. Certain species can either be allowed to enter the pores or have their transport highly restricted by carefully choosing a solvent and pore diameter combination for a specific task. With the vast catalogue of species available to synthesize DESs, they demonstrate "designer solvent" characteristics reminiscent of ILs.

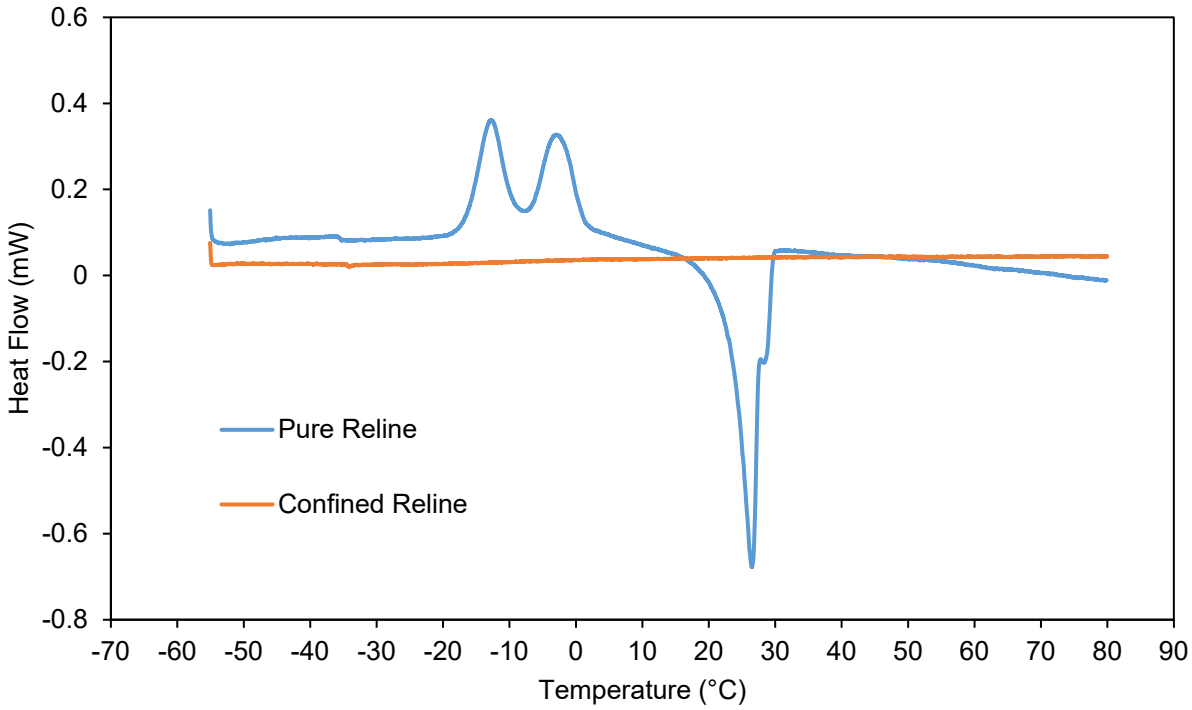

Figure 27. Differential scanning calorimetry heating curves of reline in bulk phase and confined within 9 nm mesoporous silica microparticles. Exothermic heat flow is up.

The cyclic voltammetry of the iron acetylacetonate probe ($Fe(Acac)_3$), shown in Figure 28, has very small peaks when using FTO as the working electrode, and they appear to overlap with the reduction of choline chloride similar to the behavior of the probe using GCE as the working electrode in Figure 26. The low peaks are due to low solubility of the probe within the solvent.[258] When using the 8 nm mesoporous silica as the working electrode, the current density of the peak increases, while the current density remains about the same as the FTO slide in the 3 nm case. We hypothesized that the neutral charge on $Fe(Acac)_3$ would make it easier to enter the pores and be pushed out upon reduction. If this were true, the reduction peak would have a higher magnitude than oxidation. Since the reduction peak is overlapped with choline decomposition, the peak ratios cannot be

compared. The CV curves here still demonstrate that $Fe(Acac)_3$ can reach the FTO substrate in the 8 nm pores case. With 3 nm pores, the extended layering of ethaline induced by the pore walls may again restrict the transport of any species through the pores. This may indicate that there is a lower limit to pore diameter in confined DESs beyond which transport of any solute is highly restricted.

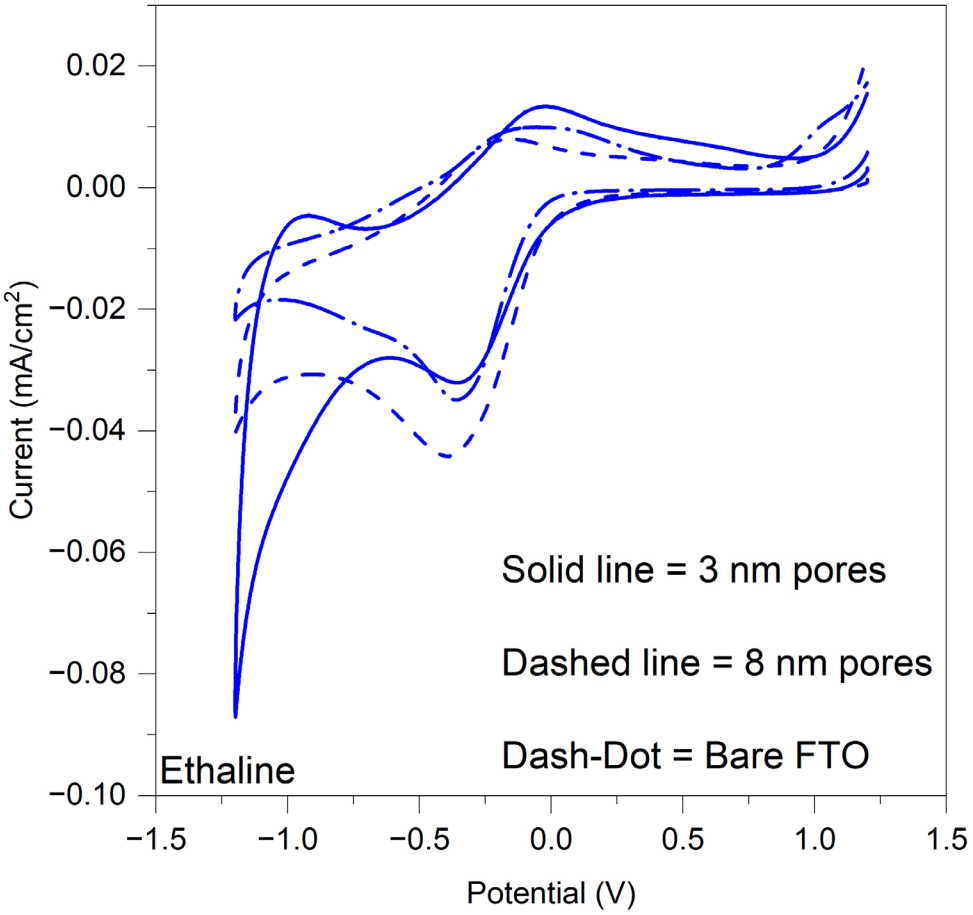

Figure 28. Cyclic voltammetry curves of iron acetylacetonate dissolved in ethaline (0.001 M). The line type denotes the working electrode where the dash-dot is FTO, the solid line is an FTO slide coated with silica having 3 nm pores, and the dash line is the FTO slide coated with 8 nm porous silica.

6.5 Conclusion

Mesoporous silica thin films with 3 and 8 nm vertically aligned, accessible pores were cast onto FTO-coated glass slides and used as an electrode to characterize the transport properties of iron-based redox probes through the pores using cyclic voltammetry. The films were characterized by GISAXS to verify a vertical pore structure and spacing. The deep eutectic solvents reline (choline chloride:urea 1:2) and ethaline (choline chloride:ethylene glycol 1:2) were chosen as the solvents of interest and the redox probes were chosen to be iron (III) chloride and iron acetylacetonate to compare and contrast the behavior of negative and neutrally charged probes. Ethaline has a lower viscosity than reline and allows faster solute diffusion using a common glassy carbon electrode in the bulk solution as a result. When confined, ethaline is able to maintain its bulk-like diffusion through 8 nm porous silica films, while the diffusion is reduced by 3 orders of magnitude in the 3 nm porous silica films. The ordering of the solvent along the pore walls due to favorable interactions between the choline chloride, ethylene glycol, and silica pore walls leads to high local viscosity near pore walls, which extends to the middle of the pore in the 3 nm system and hinders transport of the $FeCl_4^-$ probe. Electrostatic repulsion of the iron by the negative charges along the pore wall may also contribute to the reduced transport of the probe through the pores.

In contrast, confined reline is effectively not able to facilitate the transport of $FeCl_4^-$ to the FTO surface through either pore size. We hypothesize that this could be from the high viscosity of reline and is exacerbated by being confined within the pores, perhaps causing a partially ordered glassy to form so that transport is very slow. Like with ethaline, the DES has a high affinity for the pore walls that increase the local viscosity near the pore

walls and reduce diffusivity. The reduction may also have another barrier to transport since urea is polarizable and may interact with the surface of the FTO, creating competition at the electrode surface. DSC and WAXS show that the confined reline is either a liquid or amorphous solid, but not crystalline, and supports the hypothesis that the high viscosity may cause the transport reduction. The neutral probe $Fe(Acac)_3$ in ethaline shows a similar behavior as $FeCl_4^-$ because the current in 8 nm pores is slightly higher than with a bare FTO slide, while current is similar between 3 nm pores and a bare FTO slide. This suggests that the limitation to transport may be primarily limited by local interactions and not by charge within the DES.

The results from this study show that confined DES systems are highly tunable to achieve desired transport properties. With lower viscosity solvents such as ethaline, the pore diameter of the porous support needs to be a relatively large mesopore to allow for bulk-like diffusion and may be tuned to selectively transport dissolved species. Additionally, different DES combinations can lead to desired uptake or rejection of solutes within the pores. Understanding the transport of the iron based redox probes may guide the design of supported DES systems in particles or membranes for separations (e.g., of dissolved metals), energy storage devices (e.g., iron flow batteries), or catalysis (e.g. Lewis acid catalysis by halometallate deep eutectic solvents).

CHAPTER 7. CONCLUSIONS AND FUTURE WORKS

The overall goal of this dissertation is to understand how local solvent environments in confined alternative solvent systems change their thermophysical properties. Understanding the characteristics of confined IL and DES systems will lead to better designed supported solvent systems in applications of separations, catalysis, and electrochemical devices. This dissertation addresses the fundamental questions of how confinement impacts transport within supported ILs and DESs and reveals key details about the mechanisms responsible for observed property changes.

Chapter 2 investigates the transport properties of confined ILs within mesoporous silica microparticles using the FRAP technique in confocal microscopy. The particles were synthesized via the sol-gel method with 5.4 and 9 nm diameter pore measured by nitrogen adsorption (BET). Additionally, the pores of the 9 nm diameter silica were tethered with [TMS-MIM][Cl] and exchanged to [TMS-MIM][PF_6] to change the surface charge on the interior of the pores. FTIR and DSC of IL-loaded microparticles showed that the IL was confined and that ILs may interact with the pore wall surface, leading to shifts in FTIR peaks and (along with compression effects) shifts in melting temperature. The IL was mixed with fluorescent dye and investigated with confocal microscopy. The base case was 9 nm silica with neutral DCM dye. The transport properties elucidated from the FRAP technique showed that the most significant influence on transport of solutes within confined ILs is the properties of the surface and the charge of the solute. When surface properties are similar to that of the confined IL (tethered pore walls), transport is improved because the hydrophobicity is similar within the entire pore and there is less interaction between the IL and surface. Transport within tethered systems can be further tuned by

changing the surface functionality of the surface. The charge of the solute also significantly impacts transport; since ILs are inherently charged, the attraction between the solute and the IL or the substrate can hinder transport in confined ILs. Additionally, there is flexibility in the system to pore diameter and hydration, meaning less demanding handling and synthesis techniques are required for the mesoporous support. This chapter demonstrates that confined IL systems within mesoporous silica materials are tunable for transport of solute molecules and advances understanding of transport properties for the development of confined ILs in separations, catalysis, and battery applications.

Chapter 4 discusses the XPS spectra of confined [BMIM][Cl] within mesoporous silica thin films with 3.5, 8.5 nm, and tethered 8.5 nm pores. It was found that in the high resolution spectra, significant shifts occur with confined ILs regardless of pore diameter or surface functionalization. These shifts indicate that there are significant differences in the local environment of the IL compared to the bulk phase at the interface that had previously been inferred from methods such as FTIR. The carbon spectrum has complex shifts associated with the imidazolium ring but demonstrates that confinement has an effect on the electronic environment of the cation. The chlorine spectra have different shifts depending on the pore diameter: in small (3.5 nm) pore diameter, the shift is significant to higher binding energies and the environments present are likely associated with hydrogen bonding with the pore wall and the formation of a $[Cl\text{-}H\text{-}Cl]^-$ species. In the 8.5 nm pore diameter, the shift is not as strong and the middle of the pore still has free chloride, but there is a shift toward higher BE that could be due to proton-bridged chloride or H-bonding with the pore walls like in 3.5 nm pores. Tethered pores display similar shifts as the 3.5 nm case, indicating the surface may not be fully functionalized and either $[Cl\text{-}H\text{-}Cl]^-$ is

formed or hydrogen bonding between the chloride and the surface can still occur. The nitrogen spectra show a large new peak at lower binding energy in all pore environments due to strong interactions between the imidazolium head-group and the pore wall. The appearance of a new peak clearly indicates a change within the electronic environment of the imidazolium ring. FTIR[1] and MD simulations[79] also demonstrate that ILs order at interfaces, with the interaction between imidazolium and the pore wall being inferred from the FTIR spectrum. XPS probes the interface directly and provides further information about the chloride speciation that has not been previously highlighted. The results of this chapter indicate that it is important to consider the strength of imidazolium binding to the pore walls and shows that XPS is a powerful technique to probe the IL/support interface for the design of confined ILs in catalysis or separations.

Chapter 5 investigated the effects of confinement on the properties of confined halometallate IL [BMIM][$FeCl_4$] within 3.5 nm mesoporous silica thin films using XPS. The bulk phase spectrum of [BMIM][$FeCl_4$] showed that the charge delocalization on the anion caused a shift of the chloride and nitrogen peaks to higher binding energy compared to [BMIM][Cl] from lower charge transfer between the cation and anion. The shift of the nitrogen to higher BE is also consistent with a lower basicity of the anion. Compared to confined [BMIM][Cl], the nitrogen spectrum showed that the IL may not have had as strong of interactions between the imidazolium ring and the pore wall, but instead may be through an iron complex. The chloride spectrum shows that there is potential charge transfer between the anion and the pore wall leading to lower BE. This chapter demonstrates that XPS is capable of characterizing halometallate-based low vapor pressure

solvents confined within mesopores and is the first in-depth investigation of halometallate based ILs within porous materials using XPS.

Chapter 6 probes the ability of charged metal salts ($FeCl_3$) to enter pores of mesoporous silica thin films when dissolved into DES (reline and ethaline) using cyclic voltammetry for the purpose of contamination removal from waste streams. The bulk phase current response of $FeCl_3$ in ethaline was higher than reline likely due to the lower viscosity of the solution, allowing faster diffusion of the probe. In confined ethaline, the probe easily passed through 8 nm pores while having slow transport through 3 nm pores. Confined reline experienced poor transport regardless of the pore diameter. Iron acetylacetonate had a very low solubility within both solvents and the peaks in ethaline likely overlapped with the reduction of choline chloride, but still appeared to have a larger reduction peak consistent with the pore being more accessible to the neutral, oxidized state of the probe. The Randles-Sevcik equation also showed that the slopes of the peak current for each solvent correlated with the observed reduced current density of $FeCl_4^-$, thus indicating a reduction in diffusivity of the probe in reline regardless of pore size, while diffusion in ethaline is pore size dependent. Therefore, it was found that the solvent system was tunable to allow or reject the model probe by carefully selecting combinations DES components and pore diameter.

DESs are becoming increasingly important so their development as alternative solvents should continue to be investigated in future studies. Solvation and pore wall interactions of DESs could be investigated using XPS. Since DESs are held together by H-bonding, XPS could be used to probe H-bonding between DES constituents. Current techniques to understand DES structure are molecular dynamics,[92] more demanding

techniques such as neutron scattering,[15] or FTIR.[246] XPS with ILs was useful in determining the interaction mode between the cation and anion and showed that the anion choice has an impact on the electrical environment on the imidazolium ring.[224] XPS would be useful to probe the electronic environment of the DES components since it is more accessible and provides a significant amount of information. These techniques could easily extend to confined DESs which may have similar interaction mechanisms with silica as with ILs. MD simulations suggest ordering at interfaces when DESs are situated next to solid surfaces so using XPS to investigate this interaction is a natural next step.[92] Metallic DESs would be a useful next step since the metal component makes DESs useful for catalysis. However, reline and ethaline tend to crystallize under UHV so regular XPS would be difficult to perform. Ambient pressure XPS would be effective at characterizing DESs since the pressure can be kept higher and custom gas environments can be used to prevent water uptake. .

Tethering DESs to the surface of silica is a natural next step to prevent them from leaching from the pores during processing and preliminary experiments are discussed in Appendix A4. A choline chloride derivative is tethered to the surface of mesoporous silica microparticles,[88] and a HBD (urea) is added to create a DES tethered to the surface of the silica. The FTIR spectra of the tethered DES show that both choline chloride and urea are present and have small shifts associated with hydrogen bonding between them. Furthermore, TGA demonstrates that there is a reduction in thermal stability in both confined and tethered DESs.[264] This indicates that tethering was likely successful because the higher degree of hydrogen bonding between the DESs causes the choline chloride and urea to be less thermally stable. Future work in this area could be extended to other HBDs

that are more environmentally friendly like glucose or other sugars that are abundant. Additionally, catalytically active HBDs like $ZnCl_2$ could be used to have a tethered DES for heterogeneous catalysis.[265] Catalytic DESs have applications in the dehydration of glucose to 5-HMF and Friedel-Crafts acylations.[266, 267] XPS would be a useful technique to characterize speciation of the metallic components within the DESs to improve their design.

Applications of mesoporous thin films were also investigated for the degradation of model melanoidin compounds and model lignin dimers for wastewater treatment applications from distilleries and lignin upgrading found in Appendix A5. Melanoidins are brown waste compounds that are harmful to the ground and waterways, while lignin is a polymer found in plants that can be upgraded into many useful chemicals once broken down. Both materials are difficult to break down into smaller units. In preliminary work, UV light shone onto mesoporous titania films were able to catalyze the decolorization of model melanoidins based on glucose and glycine, but the decolorization was only somewhat faster than just the UV light alone. One next step for melanoidins degradation would be to reduce the path-length of the UV light through the solution so that it is not lost when reaching the titania. Another couple of next steps could be to use a mediator to facilitate electron transport from the film to the melanoidins or to use doping of the titania films to improve the visible light activity of the films. The model lignin dimer guaiacylglycerol-β-guaiacyl ether (lignin GG dimer) was also difficult to break down using charged titania. Cyclic voltammetry with an FTO slide coated with mesoporous titania produced reduction peaks rather than oxidation peaks, so future work could investigate why these peaks happen over oxidation. Lignin degradation was not successfully achieved

using mesoporous titania films, but a mediator in the solution may improve charge transfer between the titania surface and the α or γ carbon which would weaken the C-O ether bond in β-O-4 lignin dimers and allow easier cleavage.

APPENDICES

Appendix 1. Supplementary Materials for Chapter 3

Appendix Table A.1.1. Diffusivity and coefficient of determination values of all samples used in this study. Outliers were removed by the Grubbs test. Data was checked for a normal distribution using the Jarque-Bera Test, then the Grubbs test was applied. After the outliers were removed, the rest of the data followed a normal distribution with $p<0.05$ in the Jarque-Bera test and passed the Grubbs test. Total outliers removed accounted for 5.7% of total data (3 data points out of 53).

IL Condition	Sample Number	Diffusivity (D, cm^2/s)	Coefficient of Determination (R^2)
Confined IL in 9 nm pores	1	0.022	0.985
	2	0.037	0.969
	3	0.015	0.993
	4	0.035	0.982
	5	0.029	0.979
	6	0.017	0.980
Confined IL in 5.4 nm pores	1	0.031	0.991
	2	0.015	0.986
	3	0.047	0.980
	4	0.012	0.993
	5	0.021	0.962
	6	0.016	0.961
	7	0.025	0.993
	8	0.004	0.990
	9	0.007	0.955
	10	0.066	0.969

IL Condition	Sample Number	Diffusivity (D, cm^2/s)	Coefficient of Determination (R^2)
Confined IL (9 nm) with cationic dye (Rhodamine 6G)	1	0.005	0.948
	2	0.009	0.935
	3	0.012	0.887
	4	0.018	0.875
	5	0.013	0.698
	6	0.014	0.707
	7	0.004	0.799
Confined IL (9 nm) treated with water for 24 hours	1	0.043	0.988
	2	0.027	0.984
	3	0.054	0.991
	4	0.026	0.996
	5	0.026	0.993
Tethered-9 nm pores Confined IL (9 nm) with pore walls functionalized with [TMS-MIM][Cl]	1	0.071	0.916
	2	0.104	0.955
	3	0.038	0.962
	4	0.114	0.921
	5	0.083	0.893
	6	0.074	0.951
	7	0.083	0.926
	8	0.072	0.981
	9	0.079	0.952
	10	0.087	0.982
	11	0.047	0.962
	12	0.076	0.948
	13	0.089	0.952
	14	0.076	0.953
Tethered/Ion exchanged-9 nm pores Confined IL (9 nm) with pore walls functionalized with [TMS-MIM][PF_6]	1	0.005	0.927
	2	0.009	0.936
	3	0.009	0.974
	4	0.009	0.974
	5	0.018	0.963
	6	0.014	0.985
	8	0.015	0.888
	9	0.017	0.948

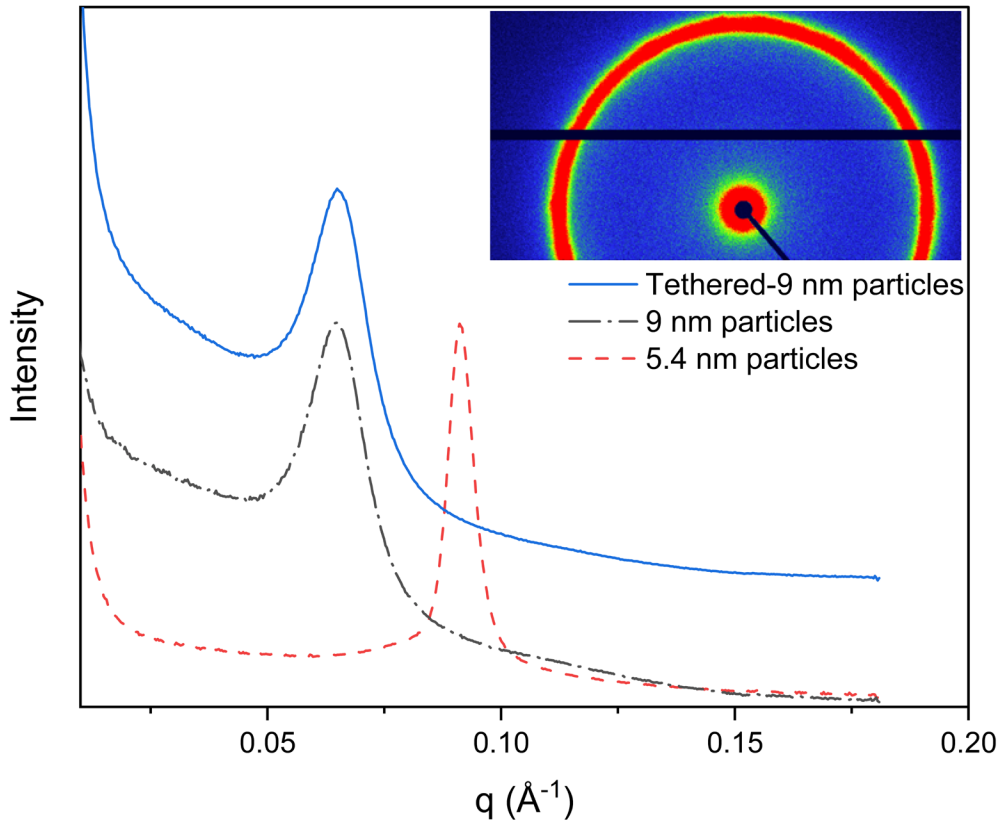

Appendix Figure A.1.1. Azimuthally integrated small angle x-ray scattering (SAXS) patterns of mesoporous silica particles used in this study. The dashed red line is the bare 5.4 nm mesoporous silica particles, dash-dot black line is bare 9-nm mesoporous silica, and the solid blue line is the tethered-9 nm silica particles without confined IL. Inset: 2D Small angle x-ray scattering pattern of 5.4 nm particles.

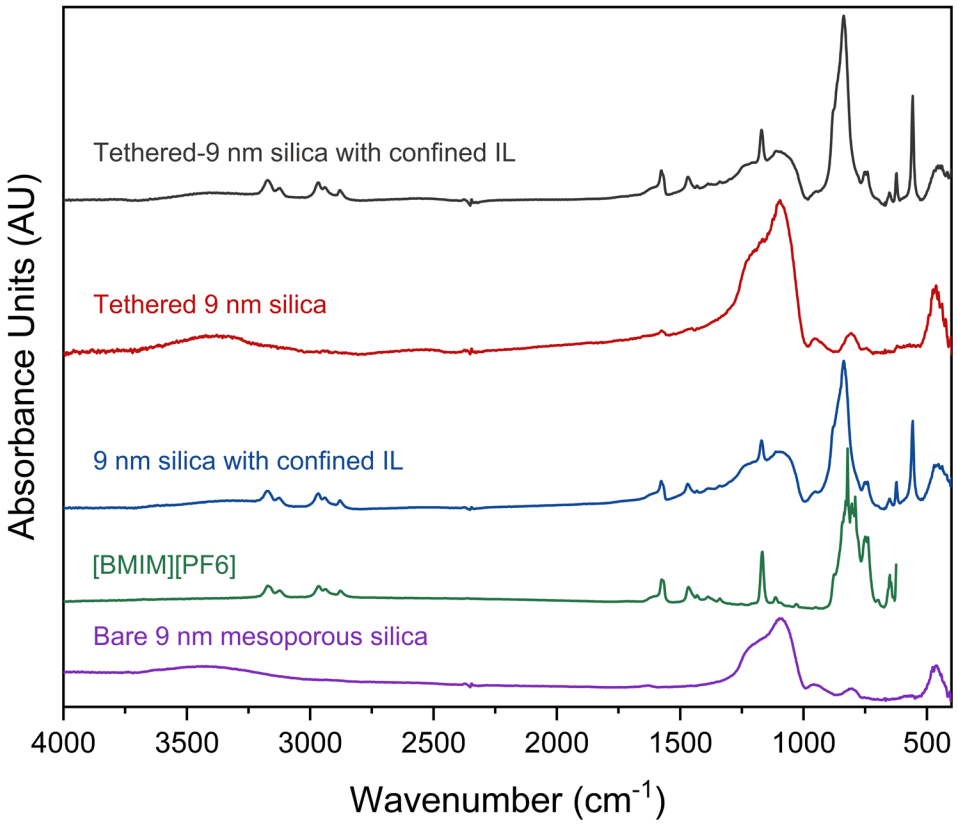

Appendix Figure A.1.2. Full Scale FTIR spectra of ILs confined within mesoporous silica microparticles (See Figure 3). From bottom to top is bare 9 nm silica particles, pure [BMIM][PF_6], 9 nm silica particles with confined IL, tethered-9 nm silica particles without additional IL, and tethered-9 nm silica particles with confined IL.

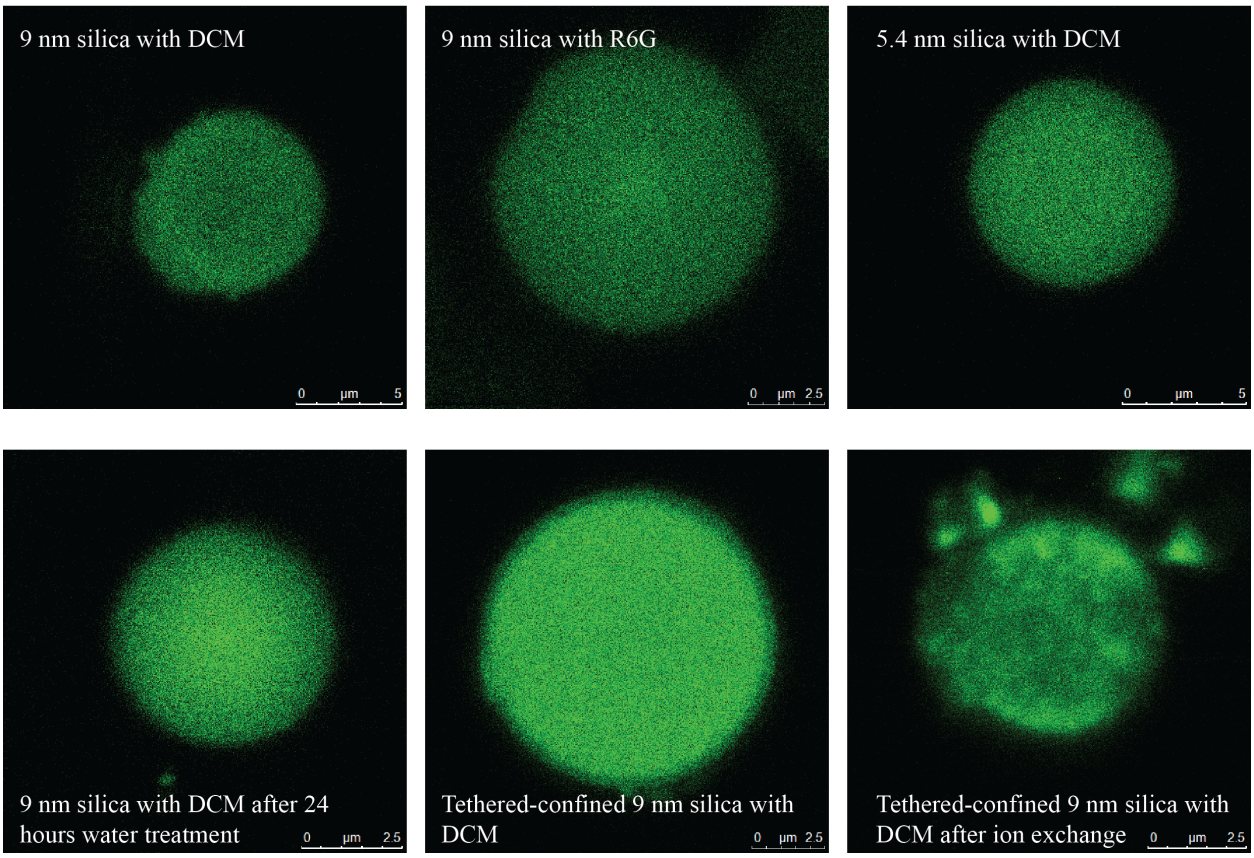

Appendix Figure A.1.3. Image examples of each particle type used in this study. On the top row from the left: 9 nm mesoporous silica particles with DCM dye, 9 nm silica particles with R6G dye, 5.4 nm silica particles with DCM dye. On the bottom row from the left: 9 nm silica particles after 24 hours water exposure and DCM dye, tethered-9 nm silica particles with DCM dye, and tethered-ion exchanged-9 nm silica particles with DCM dye.

Appendix 2. Supplementary Materials for Chapter 4

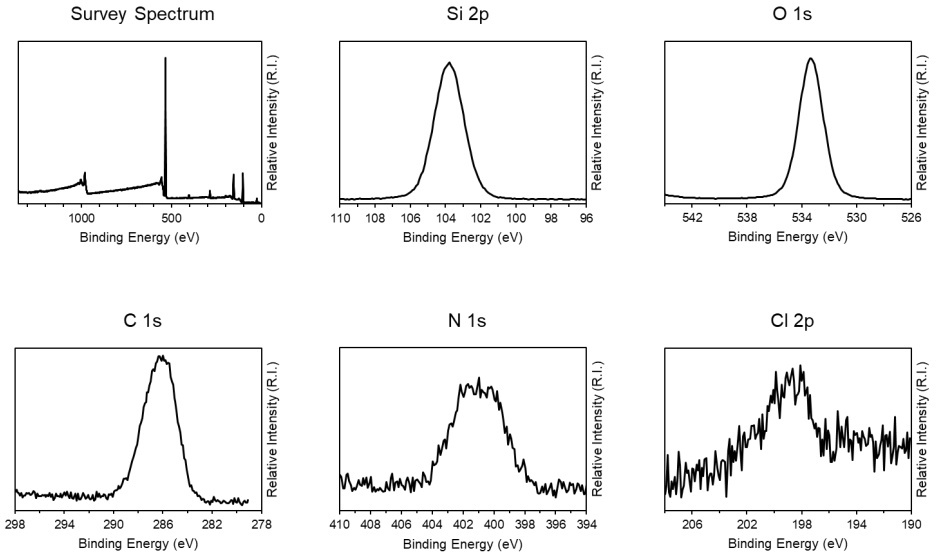

Name	Peak BE	Atomic %
O1s	533.1	56.12
Si2p	103.84	30.22
C1s	286.42	10.66
N1s	402.21	2.64
Cl2p	198.41	0.36

Appendix Figure A.2.1. Survey and HR spectra of mesoporous silica with 8.5 nm pores silica functionalized with an IL-like molecule ([TMS-MIM][Cl]) without the addition of confined [BMIM][Cl].

Theoretical confined IL contribution:

The pores are assumed to be oriented hexagonally with circular pores with a radius *r*, uniform pore wall thickness *t*, and with no IL layer on top. A graphical description of the pore geometry can be found in Figure A.2.2. The area of a single pore is given by equation A.2.1:

$$A_p = \pi * r^2 \qquad (A.2.1)$$

And the total surface area of the pore is given by equation A.2.2:

$$A_T = a * d = A_p + A_w \qquad (A.2.2)$$

Where total area (red dashed lines in Figure A.2.1) is equal to the d-spacing, *d,* multiplied by the pore-to-pore distance, *a*. The values for *d* and *a* are obtained from GISAXS. The pore wall radius, *r*, is obtained from the pore wall thickness, *t*, where $t = a - r$. The thickness is inferred based on values reported in literature. Once A_p and A_w are known, the density of silica (2 g/cm^3) and the IL (1.09 g/cm^3) are used to calculate the mass within the pore wall and center, respectively on a per-unit-depth basis:

$$m_{SiO_2} = A_w * \rho_{SiO_2} * 1\,nm\,;\; m_{IL} = A_p * \rho_{IL} * 1\,nm \qquad (A.2.3)$$

Assuming that the path length of the x-ray is identical between the pore and pore walls, the probe area depth does not need to be considered. The mass is used to find the moles of each species using equation A.2.4:

$$n_{SiO_2} = m_{SiO_2} * MW_{SiO_2} \; ; \; n_{IL} = m_{IL} * MW_{IL} \qquad (A.2.4)$$

Where the molecular weight of silica and the IL is 60.06 and 174.68 g/mol, respectively. The moles of each species are calculated from its formula. For example, one mole of silica (SiO_2) contains one mole of silicon and two moles of oxygen. The relative atomic percentage of each element (X) is then calculated using equation A.4.5:

$$At\%(X) = \frac{n_x}{n_{Si} + n_O + n_C + n_N + n_{Cl}} * 100 \qquad A.4.5$$

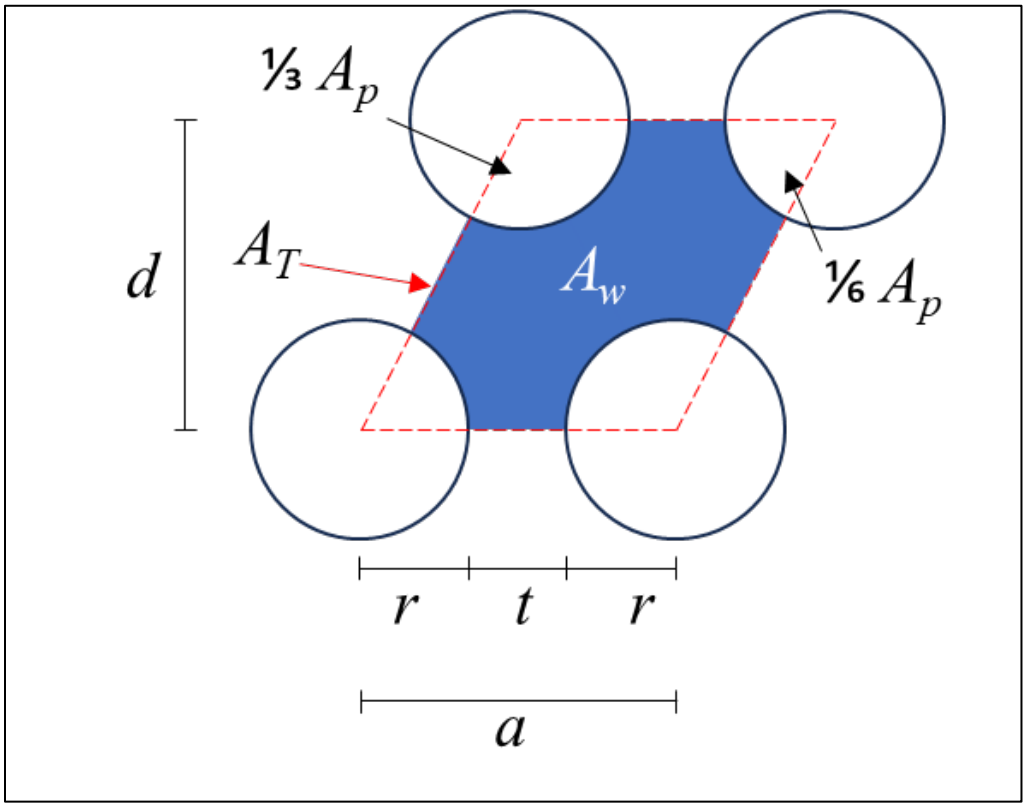

Appendix Figure A.2.2. Geometric description of the hexagonal pore geometry for mesoporous silica films.

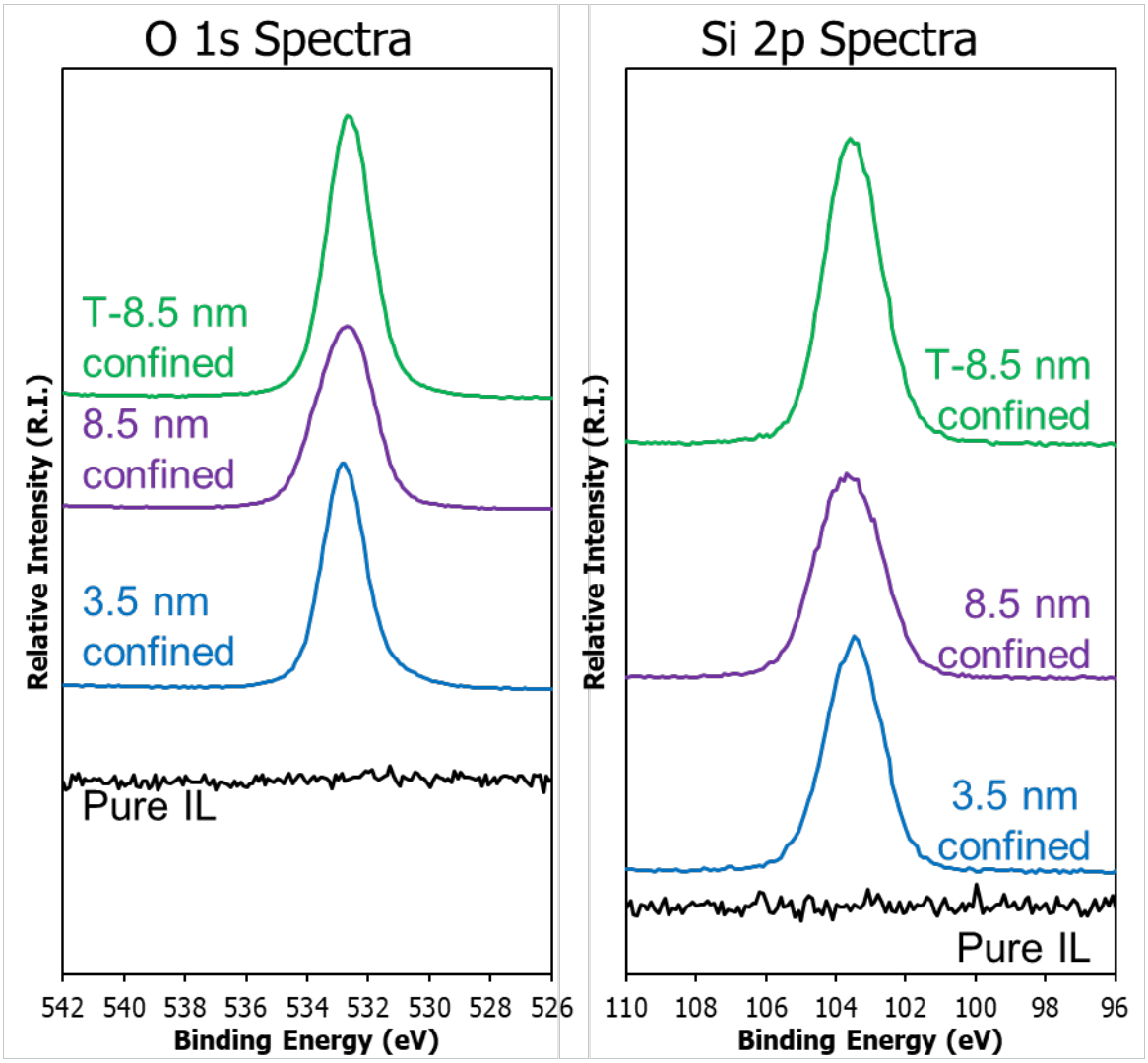

Appendix Figure A.2.3. High resolution spectra for oxygen (O 1s) and silicon (Si 2p) for bulk and confined ILs. From bottom to top is bulk, pure IL (black), confined IL in 3.5 nm pores (blue), confined IL in 8.5 nm pores (purple), and confined IL in tethered-8.5 nm pores (green). The scale of the pure IL has been multiplied 10 times to show that there is no peak present.

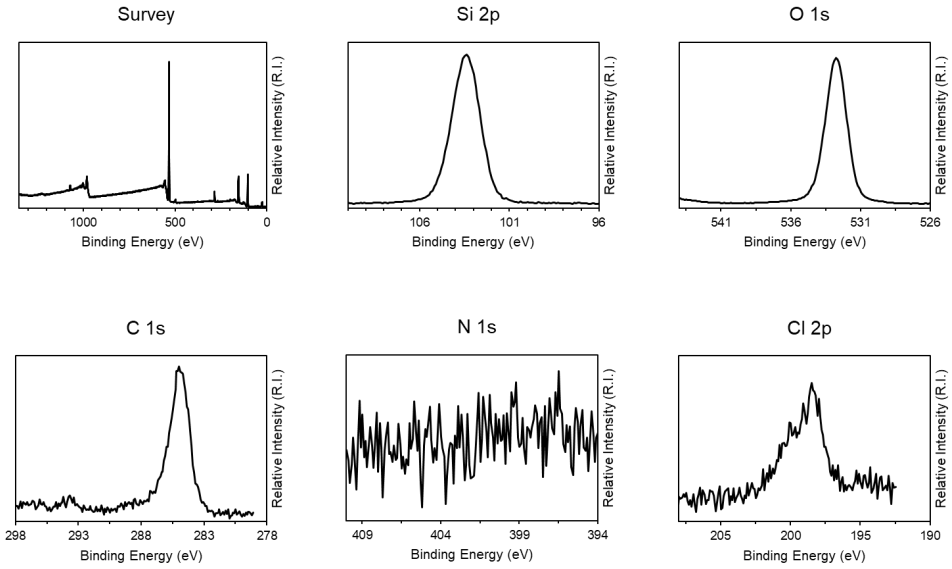

Name	Peak BE	Atomic %
O1s	532.81	57.47
Si2p	103.24	30.15
C1s	285.07	11.28
Cl2p	198.83	1.1

Appendix Figure A.4.4. Survey and HR spectra of the surface of a P123-template thin films (8.5 nm pores) without confined IL.

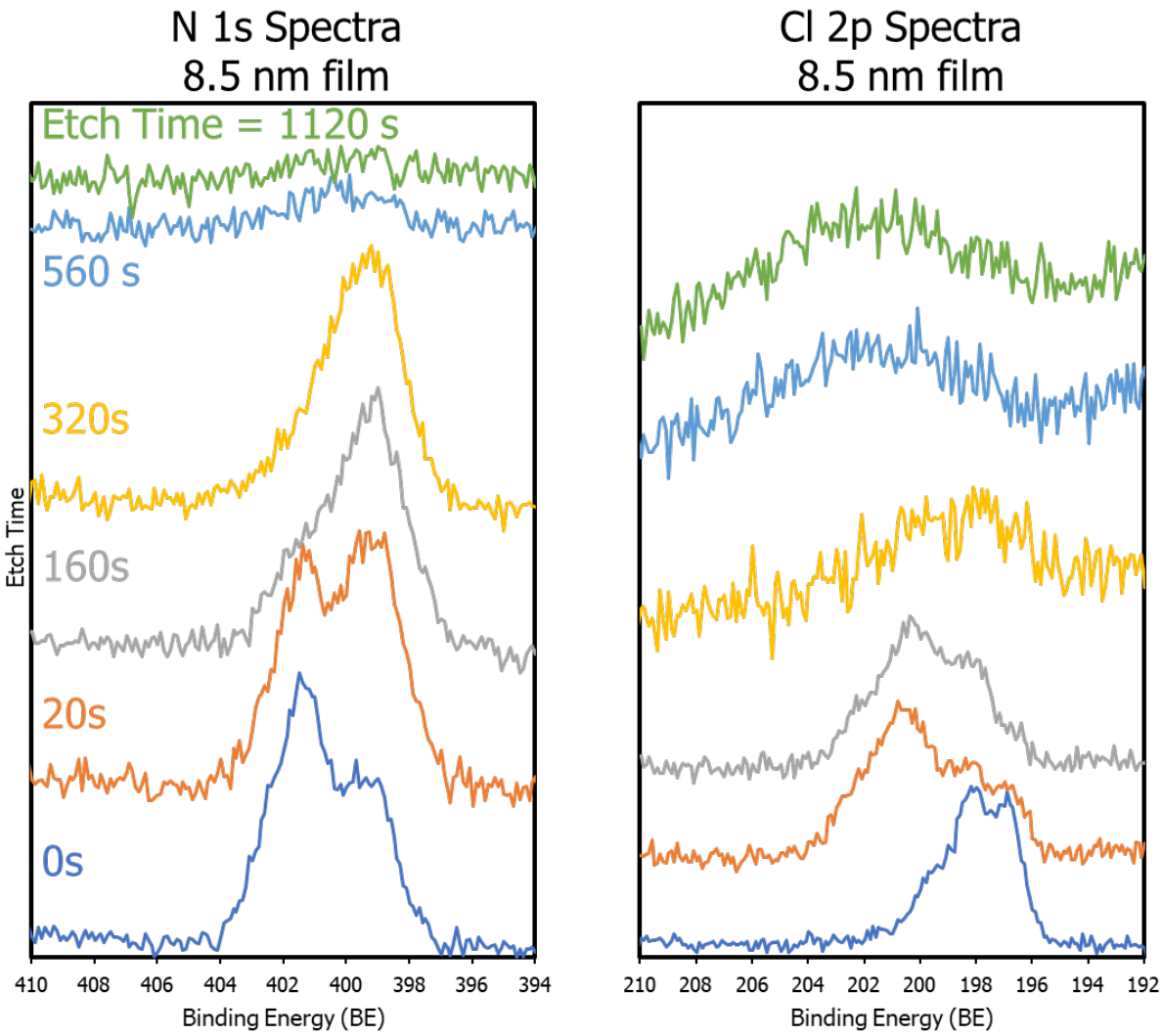

Appendix Figure A.4.5. Depth profiling of high resolution scans of the N 1s and Cl 2p spectra for IL-loaded mesoporous silica films with 8.5 nm pores.

Appendix 3. Supplementary Materials for Chapter 6

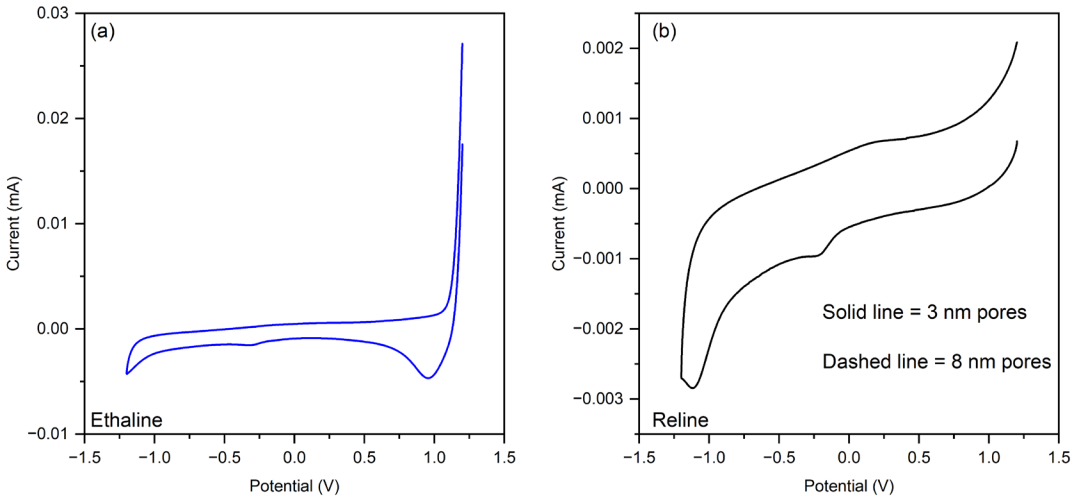

Appendix Figure A.3.1. CV of reline and ethaline without a probe using glassy carbon as the working electrode.

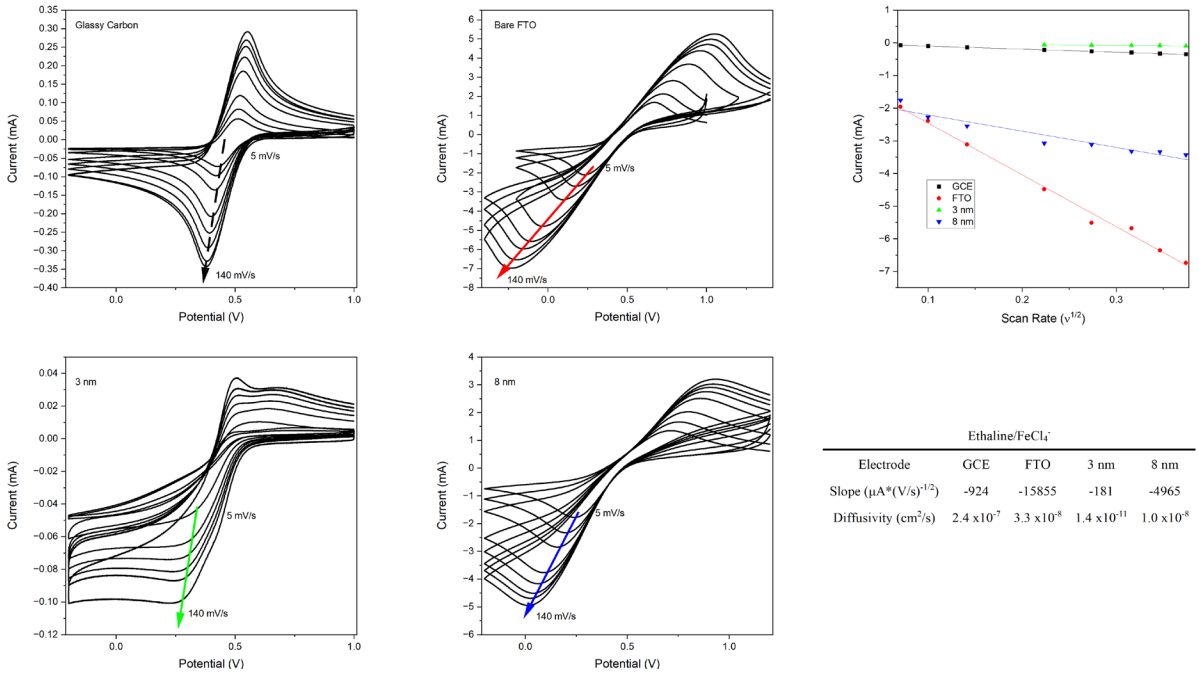

Ethaline/$FeCl_4^-$

Electrode	GCE	FTO	3 nm	8 nm
Slope ($\mu A*(V/s)^{-1/2}$)	-924	-15855	-181	-4965
Diffusivity (cm^2/s)	2.4×10^{-7}	3.3×10^{-8}	1.4×10^{-11}	1.0×10^{-8}

Appendix Figure A.3.2. The Ethaline-$FeCl_3$ system with multiple scan rates using various substrates as the working electrode: glassy carbon, bare FTO glass, and FTO glass coated with 3 or 8 nm mesoporous silica films.

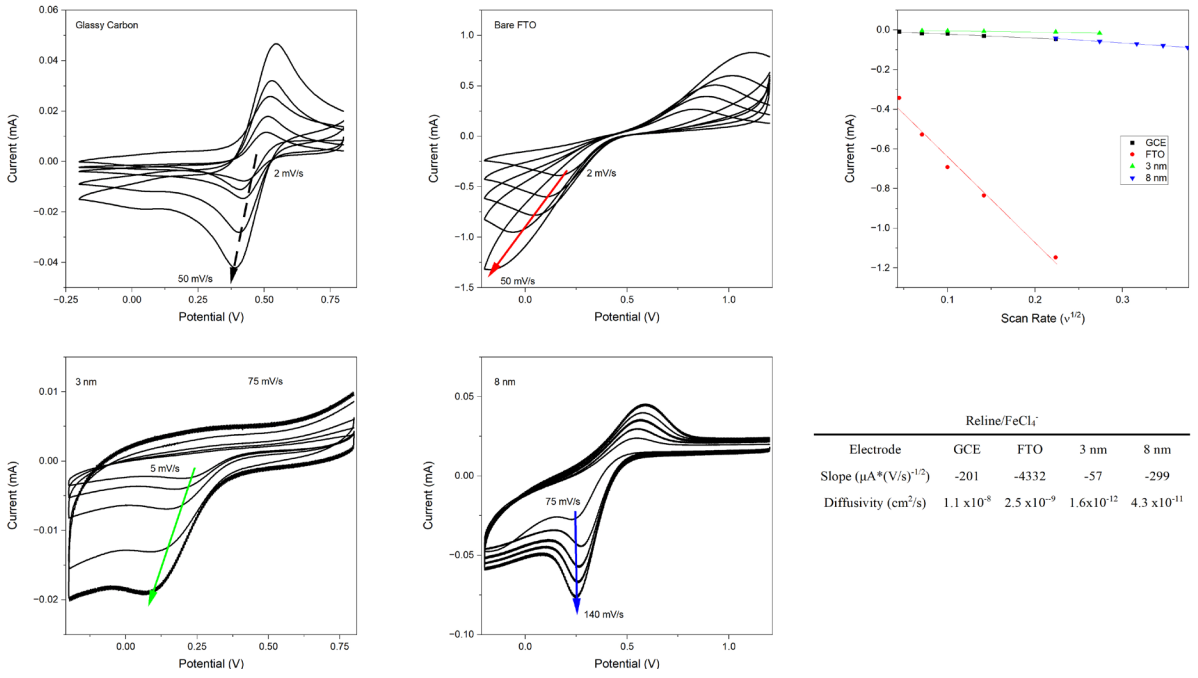

Reline/$FeCl_4^-$

Electrode	GCE	FTO	3 nm	8 nm
Slope ($\mu A*(V/s)^{-1/2}$)	-201	-4332	-57	-299
Diffusivity (cm^2/s)	1.1×10^{-8}	2.5×10^{-9}	1.6×10^{-12}	4.3×10^{-11}

Appendix Figure A.3.3. The Reline-$FeCl_3$ system with multiple scan rates: glassy carbon, bare FTO glass, and FTO glass coated with 3 or 8 nm mesoporous silica films. The GCE scan at 0.01 V/s has been shifted vertically.

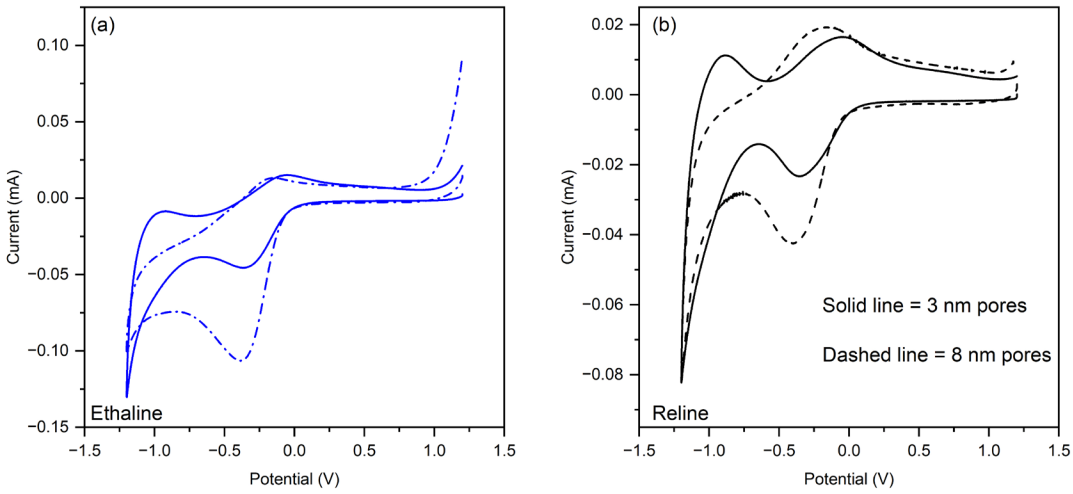

Appendix Figure A.3.4. CV scans of neat (a) ethaline and (b) reline using FTO glass slides coated with mesoporous silica thin films of 3 and 8 nm as the working electrode.

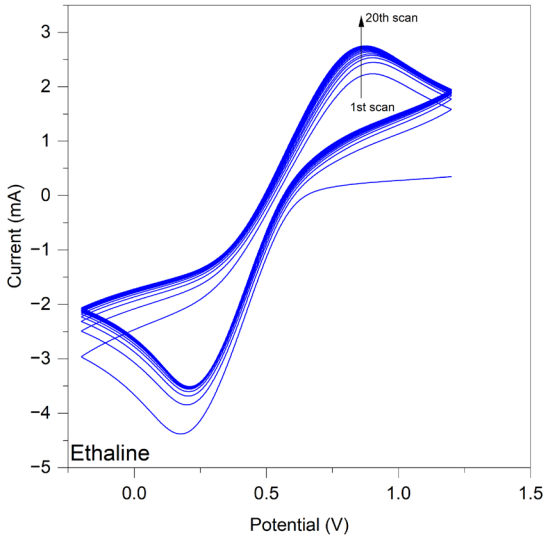

Appendix Figure A.3.5. Multiple CV scans of ethaline/$FeCl_3$ with the 8-nm porous silica FTO electrode as the working electrode.

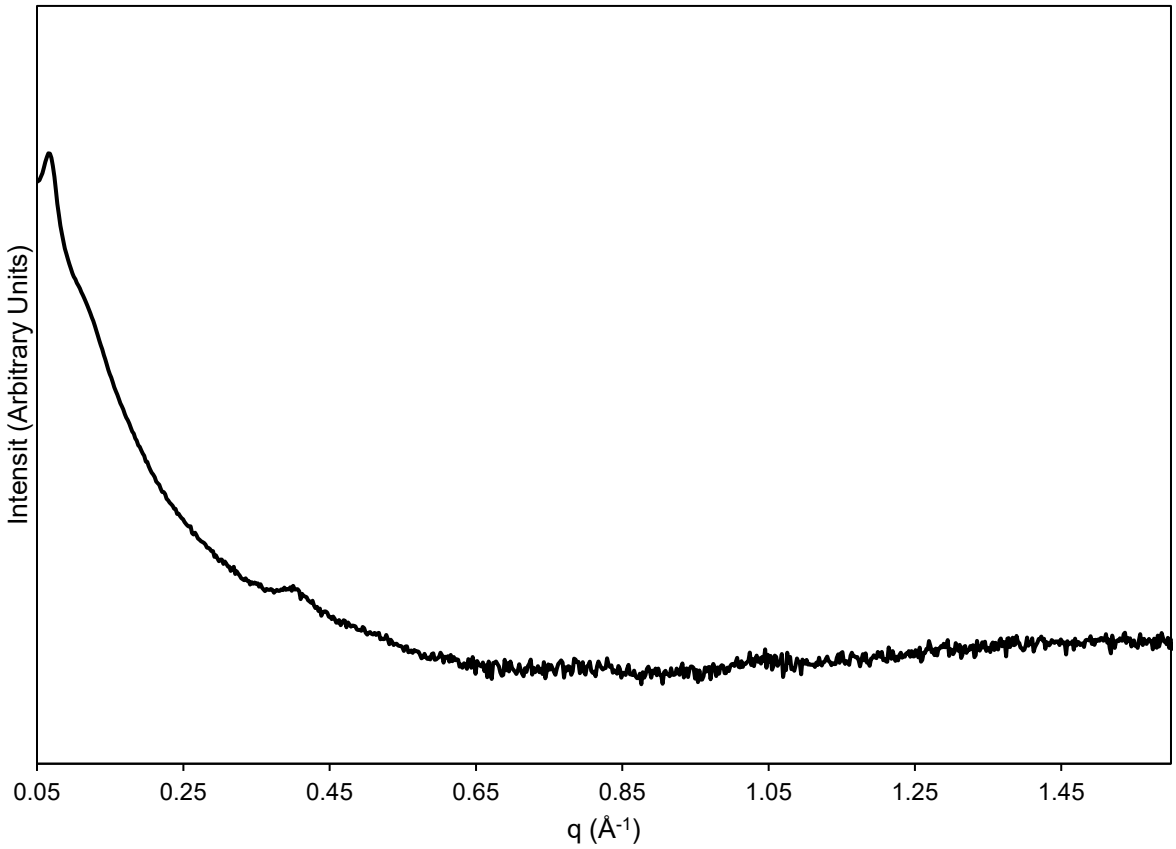

Appendix Figure A.3.6. Azimuthal linecut of wide angle x-ray scattering pattern of reline confined within mesoporous silica nanoparticles.

Appendix 4. In-Situ Synthesis of Tethered Deep Eutectic Solvents

A.4.1 Introduction

Deep eutectic solvents (DESs) are important alternative solvents that have favorable properties of low vapor pressure, high thermal stability, and tunability.[14, 265, 268, 269] DESs are often compared to ionic liquids (ILs) but benefit from being much lower cost and made from greener materials. DESs are distinctly different from ILs because they are made from two components rather than being a single cation/anion pair. They are

characterized by their real eutectic temperature being much lower than the ideal mixture eutectic temperature, and is usually below 100 °C.

DESs, like ILs, are useful in the fields of catalysis, separations, and in batteries.[234-236] While DESs are cheaper to manufacture, their high viscosity makes them difficult to work with in large quantities. Therefore, confinement is used as a method to utilize DESs while making them easier to handle. An example of confined DESs is their use in the adsorption of CO_2 from flue gases.[56, 84, 85] Confinement of DESs also is advantageous for catalysis because there is less likelihood of the DES leaching into the product stream. ILs also suffer from the potential to leach, and an extension of confinement of ILs is to covalently attach the IL to the pore wall. The tethering of ILs has been thoroughly explored in the literature.[141, 142] Tethering is advantageous because the covalent bond between the IL and support further prevents leaching and opens the door to modified surfaces that may interact differently with additional confined ILs.

Tethering could also be beneficial to DES confinement through grafting of one of the components to the surface of a support material. Since DESs are made of two components, one can be grafted to the surface of a mesoporous support and the other added later to create the DES *in-situ*. To our knowledge, there are very few examples of synthesizing a tethered DES.[270] The two components of DESs allow some flexibility by being able to choose which component is grafted first. A common method of functionalizing silica materials is to graft imidazolium groups to the surface, similar to how ILs are grafted. Grafting to silica is typically achieved by using starting materials that have a trialkoxysilane group attached to one side to provide the linkage to the surface. There are a few literature examples of grafting a choline chloride-like group to the surface using

(3-glycidyloxypropyl)trimethoxysilane (GPTS) as a starting material, followed by a ring-opening reaction using trimethylamine.[271, 272] A shorter alternative method for attaching ChCl-like functionality to the surface is to begin with chlorocholine chloride and synthesize the DES, then dispersing silica particles in the DES with heating to complete the reaction.[270] Another choline-like surface modification can be accomplished using N-trimethoxysilylpropyl-N,N,N-trimethylammonium chloride (TMTMAC).[88, 273] This provides a quaternary ammonium group attached to the surface with a slightly longer alkyl group, and neighboring silanols on the surface provide hydroxyl groups similar to choline.

In this study, the ability to tether and synthesize DESs *in-situ* is investigated using mesoporous silica microparticles (pore diameter = 8 nm) as the support. Tethering DESs would allow the synthesis of confined DESs that are more robust to leaching into product streams. Choline chloride is used as the model hydrogen bond acceptor and urea is used as the model hydrogen bond donor. Thermogravimetric analysis (TGA) and FTIR are used to gauge the success of tethering and shows that H-bonds are sufficient to hold the urea in place under mild washing procedures. However, more thorough washing leads to leaching of urea, possibly changing the balance of components required for DES behavior.

A.4.2 Experimental

Mesoporous silica particles are synthesized as described in Chapter 3 and used as the solid support for the tethered DES. The hydrothermal aging temperature used was 125 °C to generate mesoporous silica particles with ≈ 9 nm pores. In all procedures, mesoporous silica microparticles were dried in a vacuum oven overnight prior to functionalization. Three procedures were used to synthesize tethered DESs.

The first procedure for choline-like surface functionalization was based on the work of del Hierro et al.[272] The dried silica particles (0.5 g) was suspended in 7.5 mL toluene, followed by the addition of 0.256 mL (3-glycidyloxypropyl)trimethoxysilane inside of a glove bag. The solution was refluxed with stirring for 48 hours. The particles were filtered and washed with ethanol and dried in a vacuum oven overnight. Since the first step of the procedure was not successful, the second step was not performed, but could be carried out by suspending 0.5 g of the previously made particles into DI water (30 mL), followed by an addition of a solution of trimethylamine (0.35 mL, 4 mmol) in ethanol (0.6 mL). The solution would be stirred and heated at 50 °C, followed by filtration and washing with dichloromethane (2x30 mL), and dried under vacuum.

The second choline-like functionalization procedure was based on the work from Tang et al.[270] First, 200 mg mesoporous silica particles were activated by stirring in 6M HCl overnight, then dried in a vacuum oven for 4.5 hours. Chlorocholine chloride (ClChCl) and urea were mixed in a 2:1 mole ratio and was stirred with heating at 90 °C until melted. 3 g of the ClChCl/urea solution was placed into a flask with 100 mg of dried mesoporous silica particles and heated at 90 °C for 15 hours. The particles were filtered and washed with 75 mL of DI water to remove unreacted ClChCl, then dried in a vacuum oven.

The third functionalization procedure was based on the work by Cao et al.[88] Dried particles (0.2 g) were added to toluene (8 mL) and stirred for 30 minutes. TMTMAC (800 microliters; purchased as a 50% by volume concentration in methanol) was added in a nitrogen glove bag. The reaction was refluxed for 4 hours at 112 °C. The particles were recovered by centrifugation and the toluene was decanted. The particles were washed with

ethanol 3 times and DI water 1 time, followed by vacuum drying at 80°C. The quantity of DES on the surface of the particles was characterized by TGA. Urea was added in a 1:2 ChCl:urea ratio by first dissolving urea into acetonitrile, then adding the appropriate amount of urea to the modified particles. For example, TGA found that there were 0.11 g ChCl/g particles, so for 1 gram of particles, 0.106 g of urea is needed. Urea was dissolved into acetonitrile at 3.56 mg/mL, which is close to the solubility limit. Silica was measured out (9.9 mg) and slight excess of urea solution was used (300 microliters → 1.07 g urea). The particles were sonicated for 90 minutes and either dried to remove acetonitrile or the solvent was decanted followed by drying under vacuum.

Tethered DESs were compared to physically confined DESs in FTIR and TGA. The method for confinement follows the same procedure as with ILs described in Chapter 3. TGA and FTIR were the primary characterization tools for the tethered DESs. The FTIR used was the Thermo Nicolet 470 FTIR. The solid samples were mixed with FTIR grade KBr at ≈ 1% mass sample to 99% mass KBr ratio. The TGA used was a TA Instruments SDT Q600 with a ramp rate of 2.5 °C with a nitrogen atmosphere.

A.4.3 Results and Discussion

Figure A.4.1 shows the FTIR spectra of the DES and its components. The DES component peaks are used as a baseline for comparison to tethered and physical confinement of the DESs. The primary peak of choline chloride is located near 1477 cm^{-1} and is related to -N-CH_3 bending;[88] there are other peaks in ChCl, but they mostly overlap with the broad Si-O bands from the silica after tethering or confinement. In urea, there is a set of peaks located between ≈ 1600 and 1685 cm^{-1} related to asymmetric and symmetric NH_2 stretching and the C=O stretching, and a third peak near 1465 cm^{-1} related to NH

rocking.[246] The resulting DES spectrum is mostly a combination of the two component spectra, but there are a couple of shifts related to hydrogen bonding. In choline chloride, the peak at 1477 shifts to 146 cm^{-1}. The urea peaks near 1600 and 1620 cm^{-1} coalesce into a single peak at 1610 cm^{-1} in urea, while the peak in 1461 cm^{-1} shifts down to 1442 cm^{-1}. These shifts are consistent with hydrogen bonding occurring between the DES components.[246]

The three procedures used were done by trial and error until the choline group could be attached to the surface of the silica. The procedure by del Hierro was not successful. FTIR spectra of the functionalized particles with the trimethoxysilane group only showed C-H stretching modes in the 2900 cm^{-1} region shown in Figure A.4.2. No bands attributed to the glycidoxyl group could be resolved, suggesting little functionalization.

The second procedure by Tang was more successful than the first procedure. The FTIR spectra shown in Figure A.4.3 shows that there are peaks from urea (N-H symmetric and asymmetric stretching at 1633-1662 cm^{-1})[246] and the chlorocholine chloride group (742 cm^{-1}, possible C-Cl), as well as some peaks in the ≈ 1475 cm^{-1} area that could correspond to N-CH_3 bending or chlorocholine chloride. The larger peaks from CH_3 stretching near 2900 cm^{-1} are not present in the tethered silica and the presence of possible C-Cl groups at 742 cm^{-1} indicate that the tethering procedure may not have worked as anticipated. Reline was confined in the tethered particles and the spectrum is also shown in Figure A.4.3. The confined reline in the tethered system shows that there are small shifts in the choline chloride peak (1446 to 1450 cm^{-1}, N-CH_3 bending) and urea peaks (1620 to 1622 cm^{-1},) that could be due to interactions between the pore wall and the DES. The low amount of

DES present indicates that the reaction may not be complete, and further work would be needed to establish conditions to complete tethering, so a more direct method was used.

The third procedure is the most direct and shortest procedure for tethering ChCl to the surface of the silica. In the particles modified with ChCl, the -N-CH_3 peaks in Figure A.4.4 appear near the same location as in ChCl showing that the tethering procedure was successful, although they are shifted to slightly higher wavenumbers by less than 10 cm^{-1}. The addition of urea was done by mixing the tethered DES particles with a solution of urea, and the urea solution was either dried directly on the particles or decanted after mixing and then dried. The FTIR spectra for both urea additions were similar, so the decant method is shown here to demonstrate the strength of the interaction between urea and ChCl during mixing that holds urea in place. After the addition of urea, the three peaks related to urea (≈1455, 1625, and 1670 cm^{-1}) appear in the tethered system. This shows that the tethering and *in-situ* synthesis of the DES contained both components of the DES. Compared to the physically confined DES, the peaks for the tethered system are found in the same locations. The NH scissoring motion of the urea is slightly shifted down to lower wavenumbers with both tethering and confinement and is likely from H-bond interactions between the urea and ChCl.

The tethered system was further characterized by TGA. The derivative of the mass loss with respect to temperature (known as derivative TGA or DTG) is plotted against the temperature to find the maximum rate of change of thermal degradation since it could be used to identify when specific components are degraded. The DTG curves of the confined reline, unconfined reline, and ChCl at a ramp rate of 2.5 °C/min are shown in Figure A.4.5. Choline chloride has a single decomposition step with a peak decomposition temperature

at 298 °C. The decomposition for urea using a ramp rate of 10 °C/min happens in two stages – one at ≈ 210 °C[85] and the second at ≈ 320 °C[85] because urea first forms ammonia, cyanic acid, biuret, and other species that degrade in the 2nd decomposition step, although the position of the decomposition peaks can depend on the ramp rate used.[264] In the confined reline, the first large peak near 199 °C is related to the first step of urea decomposition. There are 3 other peaks that overlap in the 2nd step, with peaks at 245, 255, and 272 °C. Urea will likely form more products as it is heated and decomposes at higher temperatures which could explain the peak at 272 °C. The reduction in decomposition temperature is commonly observed in DESs.[85] When confined, the reline decomposition temperatures are further lowered to 172 and 233 °C because the new interactions with the surface of the silica through H-bonds weaken the H-bond network of the DES.[85]

The DTG curves of the tethered system are shown in Figure A.4.6. After tethering, a new peak appears at 227 °C consistent with the degradation of choline chloride tethered to the surface. There is also another broad peak at 475 °C that could be residual tethered carbon on the surface of the silica. After urea is added to the tethered particles, a new peak appears at 160 °C and the peak related to the tethered choline group shifts down slightly to 220 °C. The shift of the ChCl peak to slightly lower decomposition temperature is consistent with DES formation and confinement, and therefore indicates that the DES is formed *in-situ* on the surface of the silica. Urea was adsorbed onto bare silica particles to compare the thermal stability of physically adsorbed and a DES modified surface. The decomposition temperature of the physically adsorbed urea was 163 °C. Since urea is hypothesized to be the primarily at the surface of silica materials and can H-bond with silanols present on the surface,[56] it would make sense that the decomposition temperatures

are relatively similar because H-bonding between urea and ChCl is similar to the H-bonding with silica.

A.4.4 Conclusion

Reline was tethered and synthesized *in-situ* on the surface of mesoporous silica microparticles and characterized by FTIR and differential TGA. The FTIR spectra of tethered choline chloride showed that the characteristic peaks of $N\text{-}CH_3$ were present after the tethering procedure. DTG also showed that the peak related to choline chloride degradation was present in the tethered system. Urea was added to the tethered choline chloride by mixing the tethered particles with a urea solution for a short amount of time. The strong hydrogen bonds between urea and choline chloride kept the urea in place on the surface with the choline chloride to form the DES. The presence of urea was demonstrated by its FTIR peaks appearing and the decomposition peak appearing in DTG. The ability to tether and synthesize a deep eutectic solvent *in-situ* on the surface of a host support is a powerful method to utilize DESs while minimizing their leaching.

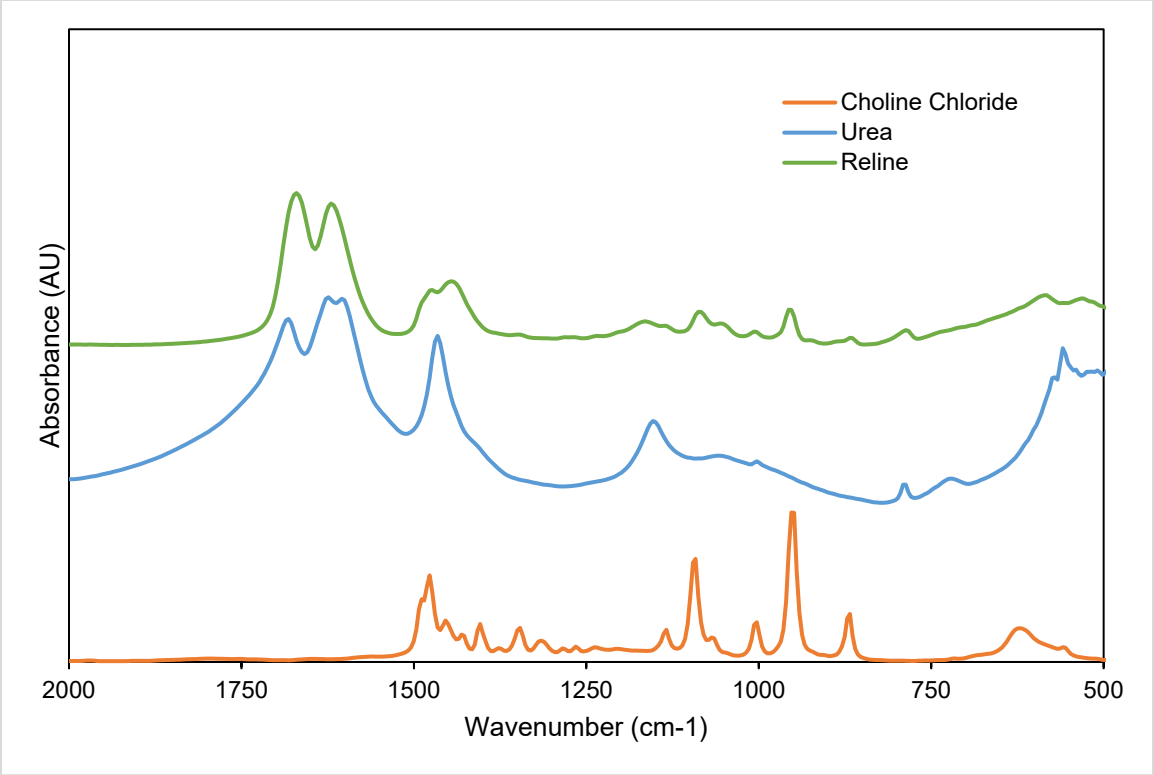

Appendix Figure A.4.1. FTIR spectra of reline and its components: choline chloride and urea.

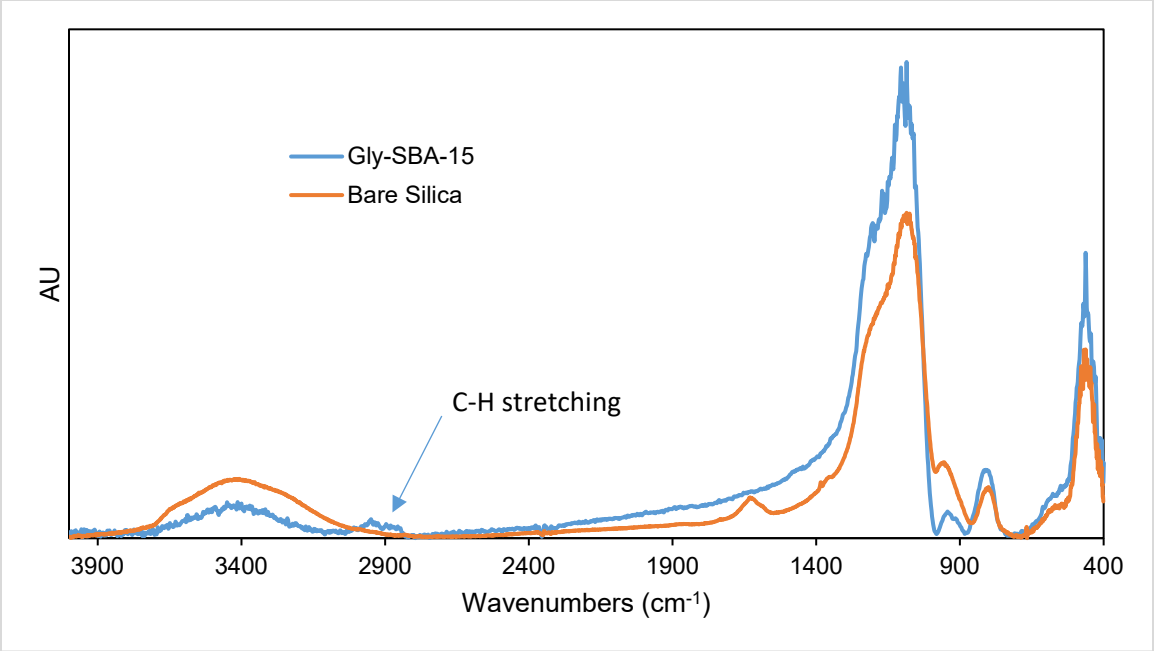

Appendix Figure A.4.2. FTIR spectra of GPTS functionalized mesoporous silica particles (Gly-SBA-15) from the first functionalization procedure.

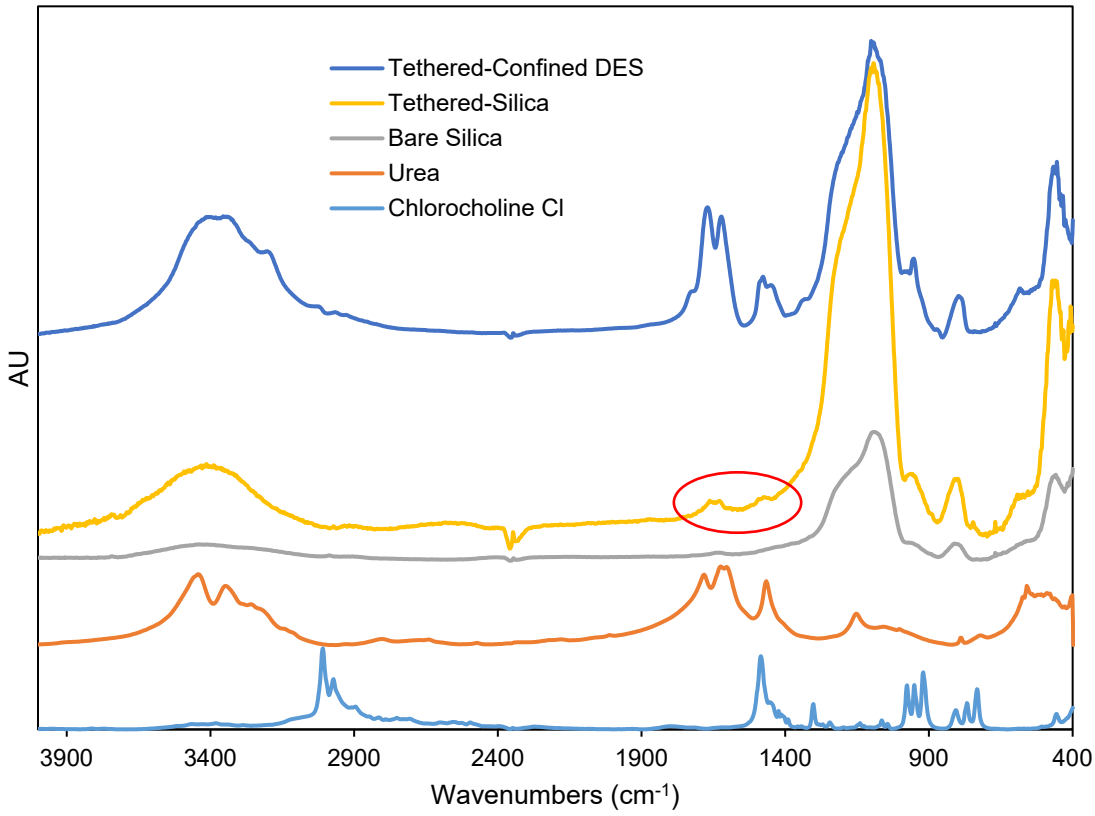

Appendix Figure A.4.3. FTIR spectra of the DES components for the second tethering DES procedure and the silica before and after tethering. Additional IL was confined within the tethered DES system (top blue line).

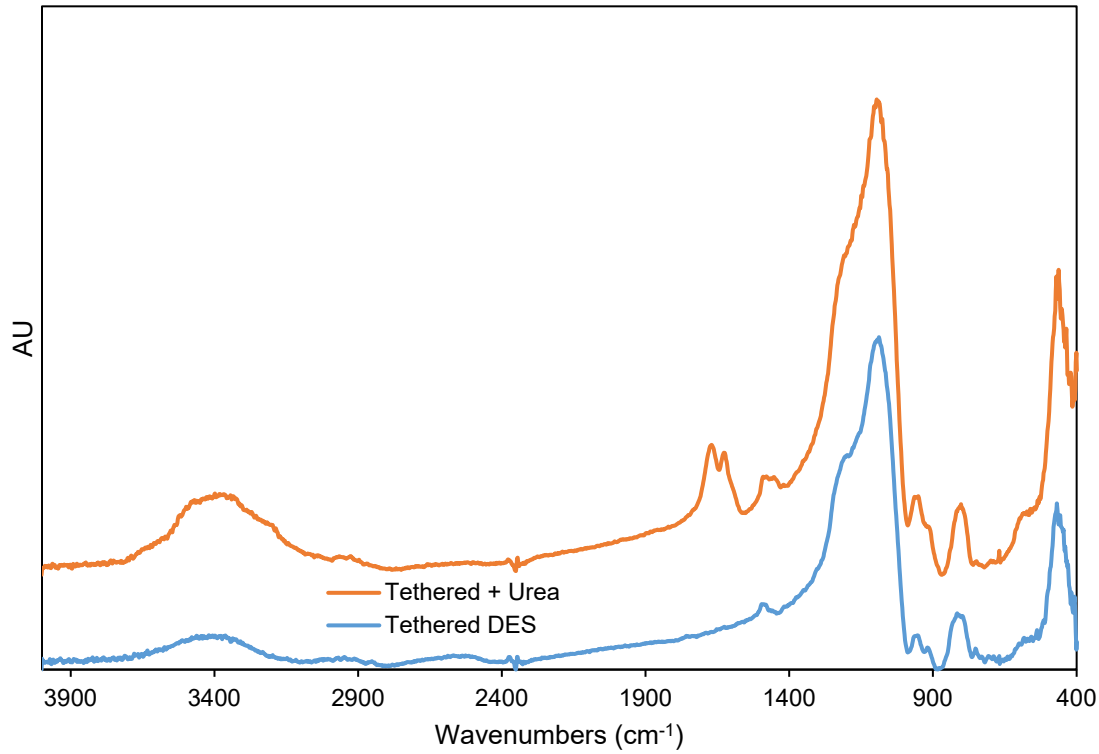

Appendix Figure A.4.4. Mesoporous silica microparticles tethered with a choline chloride group using the Cao procedure (bottom, blue) and with urea added to the tethered ChCl (orange, top).

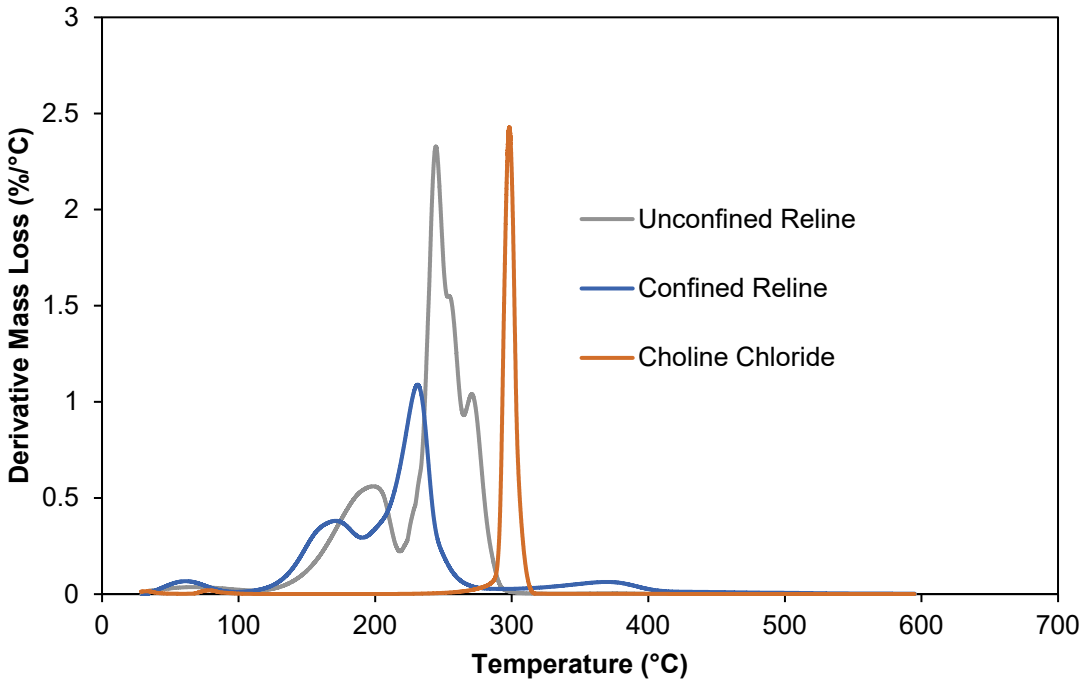

Appendix Figure A.4.5. Differential TGA (DTG) curves of choline chloride, reline, and confined reline.

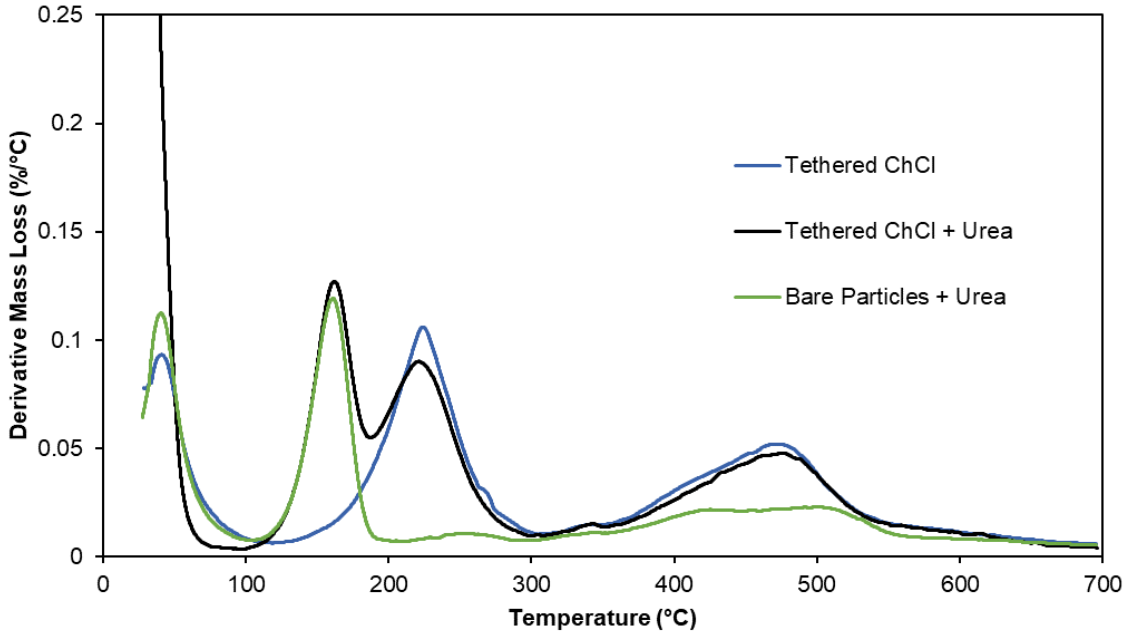

Appendix Figure A.4.6. DTG curves of the silica particles with tethered ChCl on the surface (blue), the tethered DES + urea (black), and urea physically adsorbed on the surface of silica (green).

Appendix 5. Degradation of Melanoidins using Mesoporous Titania Thin Films

A.5.1 Introduction

Melanoidins are a class of organic compounds that are generated from the Maillard reaction.[274-276] The Maillard reaction occurs between reducing sugars and amino acids, peptides, or proteins, and is responsible for the characteristic brown color in many foods.[276] The brown-colored melanoidin products of this reaction are heterogeneous and absorb light at wavelengths as high as 420 nm.[276] Melanoidins are generated in significant amounts in the industrial distillation and fermentation processes for ethanol, amino acid, and yeast production.[274] When released into bodies of water, they cause oxygen depletion and significantly increase the biological oxygen demand (BOD), and in soil they reduce alkalinity and manganese availability as well as inhibit seed germination.[275]

Currently, the methods to remove melanoidins from wastewater include electrocoagulation,[277] adsorption,[278] and catalytic degradation,[275] among others.[279] These methods are effective at removing melanoidins from wastewater but usually have high costs or space requirements, and can generate their own waste and sludge.[279] While biological methods can sometimes be effective to partially remove melanoidins, they do not remove the color from the water, and this still creates challenges in the ability of sunlight of appropriate wavelengths to reach beneficial microorganisms.[279] Therefore, effective melanoidin removal and decolorization techniques that require less equipment volume and lower costs are needed.

Photocatalytic oxidation of melanoidins is an effective method to clean wastewater from distilleries but may require significant space to perform. The oxidation of melanoidins using ozone and hydrogen peroxide has shown that they can be valorized into useful products such as polyols, diacids, and amino acids.[280, 281] Titania (titanium dioxide) has been investigated as a material for the decolorization of melanoidins in biorefinery waste.[282] Titania is readily available, low cost, and simple to synthesize. Titania thin films on a variety of substrates can be synthesized via evaporative induced self-assembly to create mesoporous titania and increase the surface area available for oxidation.[283]

In this work, mesoporous titania thin films cast onto glass slide substrates are investigated for the photocatalytic degradation of melanoidins. Preliminary experiments showed that modifying titania with dopamine sensitized the titania films to produce photo-oxidative current when blue visible light (455 nm) was shone on the films.[284] We hypothesize that melanoidins will adsorb to titania and behave in a similar way and lead to loss of color of the melanoidin solution and loss of photocatalytic activity as the melanoidins lose color. We first investigate the reaction progress through decolorization by monitoring the UV-vis absorption over time while the melanoidins are exposed to a UV LED. Titania films are also cast onto fluorine doped-tin oxide glass slides and characterized using cyclic voltammetry to further investigate the degradation process.

As part of the project, we also investigated the ability of mesoporous titania films to catalyze the cleavage of lignin dimers (another complex biologically derived copolymer) for valorization. The products of lignin depolymerization are thought of as "platform compounds" that are useful for the entire chemical industry and will lower dependency on oil.[285] Lignin is held together by ether bonds and can be broken down into lignin

monomers. Electrooxidation of lignin dimers was investigated with preliminary experiments near the end of the melanoidin project. It was recently shown that guaiacylglycol β-guaiacyl ether was able to be slowly oxidized by laccase enzymes.[286] We hypothesized that mesoporous titania films would be able to more sustainably oxidize lignin and that their reactivity could be monitored by cyclic voltammetry.

A.5.2 Experimental

Mesoporous titania films were synthesized via the sol-gel method similar to silica films.[283] First, a closed humidity chamber was made by placing an open beaker full of DI water into a glass container, which was then placed into a refrigerator to cool. Glass slides were cleaned in NoChromix or by sonication as described in Chapters 4 and 6. FTO slides were cleaned by sonicating first in DI water, then acetone, and then isopropanol for 30 minutes each, followed by UV-ozone cleaning for 20 minutes. The titania sol was prepared by suspending 0.67 g of Pluronic F127 (a triblock copolymer) into 18.43 g of anhydrous ethanol. After stirring for 10 minutes, the solution was placed into a nitrogen-filled glove bag where titanium tetrachloride (1.12 mL) was added, followed by 10 minutes of stirring. DI water (1.8 g) was slowly added to this solution and the solution was stirred for 10 additional minutes. The cleaned substrates were dip-coated in the solution at a rate of 6 cm/min, then immediately placed into the previously prepared humidity chamber (≈94% relative humidity) in a refrigerator at 4 °C for 2 hours. After aging, the titania films were calcined in a muffle furnace at 350 °C for 10 minutes with a ramp rate of 25 °C/min. The transfer to the oven was done quickly to avoid condensation on the substrate surface. The titania films were cooled rapidly after the furnace using pressurized air.

Melanoidins were synthesized using two different procedures. In one, a PBS tablet was dissolved in 100 mL of DI water, as per PBS tablet instructions. After the PBS tablet dissolved, the melanoidin precursors D-glucose (3.6032 g, 0.2 M) and glycine (1.5037 g, 0.2 M) were dissolved into the solution. The solution was then heated in a silicone oil bath at 100 °C under reflux with stirring for 18 hours (unless otherwise indicated). The solution was then removed and allowed to cool to room temperature. A second procedure was used following a procedure by Bernardo et al.[287] First, 0.42 sodium bicarbonate (0.25 M), 4.5 g D-glucose (0.25 M) and 1.88 g glycine (0.25 M) were dissolved in 100 mL water. After the components were dissolved, the solution was heated for 7 hours at 95 °C and diluted if needed. The results presented for UV-vis kinetics and cyclic voltammetry (Figures A.4.2 to A.4.5) use the first procedure, but it should be noted that there are several methods to produce melanoidin compounds and the second was used for exploratory experiments.

UV-visible spectrometry (Hewlett-Packard 8453) was used to monitor the degradation of the melanoidins over time. The melanoidins were typically too concentrated to observe significant adsorption/degradation, so they were diluted to be within the linear range of UV-vis. The absorption at 420 nm was used to quantify the relative concentration of the melanoidins over time. In a typical setup, 25 mL of the melanoidin solution was placed into a narrow cylindrical beaker. Mesoporous titania films on glass slide substrates (1 or 2 slides) were lowered into the solution. The catalytic degradation was done by exposing samples to a UV lamp (ThorLabs M365LP1-C1, 365 nm) placed close to the reaction vessel (<1 cm) over a 4 hour time period. A 1 mL aliquot was measured by UV-vis and replaced every 30 minutes.

Cyclic voltammetry (CV) was performed using a CH Instruments 660D Electrochemical Workstation. The reference electrode was an aqueous Ag/Ag^+ electrode and a platinum wire was used as the counter electrode. The titania-coated FTO slide was used as the working electrode. CV scans began from -0.1 V and swept down to -1 V, up to +1 V, and back down to -0.1 V for a total of 3 scans. The melanoidin solution was diluted by a factor of 1/16 the original concentration and 0.1 M sodium acetate was added after dilution as a supporting electrolyte. The solution volume was 25 mL and the CV curves were obtained with and without a UV lamp.

The lignin dimer employed for this study is not very soluble in water, so a non-aqueous electrolyte solution was used. Acetonitrile was used as the solvent and $NaClO_4$ (0.1 M) was used as the supporting electrolyte. The working and counter electrode were the titania film and Pt electrodes as with melanoidins. The reference electrode was a solution of $AgNO_3$ (0.01 M) and $NaClO_4$ (0.1 M) in acetonitrile. The lignin used was guaiacylglycerol β-guaiacyl ether (lignin GG dimer) and was dissolved into acetonitrile at a concentration of 2 mM for electrochemical experiments.

The films were characterized prior to use using GISAXS as in Chapters 3-6. The beam characteristics remain the same but the sample to detector distance was set at 1.01 meters. SEM images of the films were obtained using an FEI Helios Nanolab 660 at 2 kV. The titania films were directly imaged with SEM without gold or platinum coating since titania is conductive.

A.5.3 Results and Discussion

Appendix Figure A.5.1 shows a representative SEM image and GISAXS pattern of the mesoporous titania thin films deposited onto glass slides. The patterns feature spots to

the left and right of the beam stop indicating in-plane diffraction, and vertical streaks consistent with a vertically compressed cubic mesopore structure.[283] The peaks in GISAXS are located at ≈ 0.45 nm^{-1}, giving pore-to-pore distances of ≈ 16 nm assuming hexagonal geometry. The spacing between centers of pores in the SEM images is ≈ 15 nm, which is close to the value from GISAXS. The pore wall measured in SEM is close to 7 nm giving a pore diameter of 8-9 nm and is slightly larger than previous values of 7 nm pores with 5.5 nm pore wall thickness.[283]

The normalized concentration of the melanoidins was compared by dividing by the initial absorbance recorded at 420 nm using UV-vis. The melanoidins used were diluted 16x from their original concentration to be within the linear range of UV-vis. Figure A.5.2 shows the normalized concentration of the melanoidins without exposure to UV light both with and without a titania film. Without a film or light, the concentration of the melanoidins does not change significantly. It also remains unchanged when a titania film is submerged within the solution. The unchanging concentration without light shows that the melanoidin compounds do not adsorb significantly onto the titania surface.

The effect of using UV light to drive the photooxidation of melanoidins is presented in Figure A.5.3. The UV light alone is sufficient to cause the photooxidation of melanoidins and reduces the concentration by 39% after 4 hours. With the titania films, the concentration of melanoidins is reduced by 44% after 4 hours. The modest increase in photooxidative activity is caused by the titania films. When UV light impinges on the surface of the titania, an electron-hole pair is formed. The electron can react with oxygen in the water to form radicals. Radicals are highly reactive and will react with the melanoidin compounds,[288] breaking apart the large chains that make them up. A similar

effect is observed for other organic dyes, but adsorption of a cationic dye such as a commonly used methylene blue helps to promote interaction of the dye with locally produced radicals.[283] While the color of the solution is only slightly reduced by using titania films, the valorized products may be still within the solution.

The greatest rate of change was observed in the first 60 minutes of the reaction. Between 60 and 180 minutes has a slower rate of change but is constant over that time. The slowest rate of change was observed after 180 minutes. The first order rate constants of the degradation were compared through the slope of the negative natural log of the normalized absorbance over time and the data is presented in Figure A.5.4. The data follow first order kinetics well for both autophotolysis and titania-driven photocatalysis. The rate constant of the melanoidins exposed to UV light with the titania film (0.113 hr^{-1}) is faster than without the film (0.0104 hr^{-1}), demonstrating that the titania films are able to catalyze the degradation of the model melanoidins. Assuming that photocatalysis occurs in parallel with autophotolysis, the titania-induced rate coefficient is 0.009 hr^{-1} under the conditions of the experiment.

Cyclic voltammetry was used to further characterize the degradation of the melanoidins under UV light. Sodium acetate was used as a supporting electrolyte and the melanoidins were diluted 16x to maintain similarity to the UV-vis experiments. The cyclic voltammograms of the electrolyte solution with and without melanoidins are compared in Figure A.5.5. Both with and without the titania, an irreversible reduction peak is observed. When the melanoidins are added, the location of the peak shifts from -0.8 to -0.7 V. Interestingly, there are no peaks related to oxidation which is the hypothesized degradation pathway for melanoidins. This may be because there is not a strong driving force for

adsorption of melanoidins to the oxide electrodes (FTO and titania) in the experiment. Melanoidins are large polymers that do not have a very well defined structure, so it is difficult to hypothesize the pathway of their oxidation. The current in all curves decreases with additional sweeps, which could indicate the lower concentration of melanoidins over time. Melanoidin degradation could be further characterized by comparing normalized current over time using chronoamperometry curves or electrochemical impedance that may give more insight into the mechanism of melanoidin degradation.

A.5.4 Lignin Cleavage by Mesoporous Titania

Lignin is a valuable and abundant resource and can be degraded to create many chemicals through valorization. The strength of the ether bonds between lignin monomers, β-O-4, β-5, or β-β, hold together lignin and is good for plant durability, but this stability also makes it difficult to break down lignin for other uses. Cyclic voltammetry was used to characterize the degradation of the model lignin GG dimer. For comparison to literature, platinum wire electrodes were used as both the working and counter electrodes first. Figure A.4.6 shows the cyclic voltammetry curves for 5 cycles of the lignin GG dimer. Reduction peaks appear at ≈ -0.55 V and near 0 V, while an oxidative peak is found at 0.45 V. This peak matches the peak for this compound reported using a similar electrochemical setup.[286] The cyclic voltammograms over 5 cycles using mesoporous titania coated FTO as the working electrode is shown in Figure A.5.7. Interestingly, there is significant reduction and oxidation of the solvent beginning before 0 V in the reduction sweep and before 0.5 V in the oxidation sweep. The peaks related to lignin degradation seem to have disappeared from the curves. The lack of peaks could indicate that titania is not as effective for the cleavage of lignin dimers under the conditions used.

In the future, a mediator could be used to facilitate the electron transfer between the titania and the lignin dimer. The key to lignin cleavage is to oxidize the alpha or gamma carbons, which severely weakens the C-O in the β-O-4 linkage and allows it to be cleaved more easily.[289] The use of a mediator is a common strategy for the oxidation of lignin dimers, with TEMPO being a popular choice.[289-291] It could be that lignin is not very attracted to the surface and is resistant to oxidation. The mediator would be beneficial because it is able to undergo a redox reaction and transport electrons more easily to the lignin dimers.

A.5.5 Conclusion

The degradation of model melanoidin compounds using mesoporous titania thin films and UV light was investigated using UV-vis and cyclic voltammetry. The results show that there is a small increase in the degradation ability when using titania when the concentration is low enough for the light to penetrate the solution. The rate constant is improved when using titania films, but the melanoidins are still effectively destroyed by simply using UV light. Cyclic voltammetry shows that there are some changes to the reduction characteristics when melanoidins are added, but a more thorough investigation is necessary to better understand the electrochemical system. Additionally, the products of the oxidation after photocatalysis should be characterized for possible valorized product formation. This work shows that there is room for improvement for using titania in the photooxidation of melanoidins. The catalytic activity of the titania could be improved by doping the titania with other additives such as nitrogen.[283] Lignin was not successfully oxidized using a bare titania film and applied voltage, but future works using a mediator to efficiently transport electrons to the lignin could be a better route for lignin cleavage.

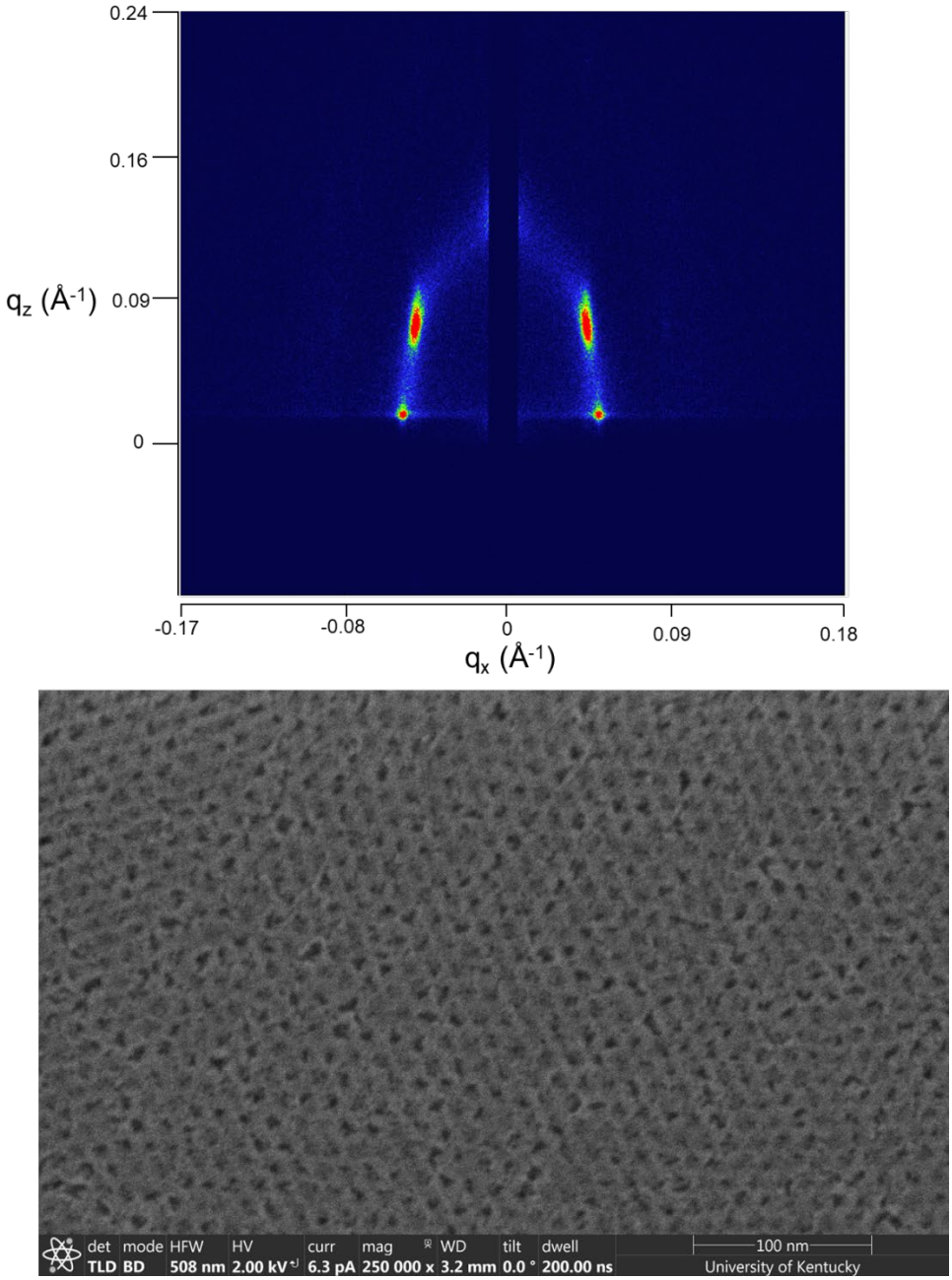

Appendix Figure A.5.1. Representative 2-D GISAXS pattern and SEM image of mesoporous titania film deposited onto a glass slide.

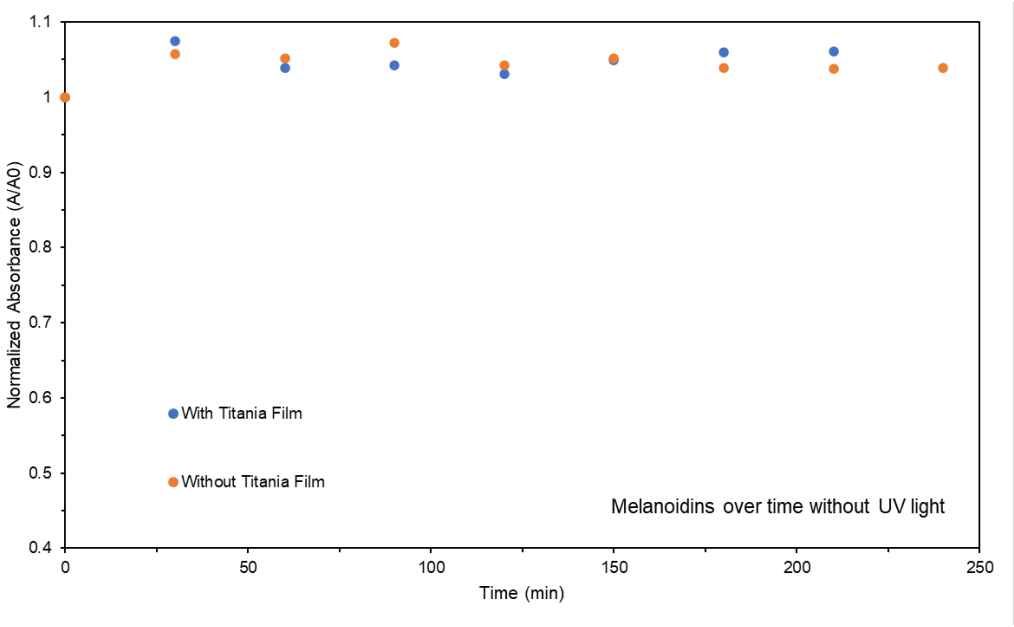

Appendix Figure A.5.2. Relative melanoidin concentration over time without UV light illumination either with or without a titania film.

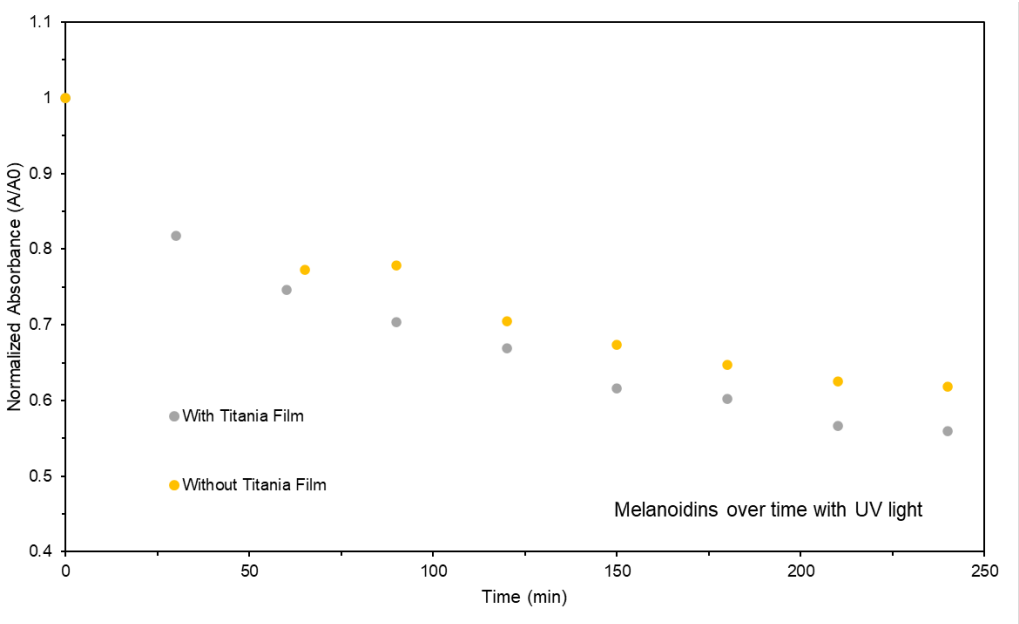

Appendix Figure A.5.3. Relative melanoidin concentration over time with UV light illumination either with or without a titania film.

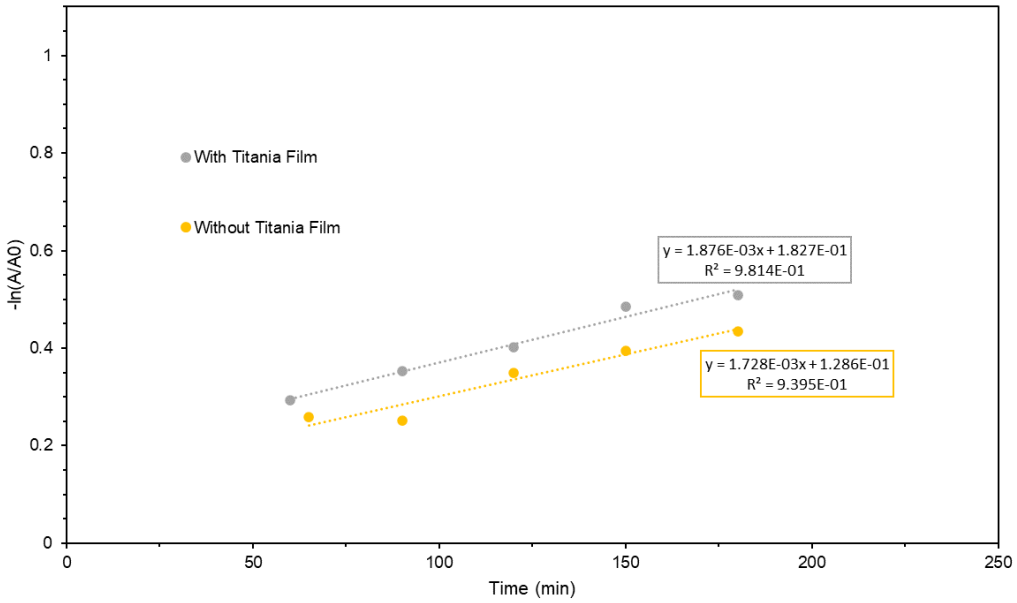

Appendix Figure A.5.4. Natural log of normalized absorbance between 60 and 180 minutes of melanoidins exposed to UV light.

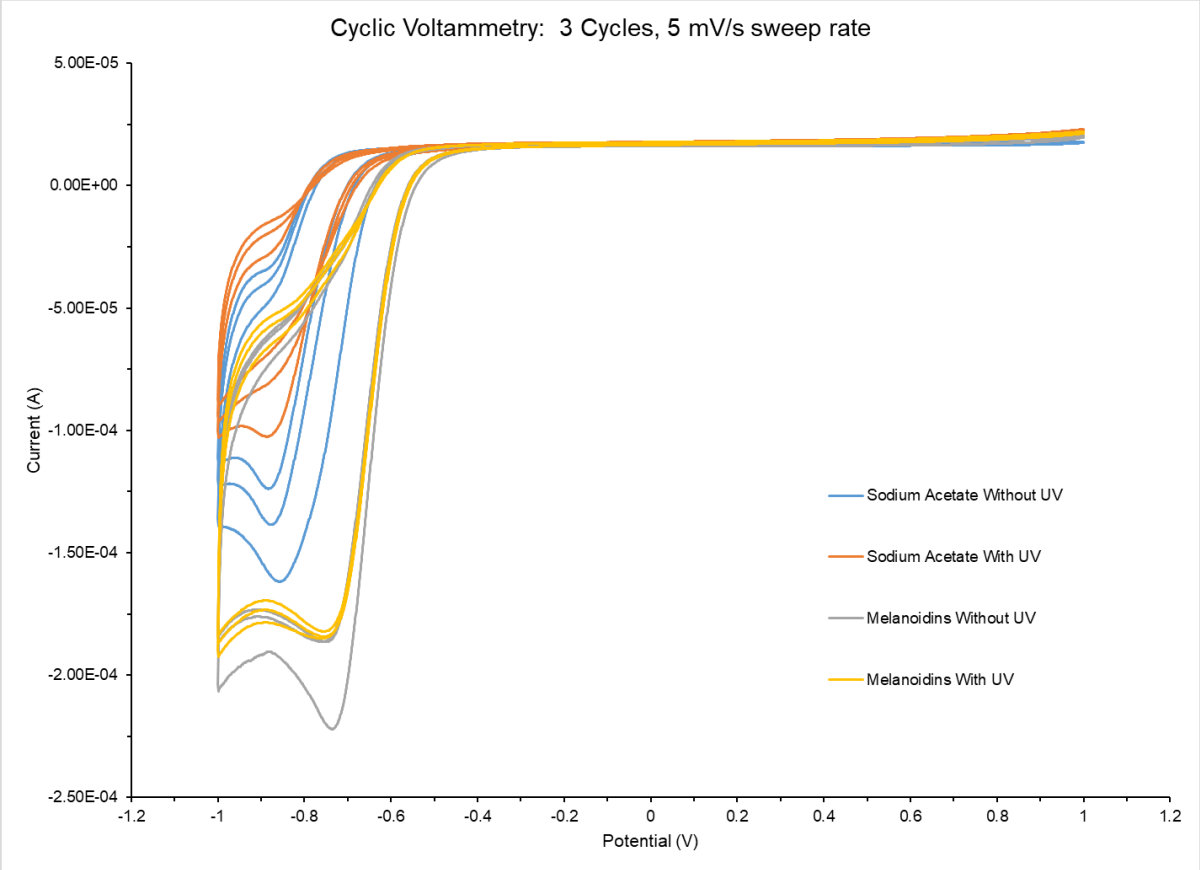

Appendix Figure A.5.5. Cyclic voltammetry sweeps of melanoidin system using an FTO electrode coated with a mesoporous titania thin film.

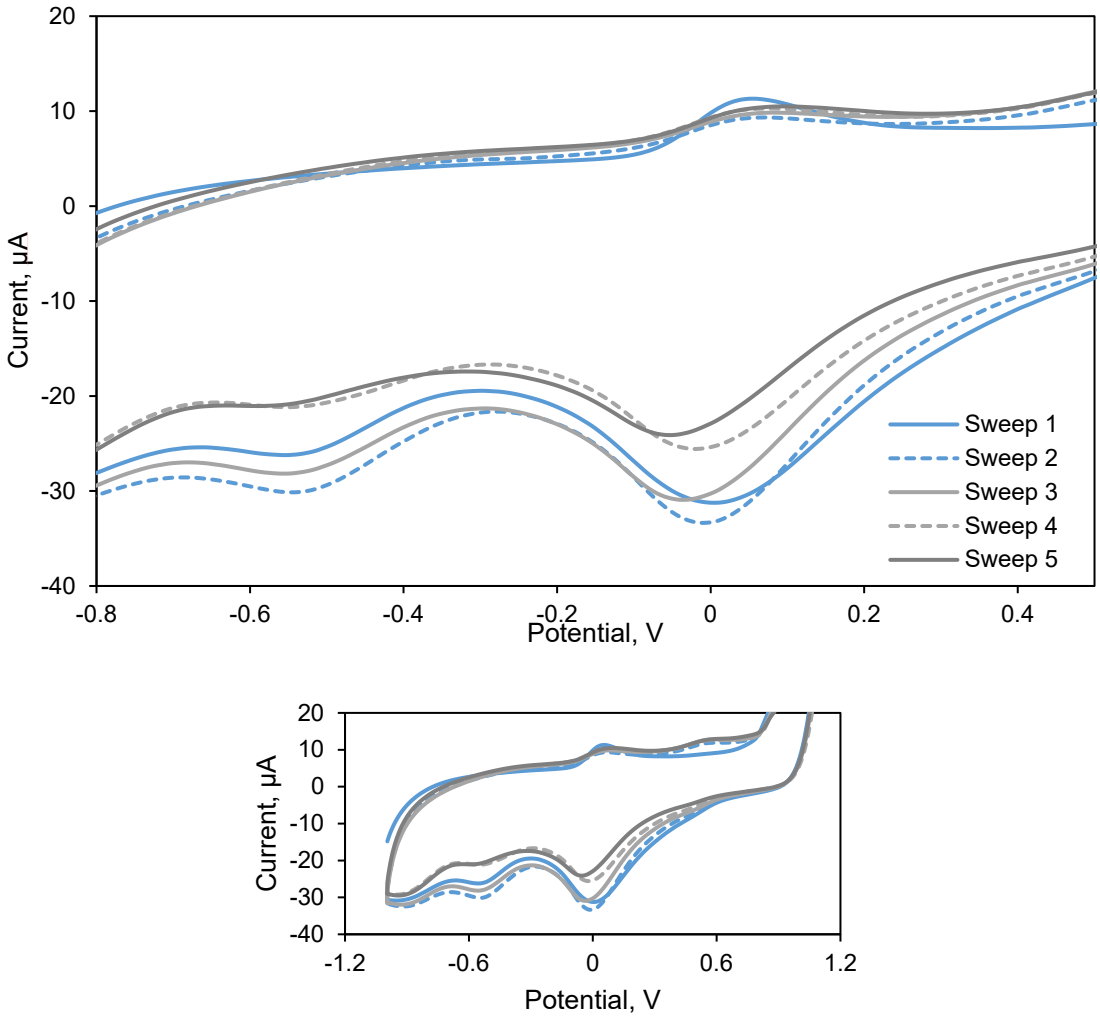

Appendix Figure A.5.6. Cyclic voltammagram of the lignin GG dimer using platinum wire as the working electrode. The bottom plot is the full scale curve while the top plot shows a portion of the data.

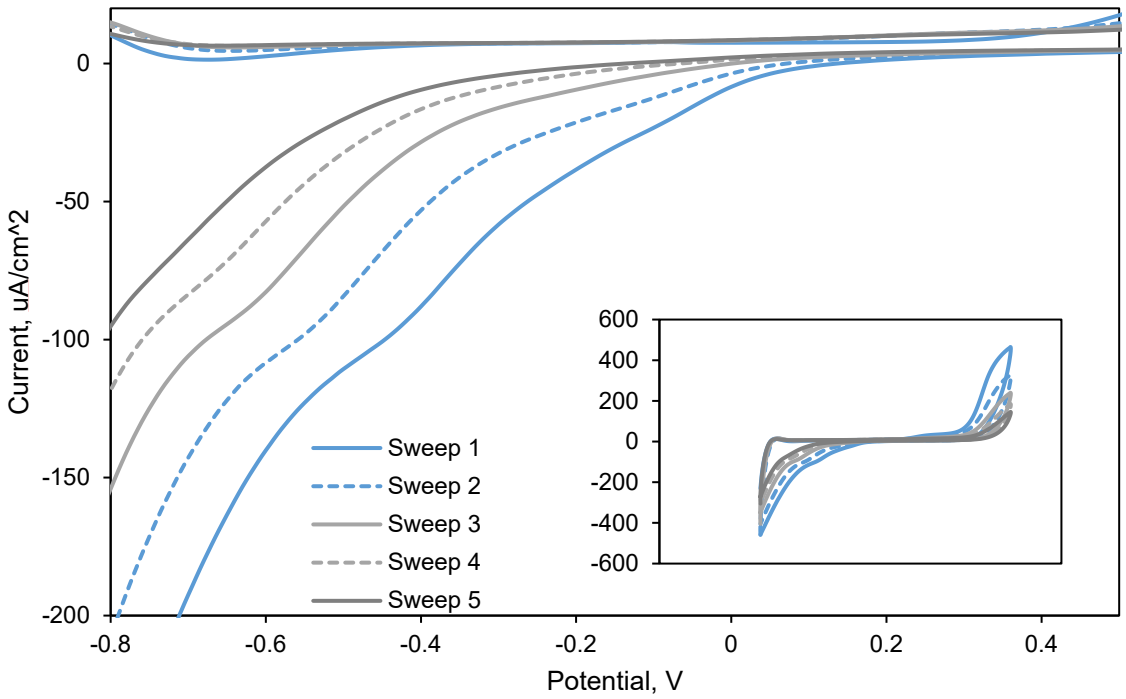

Appendix Figure A.5.7. Cyclic voltammagrams of the model lignin GG dimer using mesoporous titania coated FTO as the working electrode. Inset shows the full curve.

REFERENCES

1. He, Y.; Saang'Onyo, D.; Ladipo, F.; Knutson, B. L.; Rankin, S. E., In Situ Fourier Transform Infrared Study of the Effects of Silica Mesopore Confinement on Hydration of Ionic Liquid 1-Butyl-3-methylimidazolium Chloride. *Industrial & Engineering Chemistry Research* **2019,** *58* (50), 22609-22618.
2. Zhang, Y.; Liu, W.; Chen, S.; Gao, Q.; Li, Q.; Zhu, X., Ionic liquids for the Controllable Preparation of Functional TiO2 Nanostructures: A Review. *Ionics* **2020,** *26* (12), 5853-5877.
3. Newington, I.; Perez-Arlandis, J. M.; Welton, T., Ionic liquids as designer solvents for nucleophilic aromatic substitutions. *Organic Letters* **2007,** *9* (25), 5247-5250.
4. Hayes, R.; Warr, G. G.; Atkin, R., Structure and Nanostructure in Ionic Liquids. *Chemical Reviews* **2015,** *115* (13), 6357-6426.
5. Fox, D. M.; Awad, W. H.; Gilman, J. W.; Maupin, P. H.; De Long, H. C.; Trulove, P. C., Flammability, thermal stability, and phase change characteristics of several trialkylimidazolium saltsThe authors wish to thank the scientists at the Occupational Safety and Health Administration ? Salt Lake Technical Center for their measurement of the i. *Green Chemistry* **2003,** *5* (6), 724.
6. Ortiz-Martínez, V. M.; Gómez-Coma, L.; Pérez, G.; Ortiz, A.; Ortiz, I., The roles of ionic liquids as new electrolytes in redox flow batteries. *Separation and Purification Technology* **2020,** *252*.
7. Singh, S. K.; Savoy, A. W., Ionic liquids synthesis and applications: An overview. *Journal of Molecular Liquids* **2020,** *297*, 112038.
8. Gogoi, G.; Hazarika, S., Dissolution of lignocellulosic biomass in ionic liquid-water media: Interpretation from solubility parameter concept. *Korean Journal of Chemical Engineering* **2019,** *36* (10), 1626-1636.
9. de los Ríos, A. P.; Hernández-Fernández, F. J.; Lozano, L. J.; Sánchez, S.; Moreno, J. I.; Godínez, C., Removal of Metal Ions from Aqueous Solutions by Extraction with Ionic Liquids. *Journal of Chemical & Engineering Data* **2010,** *55* (2), 605-608.
10. Close, J. J.; Farmer, K.; Moganty, S. S.; Baltus, R. E., CO2/N2 separations using nanoporous alumina-supported ionic liquid membranes: Effect of the support on separation performance. *Journal of Membrane Science* **2012,** *390-391*, 201-210.
11. Taylor, A. W.; Men, S.; Clarke, C. J.; Licence, P., Acidity and basicity of halometallate-based ionic liquids from X-ray photoelectron spectroscopy. *RSC Advances* **2013,** *3* (24).
12. Vekariya, R. L., A review of ionic liquids: Applications towards catalytic organic transformations. *Journal of Molecular Liquids* **2017,** *227*, 44-60.
13. Martins, M. A. R.; Pinho, S. P.; Coutinho, J. A. P., Insights into the Nature of Eutectic and Deep Eutectic Mixtures. *Journal of Solution Chemistry* **2019,** *48* (7), 962-982.
14. Abbott, A. P.; Capper, G.; Davies, D. L.; Rasheed, R. K.; Tambyrajah, V., Novel solvent properties of choline chloride/urea mixtures. *Chemical Communications* **2003,** (1), 70-1.
15. Araujo, C. F.; Coutinho, J. A. P.; Nolasco, M. M.; Parker, S. F.; Ribeiro-Claro, P. J. A.; Rudić, S.; Soares, B. I. G.; Vaz, P. D., Inelastic neutron scattering study of reline: shedding light on the hydrogen bonding network of deep eutectic solvents. *Physical Chemistry Chemical Physics* **2017,** *19* (27), 17998-18009.

16. Abranches, D. O.; Coutinho, J. A. P., Everything You Wanted to Know about Deep Eutectic Solvents but Were Afraid to Be Told. *Annu Rev Chem Biomol Eng* **2023**.
17. El Achkar, T.; Greige-Gerges, H.; Fourmentin, S., Basics and properties of deep eutectic solvents: a review. *Environmental Chemistry Letters* **2021,** *19* (4), 3397-3408.
18. Craveiro, R.; Aroso, I.; Flammia, V.; Carvalho, T.; Viciosa, M. T.; Dionísio, M.; Barreiros, S.; Reis, R. L.; Duarte, A. R. C.; Paiva, A., Properties and thermal behavior of natural deep eutectic solvents. *Journal of Molecular Liquids* **2016,** *215*, 534-540.
19. Marcinkowski, Ł.; Kloskowski, A.; Namieśnik, J., Nanoconfined Ionic Liquids. In *Handbook of Smart Materials in Analytical Chemistry*, de la Guardia, M.; Esteve-Turrillas, F. A., Eds. John Wiley & Sons: Hoboken, NJ, 2019; pp 23-72.
20. Shen, Y.; Hung, F. R., A Molecular Simulation Study of Carbon Dioxide Uptake by a Deep Eutectic Solvent Confined in Slit Nanopores. *The Journal of Physical Chemistry C* **2017,** *121* (44), 24562-24575.
21. He, Y.; Khan, M. A.; Drake, A. D.; Ladipo, F.; Rankin, S. E.; Knutson, B. L., Nanoconfinement Effects on the Transport of Redox Probes in Ionic Liquid-Loaded Mesoporous Silica Thin Films. *Industrial & Engineering Chemistry Research* **2022,** *61* (33), 12107-12117.
22. Shen, Y.; He, X.; Hung, F. R., Structural and Dynamical Properties of a Deep Eutectic Solvent Confined Inside a Slit Pore. *The Journal of Physical Chemistry C* **2015,** *119* (43), 24489-24500.
23. Lan, X.; Wang, X.; Du, W.; Mu, T.; Lan, X. Z., Thermal properties and cold crystallization kinetics of deep eutectic solvents confined in nanopores. *Phys Chem Chem Phys* **2021,** *23* (25), 13785-13788.
24. Göbel, R.; Hesemann, P.; Weber, J.; Möller, E.; Friedrich, A.; Beuermann, S.; Taubert, A., Surprisingly high, bulk liquid-like mobility of silica-confined ionic liquids. *Physical Chemistry Chemical Physics* **2009,** *11* (19), 3653.
25. Slowing, I. I.; Trewyn, B. G.; Giri, S.; Lin, V. S. Y., Mesoporous Silica Nanoparticles for Drug Delivery and Biosensing Applications. *Advanced Functional Materials* **2007,** *17* (8), 1225-1236.
26. Koganti, V. R.; Dunphy, D.; Gowrishankar, V.; McGehee, M. D.; Li, X.; Wang, J.; Rankin, S. E., Generalized Coating Route to Silica and Titania Films with Orthogonally Tilted Cylindrical Nanopore Arrays. *Nano Letters* **2006,** *6* (11), 2567-2570.
27. He, Y.; Khan, M. A.; Drake, A.; Ghanim, R.; Garay, J.; Shirodkar, A.; Strzalka, J.; Zhang, Q.; Knutson, B. L.; Rankin, S. E., Formation of Vertically Oriented Channels during Calcination of Surfactant-Templated Titania-Doped Mesoporous Silica Thin Films. *The Journal of Physical Chemistry C* **2021,** *125* (40), 22262-22273.
28. Gartmann, N.; Brühwiler, D., Controlling and imaging the functional-group distribution on mesoporous silica. *Angewantie Chemie International Edition* **2009,** *48* (34), 6354-6.
29. Katiyar, A.; Pinto, N. G., Visualization of size-selective protein separations on spherical mesoporous silicates. *Small* **2006,** *2* (5), 644-8.
30. Schlipf, D. M.; Zhou, S.; Khan, M. A.; Rankin, S. E.; Knutson, B. L., Effects of Pore Size and Tethering on the Diffusivity of Lipids Confined in Mesoporous Silica. *Advanced Materials Interfaces* **2017,** *4* (9), 1601103.
31. Kang, M.; Day, C. A.; Kenworthy, A. K.; DiBenedetto, E., Simplified equation to extract diffusion coefficients from confocal FRAP data. *Traffic* **2012,** *13* (12), 1589-600.

32. Chen, S.; Liu, Y.; Fu, H.; He, Y.; Li, C.; Huang, W.; Jiang, Z.; Wu, G., Unravelling the Role of the Compressed Gas on Melting Point of Liquid Confined in Nanospace. *The Journal of Physical Chemistry Letters* **2012,** *3* (8), 1052-1055.
33. Rajput, N. N.; Monk, J.; Singh, R.; Hung, F. R., On the Influence of Pore Size and Pore Loading on Structural and Dynamical Heterogeneities of an Ionic Liquid Confined in a Slit Nanopore. *The Journal of Physical Chemistry C* **2012,** *116* (8), 5169-5181.
34. Verma, Y. L.; Singh, R. K., Conformational States of Ionic Liquid 1-Ethyl-3-methylimidazolium Bis(trifluoromethylsulfonyl)imide in Bulk and Confined Silica Nanopores Probed by Crystallization Kinetics Study. *The Journal of Physical Chemistry C* **2015,** *119* (43), 24381-24392.
35. Bica, K.; Gaertner, P., An Iron-Containing Ionic Liquid as Recyclable Catalyst for Aryl Grignard Cross-Coupling of Alkyl Halides. *Organic Letters* **2006,** *8* (4), 733-735.
36. Burba, C. M.; Chang, H. C., Confinement Effects on the Magnetic Ionic Liquid 1-Ethyl-3-methylimidazolium Tetrachloroferrate(III). *Molecules* **2022,** *27* (17).
37. Miller, M. A.; Wainright, J. S.; Savinell, R. F., Iron Electrodeposition in a Deep Eutectic Solvent for Flow Batteries. *Journal of The Electrochemical Society* **2017,** *164* (4), A796-A803.
38. Xu, Q.; Zhao, T. S.; Wei, L.; Zhang, C.; Zhou, X. L., Electrochemical characteristics and transport properties of Fe(II)/Fe(III) redox couple in a non-aqueous reline deep eutectic solvent. *Electrochimica Acta* **2015,** *154*, 462-467.
39. Walden, P., Ueber die Molekulargrosse und elektrische Leitfahigkeit einiger geschmolzenen Salze. *Bulletin of Academic Imperial Sciences (St. Petersburg)* **1914,** *8* (6), 405-422.
40. Welton, T., Ionic liquids: a brief history. *Biophysical Reviews* **2018,** *10* (3), 691-706.
41. Boon, J. A.; Levisky, J. A.; Pflug, J. L.; Wilkes, J. S., Friedel-Crafts reactions in ambient-temperature molten salts. *The Journal of Organic Chemistry* **1986,** *51* (4), 480-483.
42. Brandt, A.; Gräsvik, J.; Hallett, J. P.; Welton, T., Deconstruction of lignocellulosic biomass with ionic liquids. *Green Chemistry* **2013,** *15* (3).
43. Alvarez-Guerra, M.; Albo, J.; Alvarez-Guerra, E.; Irabien, A., Ionic liquids in the electrochemical valorisation of CO2. *Energy & Environmental Science* **2015,** *8* (9), 2574-2599.
44. Saang'onyo, D.; Parkin, S.; Ladipo, F. T., Effect of ancillary (aminomethyl)phenolate ligand on efficacy of aluminum-catalyzed glucose dehydration to 5-hydroxymethylfurfural. *Polyhedron* **2018,** *149*, 153-162.
45. Portillo Perez, G.; Mukherjee, A.; Dumont, M.-J., Insights into HMF catalysis. *Journal of Industrial and Engineering Chemistry* **2019,** *70*, 1-34.
46. Saha, B.; Abu-Omar, M. M., Advances in 5-hydroxymethylfurfural production from biomass in biphasic solvents. *Green Chem.* **2014,** *16* (1), 24-38.
47. Yang, Y.-L.; Kou, Y., Determination of the Lewis acidity of ionic liquids by means of an IR spectroscopic probe. *Chemical Communications* **2004,** (2), 226.
48. Fan, J.; Fan, Y.; Pei, Y.; Wu, K.; Wang, J.; Fan, M., Solvent extraction of selected endocrine-disrupting phenols using ionic liquids. *Separation and Purification Technology* **2008,** *61* (3), 324-331.

49. Anderson, J. L.; Armstrong, D. W.; Wei, G.-T., Ionic liquids in analytical chemistry. *Journal of Analytical Chemistry* **2006,** *78* (9), 2892-2902.
50. Ho, T. D.; Zhang, C.; Hantao, L. W.; Anderson, J. L., Ionic liquids in analytical chemistry: fundamentals, advances, and perspectives. *Analytical Chemistry* **2014,** *86* (1), 262-85.
51. Shiflett, M. B.; Yokozeki, A., Solubilities and Diffusivities of Carbon Dioxide in Ionic Liquids: [bmim][PF6] and [bmim][BF4]. *Industrial & Engineering Chemistry Research* **2005,** *44* (12), 4453-4464.
52. Yokozeki, A.; Shiflett, M. B.; Junk, C. P.; Grieco, L. M.; Foo, T., Physical and Chemical Absorptions of Carbon Dioxide in Room-Temperature Ionic Liquids. *The Journal of Physical Chemistry B* **2008,** *112* (51), 16654-16663.
53. Kollau, L. J. B. M.; Vis, M.; Van Den Bruinhorst, A.; Esteves, A. C. C.; Tuinier, R., Quantification of the liquid window of deep eutectic solvents. *Chemical Communications* **2018,** *54* (95), 13351-13354.
54. Aroso, I. M.; Paiva, A.; Reis, R. L.; Duarte, A. R. C., Natural deep eutectic solvents from choline chloride and betaine – Physicochemical properties. *Journal of Molecular Liquids* **2017,** *241*, 654-661.
55. Hansen, B. B.; Spittle, S.; Chen, B.; Poe, D.; Zhang, Y.; Klein, J. M.; Horton, A.; Adhikari, L.; Zelovich, T.; Doherty, B. W.; Gurkan, B.; Maginn, E. J.; Ragauskas, A.; Dadmun, M.; Zawodzinski, T. A.; Baker, G. A.; Tuckerman, M. E.; Savinell, R. F.; Sangoro, J. R., Deep Eutectic Solvents: A Review of Fundamentals and Applications. *Chemical Reviews* **2021,** *121* (3), 1232-1285.
56. Ghazali, Z.; Hassan, N. H.; Yarmo, M. A.; Teh, L. P.; Othaman, R., Immobilization of Choline Chloride: Urea onto Mesoporous Silica for Carbon Dioxide Capture. *Sains Malaysiana* **2019,** *48* (5), 1025-1033.
57. Liu, Q.; Zhao, X.; Yu, D.; Yu, H.; Zhang, Y.; Xue, Z.; Mu, T., Novel deep eutectic solvents with different functional groups towards highly efficient dissolution of lignin. *Green Chemistry* **2019,** *21* (19), 5291-5297.
58. Ghahremani, R.; Dean, W.; Sinclair, N.; Shen, X.; Starvaggi, N.; Alfurayj, I.; Burda, C.; Pentzer, E.; Wainright, J.; Savinell, R.; Gurkan, B., Redox-Active Eutectic Electrolyte with Viologen and Ferrocene Derivatives for Flow Batteries. *ACS Applied Materials & Interfaces* **2023,** *15* (1), 1148-1156.
59. García-Álvarez, J., Deep Eutectic Solvents: Environmentally Friendly Media for Metal-Catalyzed Organic Reactions. In *Green Technologies for the Environment*, 2014; pp 37-52.
60. Ruesgas-Ramon, M.; Figueroa-Espinoza, M. C.; Durand, E., Application of Deep Eutectic Solvents (DES) for Phenolic Compounds Extraction: Overview, Challenges, and Opportunities. *J Agric Food Chem* **2017,** *65* (18), 3591-3601.
61. Stefanopoulos, K. L.; Romanos, G. E.; Vangeli, O. C.; Mergia, K.; Kanellopoulos, N. K.; Koutsioubas, A.; Lairez, D., Investigation of confined ionic liquid in nanostructured materials by a combination of SANS, contrast-matching SANS, and nitrogen adsorption. *Langmuir* **2011,** *27* (13), 7980-5.
62. Wei, T. C.; Mack, A.; Chen, W.; Liu, J.; Dittmann, M.; Wang, X.; Barber, W. E., Synthesis, characterization, and evaluation of a superficially porous particle with unique, elongated pore channels normal to the surface. *J Chromatogr A* **2016,** *1440*, 55-65.

63. Tripathi, A. K.; Verma, Y. L.; Singh, R. K., Thermal, electrical and structural studies on ionic liquid confined in ordered mesoporous MCM-41. *Journal of Materials Chemistry A* **2015,** *3* (47), 23809-23820.
64. Evans, D. F.; Wennerström, H., The colloidal domain: where physics, chemistry, biology, and technology meet. **1999**.
65. Holmberg, K.; Jönsson, B.; Kronberg, B.; Lindman, B., Polymers in aqueous solution. *Wiley-Blackwell* **2002**.
66. Brinker, C. J., Hydrolysis and condensation of silicates: Effects on structure. *Journal of non-crystalline solids* **1988,** *100* (1-3), 31-50.
67. Wooten, M. K. C.; Koganti, V. R.; Zhou, S.; Rankin, S. E.; Knutson, B. L., Synthesis and Nanofiltration Membrane Performance of Oriented Mesoporous Silica Thin Films on Macroporous Supports. *ACS Applied Materials & Interfaces* **2016,** *8* (33), 21806-15.
68. Li, C.; Guo, X.; He, Y.; Jiang, Z.; Wang, Y.; Chen, S.; Fu, H.; Zou, Y.; Dai, S.; Wu, G.; Xu, H., Compression of ionic liquid when confined in porous silica nanoparticles. *RSC Advances* **2013,** *3* (25), 9618.
69. Su, Q.; Qi, Y.; Yao, X.; Cheng, W.; Dong, L.; Chen, S.; Zhang, S., Ionic liquids tailored and confined by one-step assembly with mesoporous silica for boosting the catalytic conversion of CO2 into cyclic carbonates. *Green Chemistry* **2018,** *20* (14), 3232-3241.
70. Verma, Y. L.; Singh, M. P.; Singh, R. K., Effect of Ultrasonic Irradiation on Preparation and Properties of Ionogels. *Journal of Nanomaterials* **2012,** *2012*, 1-6.
71. Singh, M. P.; Singh, R. K.; Chandra, S., Properties of ionic liquid confined in porous silica matrix. *Chemphyschem* **2010,** *11* (9), 2036-43.
72. Vavra, S.; Vilà, N.; Lotsari, A.; Walcarius, A.; Martinelli, A., An imidazolium ionic liquid as effective structure-directing agent for the fabrication of silica thin films with vertically aligned nanochannels. *Microporous and Mesoporous Materials* **2020**, 110407.
73. Lou, H.; Zhang, Y.; Xiang, Q.; Xu, J.; Li, H.; Xu, P.; Li, X., The real-time detection of trace-level Hg2+ in water by QCM loaded with thiol-functionalized SBA-15. *Sensors and Actuators B: Chemical* **2012,** *166-167*, 246-252.
74. Gruttadauria, M.; Riela, S.; Lo Meo, P.; D'Anna, F.; Noto, R., Supported ionic liquid asymmetric catalysis. A new method for chiral catalysts recycling. The case of proline-catalyzed aldol reaction. *Tetrahedron Letters* **2004,** *45* (32), 6113-6116.
75. Wang, G.; Yu, N.; Peng, L.; Tan, R.; Zhao, H.; Yin, D.; Qiu, H.; Fu, Z.; Yin, D., Immobilized Chloroferrate Ionic Liquid: An Efficient and Reusable Catalyst for Synthesis of Diphenylmethane and its Derivatives. *Catalysis Letters* **2008,** *123* (3-4), 252-258.
76. Nasresfahani, Z.; Kassaee, M. Z.; Eidi, E., Ionic liquid-functionalized mesoporous silica nanoparticles ([pmim]FeCl4/MSNs): Efficient nanocatalyst for solvent-free synthesis of N,N′-diaryl-substituted formamidines. *Applied Organometallic Chemistry* **2017,** *31* (11).
77. Elliott, J. A. W., Surface thermodynamics at the nanoscale. *The Journal of Chemical Physics* **2021,** *154* (19), 190901.
78. Singh, M. P.; Singh, R. K.; Chandra, S., Ionic liquids confined in porous matrices: Physicochemical properties and applications. *Progress in Materials Science* **2014,** *64*, 73-120.

79. Sha, M.; Wu, G.; Dou, Q.; Tang, Z.; Fang, H., Double-Layer Formation of [Bmim][PF6] Ionic Liquid Triggered by Surface Negative Charge. *Langmuir* **2010,** *26* (15), 12667-12672.
80. Sieffert, N.; Wipff, G., Ordering of Imidazolium-Based Ionic Liquids at the α-Quartz(001) Surface: A Molecular Dynamics Study. *The Journal of Physical Chemistry C* **2008,** *112* (49), 19590-19603.
81. Santhosh, K.; Banerjee, S.; Rangaraj, N.; Samanta, A. J. T. J. o. P. C. B., Fluorescence response of 4-(N, N′-Dimethylamino) benzonitrile in room temperature ionic liquids: observation of photobleaching under mild excitation condition and multiphoton confocal microscopic study of the fluorescence recovery dynamics. *The Journal of Physical Chemistry B* **2010,** *114* (5), 1967-1974.
82. Verma, Y. L.; Singh, M. P.; Kumar, S.; Dhar, R.; Singh, R. K., Behaviour of ionic liquid adsorbed on the surface of nano silica particles and in confined system of silica matrices. *Surface Science* **2020,** *701*, 121701.
83. Wang, X.; Wang, Y.; Dong, M.; Fang, Z.; Hu, Y.; Xue, K.; Ye, Z.; Peng, X. J. M. T. E., A two-dimensional nanochannel facilitates ionic conductivity of a deep eutectic solvent for an efficient supercapacitor. *Materials Today Energy* **2023,** *34*, 101285.
84. Ghazali, Z.; Suhaili, N.; Tahari, M. N. A.; Yarmo, M. A.; Hassan, N. H.; Othaman, R., Impregnating deep eutectic solvent choline chloride:urea:polyethyleneimine onto mesoporous silica gel for carbon dioxide capture. *Journal of Materials Research and Technology* **2020,** *9* (3), 3249-3260.
85. Ghazali, Z.; Yarmo, M. A.; Hassan, N. H.; Teh, L. P.; Othaman, R., New Green Adsorbent for Capturing Carbon Dioxide by Choline Chloride:Urea-Confined Nanoporous Silica. *Arabian Journal for Science and Engineering* **2020**.
86. Malfait, B.; Jani, A.; Morineau, D., Confining deep eutectic solvents in nanopores: insight into thermodynamics and chemical activity. *Journal of Molecular Liquids* **2022,** *349*, 118488.
87. Lin, H.; Gong, K.; Ying, W.; Chen, D.; Zhang, J.; Yan, Y.; Peng, X., CO 2 - Philic Separation Membrane: Deep Eutectic Solvent Filled Graphene Oxide Nanoslits. *Small* **2019,** *15* (49), 1904145.
88. Cao, L.; Zhou, Z.; Niu, S.; Cao, C.; Li, X.; Shan, Y.; Huang, Q., Positive-Charge Functionalized Mesoporous Silica Nanoparticles as Nanocarriers for Controlled 2,4-Dichlorophenoxy Acetic Acid Sodium Salt Release. *J Agric Food Chem* **2018,** *66* (26), 6594-6603.
89. Elbourne, A.; Besford, Q. A.; Meftahi, N.; Crawford, R. J.; Daeneke, T.; Greaves, T. L.; McConville, C. F.; Bryant, G.; Bryant, S. J.; Christofferson, A. J., The Impact of Water on the Lateral Nanostructure of a Deep Eutectic Solvent–Solid Interface. *Australian Journal of Chemistry* **2022,** *75* (2), 111-125.
90. Elbourne, A.; Meftahi, N.; Greaves, T. L.; McConville, C. F.; Bryant, G.; Bryant, S. J.; Christofferson, A. J., Nanostructure of a deep eutectic solvent at solid interfaces. *J Colloid Interface Sci* **2021,** *591*, 38-51.
91. Gao, Q.; Wu, N.; Qin, Y.; Laaksonen, A.; Zhu, Y.; Ji, X.; Lu, X., Molecular insight into wetting behavior of deep eutectic solvent droplets on ionic substrates: A molecular dynamics study. *Journal of Molecular Liquids* **2020,** *319*.

92. Kaur, S.; Sharma, S.; Kashyap, H. K., Bulk and interfacial structures of reline deep eutectic solvent: A molecular dynamics study. *The Journal of Chemical Physics* **2017,** *147* (19), 194507.
93. Mamme, M. H.; Moors, S. L. C.; Terryn, H.; Deconinck, J.; Ustarroz, J.; De Proft, F., Atomistic Insight into the Electrochemical Double Layer of Choline Chloride-Urea Deep Eutectic Solvents: Clustered Interfacial Structuring. *J Phys Chem Lett* **2018,** *9* (21), 6296-6304.
94. Zec, N.; Mangiapia, G.; Zheludkevich, M. L.; Busch, S.; Moulin, J. F., Revealing the interfacial nanostructure of a deep eutectic solvent at a solid electrode. *Physical Chemistry Chemical Physics* **2020,** *22* (21), 12104-12112.
95. Bahadori, L.; Manan, N. S.; Chakrabarti, M. H.; Hashim, M. A.; Mjalli, F. S.; AlNashef, I. M.; Hussain, M. A.; Low, C. T., The electrochemical behaviour of ferrocene in deep eutectic solvents based on quaternary ammonium and phosphonium salts. *Phys Chem Chem Phys* **2013,** *15* (5), 1707-14.
96. Zhu, F.; Deng, R. X.; Jiang, Q. H., Effects of Water on Electrochemical Behavior of ZnCl2 and FeCl3 in Deep Eutectic Solvent Composed of Choline Chloride and Urea. *Russian Journal of Electrochemistry* **2022,** *58* (7), 617-625.
97. Fryars, S.; Limanton, E.; Gauffre, F.; Paquin, L.; Lagrost, C.; Hapiot, P., Diffusion of redox active molecules in deep eutectic solvents. *Journal of Electroanalytical Chemistry* **2018,** *819*, 214-219.
98. Yang, H.; Reddy, R. G., Fundamental Studies on Electrochemical Deposition of Lead from Lead Oxide in 2:1 Urea/Choline Chloride Ionic Liquids. *Journal of The Electrochemical Society* **2014,** *161* (10), D586-D592.
99. Zhang, Y.; Han, J.; Liao, C., Insights into the Properties of Deep Eutectic Solvent Based on Reline for Ga-Controllable CIGS Solar Cell in One-Step Electrodeposition. *Journal of The Electrochemical Society* **2016,** *163* (13), D689-D693.
100. Axelrod, D.; Koppel, D. E.; Schlessinger, J.; Elson, E.; Webb, W. W., Mobility measurement by analysis of fluorescence photobleaching recovery kinetics. *Biophysical Journal* **1976,** *16* (9), 1055-1069.
101. Hashimoto, T.; Ye, Y.; Matsuno, A.; Ohnishi, Y.; Kitamura, A.; Kinjo, M.; Abe, S.; Ueno, T.; Yao, M.; Ogawa, T.; Matsui, T.; Tanaka, Y., Encapsulation of biomacromolecules by soaking and co-crystallization into porous protein crystals of hemocyanin. *Biochem Biophys Res Commun* **2019,** *509* (2), 577-584.
102. Williamson, D. E.; Sahai, E.; Jenkins, R. P.; O'Dea, R. D.; King, J. R., Parameter estimation in fluorescence recovery after photobleaching: quantitative analysis of protein binding reactions and diffusion. *Journal of Mathematical Biology* **2021,** *83* (1), 1.
103. Watanabe, R.; Hirano, Y.; Hara, M.; Hiraoka, Y.; Fukagawa, T., Mobility of kinetochore proteins measured by FRAP analysis in living cells. *Chromosome Research* **2022,** *30* (1), 43-57.
104. Stephens, N. M.; Masching, H. P.; Walid, M. K. I.; Petrich, J. W.; Anderson, J. L.; Smith, E. A., Temperature-Dependent Constrained Diffusion of Micro-Confined Alkylimidazolium Chloride Ionic Liquids. *The Journal of Physical Chemistry B* **2022,** *126* (23), 4324-4333.
105. Sasmal, D. K.; Mandal, A. K.; Mondal, T.; Bhattacharyya, K., Diffusion of organic dyes in ionic liquid and giant micron sized ionic liquid mixed micelle: fluorescence correlation spectroscopy. *The Journal of Physical Chemistry B* **2011,** *115* (24), 7781-7.

106. Werner, J. H.; Baker, S. N.; Baker, G. A., Fluorescence correlation spectroscopic studies of diffusion within the ionic liquid 1-butyl-3-methylimidazolium hexafluorophosphate. *Analyst* **2003,** *128* (6), 786-9.
107. Beamson, G.; Alexander, M. R., Angle-resolved XPS of fluorinated and semi-fluorinated side-chain polymers. *Surface and Interface Analysis: An International Journal devoted to the development and application of techniques for the analysis of surfaces, interfaces and thin films* **2004,** *36* (4), 323-333.
108. Stevie, F. A.; Donley, C. L., Introduction to x-ray photoelectron spectroscopy. *Journal of Vacuum Science & Technology A* **2020,** *38* (6).
109. Smith, E. F.; Garcia, I. J.; Briggs, D.; Licence, P., Ionic liquids in vacuo; solution-phase X-ray photoelectron spectroscopy. *Chemical Communications* **2005,** (45), 5633-5.
110. Cremer, T.; Killian, M.; Gottfried, J. M.; Paape, N.; Wasserscheid, P.; Maier, F.; Steinruck, H. P., Physical vapor deposition of [EMIM][Tf2N]: a new approach to the modification of surface properties with ultrathin ionic liquid films. *Chemphyschem* **2008,** *9* (15), 2185-90.
111. Kolbeck, C.; Cremer, T.; Lovelock, K. R. J.; Paape, N.; Schulz, P. S.; Wasserscheid, P.; Maier, F.; SteinrüCk, H. P., Influence of Different Anions on the Surface Composition of Ionic Liquids Studied Using ARXPS. *The Journal of Physical Chemistry B* **2009,** *113* (25), 8682-8688.
112. Lovelock, K. R. J.; Kolbeck, C.; Cremer, T.; Paape, N.; Schulz, P. S.; Wasserscheid, P.; Maier, F.; SteinrüCk, H. P., Influence of Different Substituents on the Surface Composition of Ionic Liquids Studied Using ARXPS. *The Journal of Physical Chemistry B* **2009,** *113* (9), 2854-2864.
113. Maier, F.; Gottfried, J. M.; Rossa, J.; Gerhard, D.; Schulz, P. S.; Schwieger, W.; Wasserscheid, P.; Steinrück, H.-P., Surface Enrichment and Depletion Effects of Ions Dissolved in an Ionic Liquid: An X-ray Photoelectron Spectroscopy Study. *Angewandte Chemie International Edition* **2006,** *45* (46), 7778-7780.
114. Lovelock, K. V.-G., Ignacio; Maier, Florian; Steinruck, Hans-Peter; Licence, Peter, Photoelectron Spectroscopy of Ionic Liquid-Based Interfaces. *Chemical Reviews* **2010,** *110*, 5158.
115. Men, S.; Lovelock, K. R. J.; Licence, P., X-ray photoelectron spectroscopy of trihalide ionic liquids: Comparison to halide-based analogues, anion basicity and beam damage. *Chemical Physics Letters* **2017,** *679*, 207-211.
116. Estager, J.; Holbrey, J. D.; Swadźba-Kwaśny, M., Halometallate ionic liquids – revisited. *Chem. Soc. Rev.* **2014,** *43* (3), 847-886.
117. Gupta, A. K.; Singh, R. K.; Chandra, S., Crystallization kinetics behavior of ionic liquid [EMIM][BF4] confined in mesoporous silica matrices. *RSC Advances* **2014,** *4* (42), 22277-22287.
118. Metwalli, E.; Slotta, U.; Darko, C.; Roth, S. V.; Scheibel, T.; Papadakis, C. M., Structural changes of thin films from recombinant spider silk proteins upon post-treatment. *Applied Physics A* **2007,** *89*, 655-661.
119. Le, T. P.; Smith, B. H.; Lee, Y.; Litofsky, J. H.; Aplan, M. P.; Kuei, B.; Zhu, C.; Wang, C.; Hexemer, A.; Gomez, E. D., Enhancing optoelectronic properties of conjugated block copolymers through crystallization of both blocks. *Macromolecules* **2020,** *53* (6), 1967-1976.

120. Renaud, G.; Lazzari, R.; Revenant, C.; Barbier, A.; Noblet, M.; Ulrich, O.; Leroy, F.; Jupille, J.; Borensztein, Y.; Henry, C. R., Real-time monitoring of growing nanoparticles. *Science* **2003,** *300* (5624), 1416-1419.
121. Als-Nielsen, J.; McMorrow, D., *Elements of modern X-ray physics*. John Wiley & Sons: 2011.
122. Olichwer, N.; Koschine, T.; Meyer, A.; Egger, W.; Rätzke, K.; Vossmeyer, T., Gold nanoparticle superlattices: structure and cavities studied by GISAXS and PALS. *RSC advances* **2016,** *6* (114), 113163-113172.
123. Nagpure, S.; Das, S.; Garlapalli, R. K.; Strzalka, J.; Rankin, S. E., In Situ GISAXS Investigation of Low-Temperature Aging in Oriented Surfactant-Mesostructured Titania Thin Films. *The Journal of Physical Chemistry C* **2015,** *119* (40), 22970-22984.
124. Khan, M. A.; Wallace, W. T.; Islam, S. Z.; Nagpure, S.; Strzalka, J.; Littleton, J. M.; Rankin, S. E.; Knutson, B. L., Adsorption and recovery of polyphenolic flavonoids using TiO2-functionalized mesoporous silica nanoparticles. *ACS applied materials & interfaces* **2017,** *9* (37), 32114-32125.
125. Elgrishi, N.; Rountree, K. J.; McCarthy, B. D.; Rountree, E. S.; Eisenhart, T. T.; Dempsey, J. L., A Practical Beginner's Guide to Cyclic Voltammetry. *Journal of Chemical Education* **2017,** *95* (2), 197-206.
126. Nicholson, R. S.; Shain, I., Theory of stationary electrode polarography. Single scan and cyclic methods applied to reversible, irreversible, and kinetic systems. *Analytical chemistry* **1964,** *36* (4), 706-723.
127. Yue, D.; Jia, Y.; Yao, Y.; Sun, J.; Jing, Y., Structure and electrochemical behavior of ionic liquid analogue based on choline chloride and urea. *Electrochimica Acta* **2012,** *65*, 30-36.
128. Yamada, H.; Yoshii, K.; Asahi, M.; Chiku, M.; Kitazumi, Y., Cyclic Voltammetry Part 1: Fundamentals. *Electrochemistry* **2022,** *90* (10), 102005-102005.
129. Renjith, A.; Lakshminarayanan, V., Electron-Transfer Studies of Model Redox-Active Species (Cationic, Anionic, and Neutral) in Deep Eutectic Solvents. *The Journal of Physical Chemistry C* **2018,** *122* (44), 25411-25421.
130. Etienne, M.; Quach, A.; Grosso, D.; Nicole, L.; Sanchez, C.; Walcarius, A., Molecular Transport into Mesostructured Silica Thin Films: Electrochemical Monitoring and Comparison between p6m, P63/mmc, and Pm3n Structures. *Chemistry of Materials* **2007,** *19* (4), 844-856.
131. Steinberg, P. Y.; Zanotto, F. M.; Soler-Illia, G. J. A. A.; Dassie, S. A.; Angelomé, P. C., Molecular Transport through TiO2 Mesoporous Thin Films: Correlation with the Partially Blocked Electrode Model. *The Journal of Physical Chemistry C* **2021,** *125* (42), 23521-23532.
132. Krossing, I.; Slattery, J. M.; Daguenet, C.; Dyson, P. J.; Oleinikova, A.; Weingärtner, H., Why Are Ionic Liquids Liquid? A Simple Explanation Based on Lattice and Solvation Energies. *Journal of the American Chemical Society* **2006,** *128* (41), 13427-13434.
133. Welton, T., Ionic liquids in catalysis. *Coordination Chemistry Reviews* **2004,** *248* (21-24), 2459-2477.
134. Galiński, M.; Lewandowski, A.; Stępniak, I., Ionic liquids as electrolytes. *Electrochimica Acta* **2006,** *51* (26), 5567-5580.

135. Huddleston, J. G.; Visser, A. E.; Reichert, W. M.; Willauer, H. D.; Broker, G. A.; Rogers, R. D., Characterization and comparison of hydrophilic and hydrophobic room temperature ionic liquids incorporating the imidazolium cation. *Green Chemistry* **2001,** *3* (4), 156-164.
136. Yunqian, M.; Jiaming, M.; Cong, X.; Yan, L.; Lihua, Z., Immobilization of functionalized ionic liquid on sol-gel derived silica for efficient removal of H2S. *China Petroleum Processing & Petrochemical Technology* **2019,** *21*, 62-70.
137. Zhao, D.; Liao, Y.; Zhang, Z., Toxicity of Ionic Liquids. *CLEAN – Soil, Air, Water* **2007,** *35* (1), 42-48.
138. Lapshin, D. N.; Gromov, A. V.; Campbell, E. E. B.; Sarkisov, L., Nanostructures of Ionic Liquids Confined in Pores of SBA-15: Insights from Experimental Studies and Mean-Field Density Functional Theory. *The Journal of Physical Chemistry C* **2021,** *125* (38), 21254-21269.
139. Zuo, Y.; Zhang, Y.; Huang, R.; Min, Y., The effect of nanoconfinement on the glass transition temperature of ionic liquids. *Physical Chemistry Chemical Physics* **2019,** *21* (1), 22-25.
140. Feng, G.; Qiao, R.; Huang, J.; Dai, S.; Sumpter, B. G.; Meunier, V., The importance of ion size and electrode curvature on electrical double layers in ionic liquids. *Physical Chemistry Chemical Physics* **2011,** *13* (3), 1152-61.
141. Khristenko, I. V.; Panteleimonov, A. V.; Iliashenko, R. Y.; Doroshenko, A. O.; Ivanov, V. V.; Tkachenko, O. S.; Benvenutti, E. V.; Kholin, Y. V., Heterogeneous polarity and surface acidity of silica-organic materials with fixed 1-n-propyl-3-methylimidazolium chloride as probed by solvatochromic and fluorescent dyes. *Colloids and Surfaces A: Physicochemical and Engineering Aspects* **2018,** *538*, 280-286.
142. Vangeli, O. C.; Romanos, G. E.; Beltsios, K. G.; Fokas, D.; Kouvelos, E. P.; Stefanopoulos, K. L.; Kanellopoulos, N. K., Grafting of Imidazolium Based Ionic Liquid on the Pore Surface of Nanoporous Materials-Study of Physicochemical and Thermodynamic Properties. *The Journal of Physical Chemistry B* **2010,** *114* (19), 6480-91.
143. Vavra, S.; Elamin, K.; Evenäs, L.; Martinelli, A., Transport Properties and Local Structure of an Imidazole/Protic Ionic Liquid Mixture Confined in the Mesopores of Hydrophobic Silica. *The Journal of Physical Chemistry C* **2021,** *125* (4), 2607-2618.
144. Chi, Y. S.; Lee, J. K.; Lee, S.-G.; Choi, I. S., Control of Wettability by Anion Exchange on Si/SiO2Surfaces. *Langmuir* **2004,** *20* (8), 3024-3027.
145. Yim, J.-H.; Ha, S.-J.; Lim, J. S., Measurement and correlation of CO2 solubility in 1-butyl-3-methylimidazolium ([BMIM]) cation-based ionic liquids: [BMIM][Ac], [BMIM][Cl], [BMIM][MeSO4]. *The Journal of Supercritical Fluids* **2018,** *138*, 73-81.
146. Chaudhary, V.; Sharma, S., An overview of ordered mesoporous material SBA-15: synthesis, functionalization and application in oxidation reactions. *Journal of Porous Materials* **2016,** *24* (3), 741-749.
147. Qu, Q.; Ma, X.; Zhao, Y., Targeted delivery of doxorubicin to mitochondria using mesoporous silica nanoparticle nanocarriers. *Nanoscale* **2015,** *7* (40), 16677-86.
148. Shi, F.; Zhang, Q.; Li, D.; Deng, Y., Silica-gel-confined ionic liquids: a new attempt for the development of supported nanoliquid catalysis. *Chemistry* **2005,** *11* (18), 5279-88.

149. Joni, J.; Haumann, M.; Wasserscheid, P., Continuous gas-phase isopropylation of toluene and cumene using highly acidic Supported Ionic Liquid Phase (SILP) catalysts. *Applied Catalysis A: General* **2010,** *372* (1), 8-15.
150. Liu, S.; Shang, J.; Zhang, S.; Yang, B.; Deng, Y., Highly efficient trimerization of isobutene over silica supported chloroaluminate ionic liquid using C4 feed. *Catalysis Today* **2013,** *200*, 41-48.
151. Durak, O.; Zeeshan, M.; Habib, N.; Gulbalkan, H. C.; Alsuhile, A. A. A. M.; Caglayan, H. P.; Kurtoğlu-Öztulum, S. F.; Zhao, Y.; Haslak, Z. P.; Uzun, A.; Keskin, S., Composites of porous materials with ionic liquids: Synthesis, characterization, applications, and beyond. *Microporous and Mesoporous Materials* **2022,** *332*, 111703.
152. Linton, P.; Alfredsson, V., Growth and morphology of mesoporous SBA-15 particles. *Chemistry of Materials* **2008,** *20* (9), 2878-2880.
153. Wang, Y.; Wang, X.; Wohland, T.; Sampath, K., Extracellular interactions and ligand degradation shape the nodal morphogen gradient. *eLife* **2016,** *5*, e13879.
154. Foroutan, M.; Fatemi, S. M.; Esmaeilian, F., A review of the structure and dynamics of nanoconfined water and ionic liquids via molecular dynamics simulation. *The European Physical Journal E* **2017,** *40* (2), 19.
155. Pal, T.; Beck, C.; Lessnich, D.; Vogel, M., Effects of Silica Surfaces on the Structure and Dynamics of Room-Temperature Ionic Liquids: A Molecular Dynamics Simulation Study. *The Journal of Physical Chemistry C* **2018,** *122* (1), 624-634.
156. Köster, R.; Vogel, M., Slow liquid dynamics near solid surfaces: Insights from site-resolved studies of ionic liquids in silica confinement. *The Journal of Chemical Physics* **2022,** *156* (7), 074501.
157. Elola, M. D.; Rodriguez, J., Ionic Mobility within Functionalized Silica Nanopores. *The Journal of Physical Chemistry C* **2019,** *123* (6), 3622-3633.
158. Khaknejad, Z.; Mehdipour, N.; Eslami, H., Molecular Dynamics Simulation of the Ionic Liquid 1-n-Butyl-3-Methylimidazolium Methylsulfate Bmim MeSO4 : Interfacial Properties at the Silica and Vacuum Interfaces. *Chemphyschem* **2020,** *21* (11), 1134-1145.
159. Horstmann, R.; Hecht, L.; Kloth, S.; Vogel, M., Structural and Dynamical Properties of Liquids in Confinements: A Review of Molecular Dynamics Simulation Studies. *Langmuir* **2022,** *American Chemical Society* (21), 6506-6522.
160. Shao, C.; Ong, W.-L.; Shiomi, J.; McGaughey, A. J. H., Nanoconfinement between Graphene Walls Suppresses the Near-Wall Diffusion of the Ionic Liquid BMIM PF6. *The Journal of Physical Chemistry B* **2021,** *125* (17), 4527-4535.
161. Dong, M.; Zhang, K.; Wan, X.; Fang, Z.; Hu, Y.; Ye, Z.; Wang, Y.; Li, Z.; Peng, X., Enhanced molecular transport in two-dimensional nanoconfined ionic liquids. *Applied Materials Today* **2022,** *27*.
162. Jayakody, N. K.; Fraenza, C. C.; Greenbaum, S. G.; Ashby, D.; Dunn, B. S., NMR Relaxometry and Diffusometry Analysis of Dynamics in Ionic Liquids and lonogels for Use in Lithium-Ion Batteries. *The Journal of Physical Chemistry B* **2020,** *124* (31), 6843-6856.
163. Ordikhani Seyedlar, A.; Stapf, S.; Mattea, C., Nuclear magnetic relaxation and diffusion study of the ionic liquids 1-ethyl- and 1-butyl-3-methylimidazolium bis(trifluoromethylsulfonyl)imide confined in porous glass. *Magnetic Resonance in Chemistry* **2019,** *57* (10), 818-828.

164. Kruk, D.; Wojciechowski, M.; Florek-Wojciechowska, M.; Singh, R. K., Dynamics of Ionic Liquids in Confinement by Means of NMR Relaxometry-EMIM-FSI in a Silica Matrix as an Example. *Materials* **2020,** *13* (19), 4351.
165. Burba, C. M.; Chang, H.-C., Confinement Effects on the Magnetic Ionic Liquid 1-Ethyl-3-methylimidazolium Tetrachloroferrate(III). *Molecules* **2022,** *27* (17), 5591.
166. Tripathi, A. K.; Singh, R. K., Immobilization induced molecular compression of ionic liquid in ordered mesoporous matrix. *Journal of Physics D: Applied Physics* **2018,** *51* (7), 075301.
167. Vavra, S.; Ahlberg, E.; Martinelli, A., Charge transfer and electrical double layer of an amphiphilic protic ionic liquid in bulk and when confined in nanochannels. *Physical Chemistry Chemical Physics* **2022,** *24* (39), 24469-24479.
168. Mandal, A. K.; Sen Mojumdar, S.; Das, A. K.; Bhattacharyya, K., Effect of Ionic Liquid on Diffusion in P123 Gel: Fluorescence Correlation Spectroscopy. *Chemphyschem* **2012,** *13* (7), 1942-1948.
169. Mendivelso-Pérez, D. L.; Farooq, M. Q.; Santra, K.; Anderson, J. L.; Petrich, J. W.; Smith, E. A., Diffusional Dynamics of Tetraalkylphosphonium Ionic Liquid Films Measured by Fluorescence Correlation Spectroscopy. *The Journal of Physical Chemistry B* **2019,** *123* (23), 4943-4949.
170. Prabhu, S. R.; Dutt, G. B., Rotational Diffusion of Organic Solutes in 1-Methyl-3-octylimidazolium Tetrafluoroborate-Diethylene Glycol Mixtures: Influence of Organic Solvent on the Organized Structure of the Ionic Liquid. *The Journal of Physical Chemistry B* **2014,** *118* (20), 5562-5569.
171. Schlipf, D. M.; Rankin, S. E.; Knutson, B. L., Pore-size dependent protein adsorption and protection from proteolytic hydrolysis in tailored mesoporous silica particles. *ACS Applied Materials & Interfaces* **2013,** *5* (20), 10111-7.
172. Kumar, S.; Jain, S. L., Non-symmetrical dialkyl carbonate synthesis promoted by 1-(3-trimethoxysilylpropyl)-3-methylimidazolium chloride. *New Journal of Chemistry* **2013,** *37* (10), 3057-3061.
173. Valizadeh, H.; Amiri, M.; Shomali, A.; Hosseinzadeh, F., Ionic liquid 1-(3-trimethoxysilylpropyl)-3-methylimidazolium nitrite as a new reagent for the efficient diazotization of aniline derivatives and in situ synthesis of azo dyes. *Journal of the Iranian Chemical Society* **2011,** *8* (2), 495-501.
174. Perrin, D. D.; Armarego, W. L. F., Purification of Organic Chemicals. In *Purification of Laboratory Chemicals*, 4th ed.; Butterworth-Heinemann: 1996; pp 63-361.
175. Pucadyil, T. J.; Chattopadhyay, A., Confocal fluorescence recovery after photobleaching of green fluorescent protein in solution. *Journal of Fluorescence* **2006,** *16* (1), 87-94.
176. Abràmoff, M. D.; Magalhães, P. J.; Ram, S. J., Image Processing with ImageJ. *Biophotonics International* **2004,** *11*, 36-42.
177. Kemmer, G.; Keller, S., Nonlinear least-squares data fitting in Excel spreadsheets. *Nature Protocols* **2010,** *5* (2), 267-281.
178. Innocenzi, P.; Falcaro, P.; Grosso, D.; Babonneau, F., Order−Disorder Transitions and Evolution of Silica Structure in Self-Assembled Mesostructured Silica Films Studied through FTIR Spectroscopy. *The Journal of Physical Chemistry B* **2003,** *107* (20), 4711-4717.

179. Ramenskaya, L. M.; Grishina, E. P., Intensification phenomenon of weak ionic interactions of 1-butyl-3-methylimidazolium hexafluorophosphate ionic liquid macro-dispersed in poly(methyl methacrylate): FTIR spectroscopic evidence. *Journal of Molecular Liquids* **2016,** *218*, 133-137.
180. Endo, T.; Kato, T.; Tozaki, K.-I.; Nishikawa, K., Phase Behaviors of Room Temperature Ionic Liquid Linked with Cation Conformational Changes: 1-Butyl-3-methylimidazolium Hexafluorophosphate. *The Journal of Physical Chemistry B* **2010,** *114* (1), 407-411.
181. Fredlake, C. P.; Crosthwaite, J. M.; Hert, D. G.; Aki, S. N. V. K.; Brennecke, J. F., Thermophysical Properties of Imidazolium-Based Ionic Liquids. *Journal of Chemical & Engineering Data* **2004,** *49*, 954-964.
182. Tretinnikov, O. N.; Ikada, Y., Dynamic Wetting and Contact Angle Hysteresis of Polymer Surfaces Studied with the Modified Wilhelmy Balance Method. *Langmuir* **1994,** *10* (5), 1606-1614.
183. Zhang, M.; Ma, N.; Dai, Z.; Song, X.; Ji, Q.; Li, L.; An, R., Immobilizing Ionic Liquids onto Functionalized Surfaces for Sensing Volatile Organic Compounds. *Langmuir* **2022,** *38* (48), 14550-14562.
184. Nandi, S.; Parui, S.; Jana, B.; Bhattacharyya, K., Local environment of organic dyes in an ionic liquid-water mixture: FCS and MD simulation. *The Journal of Chemical Physics* **2018,** *149* (5), 054501.
185. Watase, T.; Sohmiya, M.; Zhang, Z.; Kobori, Y.; Tachikawa, T., Unraveling Hidden Correlations between Molecular Diffusivity and Reactivity in Ruthenium Complex-Modified Mesoporous Silica. *The Journal of Physical Chemistry C* **2020,** *124* (39), 21502-21511.
186. Loren, N.; Hagman, J.; Jonasson, J. K.; Deschout, H.; Bernin, D.; Cella-Zanacchi, F.; Diaspro, A.; McNally, J. G.; Ameloot, M.; Smisdom, N.; Nyden, M.; Hermansson, A. M.; Rudemo, M.; Braeckmans, K., Fluorescence recovery after photobleaching in material and life sciences: putting theory into practice. *Quarterly Reviews of Biophysics* **2015,** *48* (3), 323-87.
187. Hochstrasser, J.; Svidrytski, A.; Höltzel, A.; Priamushko, T.; Kleitz, F.; Wang, W.; Kübel, C.; Tallarek, U., Morphology-transport relationships for SBA-15 and KIT-6 ordered mesoporous silicas. *Physical Chemistry Chemical Physics* **2020,** *22* (20), 11314-11326.
188. Zhang, L.-X.; Cao, X.-H.; Cai, W.-P.; Li, Y.-Q., Observations of the effect of confined space on fluorescence and diffusion properties of molecules in single conical nanopore channels. *Journal of Fluorescence* **2011,** *21* (5), 1865-70.
189. Schröder, U.; Wadhawan, J. D.; Compton, R. G.; Marken, F.; Suarez, P. A. Z.; Consorti, C. S.; de Souza, R. F.; Dupont, J., Water-induced accelerated ion diffusion: voltammetric studies in 1-methyl-3-[2,6-(S)-dimethylocten-2-yl]imidazolium tetrafluoroborate, 1-butyl-3-methylimidazolium tetrafluoroborate and hexafluorophosphate ionic liquids. *New Journal of Chemistry* **2000,** *24* (12), 1009-1015.
190. Wei, Y.; Dong, Y.; Ji, X.; Ullah Shah, F.; Laaksonen, A.; An, R.; Riehemann, K., Detailing molecular interactions of ionic liquids with charged SiO2 surfaces: A systematic AFM study. *Journal of Molecular Liquids* **2022,** *350*, 118506.

191. Abbas, U. L.; Qiao, Q.; Nguyen, M. T.; Shi, J.; Shao, Q., Structure and hydrogen bonds of hydrophobic deep eutectic solvent-aqueous liquid-liquid interfaces. *Aiche Journal* **2021,** *67* (12).
192. Kamaz, M.; Vogler, R. J.; Jebur, M.; Sengupta, A.; Wickramasinghe, R., π Electron induced separation of organic compounds using supported ionic liquid membranes. *Separation and Purification Technology* **2020,** *236*, 116237.
193. Leitch, A. C.; Abdelghany, T. M.; Probert, P. M.; Dunn, M. P.; Meyer, S. K.; Palmer, J. M.; Cooke, M. P.; Blake, L. I.; Morse, K.; Rosenmai, A. K.; Oskarsson, A.; Bates, L.; Figueiredo, R. S.; Ibrahim, I.; Wilson, C.; Abdelkader, N. F.; Jones, D. E.; Blain, P. G.; Wright, M. C., The toxicity of the methylimidazolium ionic liquids, with a focus on M8OI and hepatic effects. *Food and Chemical Toxicology* **2020,** *136*, 111069.
194. Wang, Y.; Li, C.; Guo, X.; Wu, G., The Influence of Silica Nanoparticles on Ionic Liquid Behavior: A Clear Difference between Adsorption and Confinement. *International Journal of Molecular Sciences* **2013,** *14* (10), 21045-21052.
195. Li, P.; Hu, X.; Zhang, L.; Dai, H.; Zhang, L., Sol-gel nanocasting synthesis of patterned hierarchical LaFeO3 fibers with enhanced catalytic CO oxidation activity. *Nanoscale* **2011,** *3* (3), 974-6.
196. Men, S.; Jiang, J., X-Ray Photoelectron Spectroscopy of Chlorometallate Ionic Liquids: Speciation and Anion Basicity. *Journal of Applied Spectroscopy* **2018,** *85* (1), 55-60.
197. Blundell, R. K.; Delorme, A. E.; Smith, E. F.; Licence, P., An ARXPS and ERXPS study of quaternary ammonium and phosphonium ionic liquids: utilising a high energy Ag Lα′ X-ray source. *Physical Chemistry Chemical Physics* **2016,** *18* (8), 6122-6131.
198. Fortunato, R.; Afonso, C.; Benavente, J.; Rodriguezcastellon, E.; Crespo, J., Stability of supported ionic liquid membranes as studied by X-ray photoelectron spectroscopy. *Journal of Membrane Science* **2005**.
199. Jurado, L. A.; Kim, H.; Rossi, A.; Arcifa, A.; Schuh, J. K.; Spencer, N. D.; Leal, C.; Ewoldt, R. H.; Espinosa-Marzal, R. M., Effect of the environmental humidity on the bulk, interfacial and nanoconfined properties of an ionic liquid. *Phys Chem Chem Phys* **2016,** *18* (32), 22719-30.
200. Yassin, F. A.; El Kady, F. Y.; Ahmed, H. S.; Mohamed, L. K.; Shaban, S. A.; Elfadaly, A. K., Highly effective ionic liquids for biodiesel production from waste vegetable oils. *Egyptian Journal of Petroleum* **2015,** *24* (1), 103-111.
201. Bordoloi, A.; Sahoo, S.; Lefebvre, F.; Halligudi, S., Heteropoly acid-based supported ionic liquid-phase catalyst for the selective oxidation of alcohols. *Journal of Catalysis* **2008,** *259* (2), 232-239.
202. Lee, B.; Lo, C.-T.; Seifert, S.; Winans, R. E., Silver behenate as a calibration standard of grazing-incidence small-angle X-ray scattering. *Journal of Applied Crystallography* **2006,** *39* (5), 749-751.
203. Mazzoldi, P.; Carnera, A.; Caccavale, F.; Favaro, M. L.; Boscolo-Boscoletto, A.; Granozzi, G.; Bertoncello, R.; Battaglin, G., N and Ar ion-implantation effects in SiO2films on Si single-crystal substrates. *Journal of Applied Physics* **1991,** *70* (7), 3528-3536.
204. Smith, E. F.; Rutten, F. J. M.; Villar-Garcia, I. J.; Briggs, D.; Licence, P., Ionic Liquids in Vacuo: Analysis of Liquid Surfaces Using Ultra-High-Vacuum Techniques. *Langmuir* **2006,** *22* (22), 9386-9392.

205. Villar-Garcia, I. J.; Smith, E. F.; Taylor, A. W.; Qiu, F.; Lovelock, K. R.; Jones, R. G.; Licence, P., Charging of ionic liquid surfaces under X-ray irradiation: the measurement of absolute binding energies by XPS. *Phys Chem Chem Phys* **2011,** *13* (7), 2797-808.
206. Bernardi, F.; Scholten, J. D.; Fecher, G. H.; Dupont, J.; Morais, J., Probing the chemical interaction between iridium nanoparticles and ionic liquid by XPS analysis. *CHEMICAL PHYSICS LETTERS* **2009,** *479* (1-3), 113-116.
207. Oveisi, H.; Beitollahi, A.; Imura, M.; Wu, C.-W.; Yamauchi, Y., Synthesis and characterization of highly ordered titania-alumina mixed oxide mesoporous films with high alumina content. *Microporous and Mesoporous Materials* **2010,** *134* (1-3), 150-156.
208. Coquil, T.; Richman, E. K.; Hutchinson, N. J.; Tolbert, S. H.; Pilon, L., Thermal conductivity of cubic and hexagonal mesoporous silica thin films. *Journal of Applied Physics* **2009,** *106* (3).
209. Cremer, T.; Stark, M.; Deyko, A.; Steinruck, H. P.; Maier, F., Liquid/solid interface of ultrathin ionic liquid films: [C1C1Im][Tf2N] and [C8C1Im][Tf2N] on Au(111). *Langmuir* **2011,** *27* (7), 3662-71.
210. Del Pópolo, M. G.; Kohanoff, J.; Lynden-Bell, R. M., Solvation Structure and Transport of Acidic Protons in Ionic Liquids: A First-principles Simulation Study. *The Journal of Physical Chemistry B* **2006,** *110* (17), 8798-8803.
211. Ori, G.; Villemot, F.; Viau, L.; Vioux, A.; Coasne, B., Ionic liquid confined in silica nanopores: molecular dynamics in the isobaric–isothermal ensemble. *Molecular Physics* **2014,** *112* (9-10), 1350-1361.
212. Paszkiewicz-Gawron, M.; Długokęcka, M.; Lisowski, W.; Paganini, M. C.; Giamello, E.; Klimczuk, T.; Paszkiewicz, M.; Grabowska, E.; Zaleska-Medynska, A.; Łuczak, J., Dependence between Ionic Liquid Structure and Mechanism of Visible-Light-Induced Activity of TiO2 Obtained by Ionic-Liquid-Assisted Solvothermal Synthesis. *ACS Sustainable Chemistry & Engineering* **2017,** *6* (3), 3927-3937.
213. Baldelli, S., Interfacial Structure of Room-Temperature Ionic Liquids at the Solid-Liquid Interface as Probed by Sum Frequency Generation Spectroscopy. *J Phys Chem Lett* **2013,** *4* (2), 244-52.
214. Deyko, A.; Cremer, T.; Rietzler, F.; Perkin, S.; Crowhurst, L.; Welton, T.; Steinrück, H.-P.; Maier, F., Interfacial Behavior of Thin Ionic Liquid Films on Mica. *The Journal of Physical Chemistry C* **2013,** *117* (10), 5101-5111.
215. Chastain, J.; King Jr, R. C., Handbook of X-ray photoelectron spectroscopy. *Perkin-Elmer Corporation* **1992,** *40*, 221.
216. Trulove, P. C.; Osteryoung, R. A., Proton speciation in ambient-temperature chloroaluminate ionic liquids. *Inorganic Chemistry* **1992,** *31* (19), 3980-3985.
217. Mitchell, D. F.; Sproule, G. I.; Graham, M. J., Sputter reduction of oxides by ion bombardment during Auger depth profile analysis. **1990,** *15* (8), 487-497.
218. Loula, M.; Kaňa, A.; Mestek, O., Non-spectral interferences in single-particle ICP-MS analysis: an underestimated phenomenon. *Talanta* **2019,** *202*, 565-571.
219. Santos, A. R.; Blundell, R. K.; Licence, P., XPS of guanidinium ionic liquids: a comparison of charge distribution in nitrogenous cations. *Phys Chem Chem Phys* **2015,** *17* (17), 11839-47.

220. Lee, S. H.; Ha, S. H.; Ha, S.-S.; Jin, H.-B.; You, C.-Y.; Koo, Y.-M., Magnetic behavior of mixture of magnetic ionic liquid [bmim]FeCl4 and water. *Journal of Applied Physics* **2007,** *101* (9).
221. Calisi, N.; Martinuzzi, S.; Giaccherini, A.; Pomelli, C. S.; Guazzelli, L.; Caporali, S., Temperature and angle resolved XPS study of BMIm Cl and BMIm FeCl4. *Journal of Electron Spectroscopy and Related Phenomena* **2021,** *247*.
222. Otsuka, H.; Futamura, R.; Amako, Y.; Ozeki, S.; Iiyama, T., Effect of pore size on the magnetic properties of emim FeCl4 confined in the pores of SBA-15. *Chemical Physics Letters* **2022,** *804*, 139878.
223. Nockemann, P.; Binnemans, K.; Driesen, K., Purification of imidazolium ionic liquids for spectroscopic applications. *Chemical physics letters* **2005,** *415* (1-3), 131-136.
224. Cremer, T.; Kolbeck, C.; Lovelock, K. R. J.; Paape, N.; Wölfel, R.; Schulz, P. S.; Wasserscheid, P.; Weber, H.; Thar, J.; Kirchner, B., Towards a Molecular Understanding of Cation–Anion Interactions—Probing the Electronic Structure of Imidazolium Ionic Liquids by NMR Spectroscopy, X-ray Photoelectron Spectroscopy and Theoretical Calculations. *Chemistry–A European Journal* **2010,** *16* (30), 9018-9033.
225. Grosvenor, A. P.; Kobe, B. A.; Biesinger, M. C.; McIntyre, N. S., Investigation of multiplet splitting of Fe 2p XPS spectra and bonding in iron compounds. *Surface and Interface Analysis* **2004,** *36* (12), 1564-1574.
226. Gengenbach, T. R.; Major, G. H.; Linford, M. R.; Easton, C. D., Practical guides for x-ray photoelectron spectroscopy (XPS): Interpreting the carbon 1s spectrum. *Journal of Vacuum Science & Technology A: Vacuum, Surfaces, and Films* **2021,** *39* (1), 013204.
227. Tomazett, V. K.; Chacon, G.; Marin, G.; Castegnaro, M. V.; das Chagas, R. P.; Lião, L. M.; Dupont, J.; Qadir, M. I., Ionic liquid confined spaces controlled catalytic CO2 cycloaddition of epoxides in BMIm.ZnCl3 and its supported ionic liquid phases. *Journal of CO2 Utilization* **2023,** *69*.
228. Costine, A.; Thurgate, S., Iron adsorption on SiO2/Si (111). *Surface and Interface Analysis: An International Journal devoted to the development and application of techniques for the analysis of surfaces, interfaces and thin films* **2007,** *39* (8), 711-714.
229. Keinan, E.; Mazur, Y., Reactions in dry media. Ferric chloride adsorbed on silica gel. A multipurpose, easily controllable reagent. *The Journal of Organic Chemistry* **1978,** *43* (5), 1020-1022.
230. Barzetti, T.; Selli, E.; Moscotti, D.; Forni, L., Pyridine and ammonia as probes for FTIR analysis of solid acid catalysts. *Journal of the Chemical Society, Faraday Transactions* **1996,** *92* (8), 1401-1407.
231. Bjelić, A.; Hočevar, B.; Grilc, M.; Novak, U.; Likozar, B., A review of sustainable lignocellulose biorefining applying (natural) deep eutectic solvents (DESs) for separations, catalysis and enzymatic biotransformation processes. *Reviews in Chemical Engineering* **2022,** *38* (3), 243-272.
232. Lu, P.; Sun, P.; Ma, Q.; Su, H.; Leung, P.; Yang, W.; Xu, Q., Rationally Designed Ternary Deep Eutectic Solvent Enabling Higher Performance for Non-Aqueous Redox Flow Batteries. Processes 2022, 10, 649. 2022.
233. Zhang, Q.; Vigier, K. D. O.; Royer, S.; Jérôme, F., Deep eutectic solvents: syntheses, properties and applications. *Chemical Society Reviews* **2012,** *41* (21), 7108-7146.

234. Zante, G.; Braun, A.; Masmoudi, A.; Barillon, R.; Trebouet, D.; Boltoeva, M., Solvent extraction fractionation of manganese, cobalt, nickel and lithium using ionic liquids and deep eutectic solvents. *Minerals Engineering* **2020,** *156*, 106512.
235. Tian, H.; Cheng, R.; Zhang, L.; Fang, Q.; Ma, P.; Lv, Y.; Wei, F., A ZnCl2 nonaqueous deep-eutectic-solvent electrolyte for zinc-ion hybrid supercapacitors. *Materials Letters* **2021,** *301*, 130237.
236. Xia, Q.; Liu, Y.; Meng, J.; Cheng, W.; Chen, W.; Liu, S.; Liu, Y.; Li, J.; Yu, H., Multiple hydrogen bond coordination in three-constituent deep eutectic solvents enhances lignin fractionation from biomass. *Green Chemistry* **2018,** *20* (12), 2711-2721.
237. Li, Q.; Ma, C.; Di, J.; Ni, J.; He, Y. C., Catalytic valorization of biomass for furfuryl alcohol by novel deep eutectic solvent-silica chemocatalyst and newly constructed reductase biocatalyst. *Bioresour Technol* **2022,** *347*, 126376.
238. Zhang, Y.; You, Y.; Gao, Q.; Zhang, C.; Wang, S.; Qin, Y.; Zhu, Y.; Lu, X., Molecular insight into flow resistance of choline chloride/urea confined in ionic model nanoslits. *Fluid Phase Equilibria* **2020**, 112934.
239. Robertson, C.; Beanland, R.; Boden, S. A.; Hector, A. L.; Kashtiban, R. J.; Sloan, J.; Smith, D. C.; Walcarius, A., Ordered mesoporous silica films with pores oriented perpendicular to a titanium nitride substrate. *Phys Chem Chem Phys* **2015,** *17* (6), 4763-70.
240. Mohamed, N. A. N.; Han, Y.; Hector, A. L.; Houghton, A. R.; Hunter-Sellars, E.; Reid, G.; Williams, D. R.; Zhang, W., Increasing the Diameter of Vertically Aligned, Hexagonally Ordered Pores in Mesoporous Silica Thin Films. *Langmuir* **2022,** *38* (7), 2257-2266.
241. Zhou, S.; Schlipf, D. M.; Guilfoil, E. C.; Rankin, S. E.; Knutson, B. L., Lipid Pore-Filled Silica Thin-Film Membranes for Biomimetic Recovery of Dilute Carbohydrates. *Langmuir* **2017,** *33* (49), 14156-14166.
242. Yamauchi, Y.; Sawada, M.; Noma, T.; Ito, H.; Furumi, S.; Sakka, Y.; Kuroda, K. J. J. o. M. C., Orientation of mesochannels in continuous mesoporous silica films by a high magnetic field. **2005,** *15* (11), 1137-1140.
243. Walcarius, A.; Sibottier, E.; Etienne, M.; Ghanbaja, a., Electrochemically assisted self-assembly of mesoporous silica thin films. *Nature materials* **2007,** *6* (8), 602-608.
244. Xu, J.; Ma, Q.; Su, H.; Qiao, F.; Leung, P.; Shah, A.; Xu, Q., Redox characteristics of iron ions in different deep eutectic solvents. *Ionics* **2019,** *26* (1), 483-492.
245. Audrieth, L. F., *Inorganic Synthesis*. McGraw-Hill Book Company: 1950; Vol. 3, p 4.
246. Du, C.; Zhao, B.; Chen, X.-B.; Birbilis, N.; Yang, H., Effect of water presence on choline chloride-2urea ionic liquid and coating platings from the hydrated ionic liquid. *Scientific reports* **2016,** *6* (1), 29225.
247. Timón, V.; Maté, B.; Herrero, V. J.; Tanarro, I. J. P. C. C. P., Infrared spectra of amorphous and crystalline urea ices. **2021,** *23* (39), 22344-22351.
248. Keuleers, R.; Desseyn, H. O.; Rousseau, B.; Van Alsenoy, C., Vibrational analysis of urea. *The Journal of Physical Chemistry A* **1999,** *103* (24), 4621-4630.
249. Joseph, J.; Jemmis, E. D., Red-, blue-, or no-shift in hydrogen bonds: a unified explanation. *Journal of the American Chemical Society* **2007,** *129* (15), 4620-4632.

250. Chirea, M.; Freitas, A.; Vasile, B. S.; Ghitulica, C.; Pereira, C. M.; Silva, F., Gold nanowire networks: synthesis, characterization, and catalytic activity. *Langmuir* **2011,** *27* (7), 3906-3913.
251. Gabriele, F.; Chiarini, M.; Germani, R.; Tiecco, M.; Spreti, N., Effect of water addition on choline chloride/glycol deep eutectic solvents: Characterization of their structural and physicochemical properties. *Journal of Molecular Liquids* **2019,** *291*, 111301.
252. Lu, P.; Sun, P.; Ma, Q.; Su, H.; Leung, P.; Yang, W.; Xu, Q., Rationally Designed Ternary Deep Eutectic Solvent Enabling Higher Performance for Non-Aqueous Redox Flow Batteries. *Processes* **2022,** *10* (4), 649.
253. Abbott, A. P.; Harris, R. C.; Ryder, K. S., Application of hole theory to define ionic liquids by their transport properties. *The Journal of Physical Chemistry B* **2007,** *111* (18), 4910-4913.
254. D'Agostino, C.; Harris, R. C.; Abbott, A. P.; Gladden, L. F.; Mantle, M. D., Molecular motion and ion diffusion in choline chloride based deep eutectic solvents studied by 1 H pulsed field gradient NMR spectroscopy. *Physical Chemistry Chemical Physics* **2011,** *13* (48), 21383-21391.
255. Shah, D.; Mjalli, F. S., Effect of water on the thermo-physical properties of Reline: An experimental and molecular simulation based approach. *Phys. Chem. Chem. Phys.* **2014,** *16* (43), 23900-23907.
256. Agieienko, V.; Buchner, R., Variation of density, viscosity, and electrical conductivity of the deep eutectic solvent reline, composed of choline chloride and urea at a molar ratio of 1: 2, mixed with dimethylsulfoxide as a cosolvent. *Journal of Chemical & Engineering Data* **2020,** *65* (4), 1900-1910.
257. Xu, Q.; Ji, Y. N.; Qin, L. Y.; Leung, P. K.; Shah, A. A.; Li, Y. S.; Su, H. N.; Li, H. M., Effect of carbon dioxide additive on the characteristics of a deep eutectic solvent (DES) electrolyte for non-aqueous redox flow batteries. *Chemical Physics Letters* **2018,** *708*, 48-53.
258. Chakrabarti, M. H.; Brandon, N. P.; Mjalli, F. S.; Bahadori, L.; Al Nashef, I. M.; Hashim, M. A.; Hussain, M. A.; Low, C. T. J.; Yufit, V., Cyclic Voltammetry of Metallic Acetylacetonate Salts in Quaternary Ammonium and Phosphonium Based Deep Eutectic Solvents. *Journal of Solution Chemistry* **2013,** *42* (12), 2329-2341.
259. Han, M.; Espinosa-Marzal, R. M., Electroviscous retardation of the squeeze out of nanoconfined ionic liquids. *The Journal of Physical Chemistry C* **2018,** *122* (37), 21344-21355.
260. Gil, P. S.; Jorgenson, S. J.; Riet, A. R.; Lacks, D. J., Relationships between molecular structure, interfacial structure, and dynamics of ionic liquids near neutral and charged surfaces. *The Journal of Physical Chemistry C* **2018,** *122* (48), 27462-27468.
261. Yamagata, M.; Tachikawa, N.; Katayama, Y.; Miura, T., Electrochemical behavior of several iron complexes in hydrophobic room-temperature ionic liquids. *Electrochimica acta* **2007,** *52* (9), 3317-3322.
262. Migita, T.; Tachikawa, N.; Katayama, Y.; Miura, T., Thermoelectromotive force of some redox couples in an amide-type room-temperature ionic liquid. *Electrochemistry* **2009,** *77* (8), 639-641.

263. Moradi, K.; Rahimi, S.; Ebrahimi, S.; Salimi, A., Understanding the bulk and interfacial structures of ternary and binary deep eutectic solvents with a constant potential method: a molecular dynamics study. *Phys Chem Chem Phys* **2022,** *24* (18), 10962-10973.
264. Liu, S.; Yu, D.; Chen, Y.; Shi, R.; Zhou, F.; Mu, T., High-Resolution Thermogravimetric Analysis Is Required for Evaluating the Thermal Stability of Deep Eutectic Solvents. *Industrial & Engineering Chemistry Research* **2022,** *61* (38), 14347-14354.
265. Abbott, A. P.; Capper, G.; Davies, D. L.; Rasheed, R., Ionic Liquids Based upon Metal Halide/Substituted Quaternary Ammonium Salt Mixtures. *Inorganic Chemistry* **2004,** *43* (11), 3447-3452.
266. Feng, Y.; Yan, G.; Wang, T.; Jia, W.; Zeng, X.; Sperry, J.; Sun, Y.; Tang, X.; Lei, T.; Lin, L., Synthesis of MCM-41-supported metal catalysts in deep eutectic solvent for the conversion of carbohydrates into 5-hydroxymethylfurfural. *ChemSusChem* **2019,** *12* (5), 978-982.
267. Tran, P. H.; Nguyen, H. T.; Hansen, P. E.; Le, T. N., An efficient and green method for regio-and chemo-selective Friedel–Crafts acylations using a deep eutectic solvent ([CholineCl][ZnCl 2] 3). *RSC advances* **2016,** *6* (43), 37031-37038.
268. Abbott, A. P.; Boothby, D.; Capper, G.; Davies, D. L.; Rasheed, R. K., Deep Eutectic Solvents Formed between Choline Chloride and Carboxylic Acids: Versatile Alternatives to Ionic Liquids. *Journal of the American Chemical Society* **2004,** *126* (29), 9142-9147.
269. Adeyemi, I.; Sulaiman, R.; Almazroui, M.; Al-Hammadi, A.; AlNashef, I. M., Removal of chlorophenols from aqueous media with hydrophobic deep eutectic solvents: Experimental study and COSMO RS evaluation. *Journal of Molecular Liquids* **2020,** *311*.
270. Tang, B.; Park, H. E.; Row, K. H., Preparation of chlorocholine chloride/urea deep eutectic solvent-modified silica and an examination of the ion exchange properties of modified silica as a Lewis adduct. *Anal Bioanal Chem* **2014,** *406* (17), 4309-13.
271. del Hierro, I.; Pérez, Y.; Fajardo, M., Silanization of Iron Oxide Magnetic Nanoparticles with ionic liquids based on amino acids and its application as heterogeneous catalysts for Knoevenagel condensation reactions. *Molecular Catalysis* **2018,** *450*, 112-120.
272. Hierro, I. d.; Pérez, Y.; Fajardo, M., Supported choline hydroxide (ionic liquid) on mesoporous silica as heterogeneous catalyst for Knoevenagel condensation reactions. *Microporous and Mesoporous Materials* **2018,** *263*, 173-180.
273. Borodina, E.; Karpov, S. I.; Selemenev, V. F.; Schwieger, W.; Maracke, S.; Fröba, M.; Rößner, F., Surface and texture properties of mesoporous silica materials modified by silicon-organic compounds containing quaternary amino groups for their application in base-catalyzed reactions. *Microporous and Mesoporous Materials* **2015,** *203*, 224-231.
274. Oliveira, J. S. d.; Salla, J. d. S.; Kuhn, R. C.; Jahn, S. L.; Foletto, E. L., Catalytic Ozonation of Melanoidin in Aqueous Solution over CoFe2O4 Catalyst. *Materials Research* **2018,** *22* (1).
275. Singh, R.; Singh, T. A.; Singh, T.; Gaur, R.; Pandey, P. K.; Jamal, F.; Bansal, S.; Pandey, L. K.; Sarsaiya, S.; Nagpure, J.; Mishra, S.; Gaur, M. K.; Gupta, P.; Uikey, P.; K. Patel, S.; Patel, R., Origin and Remediation of Melanoidin Contamination in Water

Sources. *International Journal of Current Microbiology and Applied Sciences* **2019,** *8* (02), 1399-1415.
276. Wang, H.-Y.; Qian, H.; Yao, W.-R., Melanoidins produced by the Maillard reaction: Structure and biological activity. *Food chemistry* **2011,** *128* (3), 573-584.
277. Wagh, M. P.; Nemade, P. D.; Naik, U.; Sengupta, A., Enhancing color and chemical oxygen demand degradation in distillery spent wash by electrocoagulation and ozone assisted electrocoagulation. *Desalination and Water Treatment* **2020,** *197*, 213-223.
278. Ahmed, S.; Unar, I. N.; Khan, H. A.; Maitlo, G.; Mahar, R. B.; Jatoi, A. S.; Memon, A. Q.; Shah, A. K., Experimental study and dynamic simulation of melanoidin adsorption from distillery effluent. *Environmental Science and Pollution Research* **2020,** *27*, 9619-9636.
279. Rizvi, S.; Singh, A.; Kushwaha, A.; Gupta, S. K., Recent advances in melanoidin removal from wastewater: Sources, properties, toxicity, and remediation strategies. *Emerging Trends to Approaching Zero Waste* **2022**, 361-386.
280. Kim, S. B.; Hayase, F.; Kato, H., Decolorization and degradation products of melanoidins on ozonolysis. *Agricultural and Biological Chemistry* **1985,** *49* (3), 785-792.
281. Hayase, F.; Kim, S. B.; Kato, H., Decolorization and degradation products of the melanoidins by hydrogen peroxide. *Agricultural and Biological Chemistry* **1984,** *48* (11), 2711-2717.
282. Takle, S. P.; Naik, S. D.; Khore, S. K.; Ohwal, S. A.; Bhujbal, N. M.; Landge, S. L.; Kale, B. B.; Sonawane, R. S., Photodegradation of spent wash, a sugar industry waste, using vanadium-doped TiO 2 nanoparticles. *RSC advances* **2018,** *8* (36), 20394-20405.
283. Islam, S. Z.; Reed, A.; Kim, D. Y.; Rankin, S. E., N2/Ar plasma induced doping of ordered mesoporous TiO2 thin films for visible light active photocatalysis. *Microporous and Mesoporous Materials* **2016,** *220*, 120-128.
284. Garay, J., Characterization and Electrochemical Performance of Dopamine-sensitized Titania Thin Films. **2020**.
285. Jiang, H.; Cheng, Y.; Wang, Z.; Bai, Z.; Tang, Y.; Sun, Y.; Wan, P.; Chen, Y., Degradation of a Lignin Model Compound by ROS Generated In Situ through Controlled ORR in Ionic Liquid. *Journal of The Electrochemical Society* **2021,** *168* (1).
286. Lahtinen, M.; Kruus, K.; Boer, H.; Kemell, M.; Andberg, M.; Viikari, L.; Sipilä, J., The effect of lignin model compound structure on the rate of oxidation catalyzed by two different fungal laccases. *Journal of Molecular Catalysis B: Enzymatic* **2009,** *57* (1-4), 204-210.
287. Bernardo, E. C.; Egashira, R.; Kawasaki, J., Decolorization of molasses' wastewater using activated carbon prepared from cane bagasse. *Carbon* **1997,** *35* (9), 1217-1221.
288. Dwyer, J.; Kavanagh, L.; Lant, P., The degradation of dissolved organic nitrogen associated with melanoidin using a UV/H2O2 AOP. *Chemosphere* **2008,** *71* (9), 1745-1753.
289. Nguyen, J. D.; Matsuura, B. S.; Stephenson, C. R. J., A photochemical strategy for lignin degradation at room temperature. *Journal of the American Chemical Society* **2014,** *136* (4), 1218-1221.

290. Chen, C.; Liu, P.; Xia, H.; Zhou, M.; Zhao, J.; Sharma, B. K.; Jiang, J., Photocatalytic cleavage of β-O-4 ether bonds in lignin over Ni/TiO2. *Molecules* **2020,** *25* (9), 2109.
291. Yang, C.; Maldonado, S.; Stephenson, C. R. J., Electrocatalytic Lignin Oxidation. *ACS Catalysis* **2021,** *11* (16), 10104-10114.

VITA

Education institutions attended and degrees already awarded:

Associate of Science, Volunteer State Community College, Gallatin, TN, 2014

Bachelor of Science in Chemical Engineering, University of Tennessee at Chattanooga, Chattanooga, TN, 2017

Professional positions held:

Graduate Research Assistant, Chemical and Materials Engineering Department, University of Kentucky, Lexington, KY, Aug 2018 - Present

Teaching Assistant, Chemical and Materials Engineering Department, University of Kentucky, Lexington, KY, Aug 2018 - May 2019

NBMC Graduate Student Internship, UES Inc. and Air Force Research Lab, Dayton, OH, June 2022 – Sept 2022

Field Engineer III, Ecolab, Spring Hill, TN, Oct 2017 – July 2018

Professional Publications:

Journal publications:

1. He, Y.; Khan, M. A.; **Drake, A. D.**; Ladipo, F.; Rankin, S. E.; Knutson, B. L., Nanoconfinement Effects on the Transport of Redox Probes in Ionic Liquid-Loaded Mesoporous Silica Thin Films. Industrial & Engineering Chemistry Research 2022.
2. He, Y.; Khan, M. A.; **Drake, A.**; Ghanim, R.; Garay, J.; Shirodkar, A.; Strzalka, J.; Zhang, Q.; Knutson, B. L.; Rankin, S. E., Formation of Vertically Oriented Channels during Calcination of Surfactant-Templated Titania-Doped Mesoporous Silica Thin Films. The Journal of Physical Chemistry C 2021, 125 (40), 22262-22273.

Andrew Drake